INTEGRATING GEOLOGY, ROCK PHYSICS, AND SEISMOLOGY
FOR RESERVOIR-QUALITY PREDICTION

A DISSERTATION

SUBMITTED TO THE DEPARTMENT OF GEOPHYSICS

AND THE COMMITTEE ON GRADUATE STUDIES OF

STANFORD UNIVERSITY

IN PARTIAL FULFILLMENT OF THE REQUIREMENTS

FOR THE DEGREE OF

DOCTOR OF PHILOSOPHY

Juan-Mauricio Flórez-Niño

May 2005

I certify that I have read this dissertation and that is my opinion it is fully adequate in scope of and quality as a dissertation for the degree of Doctor of Philosophy.

_____

Gary Mavko (Principal Adviser)

I certify that I have read this dissertation and that is my opinion it is fully adequate in scope of and quality as a dissertation for the degree of Doctor of Philosophy.

_____

Stephan Graham

I certify that I have read this dissertation and that is my opinion it is fully adequate in scope of and quality as a dissertation for the degree of Doctor of Philosophy.

_____

Jack Dvorkin

Approved by the University Committee on Graduate Studies:

_____

Abstract

Prediction and mapping of reservoir properties in the subsurface requires the integration of knowledge and concepts from different disciplines. This research focuses on prediction of reservoir quality from seismic and well-log data, integrating concepts from sedimentary geology, rock physics, geostatistics, reflection seismology, and geomechanics. My main purpose has been to understand the geologic processes that control lateral variations in acoustic impedance and porosity. That is, the origin and variability of elastic and bulk properties, like porosity and permeability, of sedimentary rocks within stratigraphic sequences. This work focuses on the effect of rock texture and fractures on the elastic properties of sedimentary rocks. I address three main aspects of this general problem: (1) improving the understanding of how textural variations affect the elastic and bulk properties of clastic sedimentary rocks; (2) mapping and explaining the patterns and changes in seismic properties of lithofacies and stratigraphic sequences (packages of lithofacies) in the rock-physics planes (velocity-porosity, velocity-density); and (3) using outcrop information and seismic data to constrain static geologic modeling of fractured reservoirs in the subsurface.

I review the concepts of depositional and diagenetic rock-physics trends and improve the current understanding of effective-medium models for sedimentary rocks. I show that the modified Hashin-Shtrikman lower bound can be used to distinguish between sorting and packing effects, since it actually constitutes an upper bound for the sorting effect and a lower bound for the packing effect. Pressure solution is analyzed as an alternative mechanism to reproduce the rock-physics diagenetic trend for high-porosity quartzose sands. I propose the Digby-Rutter pressure-solution model, a new model based on the combination of Digby's solution for the intergranular force and Rutter's model for pressure-solution.

I explore the patterns that clastic sedimentary sequences present in the rock-physics planes, and show how these patterns agree with predictions from models derived from theoretical and experimental studies. Dispersed sand-clay mixtures

predominate in fluvial deposits, whereas laminar mixtures tend to predominate in mud-rich deep-water deposits. Scarcity of mixed lithofacies characterizes sand-rich deep-water deposits, whereas abundance of these lithofacies occurs in low-energy shallow marine deposits. The results obtained demonstrate that the elastic properties of clastic mixed lithofacies strongly vary depending on the mixture's proportion and fabric, and rock-physics models can be used to predict these variations.

The second part of this research focuses on the use of outcrop information and seismic data to predict fracture distribution in the subsurface. Based on outcrop descriptions, this work documents a fundamental link between fracture hierarchies and sequence stratigraphy. Fracture spacing and dimensions of different fracture hierarchies are constrained by the thickness of the confining stratigraphic interval. This work also documents clear examples of hierarchical shearing and progressive deformation, a new concept in geomechanics that explains the evolution of faults and fracture systems. I also evaluate different geostatistical techniques to create digital static models of fractured reservoirs using outcrop data. The stochastic-fault-modeling technique creates maps of fracture density based on stochastic simulation, using an object-based indicator approach. Finally, this study presents an example of a truly integrated approach to the prediction of fracture swarms from seismic data, starting from the fundamental geomechanical understanding of fracture localization, analyzing the expected seismic response using rock-physics concepts, and applying these concepts to the interpretation of seismic attributes.

Acknowledgements

These five years at Stanford have been a wonderful, enriching, and delightful experience for my family and myself. I am very grateful to the people that have made this possible.

First of all, I extend my gratitude to my advisor Gary Mavko. During all these years Gary has been a supportive and assertive adviser, an example of excellence in teaching, an open-minded dynamic researcher, and a source of wise advice. I have been honored with and fortunate of having the opportunity to work with Gary.

I would also like to thank my defense and reading committee members, Stephan Graham, Jack Dvorkin, Biondo Biondi, and Youngseuk Kheem. In addition to their teachings, along these years they have made valuable comments and suggestions that definitely improved the results of this research.

I extend my gratitude to the Stanford Rock Physics and Borehole Project, particularly to Amos Nur, Gary Mavko, Jack Dvorkin, Tapan Mukerji, and Manika Prasad. Thanks also to all the SRB students who shared this experience with me. The SRB provided the support and creative environment that allowed me to grow as a researcher. Obviously, special thanks to Margaret Muir who takes care of all the painful administrative processes, making the paper work a smooth process for the SRB students. Thanks also to my officemates Sandra, Emma, Aya, Futoshi, Ezequiel, and Laura, for their patience and company.

This research has also benefited from my interaction with different professors and students at Stanford. In addition to Gary and my committee members, I would like to thank professors Atilla Aydin, Dave Pollard, and Mark Zoback. I am also thankful to other professors who taught me about their respective expertise: Jeff Caers, John Claerbout, Peter Eichbul, Margot Gerritsen, Jerry Harris, Andre Journel, Simon Kemplerer, Andre Lew, Tim McHargue, Tapan Mukerji, and Amos Nur.

Thanks also to Mario Gutierrez, Ezequiel Gonzalez, Diana Sava, Mike Zimmer, Per Avseth, Laura Chiaramonte, Frantz Maerten, Asterio Ayaviri, Marco Antonellini, Nick Davatzes, Elizabeth Diaz, Gabriel Alvarez, and Anyela Morcote.

All of them collaborated with my research, either throughout enriching academic discussions or with rigorous fieldwork.

Finally, I would like to express my profound gratitude to my wife Anyela. She has always been there, taking care of all the little things that keep the harmony of our life. Obviously, my gratitude extends to my daughter, Nadia, and my son, Juan-Sebastian. They are two wonderful kids that behave themselves very well, having the patience and consideration that allowed me to steal hours and days from the time they deserved.

Table of Contents

List of Tables

List of Figures

Chapter 1

Introduction

Prediction and mapping of reservoir properties in the subsurface requires the integration of knowledge and concepts from different disciplines, which by itself is an epistemological problem. Although the benefits of integrating data and concepts from different sources and disciplines have long ago been recognized, the epistemological barriers that obstruct the flow of knowledge and information between different disciplines have not. Throughout this dissertation I have made an effort to put within the same framework concepts and methods from disciplines that, although they deal with the same problem, look at it from different perspectives.

This research focuses on prediction of reservoir quality from seismic and well-log data, integrating concepts from sedimentary geology, rock physics, geostatistics, reflection seismology, and geomechanics. This work has developed concepts and methods that will help in the assessment of reservoir quality from seismic data. The main purpose has been the understanding of the origin and the variability of elastic and hydraulic properties of sedimentary rocks within stratigraphic sequences, associated with changes in the dry rock framework, that is, the effect of rock texture and fractures on the elastic properties of sedimentary rocks. The work concentrates on clastic deposits composed of mixtures of sand, silt, clay, and cement, and the distribution of fractures and their elastic effect on these sedimentary packages. I address three main aspects of this general problem: (1) improving the understanding of the effect of textural variations on the elastic and hydraulic properties of clastic sedimentary rocks; (2) mapping and explaining the patterns and changes in seismic properties of lithofacies and stratigraphic sequences (packages of lithofacies) in the various rock-physics planes; and (3) characterizing and geologic modeling of fractured reservoirs in the subsurface using outcrop analogues and seismic data.

1.1. Seismology, Seismic Stratigraphy and Reservoir Quality Prediction

Prediction of fluid types, saturations and petrophysical properties (porosity and permeability) of reservoir rocks is a critical issue for exploration and development of hydrocarbon resources in sedimentary basins (i.e. Kupecz *et al.*, 1997). Spatial, temporal and scale-dependent variability of these properties is of primary importance for evaluating the economic potential of hydrocarbon accumulations. In the future, this issue may become a significant problem for other resources, like water, since appropriate determination of these properties is key to obtaining accurate hydrologic fluid-flow models.

The seismic reflection method is a cost-effective and efficient way to sample the subsurface. It has been extensively used in hydrocarbon exploration and exploitation, and has been particularly successful in reservoir delineation, characterization and monitoring (i.e. Berg and Woolverton, 1985; Sheriff and Geldhart, 1995; Brown, 1991). Routine application of shallow seismic reflection for engineering purposes started in the 1980s (Burger, 1992) and may become significantly more important in this century.

Reflection seismology allowed the development of seismic stratigraphy (Payton, 1977). Seismic stratigraphy focused on the analysis of geometric patterns of reflections to infer depositional systems and sequences (Mitchum *et al.*, 1977), and therefore predict lithofacies. The findings in this discipline paved the road to the emergence of sequence stratigraphy (Sloss, 1963; Mitchum *et al.*, 1977) as a new paradigm in geology, which constituted an important revolution in sedimentary geology (Miall, 1997). Further developments in seismic stratigraphy introduced seismic velocities and amplitudes to predict lithologies and reservoir properties (e.g., Peickert, 1985; Neidel *et al.*, 1985).

Impedance inversion and analysis of seismic attributes are the current techniques to delineate the elastic properties of reservoir rocks using seismic data (e.g. Brown, 1991). Analysis of seismic velocities, amplitudes, AVO response, shear waves and frequency are some of the most useful attributes for reservoir identification from 3D seismic data (i.e. Avseth, 2000; Brown, 1991). During the last decade, inversion of the spatial distribution of seismic velocities and densities to determine lithology, porosity and fluid content (Lortzer and Berkhout, 1992) has become a common technique for reservoir characterization (e.g., Gutierrez, 2001). Interpretation of inverted seismic cubes requires adequate theories to relate the intrinsic rock

properties to seismic velocities (e.g. Lortzer and Berkhout, 1992). Gutierrez *et al.* (2001), and more recently Zeng *et al.* (2003), have demonstrated the importance of using stratigraphy to constrain the interpretation of impedance inversions. Both laboratory and theoretical rock-physics studies have provided a better understanding of the relationships between rock textures and seismic velocities (e.g. Murphy, 1982; Han; 1986; Nur *et al.*, 1991; Mavko and Jizba, 1991; Marion, 1990; Yin, 1992; Marion *et al.*, 1992; Estes *et al.*, 1994; Nur *et al.*, 1995; Dvorkin and Nur, 1996; Avseth *et al.*, 2000; Dvorkin *et al.*, 2002; Zimmer *et al.*, 2002; Zimmer, 2003). These relationships constitute the key to transforming the inverted seismic properties into volumes of porosity, permeability and fluid saturation.

1.2. The Problem: What Geologic Processes Determine Impedance

Our ultimate goal is to improve the methods for reservoir-quality prediction from seismic data in sedimentary sequences. In other words, we want to predict lithofacies and porosity based on the rocks' responses to seismic waves. To achieve this objective, we need to understand the physics behind the variability of seismic impedance in clastic sedimentary sequences. This understanding is necessary in order to develop predictive methods for seismic impedance using rock-physics forward modeling, and to evaluate the uncertainty associated with these predictions.

1.2.1 Lithofacies: the Link between Sedimentology and Rock Physics

It is generally accepted (Wang and Nur, 1992; Yin, 1992) that seismic velocities, and therefore acoustic and elastic impedances, depend on lithology, porosity, cracks and fractures, cement and diagenesis, clay content, tectonic stresses, pore pressure, temperature, pore fluids, saturation, and density. We can separate these eleven factors into three main groups as follows:

1. Factors related to the dry-frame properties: porosity, grain size distribution (sorting), mineral composition, clay content, cement, density, and fractures.
2. Factors associated with the fluid content: pore fluids, fluid densities, and saturations.
3. Factors linked to the ambient conditions: tectonic stress, temperature, and pore pressure.

Splitting these factors into groups gives us a better idea of which parameters are closely related and which can be predicted or evaluated separately. For example, the

role of fluid content can be separated from the effects of factors in the other two groups and can be independently evaluated using fluid substitution methods. The same is true for the ambient conditions, which basically depend on burial depth, pressure and temperature gradients, and tectonic stresses. A fundamental aspect of this research is that changes in seismic response linked to the dry-frame properties are the consequence of changes in rock texture. This is actually the basis for the Rock Physics Diagnostics technique (Dvorkin and Nur, 1996; Avseth *et al.*, 2000).

In sedimentary geology, rock texture and fabric are described and classified using the concept of facies (Teichert, 1958). Geologists use the term lithofacies to specify a particular set of textural parameters. The main textural parameters for sandstones are: grain size, grain size distribution (sorting), clay content (matrix), grain sphericity, grain roundness, packing, cement, and contact strength (Fuchtbauer, 1974). Previous studies have demonstrated that grain size, clay-content (matrix), sorting, packing, and cement are the key parameters controlling porosity and permeability (e.g., Fuchtbauer, 1974; Beard and Weyl, 1973; Atkins and McBride, 1992). In addition to mineral composition, textural parameters provide the link between sedimentary facies, dry-frame seismic response, and petrophysical properties.

1.2.2   The Fundamental Questions

At specific pressure and temperature conditions, good porous and permeable sandstones with hydrocarbons may have a distinctive seismic response (often constituting an anomaly). This characteristic signature should allow the discrimination of this reservoir from the surrounding low-porosity, low-permeability or water-bearing rocks. However, is this characteristic seismic signature the same regardless of the depositional environment, the stratigraphic arrangement of the sediments, and the burial depth? Or, on the contrary, does this characteristic seismic signature vary depending on these factors?

The fundamental problems to solve are summarized in four main questions:

1. How does seismic impedance vary within clastic sedimentary sequences?
2. Does the variability of seismic impedance follow similar patterns predicted from rock-physics models, regardless of the specificities of the depositional environment? Therefore, can we use the various rock-physics planes to identify depositional environments? Or, on the contrary, can we establish a relationship between seismic properties and

petrophysical properties (porosity and permeability) independent of the specific depositional environment?

3. How does the pattern of seismic impedance variation within a stratigraphic sequence change with depth, and specifically with compaction and cementation?

4. Can we mathematically model these variations, and therefore predict the seismic response of sedimentary rocks given the depositional and diagenetic facies?
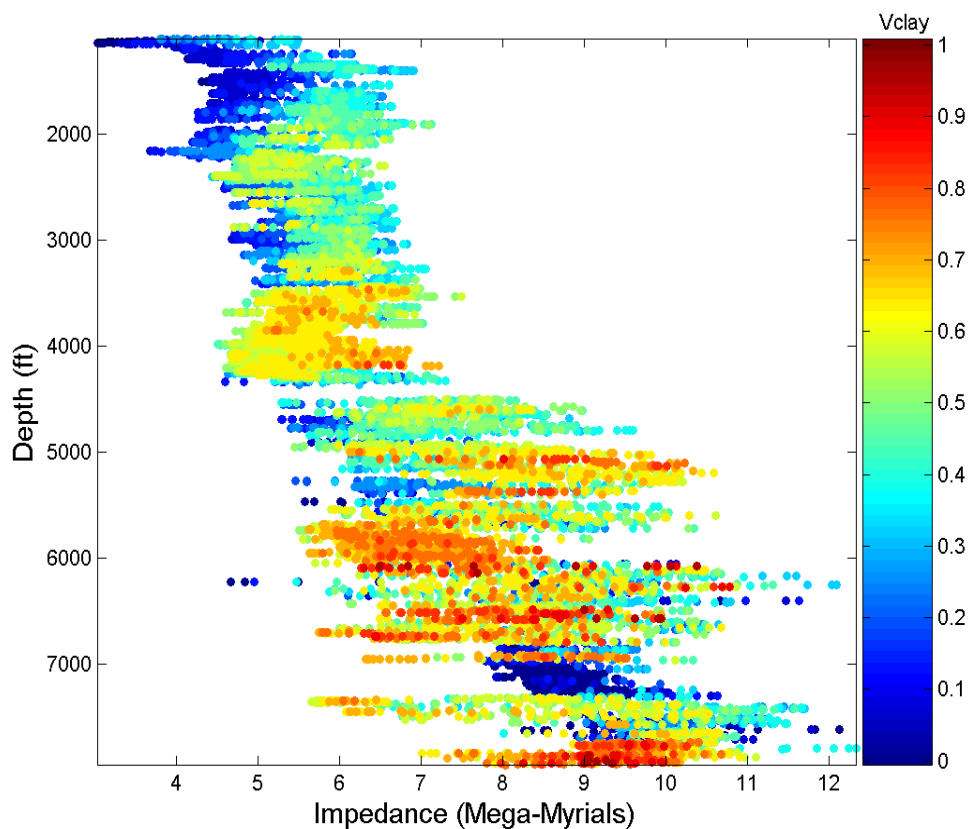
Figure 1.1: The basic problem: *the variability of seismic impedance in clastic sedimentary sequences*. Plot of impedance vs. depth, color-coded by volume of clay (Vclay) as determined from the gamma ray log and the separation between neutron (NPHI) and density (PHID) porosities. The data corresponds to the Oligocene to Pliocene section at Apiay-1, in the Llanos Basin of Colombia. The clay-rich intervals mark the base of each stratigraphic sequence. Within each sequence the environments change from shallow marine at the bottom to fluvio-estuarine towards the top. Notice the change in acoustic impedance for the same lithofacies from one sequence to another.

To solve the questions stated above, we need to integrate concepts derived from sedimentary geology, stratigraphy, seismology and rock physics. As an example, let's analyze a plot of impedance variation as a function of depth (Figure 1.1), color-

coded by clay fraction (Vclay). In this plot, the base of each main stratigraphic sequence is approximately the base of each clay-rich interval, identified with red in Figure 1.1 (for instance, the interval at 4000'). Acoustic impedance increases with depth for every facies, but instead of a uniform linear trend, there is a change in the slope at the base of the uppermost sequence (~4400'). This boundary happens to be a conspicuous seismic reflector, as expected from the contrast in impedance between the layers above and below that limit. However, is this change due just to the contrast in lithofacies? Or is it also due to differential compaction and cementation between the uppermost sequence and the sequence below?

1.2.3   Fractured Reservoirs

Integration is crucial in characterization of fractured reservoirs in the subsurface. Fractures constitute the main fluid conduits in many low-porosity rocks. Mapping the distribution of fractures within subsurface reservoirs is an ongoing area of research in exploration and reservoir-characterization seismology. Seismic methods for fracture detection provide direct information about the geometry and the elastic properties of the reservoir; however an accurate interpretation of seismic data requires inputs from other sources of information, such as outcrop analogues (Teng, 1998), or geomechanical modeling (e.g. Maerten *et al*., 2000). Outcrop studies supply significant qualitative and quantitative information for geologic modeling of fractured reservoirs. Outcrop information can be used for either stochastic geostatistical modeling or deterministic geomechanical modeling. For any of these approaches, outcrop descriptions provide constraints to the modeling parameters since 1) they show the spatial variability of fracture density at reservoir scale, which can be translated to the subsurface modeling using geostatistics; 2) they indicate the different mechanisms that generate fractures for specific rock types and deformation styles; and 3) they fill the scale gap between core, well-log and seismic data. The problem that this dissertation addresses regarding fractured reservoirs reduces to the following question: how can we translate the descriptions and data obtained at outcrops into relevant information for seismic modeling and engineering characterization of fractured reservoirs?

1.3.   Outline

The first part of this dissertation, chapters 2 to 4, presents the results regarding textural effects on the elastic properties of clastic sedimentary rocks. The second part, chapters 5 to 7, deals with the problem of fractured reservoirs.

Chapter 2 specifically deals with the distinction between sorting effects and packing effects on both elastic properties and porosity. Based on a theoretical analysis and stochastic simulation, I demonstrate that variations in particle grain size can reduce the elastic stiffness of granular materials while reducing porosity, an effect that definitely differs from the one produced by packing. The chapter also summarizes experimental and empirical data that show a flatter trend for the effect of sorting in the velocity-porosity plane, consistent with the theoretical analysis. The modified Hashin-Shtrikman lower bound, in the velocity-porosity plane, is proposed as a boundary to distinguish between sorting and packing effects in granular materials.

Chapter 3 analyzes the effect of pressure solution on the elastic properties of quartzarenites, and its relationship with the rock-physics diagenetic trend. Combining a classical pressure-solution model (Rutter, 1976) with Hertz-Mindlin theory, and Digby's solution for intergranular force in granular materials (Digby, 1981), I develop a method to simulate the effect of pressure solution through geologic time. The results are calibrated in terms of the burial constant (Stephenson *et al*., 1992), the ratio between the radius of the area of grain contact and the grain radius. Pressure solution produces an elastic effect similar to the effect of incipient cementation, and for the analyzed data set it provides a more consistent explanation for the sudden increase in elastic stiffness at depths above the threshold temperature for quartz cementation.

Chapter 4 demonstrates that current rock-physics models can be used to predict the patterns of clastic depositional sequences in different rock-physics planes (velocity-density, velocity-porosity, and porosity-clay fraction). The match between the predictions and the observed patterns goes beyond the well-known patterns predicted by the Marion-Yin model. The patterns of clastic depositional sequences in the rock-physics planes vary according to the proportion and type of mixed lithofacies. I present and discuss four selected examples of decameter-scale lithofacies sequences illustrating the difference between dispersed and laminar mixtures. I show that the applicability of these patterns to predict the seismic properties of larger-scale sequences depends on the lateral and vertical persistence of

the lithofacies assemblages. Similarly, the extrapolation of these patterns from one basin to another depends on the repeatability of these lithofacies assemblages and the diagenetic effects.

Chapter 5 documents the faults and fracture systems observed in a fold-and-thrust belt within the Bolivian Andes. The study demonstrates the relationship that exists between fracture hierarchies and stratigraphic hierarchies, and presents field evidence in support of the model of fault and fault-system evolution through hierarchical shearing and progressive deformation.

Chapter 6 presents a geostatistical method to generate static geologic models of fractured reservoirs. The technique constitutes an alternative to the discrete fracture networks currently used for this purpose. The method uses stochastic simulation to generate indicator maps that resemble the architecture and distribution of fault zones. Then, fault zones are filled with realizations of high-fracture-density maps using the cookie-cutter technique. The background regions are filled with realizations of low-fracture-density maps. The statistical parameters are obtained from outcrop data. The technique allows the reproduction of the fracture distribution and orientation observed at outcrops.

Chapter 7 synthesizes three different studies that together comprise a good example of integration. The first section analyzes the evolution of conjugate faults and its role in fracture localization. Based on outcrop observations and geomechanic modeling, it shows that antithetic conjugate faults constitute ideal conditions for the development of fault-associated fracture swarms. The second section presents a method to translate outcrop-based fracture-spacing data into Hudson's crack-density parameter (i.e. Mavko *et al.*, 1998) for seismic modeling, and uses one-dimensional seismic modeling to demonstrate that dimming-amplitude anomalies and flexure are the main indicators of small faults. Finally, these concepts are tested in the interpretation of VSP data, at the well Hendersson-1 (Neuville Field, East Texas), using seismic attributes.

1.4.   References

Atkins, J. E. and E. F., McBride, 1992, Porosity and packing of Holocene river, dune, and beach sands, American Association of Petroleum Geologists Bulletin, **76**, 339-355.

Avseth, P., J. Dvorkin, G. Mavko, and J. Rykkje, 2000, Rock physics diagnostic of North Sea sands: Link between microstructure and seismic properties, Geophysical Research Letters, **27**, 2671-2764.

Avseth, P., 2000, Combining Rock Physics and Sedimentology for Seismic Reservoir Characterization in North Sea Turbidite Systems, Ph. D. thesis, Stanford University.

Beard, D. C., and P. K. Weyl, 1973, Influence of texture on porosity and permeability of unconsolidated sand, American Association of Petroleum Geologists Bulletin, **15**, 349-369.

Berg, R., and D. Woolverton, 1985, Seismic Stratigraphy II: An integrated Approach to Hydrocarbon Exploration, American Association of Petroleum Geologists Memoirs, **39**.

Brown, A., 1991, Interpretation of Three-dimensional Seismic Data, third edition, American Association of Petroleum Geologist Memoirs, **42**.

Burger, R., 1992, Exploration Geophysics on the Shallow Subsurface, Prentice Hall, 489 pp.

Dvorkin, J., A. Nur, and H. Yin, 1994, Effective properties of cemented granular materials, Mechanics of Materials, **18**, 351-366.

Dvorkin, J., and A. Nur, 1996, Elasticity of high-porosity sandstones: Theory for two North Sea datasets, Geophysics, **61**, 1363-1370.

Dvorkin, J., M. Gutierrez and A. Nur, 2002, On the universality of diagenetic trends, The Leading Edge, **21**, 40-43.

Estes, C.A., G. Mavko, H. H. Yin, and T. Cadoret, 1994, Measurements of velocity, porosity and permeability on unconsolidated granular materials, Stanford Rock Physics and Borehole Geophysics Project, annual report, **55**, G1-G9.

Fuchtbauer, H., 1974, Sediments and sedimentary rocks 1, in Sedimentary Petrology by W. V. Engelhardt, H. Fuchtbauer and G. Muller, Part II. John Wiley and Sons, New York, 464 pp.

Gutierrez, M., 2001, Rock Physics and 3D Seismic Characterization of Reservoir Heterogeneities to Improve Recovery Efficiency, Ph. D. thesis, Stanford University.

Gutierrez, M., J. Dvorkin and A. Nur, 2001, Stratigraphy-guided rock-physics reservoir characterization, American Association of Petroleum Geologists Meeting, Abstracts.

Han, D., 1986, Effects of Porosity and Clay Content on Acoustic Properties of Sandstones and Unconsolidated Sediments, Ph. D. thesis, Stanford University.

Kupecz, J. A., J. C. Gluyas and S. Bloch, 1997, Reservoir Quality Prediction in Sandstones and Carbonates, American Association of Petroleum Geologist Memoirs, **69**.

Lortzer, G. J. M., and A. J. Berkhout, 1992, An integrated approach to lithologic inversion-Part I-Theory, Geophysics, **57**, 233-244.

Maerten, L., Pollard, D. D., Karpuz, R*.,* 2000, How to constrain 3-D fault continuity and linkage using reflection seismic data: a geomechanical approach, American Association of Petroleum Geologist, **84**, 1311-1324.

Marion, D., 1990, Acoustical, Mechanical and Transport Properties of Sediments and Granular Materials, Ph. D. Thesis, Stanford University.

Marion, D., Nur, A., Yin, H., and Han, D., 1992, Compressional velocity and porosity in sand-clay mixtures, Geophysics, **57**, 554-563.

Mavko, G., and Jizba, D., 1991, Estimating grain-scale fluid effects on velocity dispersion in rocks, Geophysics, **56**, 1155-1164.

Mavko, G., T. Mukerji and J. Dvorkin, 1998; The Rock Physics Handbook: Tools for Seismic Analysis in Porous Media, Cambridge University press, New York, 329 pp.

Miall, A. D., 1997, Geology of Stratigraphic Sequences, Springer Verlag, New York, 433 pp.

Mitchum, R. M. Jr., P. R. Vail and S. Thompson III, 1977, Seismic stratigraphy and global changes of sea level, part II: The depositional sequence as a basic unit for stratigraphic analysis, In: Payton, Ch. ed., Seismic Stratigraphy: Applications to Hydrocarbon Exploration, American Association of Petroleum Geologists Memoirs, **26**, 53-62.

Murphy, W. F., III, 1982, Effects of Microstructure and Pore Fluids on the Acoustic Properties of Granular Sedimentary Materials, Ph. D. dissertation, Stanford University.

Neidell, N., J. H. Beard and E. Cook, 1985, Use of seismic-derived velocities for stratigraphic exploration on land: Seismic Porosity and Direct Gas Detection, In: Berg, O. R. and D. Woolverton, eds., Seismic Stratigraphy II: An Integrated Approach to Hydrocarbon Exploration, American Association of Petroleum Geologists Memoirs, **39**, 49-77.

Nur, A., Marion, D., and Yin, H., 1991, Wave velocities in sediments, in Hovem, J.M., M. D. Richardon and R. D. Stoll, eds., Shear Waves in Marine Sediments, Kluwer Academic Publishers, Dordrecht, The Netherlands, 131-140.

Nur, A., Mavko, G., Dvorkin, J., and Gal, D., 1995, Critical porosity: The key to relating physical properties to porosity in rocks, in Proceedings, 65th Annual International Meeting, Soc. Expl. Geophys., 878.

Payton, C. E. ed., 1977, Seismic Stratigraphy: Applications to Hydrocarbon Exploration, American Association of Petroleum Geologists Memoirs, **26**.

Peikert, E. W., 1985, Stratigraphic velocity interpretation: National Petroleum Reserve-Alaska, In: Berg, O. R. and D. Woolverton, eds., Seismic Stratigraphy II: An Integrated Approach to Hydrocarbon Exploration, American Association of Petroleum Geologists Memoirs, **39**, 209-222.

Rutter, E.H., 1976, The kinetics of rock deformation by pressure solution, Philos. Trans. Royal Soc. London A, **283**, 203-219.

Sheriff, R., and L. P. Geldart, 1995, Exploration Seismology, 2nd edition, Cambridge University Press, 520 pp.

Sloss, L. L., 1963, Sequences in the cratonic interior of North America, Geological Society of America Bulletin, **74**, 93-113.

Stephenson, I. P., W. J. Plumley and V. V. Palciauskas, 1992, A model for sandstone compaction by grain interpenetration, Journal of Sedimentary Petrology, **62**, 11-22.

Teichert, 195, Concept of facies, American Association of Petroleum Geologists Bulletin, **42**, 2718-2744.

Teng, L., 1998, Seismic and Rock Physics Characterization of Fractured Reservoirs, Ph. D. dissertation, Stanford University.

Wang, Z., and A. Nur, 1992, Seismic and acoustic velocities in reservoir rocks, Vol. 2, Theoretical and model studies, Society of Exploration Geophysicists, Geophysics Reprint Series, 457 pp.

Yin, H., 1992, Acoustic Velocity and Attenuation of Rocks: Isotropy, Intrinsic Anisotropy, and Stress-Induced Anisotropy, Ph. D. thesis, Stanford University.

Zeng, H., Ch. Kerans, and S. Ruppel, 2003, Integrating Detailed Stratigraphic Architecture with 3D Seismic for High-resolution Reservoir Modeling, American Association of Petroleum Geologists Meeting, Abstracts.

Zimmer, M., M. Prasad and G. Mavko, 2002, Pressure and porosity influences on Vp-Vs ratio in unconsolidated sands, The Leading Edge, 21, 178-180.

Zimmer, M., 2003, Controls on the Seismic Velocities of Unconsolidated Sands: Measurements of Pressure, Porosity and Compaction Effects, Ph. D. dissertation, Stanford University.

Chapter 2

Sorting and Packing Effects on the Elastic Properties of Sands

2.1. Abstract

This chapter analyzes the effects of grain-size distribution (sorting) and packing on the porosity and elastic properties of granular materials, and how their effects differ. The effective medium contact theory for random packings of granular aggregates is used to approximate the effect of grain-size distributions. Based on that theory, an idealized model for tight (rhombohedric) packing of quinary mixtures is used to calculate the effective elastic properties of the aggregate, by performing stochastic simulations. The main source of uncertainty in these simulations comes from the coordination number. In spite of the approximations, the uncertainty in coordination number, and the limitations of using an idealized packing model, the results demonstrate that the sorting effect in the velocity-porosity plane follows a flatter trend than the modified Hashin-Shtrikman lower bound (MHSLB). In fact, the theoretical analysis demonstrates that the MHSLB should constitute an upper bound for the effect of sorting. On the contrary, the effect of packing can generate a trend with a steeper slope than the one predicted from the MHSLB. This steeper trend has been observed in laboratory studies and can be explained as the result of increasing grain-contact areas and incremental grain stabilization. Consequently, whereas the MHSLB is an approximate upper bound for the sorting effect, it should be considered a lower bound for the effect of packing. These conclusions are in agreement with results obtained from laboratory data in previous studies, and with subsurface core and well-log data.

2.2. The Rock-Physics Depositional Trend: Sorting or Packing?

Sandstones at similar depths or confining pressures present a relatively flat trend in the velocity-porosity plane (Figure 2.1). This flat trend results from significant changes in porosity associated with very small changes in elastic stiffness. The main porosity-reduction mechanisms related to this flat-trend are matrix (clay) content, sorting, and mechanical compaction, as shown by Marion *et al.* (1992), Avseth *et al.* (2000), Dvorkin and Gutierrez (2001), Zimmer *et al.* (2002), and Zimmer (2003). For uncemented sandstones at the same pressure conditions, sorting and clay are considered to be the dominant mechanisms affecting this velocity-porosity trend. The trend can be reproduced using the modified Hashin-Strickman lower mound (MHSLB), and has been called the uncemented sandstone model (Mavko *et al.*, 1998), or the rock physics depositional trend (Avseth, 2000).

Grain-size distribution, or sorting, significantly affects not only the porosity (e.g. Beard and Weyl, 1973) but also the elastic properties of granular materials, as demonstrated by Estes *et al.* (1994), Avseth *et al.* (2000), Gutierrez and Dvorkin (2001), Gutierrez (2001), and Zimmer (2003). In spite of this importance, there are few experimental and theoretical studies about the effect of sorting. Dvorkin and Gutierrez (2001) present a model for binary mixtures that combines Hertz-Mindlin theory with modified Hashin-Shtrikman lower bounds to predict the elastic properties of the mixture. According to these authors, the sorting effect can be approximated using the MHSLB.

In the case of clean sand aggregates at similar pressure conditions, the uncemented trend is considered to be solely the effect of sorting (Avseth, 2000; Gutierrez, 2001). However, mathematical models of identical spheres demonstrate that a similar effect can be obtained by changing the packing of the aggregate, without increasing the confining pressure. Therefore, packing and sorting seem to have a similar effect on the velocity-porosity trend. The assumption that the uncemented trend is controlled by depositional factors (Avseth, 2000) disregards the effect of packing, which is often post-depositional. So far, there is not a physical explanation for the use of the MHSLB to model the effect of sorting. In addition to this, current rock physics models do not explain how we can distinguish between the sorting and packing effects on porosity and the elastic properties of granular aggregates.

Characterizing the effect of sorting on the elastic properties of granular materials can improve the methods to estimate and determine lithofacies and reservoir quality

using sonic logs. The sorting effect can also be used to predict the variation in seismic response away from well control. Therefore, understanding the effect of sorting on the elastic properties of sands can help to assess the uncertainties associated with these predictions.

This chapter presents an analysis of the effects of grain-size distribution and packing on the elastic properties of granular materials, based on effective medium models. The next section discusses the measures of sorting or grain-size distribution, explains the relationships between porosity, sorting and packing, and their link to the depositional environments. After that, the following section reviews the aspects of the effective medium theories that are relevant to sorting and packing effects, and postulates some approximations to account for the presence of different grain sizes in the contact models. The succeeding section introduces an old, idealized model for quinary mixtures. This model is used in the stochastic simulation of the effect of sorting on the elastic properties, explained in the section afterwards. The final sections show the comparison to real data, discuss the results and present the conclusions.
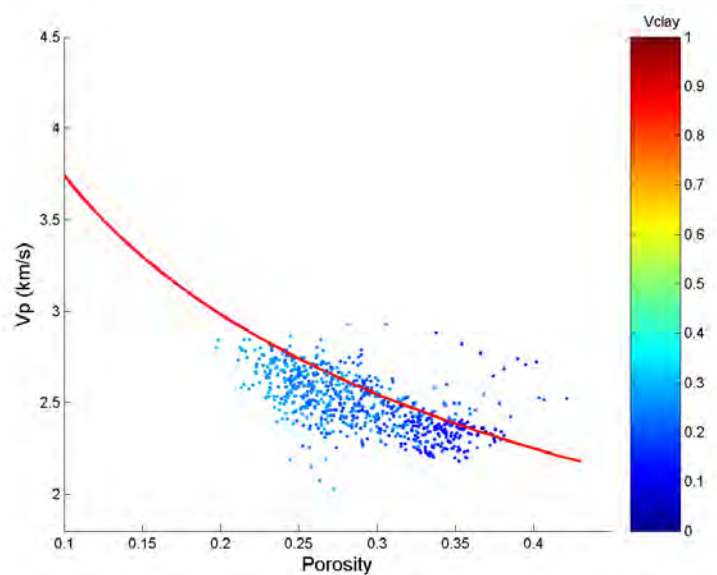
Figure 2.1: The depositional trend of sands in the velocity-porosity plane. The data corresponds to uncemented sands from fluvial deposits (well Apiay-1). Data color-coded by clay fractio (Vclay).

2.3. Sorting, Packing, Porosity and Depositional Lithofacies

Sorting and packing are textural properties of the sediment, initially associated with the depositional processes. Sorting, or grain-size distribution, refers to the

spread of the grain-size population. The grain size by itself is a measure of the center of that population. Packing refers to the grain concentration and is closely linked to porosity. Indeed, sorting, packing and porosity are closely related. The main textural components of sandstones are: grains, pores, matrix (clay), and cement (e.g. Selley, 1988). If we incorporate the matrix within the grain-size population, sorting and packing become the two dominant factors controlling porosity, and to some extent permeability, in uncemented sands. Permeability is linked to sorting and packing because of the effect of porosity, however permeability also depends on grain size and clay content.

2.3.1. Measures of Grain Size and Sorting

Grain size and sorting describe, respectively, the measures of the center and the spread of a grain population. In general, the grain size can be any measure of the population's center, either the mean, the median, or the mode, whereas sorting should be the respective measure of the population's spread, such as the standard deviation, the interquantile range, or the maximum absolute deviation. Although the application of these definitions to unconsolidated sands should be straightforward, there is no general agreement on which statistical parameters are the most appropriate measures, as explained below.

The grain size depends on the choice of the measure of the center. The logarithmic PHI scale was proposed by Krumblein (1936), as the most convenient scale to perform statistical analysis of grain-size distributions in sediments. As shown in Equation 2.1, PHI is the negative, base-2 logarithm of the grain size in millimeters *(D)*. The classes are defined according to Wentworth's arithmetic scale (Wentworth, 1922). This usage conforms to the fact that most of the natural grain-size populations follow a log-normal distribution function. This fact introduces the first problem regarding the actual measure of the grain size: what is the right measure of the center, the mean or the median? For example, Pettijohn (1975) pointed out that sedimentologists commonly use the mode as the measure of grain size. Given that many populations show a lognormal distribution function, the median is probably the best measure of the center.

$$PHI = -\log_2(D) . \qquad\qquad (2.1)$$

There is no unified measure of the spread of the grain-size distribution. Inter-percentile ranges in the PHI scale have been proposed as the most rigorous measures

of sorting (Krumbein, 1938; Inman, 1956). However, the coefficient of variation (Equation 2.2) is also a consistent measure of sorting. Authors proposing inter-percentile ranges have differed in the bounding percentiles: Krumbein (1936; 1938) proposed the interquartile range, which is equivalent to the sorting coefficient defined by Trask (1932); while Inman (1956), and Otto (1939), proposed the difference between the P_{84} and P_{16} percentiles. Some authors have found it convenient to normalize the inter-percentile ranges by the median (i.e. Rogers and Head, 1961). Sohn and Moreland (1968) used the coefficient of variation, defined as the standard deviation (σ) normalized by the mean (μ) of the grain-size distribution. Both methods of normalization provide consistent measures of sorting and are approximately equivalent. However, the coefficient of variation is preferable, since the normalized inter-percentile range presents the inconvenience of a singularity around grain sizes of 1 mm. Throughout this chapter I use the coefficient of variation as the Sorting Index (SI):

$$SI = \frac{\sigma}{\mu}. \qquad (2.2)$$

2.3.2. Grain-size Distribution, Porosity and Permeability

Given a similar stage of packing, porosity of granular materials decreases as the standard deviation of the grain-size distribution increases. In other words, porosity decreases as sorting deteriorates (Figure 2.2). This relationship has been demonstrated by various authors (Walton and White, 1937; Sohn and Moreland, 1968; Beard and Weyl 1973; and Zimmer, 2003). Other authors have observed a similar effect in binary mixtures (Fraser, 1935; Cumberland and Crawford, 1987), though they could not identify similar trends in multi-component mixtures. A linear trend between porosity and the sorting index can be derived from the published data (Figure 2.3), which in general can be expressed as follows:

$$\phi = \phi_0 - \beta \frac{\sigma}{\mu}, \qquad (2.3)$$

where ϕ_0 is the critical porosity of the aggregate, and the slope (β) has been found to vary between 0.11 and 0.19. The critical porosity, as defined by Nur *et al.* (1995), can be considered the well-sorted end member. Since porosity determines both the reservoir's final storage capacity and its permeability, grain-size distribution is therefore affecting both reservoir volumes and fluid flow in uncemented sand

reservoirs. As can be observed in Figure 2.4, the other property controlling permeability is the dominant grain size.
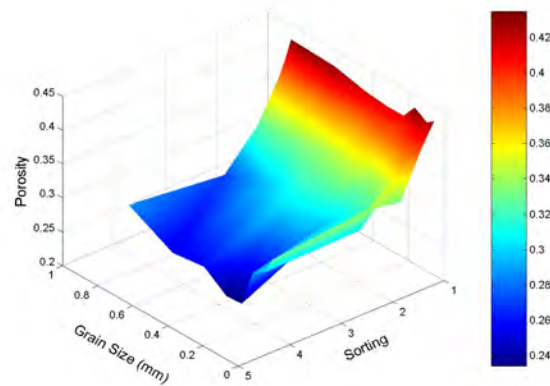
Figure 2.2: Porosity of artificial sand mixtures as a function of grain size and sorting. Sorting is expressed as standard deviation. Based on data by Beard and Weyl (1973).
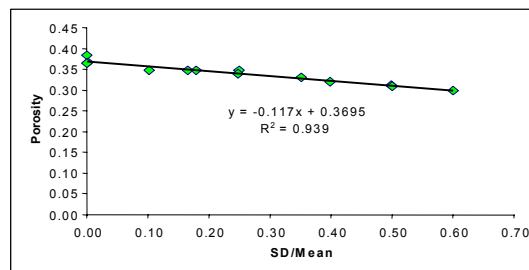
(a)
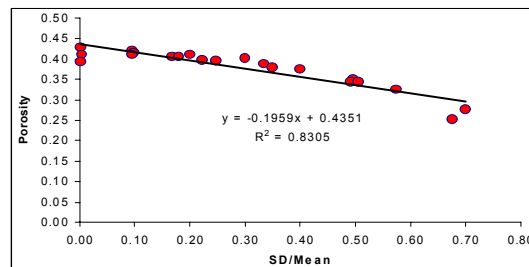
(b)
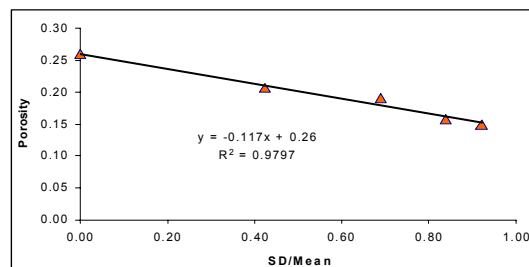
(c)

Figure 2.3: Linear relationship between porosity and the sorting index σ/μ; (a) and (b) correspond to laboratory results published by Sohn and Moreland (1968); (c) corresponds to an idealized quinary mixture modeled by White and Walton (1937).
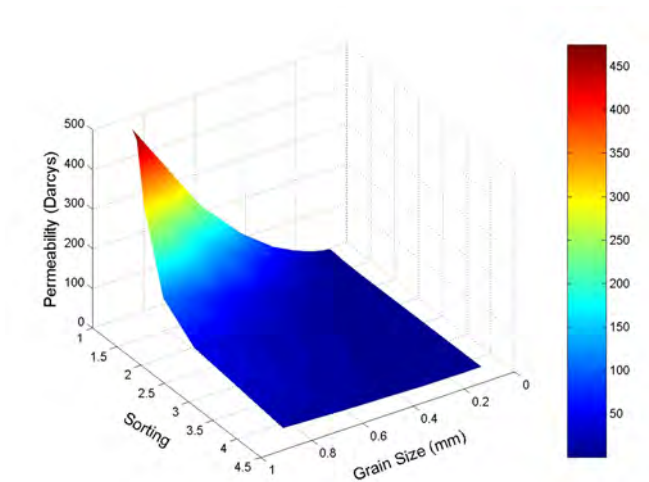
Figure 2.4: Permeability of artificial sand mixtures as a function of grain size and sorting. Sorting is expressed as standard deviation. Based on data by Beard and Weyl (1973).

2.3.3.   Sorting and Depositional Environments

Grain-size distributions reflect provenance, sediment-transport conditions, and the depositional process (Visher, 1999). According to Visher (1969), a grain-size distribution is composed of multiple log-normal populations. These populations are combined by multiple processes of sediment transport associated with traction, saltation and suspension, the three mechanisms of sediment transport in fluidized flows (e.g. Selley, 1988).

Visher (1969) divided the cumulative distribution function (CDF) of grain size, in the PHI scale, into three main components, each one corresponding to the main transporting mechanisms: traction, saltation and suspension (Figure 2.5). The major truncation points occur about the transitional grain size values, which are those affected by two transporting mechanisms. These truncation points are defined as the 2-phi and the 3-phi break points. The former marks the transition between traction and saltation, and decreases in response to decreasing shear stress. The latter indicates the transition from saltation to suspension and decreases according to decreasing turbulence (Visher, 1999).

Although the relationship between sorting and depositional environments is not unique, grain-size distributions are always linked to the physics of the sedimentary processes. The non-uniqueness of sorting as an indicator of specific depositional settings derives from the fact that there are other variables involved, like provenance and sediment transport. Grain-size distribution depends not only on the specificities

of the depositional setting, but also on the ability of the transporting current to separate different grain-size populations. Beach sediments, for example, are constantly reworked and sorted, therefore beach deposits tend to be well to very well sorted. However, if non-sorted sediments, like debris flows, are constantly discharged to the beach, then the most likely final result will be poorly to moderately sorted sediments. In spite of this non-uniqueness, the variations of sorting within a specific stratigraphic unit are always governed by the mechanics of sedimentation, as demonstrated by Inman (1949) and Visher (1969).
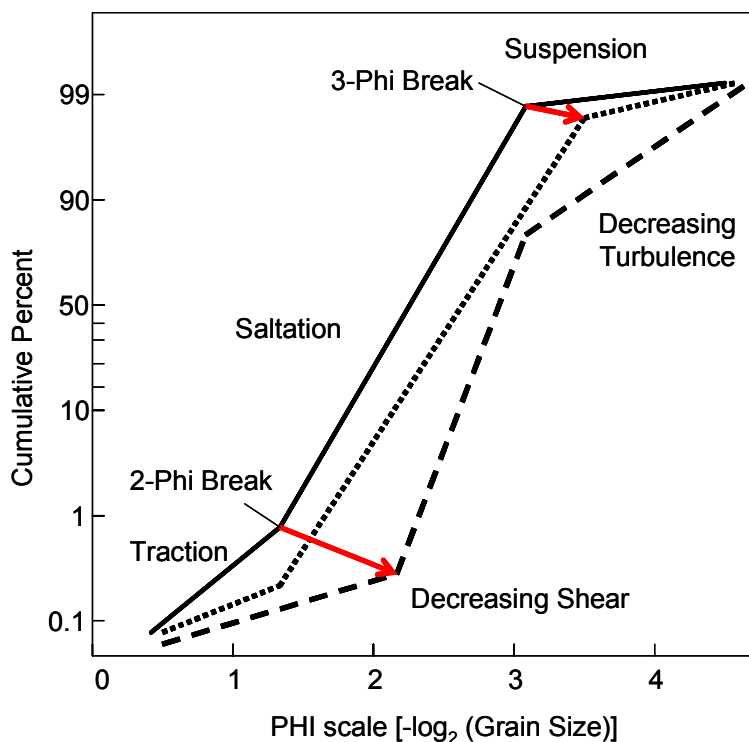
Figure 2.5: Schematic cumulative frequency plots of grain-size distribution, illustrating the concept of the 2-phi and 3-phi breaks, and their general relationship with the mechanics of sedimentation according to Visher (1999).

2.3.4. Measures of Packing

Among several measures of packing the most common are the grain concentration, the coordination number (Allen, 2001), and the intergranular contact (Fuchtbauer, 1974). The grain concentration, or fractional volume concentration of particles (X), is directly related to porosity (ϕ):

$$\phi = 1 - X \qquad (2.4).$$

The coordination number (C), the average number of grains in contact with each individual grain, affects the stiffness of the aggregate. The intergranular contact

describes the type of grain contact –punctual, tangential, concave-convex, or sutured–, and is usually a measure of the degree of mechanical compaction and pressure-solution, two processes related to diagenesis rather than to the depositional environment. According to Murphy (1982), and Zimmer (2003), porosity and coordination number can be related by the following expression:

$$C = 24e^{-2.547\phi} - 0.3731$$ (2.5).

However, there are other factors affecting porosity, like sorting (Beard and Weyl, 1973; Allen, 2001), grain shape (Allen, 2001), and grain angularity. Therefore the relationship between coordination number and porosity is not unique (Allen, 2001).

Table 2.1: Main packing types for identical sphere packs (after Mavko *et al.*, 1998; Bourbie, 1987).

Packing Type	Porosity	Coordination Number	Comments
Cubic	0.476	6	Unlikely
Hexagonal	0.395	8	Lose
Rhombohedric	0.259	12	Tight
Random	~0.36	~9	Most Likely

Like sorting, packing has a strong effect on porosity and therefore on permeability. The relationship between packing, coordination number and porosity has been analyzed by several authors (Graton and Fraser, 1935; Bourbie *et al*., 1987; Murphy, 1982; Cumberland and Crawford, 1987). The effect of packing on both porosity and permeability was extensively analyzed by Graton and Fraser (1935). Murphy (1982) and Cumberland and Crawford (1987), identified the concomitant variation in both porosity and coordination number associated with changes in packing. For idealized packs of identical spheres these relationships are shown in Table 2.1.

2.3.5. Packing and Depositional Environments

According to Allen (2001), laboratory experiments demonstrate that the conditions of deposition have a strong effect on the concentration of natural sediments. The results from different studies (Steinour, 1944; Kolbuszewski, 1948; Walker and Whitaker, 1967; and Macrae and Gray, 1961) indicate that the grain concentration varies from a constant value of about 0.65, comparable with that of dense haphazard packing, at small rate of deposition, to a lower constant value of

about 0.55, comparable with that of loose haphazard packing, at higher rate of deposition.

A systematic relationship between depositional environments and packing has not been established. There are some general observations: e.g. clean turbiditic sands tend to preserve high porosities at significant burial depths in spite of having moderate sorting; beach deposits tend to have a tighter packing than fluvial point bars and therefore similar initial porosities, in spite of their better sorting. However, a systematic analysis does not exist. One reason might be that porosity variations associated with differences in packing linked to the depositional environment are, in many cases, overprinted by mechanical compaction during the early stages of burial.

2.4. Incorporating Sorting into Effective-Medium Models

In order to take into account the effect of grain-size distributions on the effective elastic properties of granular material, our approach is to take the existing effective-medium models for uniform sphere packs, and modify them to incorporate the appropriate grain-size average. In other words, by finding the relevant averages of the variables involved in the computation, we can find approximate solutions to the effective elastic modulus. The following paragraphs will demonstrate that the appropriate averaging method varies, depending on the assumptions made during the derivation of each particular expression. For example, the harmonic average is the exact solution for the radius of curvature at the grain contact, whereas the average surface area requires a different averaging expression.

2.4.1. Contact Models

The starting point of effective-medium models based on contact mechanics is the solution of the normal and shear stiffness for two grains in contact. The following paragraphs outline this solution and explain the average required in the case of grains with different grain radii.

2.4.1.1 Radius of Grain-Contact Area

Timoshenko and Goodier (1956, p. 412) present the general solution for the pressure distribution within the contact area of two grains with identical elastic properties but different grain radii (R_1 and R_2). The radius of the surface of contact (a) is given by

$$a = \left(\frac{3}{4} \frac{F(1-\nu)}{G} \frac{R_1 R_2}{(R_1 + R_2)} \right)^{1/3} , \tag{2.6}$$

where F is the force applied at the grain contact, ν is the Poisson's ratio of the mineral, and G is the shear modulus. This expression is equivalent to the following equation

$$a = \left(\frac{3}{8} \frac{F(1-\nu)}{G} R_c \right)^{1/3} , \tag{2.7}$$

where

$$R_c = 2\left(\frac{R_1 + R_2}{R_1 R_2} \right)^{-1} . \tag{2.8}$$

Equation 2.7 is general for isotropic, linear elastic grains and can be extended to the case of a small sphere in contact with a hypothetical sphere with infinite radius.

2.4.1.2 Normal and Shear Stiffness at the Grain Contact

Solutions for the normal stiffness of two grains in contact are presented by Mindlin (1949), Digby (1981), Walton (1987), and Johnson (1992), among others. Both normal and shear stiffness depend on the radius of the area of grain contact. The magnitude of this dependence varies with the loading sequence or the friction coefficient assigned to the grain surfaces. In general the normal stiffness is given by (Mindlin, 1949):

$$Sn = \frac{4aG}{1-\nu} . \tag{2.9}$$

The variation of the shear stiffness is more sensitive to the sequence of loading, the area of contact, and the friction coefficient. Different solutions to the shear stiffness have been given; in general they agree in proposing that the shear stiffness at the grain contact may vary from 0 to a maximum value given by

$$St = \frac{8aG}{2-\nu} . \tag{2.10}$$

Different mechanisms have been proposed to explain the variations in the shear stiffness at the grain contact. For example, Mindlin (1949) proposed that the controlling factor is the coefficient of friction, according to the expression:

$$St = \frac{8aG}{2-v}\left(1 - \frac{F_x}{\xi F_z}\right)^{1/3},$$ (2.11)

where F_x and F_z stand for the shear and normal tractions at the grain contact, and γ is the coefficient of friction. From this equation it follows that if F_x equals the product ξF_z, then the shear stiffness is null. A similar model was proposed by Walton (1987). Digby (1981) related the shear stiffness to the pre-existing radius of the area of grain contact *(b)*, as follows:

$$St = \frac{8bG}{2-v}.$$ (2.12)

From this expression follows that if the pre-existing radius of the grain-contact area is close to zero, the initial shear stiffness is negligible. Null shear stiffness at the grain contacts does not necessarily imply lack of rigidity of the aggregate. Bachrach (1998) associated variations in the rigidity of shallow unconsolidated sands with the proportion of null-shear-stiffness contacts.

2.4.1.3 Normal Force at the Grain Contact

Approximate solutions for the normal force at the grain contact are presented by Digby (1981) and Walton (1987). Digby (1981) demonstrates that the normal force is given by

$$F = \frac{4\pi R^2 P}{(1-\phi)C},$$ (2.13)

where P is the applied hydrostatic pressure and ϕ is porosity. R and C stand for the sphere radius and the coordination number, respectively. According to Digby (1981), this result agrees exactly with the solution for different grain sizes obtained by Brandt (1955). This expression is also equivalent to the equations presented by Walton (1987). The expression $4\pi R^2$ represents the surface area of each identical sphere. For varying grain sizes, the normal force at the grain contact becomes a function of the average grain surface area (S_{avg}) and the grain coordination number (C_g).

2.4.1.4 The Coordination Number of a Binary Mixture

The average coordination number of a mixture (C_{avg}) increases as sorting deteriorates; however the variation of C_{avg} in binary mixtures is not linear and reach an upper limit as the number of small spheres, with low coordination number, increases. This is because the average coordination number depends not only on the

number of grains per volume, but also on the volumetric average of grain sizes. The maximum number of small spheres (C_{big}), of radius R_{small}, surrounding a bigger sphere, of radius R_{big}, depends on the ratio between the total surface area around the big sphere, and the area of a circle of radius R_{small}. This maximum coordination number can be approximated by the following expression:

$$C_{big} \approx \frac{3}{4}\left[4\left(\frac{R_{big}^2}{R_{small}^2} + 2\frac{R_{big}}{R_{small}} + 1\right)\right].\tag{2.14}$$

The fraction (3/4) has been introduced to fit the maximum coordination number of identical spheres to 12, instead of 16. Assuming C_{small} as the average coordination number for the small spheres, where $C_{small} \leq C_{big}$, the average coordination number of the whole aggregate is:

$$C_{avg} = \frac{\#Contacts}{\#Spheres} = \frac{AC_{big} + AC_{big}C_{small} + ABC_{big}C_{small}}{A + AC_{big} + ABC_{big}},\tag{2.15}$$

where A is the total number of spheres, and B is the proportion of small spheres that are not in contact with the big spheres. Figure 2.6 illustrates the results obtained from Equations 2.14 and 2.15, taking $A = 8$, and different values for C_{small} and B. It clearly shows that the ratio between C_{avg} and C_{big} rapidly decreases to almost zero, as the ratio of R_{big} to R_{small} increases. Meanwhile the ratio of C_{avg} to C_{small} increases and exponentially reaches an upper limit, where C_{avg} is slightly larger than C_{small}.
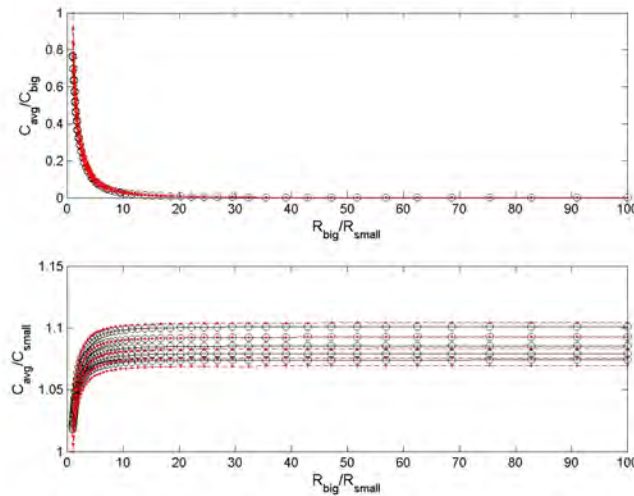
Figure 2.6: Variation of C_{avg} as the ratio between R_{big} and R_{small} increases (sorting deteriorates). For large values of R_{big}/R_{small}, C_{big} is much larger than both C_{small} and C_{avg}. C_{avg} increases as sorting deteriorates; however it rapidly reaches an upper limit slightly larger than C_{small}.

2.4.1.5 The Softening Effect of Variable Grain Size

Putting small spheres in between larger spheres has a softening effect on the elastic modulus of sphere packs. This can be mathematically demonstrated throughout the analysis of uniaxial deformation of three grains in contact, based on the sketch shown in Figure 2.7. The elastic modulus (M_1 and M_2) for the uniaxial deformation of the two configurations shown in Figure 2.7 are given by

$$M_1 = \frac{\partial P}{\varepsilon_1} = \frac{L_1}{\partial \delta_0 + \partial \delta_1} \partial P,$$ (2.16)

$$M_2 = \frac{\partial P}{\varepsilon_2} = \frac{L_2}{\partial \delta_0 + \partial \delta_2} \partial P.$$ (2.17)

where ε_1 and ε_2 are the respective uniaxial strains. To demonstrate that M_1 is also larger than M_2 we need to prove that $\Delta \delta_1$ is smaller than $\Delta \delta_2$, since L_1 is larger than L_2. For any grain contact $\Delta \delta$ is given by (i.e. Mavko *et al.*, 1998)

$$\partial \delta = \frac{\partial F}{Sn}.$$ (2.18)

Considering that the force at the grain contacts is the same, and recalling equations 2.6 and 2.9, it follows that Sn_1 is larger than Sn_2 and consequently:

$$\partial \delta_1 = \frac{\partial F}{Sn_1} < \frac{\partial F}{Sn_2} = \partial \delta_2.$$ (2.19)

Therefore M_1 is larger than M_2.
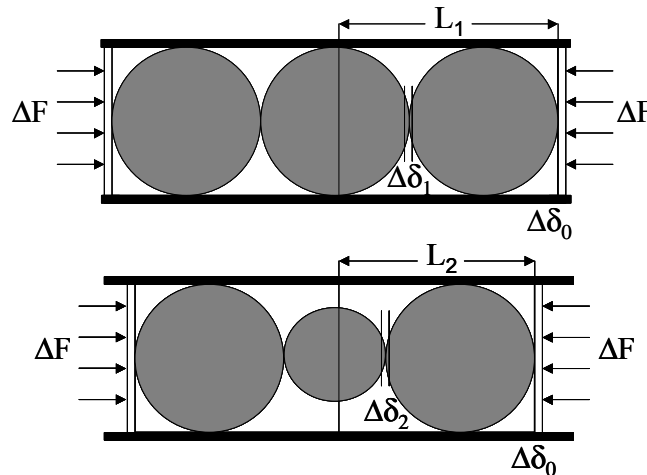
Figure 2.7: Sketch for the analysis of uniaxial deformation of three grains in contact.

2.4.1.6 Effective Elastic Modulus of Sphere Packs with Variable Grain Size

Winkler (1983) demonstrated that the general solutions for the effective elastic properties of random packs of identical spheres, derived by Digby (1981), are not specific to Digby's model and can be generalized to different contact models. From Digby's derivation, the effective elastic properties of a random packing of spheres is given by (Winkler, 1983):

$$Keff \approx \frac{C(1-\phi)}{12\pi R} Sn, \tag{2.20}$$

$$Geff \approx \frac{C(1-\phi)}{20\pi R}\left(Sn + \frac{3}{2}St\right). \tag{2.21}$$

To incorporate the effect of grain-size distribution into these models, grain radius *(R)*, coordination number *(C)*, normal stiffness *(Sn)*, and shear stiffness *(St)* are replaced in the expressions above for their equivalent averages. Then we can rewrite the previous equations:

$$Keff_{sort} \approx \frac{C_{avg}(1-\phi)}{12\pi R_{avg}} Sn_{avg}, \tag{2.22}$$

$$Geff_{sort} \approx \frac{C_{avg}(1-\phi)}{20\pi R_{avg}}\left(Sn_{avg} + \frac{3}{2}St_{avg}\right). \tag{2.23}$$

These equations can be used as a first approximation to model the effect of sorting on the effective elastic properties. The question is then, which are the appropriate averages to use?

2.4.1.7 What are the Appropriate Averages?

The averages required refer to either the local average for two grains in contact, or the global average of the aggregate. Whereas the different averages for sphere radii have an exact solution, the averages for coordination number and the average ratio *a/R* are inferred. For example, the harmonic average for the radius of curvature for two grains in contact is exact (Timoshenko and Goodier, 1956). For a sphere configuration like that shown in Figure 2.8, the different averages are indicated in Table 2.2.

It becomes clear, by looking at Table 2.2, that variable sphere sizes in contact require the evaluation of different average radii for each expression. The best example is the difference between the local average radius of curvature (*Rc*) and the average grain radius required for the average surface area (*R*$_{avg}$). The former requires

the harmonic average of the sphere radii in contact, whereas the later average is given by the following expression:

$$R_{avg} = \left(\sum_k f_k R_k^2 \right)^{1/2} \qquad (2.24)$$

These two are exact results. Another difference seems to exist between the local radius of curvature and the global average sphere radius (Rg). Either the arithmetic average or the geometric average is proposed for Rg. The arithmetic average provides the best results during stochastic simulation, since enhances the softening effect of variable grain sizes. However a rigorous justification of its use is lacking. It is important to point out that coordination numbers vary within a small range; therefore the different choices of averages for local and global coordination numbers do not have a dominant effect in the final result. Notice also that all these expressions reduce to the Hertz-Mindlin model when we consider identical spheres. They will also reduce to Hertz-Mindlin expressions if we use the harmonic average for local radius of curvature, average sphere radius, and average surface area.

The expressions presented in Table 2.2 imply that introducing small spheres between the contacts of larger spheres may actually decrease the aggregate stiffness. This effect has been explained in section 2.4.1.5. Although this effect might not be intuitively obvious, it agrees with the fact that the area of grain contact is controlled by the radius of the small sphere, whereas the average sphere radius is dominated by the large sphere. This softening effect of small spheres is comparable to the effect of grain angularity analyzed by Bachrach *et al.* (2000).
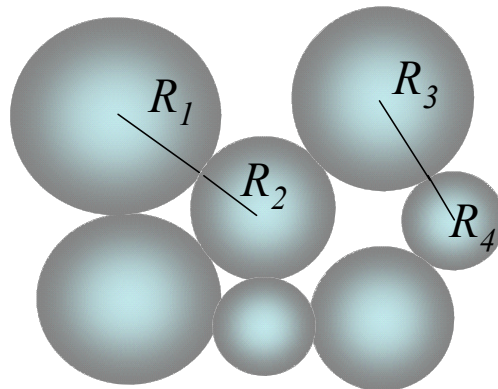
Figure 2.8: An aggregate of spheres with variable radii.

Table 2.2: Summary of equations and variables used to incorporate variable sphere
radii into effective-medium contact models.

Variable	Expression	Reference or Assumption
Local grain-contact area between R_i and R_j	$a_{ij} = \left(\dfrac{3}{8} \dfrac{F_{ij}(1-\nu)}{G} Rc_{ij} \right)^{1/3}$	Timoshenko and Goodier (1956)
Local radius of curvature of R_i and R_j	$Rc_{ij} = 2\left(\dfrac{R_i + R_j}{R_i R_j} \right)^{-1}$	Timoshenko and Goodier (1956)
Local coordination number	$C_{ij} = 2\left(\dfrac{1}{C_i} + \dfrac{1}{C_j} \right)^{-1}$	C controlled by the weakest contact
Volumetric average radius	$R_e = \left(\sum_k f_k R_k^3 \right)^{1/3}$	Exact solution for the average volumetric radius.
Global average surface area	$S_{avg} = 4\pi \sum_k f_k R_k^2$	Exact solution for the average surface area.
Intergranular force between R_i and R_j	$F_{ij} = \dfrac{S_{avg} P}{C_{ij}(1-\phi)}$	Digby (1981)
Global average ratio $\alpha = \dfrac{a}{Rg}$	$\alpha_{avg} = \sum_k f_k \alpha_k$; where: $\alpha_k = \dfrac{a_{ij}}{Rg_{ij}}$	Rg differs from the radius of curvature and corresponds to the global volumetric average radius
Global average coordination number	$C_{avg} = \sum_k f_k C_k$	C_k varies between 6 and 12
Effective Bulk Modulus	$Keff_{sort} = \dfrac{C_{avg} G(1-\phi)}{3\pi(1-\nu)} \alpha_{avg}$	Generalized Hertz-Mindlin for average C and α

2.4.2. The Modified Hashin-Shtrikman Lower Bound (MHSLB) and Sorting

The MHSLB can be considered an upper bound for the sorting effect on the elastic properties of granular materials. Dvorkin and Gutierrez (2001) used the MHSLB to model the effect of sorting in unconsolidated sandstones, based on the theoretical analysis and experimental results for binary mixtures. Although a good approximation, the use of binary mixtures and the MHSLB to estimate the effect of variable grain size does not take into account the softening effect of introducing small spheres between large spheres, discussed in the section 2.4.1.5. As a result of the variable grain size, the normal and shear stiffness at these contacts decrease, resulting in an effective elastic modulus lower than that predicted from the MHSLB. Recent laboratory studies by Zimmer (2003) show that the effect of sorting follows a

flatter trend than the one predicted by the MHSLB (Figure 2.9). Consequently, the MHSLB provides a stiffer estimate of the actual impact of varying grain size, and constitutes an empirical upper bound for the concomitant effect of sorting on the elastic properties and porosity of granular materials.
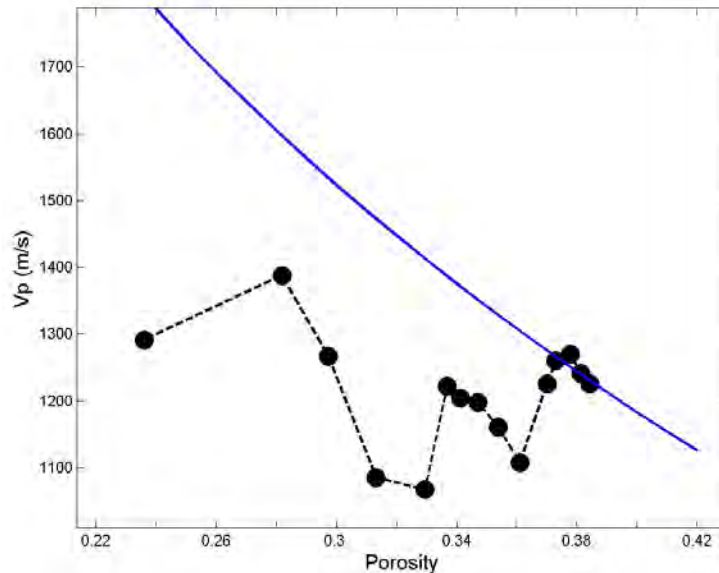
Figure 2.9: Sorting trend for six different sand aggregates, with variable sorting, at 5 MPa confining pressure (after Zimmer, 2003). The large variations in porosity are related to the changes in sorting. The blue line corresponds to the Hashin-Strickman lower bound, after fitting the first data value. Notice the flat and irregular trend associated with the variations in sorting.

2.5.   Modeling the Effect of Packing

In the case of idealized spheres, the main effects of grain rearrangement are reducing porosity and incrementing coordination number, as shown in Table 2.1. Other possible additional effects involve grain stabilization and change in the grain-contact area. The packing effect can be modeled using either Hertz-Mindlin contact theory or the MHSLB. In both cases, the modeling results underestimate the increase in elastic stiffness associated with packing, as observed in laboratory analysis (Zimmer, 2003). Hertz-Mindlin and MHSLB models provide similar results, both neglecting the impact of grain stabilization and local increase in grain-contact area. From this analysis it follows that the MHSLB constitutes a lower bound for the packing trend in the velocity-porosity plane. Consequently, it also constitutes an empirical lower bound for the overall effect of mechanical compaction on the elastic properties of granular materials.

2.5.1. Modeling the Packing Effect with Hertz-Mindlin Theory

The pure packing effect obtained from the Hertz-Mindlin model underestimates the slope observed in laboratory data, as shown in Figure 2.10. Hertz-Mindlin theory for the elastic properties of granular materials is summarized in Equations 2.6 to 2.13, and Equations 2.20 to 2.21. As documented by Mavko et al. (1998), for identical spheres the model becomes independent of the sphere radius. Besides the elastic properties of the minerals (G and v) and the confining pressure (P), the dominant parameters become the grain-contact area (a), porosity (ϕ) and coordination number (C). For the case of ideal spheres, the change in grain-contact area is exclusively associated with confining pressure, because the grains do not have rectilinear faces. Therefore, the only variables controlling the change in elastic properties associated with grain accommodation are porosity and coordination number. To use Hertz-Mindlin theory to model the packing effect, the mutual change of porosity and coordination number can be estimated from Murphy's relationship (Equation 2.5). Figure 2.10 compares the trend obtained from Hertz-Mindlin model, with the trend observed from laboratory results (Zimmer, 2003). An assumption of no shear stiffness at the grain contacts was necessary to match the laboratory data. The slope of the data is slightly larger than the slope obtained from the Hertz-Mindlin model.
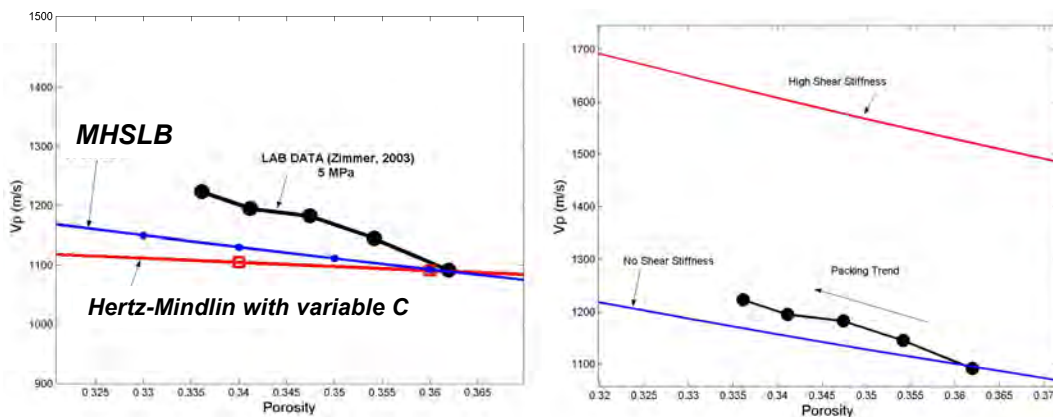
Figure 2.10: Comparison between laboratory results showing the effect of packing (Zimmer, 2003), and the modeled effect of packing using the modified Hashin-Shtrikman lower bound (MHSLB), and Hertz-Mindlin (HM) theory combined with Murphy's relationship for *C* and ϕ (Eq. 2.5). Figure on the left shows the results for the Unconsolidated Sandstone Model (Mavko, et al., 1998), which combines both the HM theory (for the anchor point) and the MHSLB. The red line shows that HM theory overestimates the velocity for unconsolidated sands. To fit the data, a correction factor for shear stiffness is necessary. The slope of the packing trend is slightly but systematically steeper than the MHSLB.

Another effect associated with mechanical compaction is grain stabilization (i.e. Zimmer, 2003). Laboratory and field studies of unconsolidated sandstones at low confining pressure demonstrate that to fit the data, low or no shear stiffness at the grain contacts has to be assumed (Bachrach, 1998; Zimmer, 2003). This discrepancy has been explained as the result of grain angularity (Bachrach, 1998) and grain sliding or rolling (Zimmer, 2003). On the other hand, Avseth (2000) and Gutiérrez (2001) have successfully used Hertz-Mindlin to model velocities of friable (uncemented) sandstones at depth. This discrepancy suggests that there is a compaction stage at which grain sliding or rolling is no longer feasible because of tight packing, and therefore the assumptions of the Hertz-Mindlin theory become valid. Figure 2.10 illustrates the difference between the assumptions of no shear stiffness and high shear stiffness at the grain contacts.
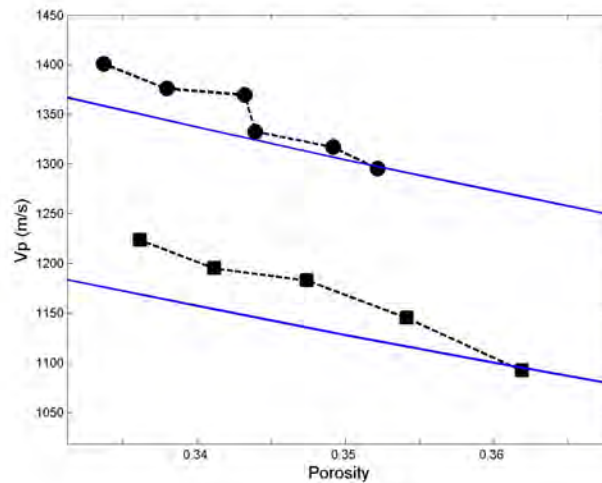
Figure 2.11: Compaction trend for a sand aggregate at 5 and 10 MPa confining pressures, after different loading cycles (Zimmer, 2003). The blue curves are the Hashin-Strickman lower bounds, after fitting the first data point. Notice the steeper slope of the compaction trend.

2.5.2. The Modified Hashin-Shtrikman Lower Bound and Packing

The comparison of the packing trend obtained from the MHSLB and laboratory results (Figure 2.11), shows that the MHSLB underestimates the effect of packing. The packing trend obtained from the MHSLB is about the same as that obtained from the Hertz-Mindlin model (Equations 2.7, 2.9, 2.10, 2.13, 2.20, and 2.21). The trends obtained from Hertz-Mindlin theory and MHSLB do not account for the effect of grain stabilization. In addition to this, the Hertz-Mindlin theory assumes idealized spheres that do not increase the grain-contact area after grain rearrangement These

two factors will increase the aggregate's elastic modulus, as the steeper slope of the laboratory data indicates. Consequently, both the Hertz-Mindlin model and the MHSLB constitute lower bounds for the effect of grain accommodation on both porosity and the elastic properties of granular materials. In particular, the MHSLB can be considered a lower bound for the effect of mechanical compaction.

2.6.   An Idealized Quinary Mixture

In order to mathematically evaluate the effect of sorting, we use a model for gradual infilling of a tight rhombohedric packing of spheres developed by White and Walton (1937). These authors calculated the size and the number of gradually smaller spheres required to fill the spaces between larger spheres. Starting from the tight packing of identical spheres, they made the analysis for five different sphere sizes forming a quinary mixture (Table 2.3). They also calculated the porosity reduction and the increment in surface area, as the mixture changed to binary, ternary, quaternary and quinary. The sorting index for each mixture has been derived from their results. Table 2.3 summarizes their results, and includes the sorting index of these mixtures. In spite of its idealized rhombohedric packing, White and Walton's study gives us the basic information to calculate the effect of sorting using the equations in Table 2.2.

Table 2.3: Parameters for the groups of infilling spheres for a rhombohedric packing (after White and Walton, 1937). The first column corresponds to the rhombohedric packing of identical spheres. The following columns indicate the size and volumes of the infilling spheres, and the final volume, porosity, surface area and sorting index of the resulting mixture.

	1st	2nd	3rd	4th	5th	Filler
Radius	r	0.414r	0.225r	0.177r	0.116r	Very small
Relative # of spheres	1	1	2	8	8	
Volume	$4.189r^3$	$0.298r^3$	$0.0476r^3$	$0.0225r^3$	$0.0066r^3$	
Added volume	$4.189r^3$	$0.298r^3$	$0.0952r^3$	$0.180r^3$	$0.0526r^3$	$0.622r^3$
Total volume of spheres	$4.189r^3$	$4.487r^3$	$4.582r^3$	$4.762r^3$	$4.815r^3$	$5.437r^3$
Porosity	0.2595	0.207	.19	0.158	0.149	0.039
Surface area	$12.566r^2$	$14.732r^2$	$16.004r^2$	$19.080r^2$	$20.456r^2$	
Sorting Index (SD/mean)	0.0	0.42	0.69	0.84	0.92	

2.7. Stochastic Simulation of Effective Elastic Properties

In order to evaluate the effect of grain-size distribution we use the quinary-mixture model from White and Walton (1937), and perform stochastic simulations using the equations in Table 2.2. The input parameters for this algorithm are the grain-size distributions, the porosity, the coordination numbers for each grain size, and the elastic properties of the solid. The grain-size distributions vary as we add smaller fractions to the aggregate, starting from identical spheres (1st column in Table 2.3), and then adding smaller spheres: 2nd column for a binary mixture, 3rd column for a ternary mixture, and so on. For each case we modeled a mixture with 2400 grains. The coordination numbers for the larger spheres increase as we add smaller spheres, reaching a top value of 19, under the assumption that all the added spheres are in contact with the largest spheres. However the coordination number of the added smaller spheres is always low (6-9). The harmonic average for the local C_{ij} was used in order to give more weight to the small sphere's C.
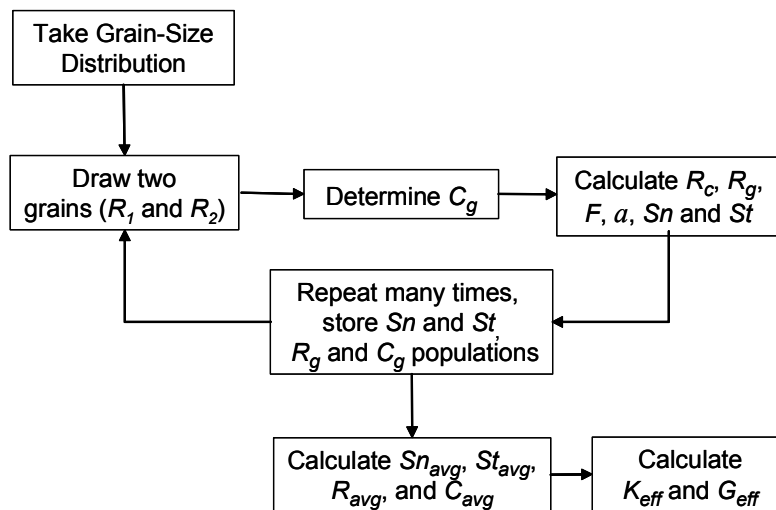
Figure 2.12: Algorithm to evaluate the effect of grain-size distribution on elastic properties, using stochastic simulation. C_g, R_c, and R_g are the averages of coordination number, radius of curvature and grain radius at each grain contact; F, a, Sn and St are force, radius of grain contact area, normal and shear stiffness at each grain contact. Sn_{avg}, St_{avg}, R_{avg}, and C_{avg} are the global averages of normal and shear stiffness, grain radius, and coordination number.

The algorithm steps are schematically shown in Figure 2.12, and the green lines in Figure 2.13 outline the results obtained from this algorithm. For every grain-size distribution, each grain size has a specific coordination number; therefore the coordination number at each grain contact (C_{ij}) is determined from the drawn grain radii R_i and R_j. The global averages of grain radius and coordination number are

calculated from the populations Rg_{ij} and C_{ij}. To evaluate the uncertainty associated with the which local and global coordination numbers are appropriate, additional simulations were performed using different options for the global (C_{avg}) and local (C_{ij}) coordination numbers. The results, also shown in Figure 2.13, indicate a variation from 10% to 16% for a given grain-size distribution, specified by porosity and sorting. As expected, the assumption of constant C_{avg} and C_{ij} generates the lowest variability. Remarkably, the algorithm outlined in Figure 2.12 produces an irregular trend similar to the one observed in the laboratory data.

The range of variability obtained from the stochastic models is small, and outlines a velocity-porosity trend flatter than the one predicted from the MHSLB. Fluid substitution puts the results within the framework of the well-established rock physics depositional and diagenetic trends. The final results are shown in Figure 2.14. Within this framework, it is clear that the scatter introduced by the uncertainty of the coordination number is relatively small, and all the different results follow a relatively flat trend. Using the highest-porosity value as the anchor point, it is clear that the results from the stochastic simulations follow a flatter trend than the MHSLB.
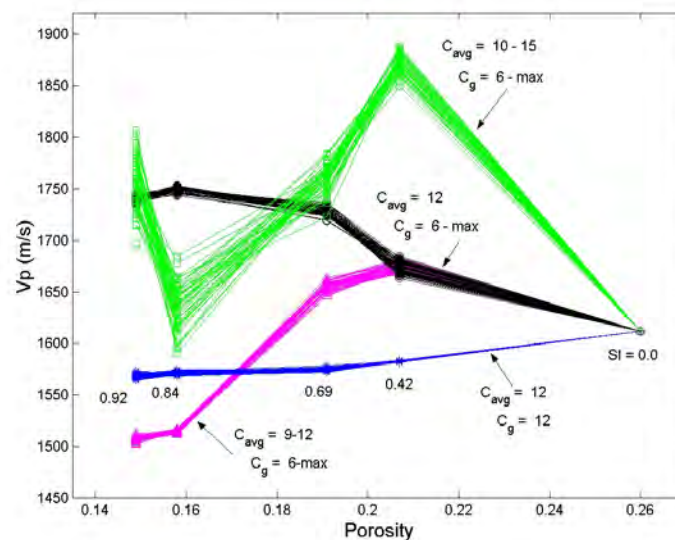
Figure 2.13: Results from the stochastic simulation. The green line corresponds to the algorithm outlined in Figure 2.12. SI corresponds to the sorting index for each grain-size distribution (Equation 2). The other lines show results from different simulations, assuming C_{avg} either is 12 or varies from 9 to 12, and C_g either is 12 or varies from 6 to the maximum possible for each mixture.
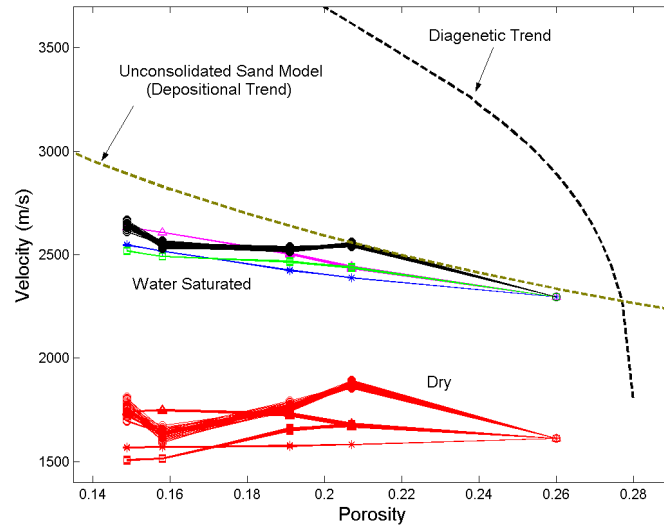
Figure 2.14: Comparison of the results from the stochastic simulation with the rock-physics diagenetic trend and the unconsolidated sandstone model. The slope of the results, after fluid substitution, show a flatter trend than the one predicted from the unconsolidated sandstone model (modified Hashin-Strickman lower bound).

2.8.   Comparison with Real Data

In essence, the theoretical modeling and the results from the stochastic simulations predict that the sorting effect has a flatter trend in the velocity-porosity plane than the packing effect. Whereas the MHSLB constitutes an upper bound to the sorting effect, it can be considered a lower bound for the packing effect. As shown below, both laboratory and subsurface data corroborate that the sorting effect follows a flatter trend than the MHSLB.

2.8.1. Comparison with Laboratory Data

There is good agreement between the sorting effect in both velocity and porosity observed in laboratory experiments (Zimmer, 2003), and the one predicted from the stochastic simulation (Figure 2.15). The shown laboratory data correspond to measurements of sand and glass-bead aggregates with different sorting, at the same confining pressure (5 MPa). The samples were prepared under similar protocols; therefore, the porosity variation between samples is assumed to be exclusively caused by sorting (Zimmer, 2003). The lower porosity for the theoretical textural models is the consequence of the idealized rhombohedric packing, a very unlikely configuration for unconsolidated sands. The comparison, however, is based on the departure of each trend from its respective MHSLB. As can be observed in Figure

2.15, the overall trend is flatter than the MHSLB, especially because of the break in the trend as the sorting deteriorates. In the theoretical models, this break is driven by the introduction of the smaller spheres. A similar break is observed in the laboratory data, suggesting that indeed small spheres have a softening effect on the aggregate.

A better understanding of this comparison can be obtained by looking at the slope of the velocity change, rather than the actual velocity values (Figure 2.16). In this comparison you can clearly see that the laboratory data show abrupt changes in the slope of the velocity-porosity trend. The MHSLB predicts a constantly increasing slope, which cannot reproduce the actual variability in the data. On the contrary, the results from the stochastic simulations reproduce the variable slopes, which overall create a flatter trend for the sorting effect.
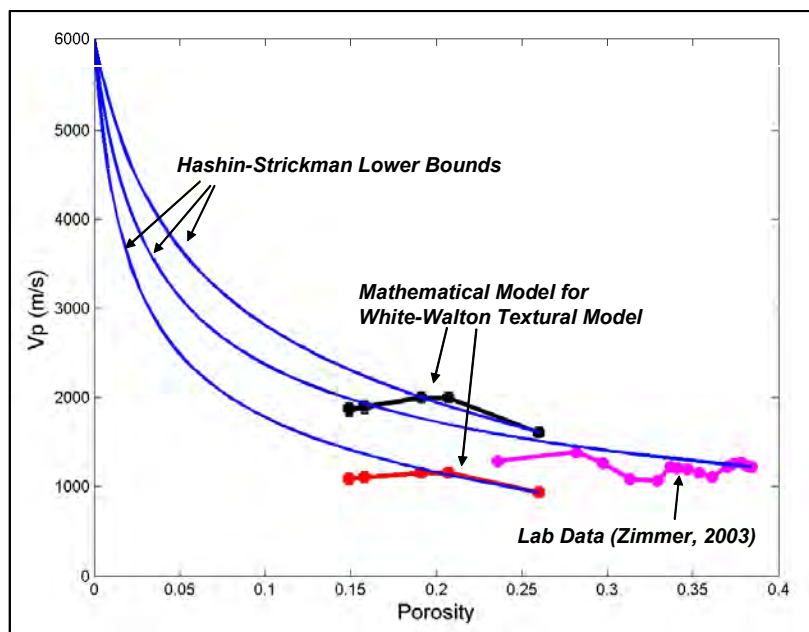
Figure 2.15: Comparison of the theoretical results from stochastic simulation for water saturated (black) and dry (red) aggregates, and fluid-substituted laboratory measurements (magenta) performed by Zimmer (2003). Whereas the MHSLB predicts a gradually increasing velocity, both the results from the stochastic simulation and the laboratory data show a highly variable slope, which overall translates into a flatter trend for the sorting effect.
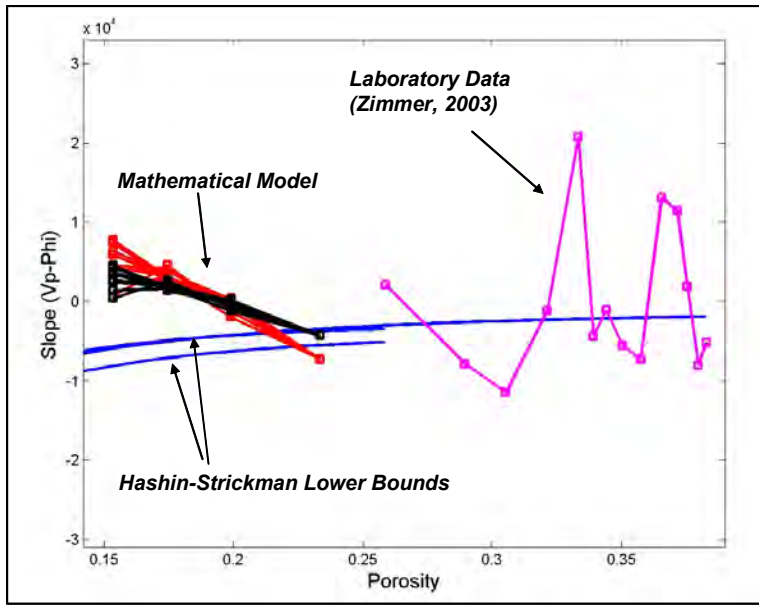
Figure 2.16: Comparison of the velocity-porosity slopes predicted from MHSLB, the stochastic simulation, and the actual slopes observed in laboratory data. Contrary to MHSLB, the stochastic simulation based on the theoretical formulation presented here can generate variable slopes such as those observed in the data.
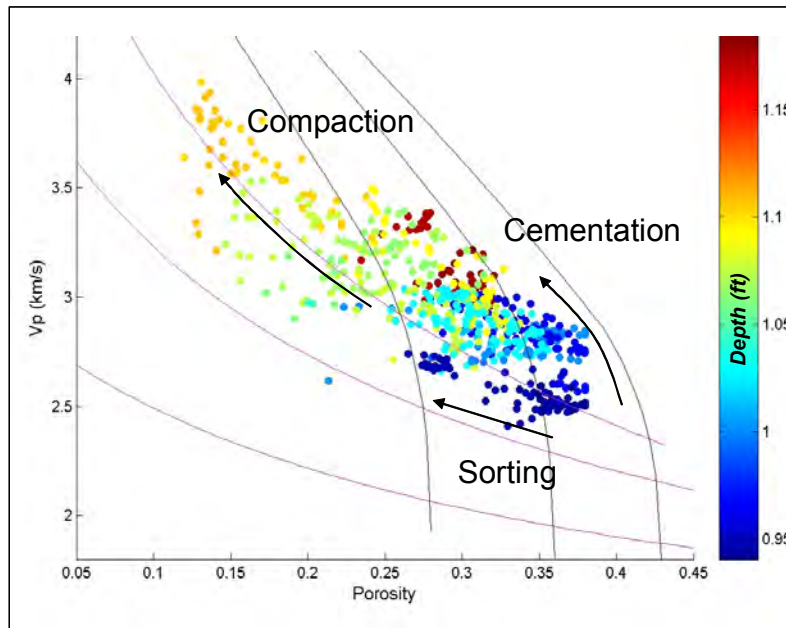
Figure 2.17: Well-log data of sandstones from one single stratigraphic sequence within an oil field. The graph shows the three main trends for sandstones: the flat trend associated with the sorting effect, the compaction trend, and the steep diagenetic trend. As predicted from the theoretical model, the MHSLB constitutes an upper bound for the sorting trend.

2.8.2. Comparison with Subsurface Data

The velocity-porosity trend observed in uncemented sandstones in the subsurface agrees with the flat trend predicted from our theoretical analysis (Figure 2.17). The flat trend is depicted by the shallower sands (blue dots in Figure 2.17), and follows a gentler slope than the one predicted from the MHSLB (magenta lines in Figure 2.17). The velocity and porosity data shown correspond to well-log measurements obtained along an interval where core porosity and sorting data were also available (Figure 2.18 and Figure 2.19). A least-squares regression was obtained for the correspondence between sorting and porosity from the core data (Figure 2.19). The least-squares regression also indicates a small negative correlation between porosity and the grain size, which indicates a minor influence of packing, probably associated with grain angularity (fine grains tend to be more angular than coarser sands). However, the effect of sorting on porosity, in these sands, is stronger than the effect of packing. The high-porosity have better sorting than the low-porosity clean sands. These two different types of sands create the flat trend observed in the velocity-porosity plane.

The grain-size distribution was obtained from laser particle size analysis (LPSA). Similar data were available from other cores (Figure 2.20), but the depth shifts required to compare with well-log data was not available. In both cases, the least-squares regressions show that although sorting has a strong effect on porosity, there is a small component associated with grain size itself (Figure 2.21). This grain-size component is probably the effect of grain angularity, since finer grain sizes tend to be more angular. It is important to emphasize that the coefficient of variation (Sorting Index) of these log-normal distributions is the best parameter to model the relationship between sorting and porosity. Similarly, the median is a better measure of the average grain size than the mean. The combination of the two core data sets provide a linear regression that approximates the regressions obtained from previous laboratory data, and from the modeled quinary mixture (Figure 2.3).
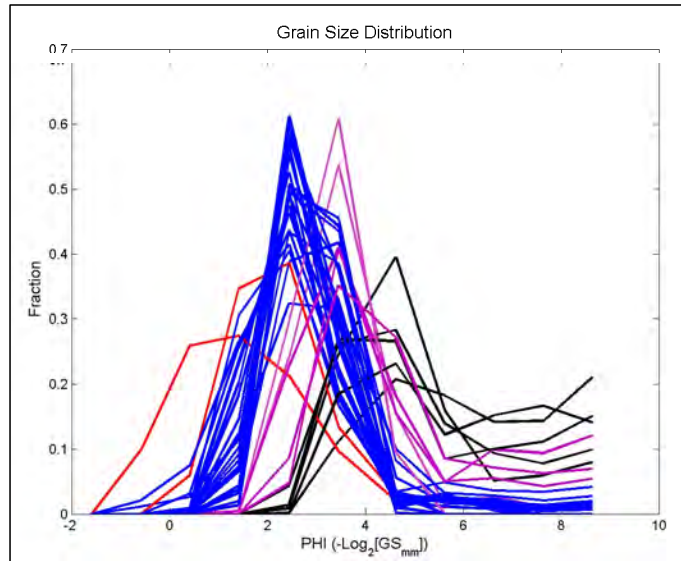
Figure 2.18: LPSA grain-size distribution from core samples. The sampled interval corresponds to the same well-log data shown in Figure 2.17.

$$\phi = -16.3883\left(\frac{\sigma}{\mu}\right) + 2.306(med_{PHI}) + 34.108$$
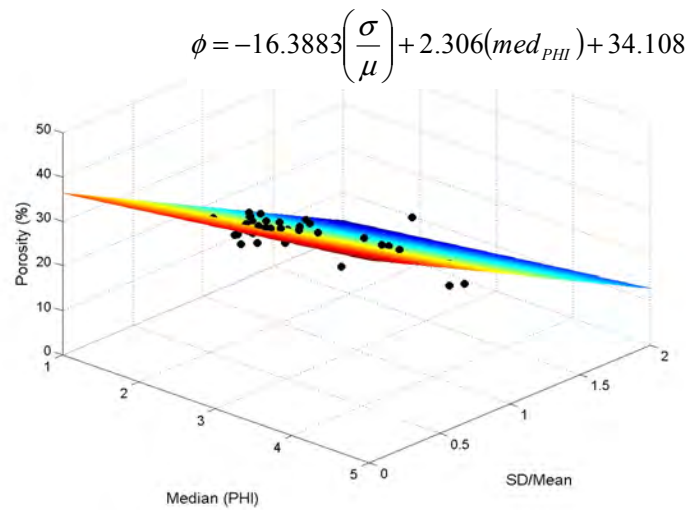
Figure 2.19: Visualization of the least-squares regression between porosity (ϕ), the coefficient of variation (σ/μ), and the median grain size in PHI scale (med_{PHI}), from core samples. Porosity is given in percentage or porosity units. The samples are sandstones and correspond to the grain-size distributions shown in Figure 2.18 and the well-log data shown in Figure 2.17.
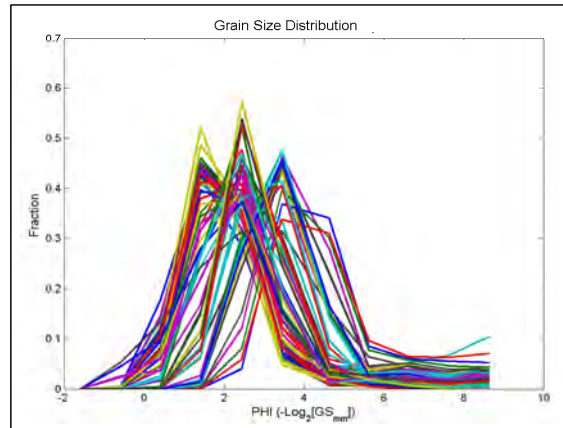
Figure 2.20: LPSA grain-size distribution obtained from a different well and stratigraphic interval than the one shown in Figure 2.18.

$$\phi = -7.5612\left(\frac{\sigma}{\mu}\right) + 1.0901(med_{PHI}) + 33.0116$$
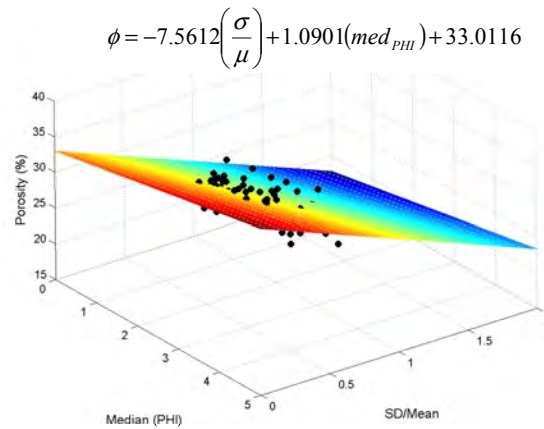
Figure 2.21: Visualization of the least-squares regression between porosity, median grain size (PHI scale) and coefficient of variation, corresponding to the data shown in Figure 2.20.

$$\phi = -11.8996\left(\frac{\sigma}{\mu}\right) + 1.2168(med_{PHI}) + 35.082$$
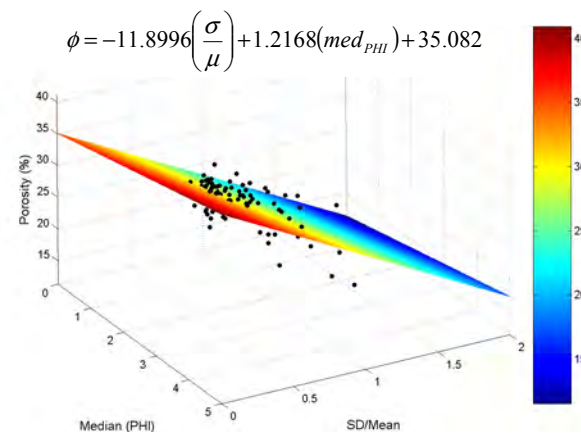
Figure 2.22: Visualization of the least-squares regression between porosity, median grain size (PHI scale), and coefficient of variation, corresponding to the combination of the data shown in Figure 2.18 and Figure 2.20.

2.9.   Discussion

Local and global average parameters and stochastic simulation have been necessary to introduce variable grain sizes into effective-medium contact models. A rigorous analytical solution of the elastic modulus of aggregates with variable grain size has not been the purpose of this work. Such a solution would vary depending on the spatial distribution of grain sizes. The stochastic approach followed in this work accounts for this variability, assuming is random, and allows us to evaluate the uncertainties associated with the local coordination number and the averaging methods. The results obtained by this approach suggest that statistical mechanics rather than deterministic solutions might be the right direction for further improvements in the effective-medium theory for granular aggregates.

The theoretical analysis, laboratory measurements, and subsurface data, all indicate that effect of sorting on the elastic properties of granular materials generates a flatter trend in the Vp-ϕ plane than the one predicted by the MHSLB. This flatter trend seems to be the consequence of a softening effect caused by introducing small spheres between large spheres. This softening effect of the small spheres is comparable to the effect of grain angularity analyzed by Bachrach *et al.* (2000). The effect has been theoretically modeled and observed in laboratory, and becomes evident in samples with large contrasts in grain size. For all practical purposes, the MHSLB should be considered an upper bound for the concomitant effect of sorting on the elastic properties and porosity of granular materials.

In contrast to the case of sorting, the MHSLB constitutes an approximate lower bound for the packing effect. The comparison of Hertz-Mindlin models, MHSLB and laboratory data shows that the trend associated with packing follows a steeper slope than the one predicted by any of these models. Grain stabilization and increasing grain-contact area by grain accommodation can both increase the aggregate stiffness. Zimmer (2003) obtained a similar conclusion. Bachrach (1998) modeled the variation in Poisson's ratio and shear stiffness based on the proportional increment of non-zero shear stiffness contacts. Since the slope predicted from both Hertz-Mindlin and the MHSLB models are similar, we can conclude that the MHSLB underestimates the actual packing trend.

Overall, the MHSLB constitutes a good approximation for the depositional trend in high-porosity sands (Avseth, 2000; Gutierrez and Dvorkin, 2001). The success of the MHSLB in reproducing the depositional trend might be the result of a combined effect of sorting and packing. Extension of the depositional trend to low-porosity

sands should be cautiously done. The difference in surface area associated with changes in sorting may influence the distribution of quartz cementation. Other factors like grain dissolution of feldspars may also have an effect. Although the trend observed in the velocity-porosity plane can be used to infer the variations in sorting of clean sands, it is always convenient to verify by looking at cuttings descriptions, thin sections and cores.

The effect of sorting on the elastic properties of high-porosity sands and sandstones differs from those of clay content and mechanical compaction. Although poor sorting is commonly associated with clay content, imposing an additional mineralogic effect on the elastic properties, the effect discussed here refers to grains with similar composition. For example, small amounts of clay can actually increase the elastic stiffness of an aggregate by acting as weak cementing material at the grain contacts (e.g. Dvorkin *et al.*, 1994). The sorting effect discussed here is independent and additional to the effect of clay content. On the other hand, mechanical compaction induces grain rearrangement, stabilization, and elastic deformation. Elastic deformation by itself does not induce a significant porosity reduction (e.g. Zimmer, 2003), and is induced by increasing confining stress. In contrast, grain rearrangement is an inelastic process that induces significant porosity reduction concomitant with the increment of the elastic stiffness. Grain rearrangement and stabilization tend to increase with depth, whereas sorting does not change with depth. Consequently, the gradual and concomitant variation of porosity and velocity with depth can be an additional criteria to distinguish between the sorting and packing effects.

2.10. Conclusions

The theoretical analysis presented in this paper indicates that the effect of sorting on both porosity and the elastic properties of granular materials differs from the effect of packing. This conclusion is also corroborated by the laboratory measurements and subsurface data. According to these results, variations in sorting generate a flatter trend in the velocity-porosity plane, with a slope gentler than the modified Hashin-Shtrikman lower bound (MHSLB). In contrast, variations in packing tend to generate a steeper slope than that predicted using the MHSLB. In general, whereas the MHSLB is a reasonable upper bound for the sorting effect, it constitutes a lower bound for the packing effect.

2.11. Acknowledgements

2.12. References

Allen, J. R. L., 2001, Principles of Physical Sedimentology, George Allen & Unwin (Publishers), London, 272 p.

Avseth, P., J. Dvorkin, G. Mavko, and J. Rykkje, 2000, Rock physics diagnostic of North Sea sands: Link between microstructure and seismic properties. Geophysical Research Letters, **27**, 2671-2764.

Avseth, P., 2000, Combining Rock Physics and Sedimentology for Seismic Reservoir Characterization in North Sea Turbidite Systems. Ph.D. thesis, Stanford University.

Bachrach, R., 1998, High-resolution shallow seismic subsurface characterization. Ph. D. thesis, Stanford University.

Bachrach, R., J. Dvorkin, and A. Nur, 2000, Seismic velocities and Poisson's ratio of shallow unconsolidated sands, Geophysics, **65**, 559-564.

Beard, D. C., and P. K. Weyl, 1973, Influence of texture on porosity and permeability of unconsolidated sand. American Association of Petroleum Geologists Bulletin, **15**, 2, 349-369.

Bourbie, T., O. Coussy, and B. Zinsner, 1987, Acoustics of Porous Media, Gulf Publishing Co., Houston, 334 pp.

Brandt, H., 1955, A study of the speed of sound in porous granular media, Journal of Applied Mechanics, **22**, 479-486.

Cumberland, D. J. and R. J. Crawford, 1987, The Packing of Particles, Elsevier Science Publishers, Amsterdam.

Digby, P. J., 1981, The effective elastic moduli of porous granular rocks, Journal of Applied Mechanics, **48**, 803-808.

Dvorkin, J., A. Nur, and H. Yin, 1994, Effective properties of cemented granular materials, Mechanics of Materials, 18, 351-366.

Dvorkin, J., and M. A. Gutierrez, 2001, Textural sorting effect on elastic velocities, part II: elasticity of a bimodal grain mixture, Society of Exploration Geophysicist Annual Meeting, Expanded Abstracts.

Estes, C.A., G. Mavko, H. H. Yin, and T. Cadoret, 1994, Measurements of velocity, porosity and permeability on unconsolidated granular materials, Stanford Rock Physics and Borehole Geophysics Project, annual report, **55**, G1-G9.

Fraser, H. J., 1935, Experimental study of the porosity and permeability of clastic sediments: Journal of Geology, **43**, 910-1010.

Fuchtbauer, H., 1974, Sediments and Sedimentary Rocks 1, in Sedimentary Petrology by W. v. Engelhardt, H. Fuchtbauer and G. Muller, Part II. John Wiley and Sons, New York, 464 pp.

Graton, L. C., and H. J. Fraser, 1935, Systematic packing of spheres –with particular relation to porosity and permeability: Journal of Geology, **43,** 785-909.

Gutierrez, M., 2001, Rock physics and 3D Seismic Characterization of Reservoir Heterogeneities to Improve Recovery Efficiency, Ph. D. dissertation, Stanford University.

Gutierrez, M., J. Dvorkin, and A. Nur, 2001, Textural sorting effect on elastic velocities, part I; laboratory observations, rocks physics models, and applications to field data, Society of Exploration Geophysicist Annual Meeting, Expanded Abstracts.

Inman, D. L., 1949, Sorting of sediments in the light of fluid mechanics, Journal of Sedimentary Petrology, **19**, 51-70.

Inman, D. L., 1956, Measures for describing the size distribution of sediments, Journal of Sedimentary Petrology, **22**, 125-145.

Johnson, K. L., 1985, Contact Mechanics, Cambridge University Press, 452 pp.

Kolbuszewski, J., 1948, An experimental study of the maximum and minimum porosities of sands, Proc. 2nd Int. Congress of Soil Mechanics, **7**, 47-49.

Krumblein, W. C., 1936, The use of quartile measures in describing and comparing sediments, American Journal of Science, **32**, 98-111.

Krumblein, W. C., 1938, Size frequency distributions of sediments and the normal phi curve, Journal of Sedimentary Petrology, **8**, 84-90.

Macrae, J. C. and W. A. Gray, 1961, Significance of the properties of materials in the packing of real spherical particles, Br. J. Appl. Phys., **12**, 162-172.

Marion, D., A. Nur, H. Yin, and D. Han, 1992, Compressional velocity and porosity in sand-clay mixtures, Geophysics, 57, 4, 554-563.

Mavko, G., J. Dvorkin, and T. Mukerji, 1998, The Rock Physics Handbook, tools for seismic analysis in porous media, Cambridge University press, New York, pp 329.

Mindlin, R. D., 1949, Compliance of elastic bodies in contact, Journal of Applied Mechanics, **16**, 259-268.

Murphy, D. W., III, 1982, Effect of Microstructure and Pore Fluids on The Acoustic Properties of Granular Sedimentary Materials, Ph. D. dissertation, Stanford University.

Nur, A., G. Mavko, J. Dvorkin, and D. Gal, 1995, Critical porosity: The key to relating physical properties to porosity I rocks, in Proc., 65th Annual International Meeting, Society of Exploration Geophysicists, 878.

Otto, G. H., 1939, A modified logarithmic probability graph for the interpretation of mechanical analyses of sediments, Journal of Sedimentary Petrology, **9**, 62-76.

Pettijohn, F. J., 1975, Sedimentary Rocks, 3rd edition, Harper and Row publishers, New York, 628 pp.

Rogers, J. J. and W. B. Head, 1961, Relationship between porosity, median size, and sorting coefficients of a synthetic sand, Journal of Sedimentary Petrology, **31**, 467-470.

Selley, R., 1988, Applied Sedimentology, Academic Press, San Diego, 523 pp.

Sohn, H. Y. and C. Moreland, 1968, The effect of particle size distribution on packing density, Canadian Journal of Chemical Engineering, **46**, 162-167.

Steinour, H. H., 1944, Rates of Sedimentation, Ind. Engng. Chem., **46**, 162-167.

Timoshenko, S. P., and J. N. Goodier, 1956, Theory of Elasticity, 2nd edition, McGraw-Hill, New York, 567 pp.

Trask, P. D., 1932, Origin and environments of source sediments of petroleum, Gulf Pub. Co., Houston, 323 pp.

Visher, G. S., 1969, Grain size distributions and depositional processes, Journal of Sedimentary Petrology, **39**, 1074-1106.

Visher, G. S., 1999, Stratigraphic Systems: Origin and Application, Academic Press, New York, 700 pp.

Walker, B. P., and T. Whitaker, 1967, An apparatus for forming uniform beds of sand for model foundations tests, Geotechnique, **17**, 161-167.

Walton, K., 1987, The effective elastic moduli of a random packing of spheres, Journ. Mech. Phys. Solids, **35**, 213-226.

Wentworth, C. K., 1922, A scale of grade and class terms for clastic sediments, Journal of Geology, **30**, 377-392.

White, H. E., and S. F. Walton, 1937, Particle packing and particle shape, Journal of the American Ceramists Society, **20**, 155-166.

Winkler, K. W., 1983, Contact stiffness in granular porous materials: comparison between theory and experiment, Geophysical Research Letters, **10**, 1073-1076.

Zimmer, M., M. Prasad, and G. Mavko, 2002, Empirical velocity-pressure and porosity-pressure trends in unconsolidated sands, SEG Annual Meeting, Expanded Technical Program Abstracts, **72**, 1866-1869.

Zimmer, M., 2003, Controls on the Seismic Velocities of Unconsolidated Sands: Measurements of Pressure, Porosity and Compaction Effects, Ph. D. dissertation, Stanford University.

Chapter 3

Pressure-Solution and the Rock-Physics Diagenetic Trend

3.1. Abstract

Based on well-log data, I show the rock-physics diagenetic trend for quartzose sandstones and present a pressure-solution model to reproduce this trend for high-porosity sandstones. In the low-velocity domain (Vp < 3.5 km/s), or high-porosity range (ϕ >0.18), the diagenetic trend shows a very steep slope in the velocity-porosity plane. This steep slope can be approximated using either the coating-cement or the Hertz-Mindlin effective-medium models. To calculate velocities, both models use the burial constant (a/R), defined as the ratio of the radius of grain-contact (a) to the grain radius (R). The steep slope observed in the data indicates increments of the burial constant without major changes in porosity, a relationship that can be the result of elastic deformation, cementing, or pressure-solution processes. The use of a cementing model at temperatures below the threshold for quartz cementation is questionable. Similarly, the Hertz-Mindlin model accurately predicts the burial constant for limited depth ranges. Alternatively, this study presents the Digby-Rutter pressure-solution model as a method to estimate the burial constant. This method, combined with Hertz-Mindlin theory to calculate velocities, reproduces the diagenetic trend and the velocity-porosity-depth relationships observed in the data.

3.2. Introduction

Steep velocity-porosity trends in sandstones, characterized by a fast increase in rock stiffness accompanied by a small decrease in porosity, are considered to be the consequence of diagenetic processes (Dvorkin and Nur, 1996; Avseth *et al.*, 2000). A good example of this diagenetic trend is shown in Figure 3.1, which corresponds

to well-log data from quartzose sandstones in the Llanos Basin (Colombia). In the low-velocity range (Vp < 3.5 km/s) this diagenetic trend shows a steep slope that has been explained as the result of incipient cementation (Dvorkin and Nur, 1996; Avseth *et al.*, 2000). Although pressure-solution has also been mentioned as an important factor, the relationship between this mechanism and the diagenetic trend in the velocity-porosity plane has not been established.
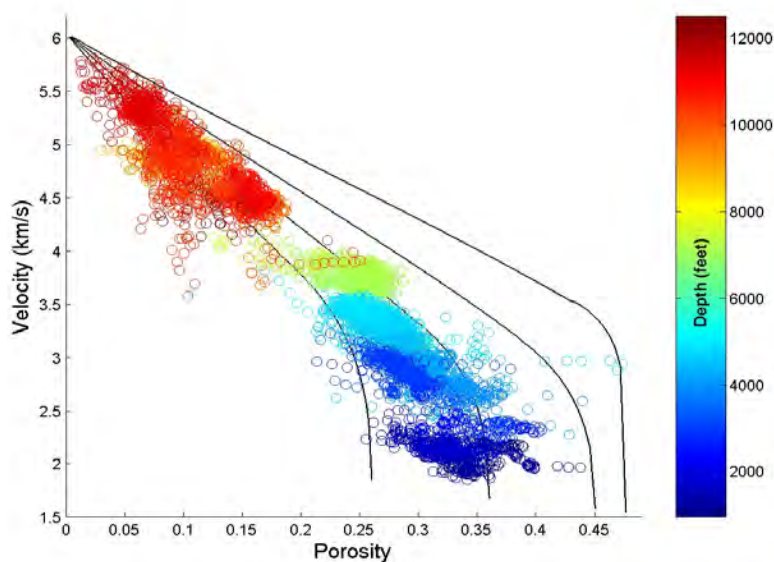
Figure 3.1: Velocity-Porosity well-log data, color-coded by depth. The data set consists of 6162 points from 6 wells, and corresponds to water-saturated quartzose sandstones in the Llanos Basin (Colombia).

Although the steep slope in the low-velocity range can be replicated using either the coating-cement (e.g. Dvorkin and Nur, 1996) or the Hertz-Mindlin (Mavko *et al.*, 1998) models, there still are some inconsistencies to be solved. Advocating quartz cementation to explain the velocities of shallow deposits is questionable. For example, in the data shown in Figure 3.1, the steep slope mainly involves rocks at depths between 1000' to 5000' (~300 to 1500 m), where temperatures are well below the threshold temperature for significant quartz cementation. On the other hand, the Hertz-Mindlin model is valid for a limited depth range. Beyond a certain depth, Hertz-Mindlin theory underestimates the velocity. Therefore, to reproduce some of the data points observed in Figure 3.1, we need either to advocate the presence of cement where it might not exist or use high, unrealistic, confining pressures. We solve these inconsistencies by introducing pressure solution in the analysis of the rock-physics diagenetic trend.

3.2.1 Diagenesis in Quartzarenites

Porosity reduction in sandstones occurs because of mechanical compaction, pressure solution, and cementation (e.g. Fuchtbauer, 1974; Stone and Siever, 1996; Paxton *et al.*, 2002). Diagenesis in quartzarenites and sandstones has been studied since more than a century ago (i.e., Sorby, 1863). Stone and Siever (1996) and Fuchtbauer (1974) present a comprehensive summary of this topic. Mechanical compaction and cementation are two opposite processes. If deposited at the grain contacts, cement precipitation inhibits compaction. Therefore, it reduces porosity without significant reduction of rock bulk volume (Figure 3.2a). Cement precipitation is controlled by fluid saturation of cementing minerals. Compaction can be induced either mechanically (grain sliding and accommodation) or chemically (pressure-solution) and implies bulk volume reduction (Figure 3.2b).

(a)   (b)
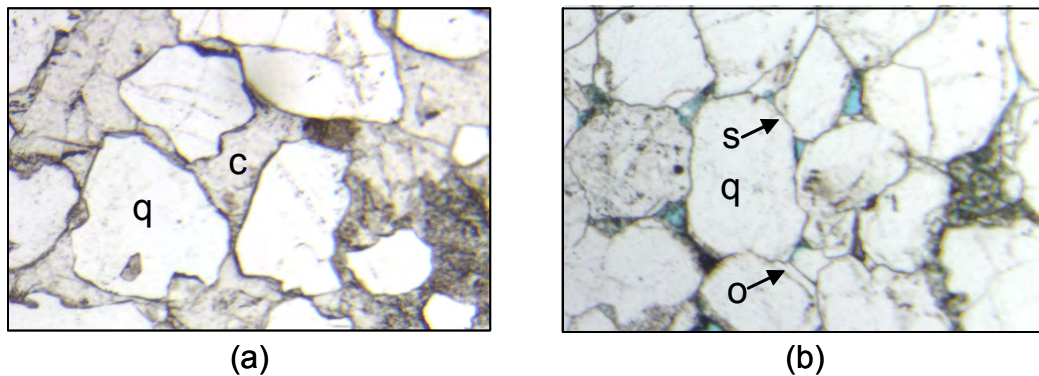
Figure 3.2: Comparison between a cemented rock with little compaction (a) and a cemented rock with significant compaction (b). The inter-granular volume (IGV) of (a) is much larger than (b). Coordination number of (b) is larger than (a). Grains are made of quartz (q), and average diameter is about 0.4 mm. Sample in (a) is cemented with calcite (c). Arrows indicate examples of quartz overgrowth (o) and pressure-solution contacts (s).

Stone and Siever (1996) showed that mechanical compaction is dominant until grain stabilization is reached. Most of the porosity reduction associated with mechanical compaction is caused by grain rearrangement and sliding, therefore beyond the point of grain stabilization mechanically induced porosity reduction is negligible (Stone and Siever, 1996; Paxton et al., 2002). The critical porosity of sand aggregates is considered to be around 0.4 (Nur *et al.*, 1995). This is the porosity at deposition of well-sorted, randomly packed sands, or the porosity of loosely packed, moderately-sorted sands. The effect of sorting can significantly decrease the porosity at deposition. Samples with different sorting and similar preparation protocols show a variation in critical porosity from 0.26 to 0.42 (Beard and Weyl, 1973; Zimmer, 2003). Nevertheless, sands with moderate sorting may have porosities of about 0.4

because of loose packing (e.g. Beard and Weyl, 1973; Atkins and McBride, 1992). Based on the changes of intergranular volume (IGV) and tight packing index (TPI) as a function of depth, Stone and Siever (1996) showed that pre-cementing porosity is about 0.3. Assuming that cementation starts at the point of grain stabilization, and also assuming an initial porosity of 0.4, we can infer a porosity reduction from mechanical compaction of about 0.1. A similar conclusion was obtained by Fuchtbauer (1974). Beyond the grain-stabilization point, additional compaction in rigid-grain sands may occur by pressure-solution (Fuchtbauer, 1974); while further mechanical compaction may occur in ductile-grain aggregates by significant grain deformation (Stephenson *et al.*, 1992; Giles, 1998). Based on the data from Paxton *et al.* (2002), I obtained the following expression for the mechanical compaction in rigid-grain sands:

$$\phi = \phi_0 e^{-0.075Z} , \tag{1}$$

where ϕ is porosity, ϕ_0 is the initial porosity and Z is depth (in km).
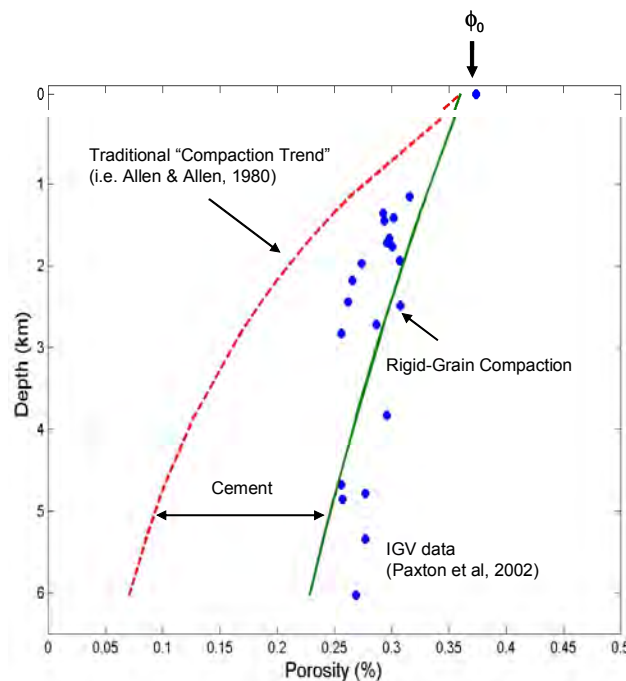
Figure 3.3: Porosity reduction for rigid-grain sandstones, according to IGV data from Paxton *et al.* (2002). The difference between the IGV and the final porosity, calculated using a traditional exponential "compaction trend" for sandstones (e.g. Allen and Allen, 1980), is presumed to be the result of cementation.

Cementation has been proposed by several authors as the dominant porosity-reduction mechanism after grain stabilization (e.g. Stone and Siever, 1996; Paxton *et*

al., 2002), although pressure solution can also reduce porosity by changing grain packing (Fuchtbauer, 1974). Cementation occurs by precipitation of minerals at either the grain contacts or at the interface between the grains and the fluid. Cement precipitation, which is controlled by fluid saturation of the cementing mineral or its components (e. g., Boudreau, 1997), increases rock strength (Dvorkin and Nur, 1996) and therefore inhibits compaction (Stephenson *et al.*, 1992; Stone and Siever, 1996). Onset of cementation is commonly controlled by temperature, although other conditions like EH and PH may also be important (e.g. Boudreau, 1997). Cementation at shallow depths, known as early diagenesis, is common for carbonate cements. A threshold temperature of 70-75° C has been established for significant quartz cementation (Stone and Siever, 1996; Walderhaug, 1994). Stone and Siever (1996) and Paxton *et al.* (2002) concluded that quartz cementation starts after grain stabilization, and is the most important factor causing porosity reduction in quartzarenites (Figure 3.3). Pressure solution by itself does not significantly reduce porosity (e.g. He *et al.*, 2002). However, Fuchtbauer (1974) demonstrated that pressure solution can change grain packing and induce additional significant porosity reduction, a conclusion supported by some laboratory experiments (Sprunt and Nur, 1977).

3.2.2   Pressure Solution

Pressure solution is the mechanism that explains the common occurrence of grain-contact dissolution and indentation of rigid grains in the subsurface (Figure 3.4). It is explained as the result of local grain dissolution enhanced by stress amplification at the contact. The concept that subjecting a mineral to stress enhances its solubility has been recognized for more than a century (Sorby, 1863). The process has been reproduced in the laboratory by several researchers (e.g. Sprunt and Nur, 1977; Rutter, 1983; Tada and Siever, 1986; Hickman and Evans, 1991, 1992; Dewers and Hajash, 1995; and Niemeijier *et al.*, 2002), and has been the subject of several theoretical analyses (e.g. Rutter, 1976; Tada and Siever, 1989; Renard *et al.*, 1999; Galmudi, 1999; He *et al.*, 2002), and numerical models (e. g. Angevine and Turcotte, 1983; Yang, 2001).

Different mechanisms have been proposed for the process of pressure solution. The three best known are water-film diffusion (Rutter, 1976), free-face pressure solution (Hickman and Evans, 1991), and the channels-and-islands model (Renard *et al.*, 1999). However, none of these models explains the development of stylolites, a common geologic structure also explained as the result of pressure solution. Galmudi

(1999) demonstrated that the asymmetric character of pressure solution contacts (Figure 3.4c) can be the result of minor differences in elastic strain energy on both sides of the contact. Stephenson *et al.* (1992) modeled grain deformation, commonly associated with pressure solution, using exclusively mechanical principles.
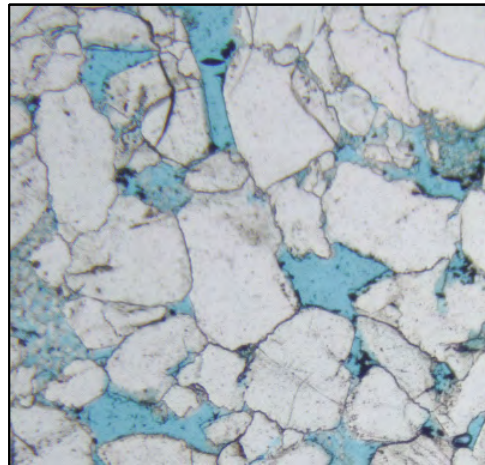
(a)
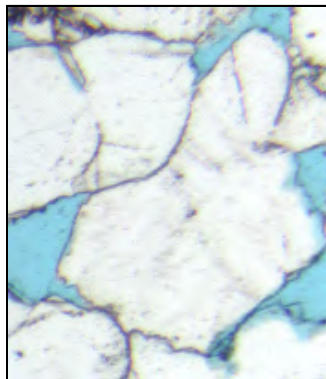
(b)   (c)

Figure 3.4: (a) Compacted sand. The scarcity of quartz overgrowths in this image suggests that pressure solution is the dominant mechanism increasing the grain-contact area in this sample. (b) Concave-convex contact. (c) Sutured concave-convex contact with asymmetric micro-stylolites. Both (b) and (c) are examples of advanced stages of pressure solution.

The process of pressure solution is controlled by the chemical potential and implies grain deformation through two basic steps: dissolution and diffusion. Precipitation may also be considered a third step, under the assumption that the process takes place within a closed system. However, Rittenhouse (1971) demonstrated that pressure solution most likely occurs within open systems, where solutes can be transported away from the regions where pressure solution takes place. The concepts of diffusion and chemical potential bring out the existence of a

medium of dissolution and diffusion of matter at the interface between the grain boundaries. It is assumed that a water film is trapped inside this interface. In fact, except for that of Stephenson *et al.* (1992), all the models mentioned above involve the presence of a thin water film between the grains. This implies that the pressure solution process is controlled by either the dissolution rate or the diffusion rate.

The rate of dissolution is controlled by the chemical potential, or molal free energy, defined by Krauskopf and Bird (1995) as a measure of the escaping tendency. The chemical potential, μ, of a given species or component (i.e. SiO_2) with respect to an assumed standard state, μ_0, is given by the following expression (Krauskopf and Bird, 1995):

$$\mu = \mu_0 + \Gamma T \ln \frac{f}{f_0}, \tag{3.2}$$

where Γ is the gas constant and the ratio f / f_0 is the relative fugacity of the component. According to Galmudi (1999) and Asaro and Tiller (1972), in the case of dissolution at the interface between a solid and a free fluid, the second term on the right side of Equation 3.2 depends on the effective normal stress (σ_n), the elastic strain energy (ε_{ij}), and the surface-energy density (γ), as follows:

$$\mu = \mu_0 - \sigma_n \Omega + \tfrac{1}{2} \sigma_{ij} \varepsilon_{ij} \Omega + \gamma \kappa \Omega . \tag{3.3}$$

In this expression, μ_0 is the chemical potential of the solid, Ω stands for the specific atomic volume, and κ is the surface curvature. Since $\varepsilon \ll 1$ and the curvature is small compared to the scale of the water film, it follows that the dissolution rate is controlled by the confining stress and pore pressure.

In his model for pressure solution, Rutter (1976) assumed that diffusion is the rate-controlling process. The solution of the diffusion equation with the boundary conditions established by Rutter (1976), obtained by Carslaw and Jaeger (1959), can be written a follows:

$$\chi(r) = \chi_0 + \frac{A_0}{4D_b}\left(a^2 - r^2\right), \tag{3.4}$$

where $\chi(r)$ is the concentration at radius r, A_0 is the dissolution rate, D_b is the grain boundary diffusivity, a is the radius of the interface, and χ_0 is the concentration of the solution outside the interface. From this expression it follows that the pressure-solution rate can be controlled by the concentration of solute (in this case silica) in the fluid. If this concentration is high, then diffusion will not take place.

3.2.3 The Rock Physics Diagenetic Trend

The overall diagenetic trend, often observed in sandstones, in the velocity-porosity plane can be reproduced by combining the modified Hashin-Shtrickman upper bound (MHSUB) with the coating-cement model (scheme 2 of Dvorkin and Nur, 1996), as proposed by Gal *et al.* (1999). The MHSUB model follows very well the trend in the high-velocity domain (Vp > 3.5 km/s), while the cementing models reproduce both the steep slope in the low-velocity domain (Vp < 3.5 km/s) and the gradual transition between the two domains (Figure 3.5). In Figure 3.5, the three lines towards the left (blue, red, and green), which bound the data, correspond to various combinations of the MHSUB and the coating-cement models. The key parameter is the initial porosity (porosity at deposition). For sands with similar packing, variations in initial porosity are associated with variations in sorting (Beard and Weyl, 1973; Zimmer *et al.*, 2002).

In high-porosity sandstones, the diagenetic trend clearly differs from the depositional trend. Sandstones at similar depths typically present a flatter trend in the velocity-porosity plane. This flatter trend, which corresponds to the bands of similar color in Figure 3.1, results from significant changes in porosity associated with minor changes in elastic stiffness. The main porosity-reduction mechanisms related with this flat-trend are matrix (clay) content, sorting, and mechanical compaction, as shown by Marion *et al.* (1992), Avseth (2000), Dvorkin and Gutierrez (2001), and Zimmer *et al.* (2002). For rocks at the same pressure conditions, sorting and clay are the dominant mechanisms. Therefore this trend is called the depositional trend. The depositional trend can be reproduced using either the modified Hashin-Shtrickman Lower Bound (MHSLB), or the Reuss average.

The four lines shown in Figure 3.5 constitute theoretical trends that can be used as a reference to diagnose the rock texture. The black line represents the stiffest possible quartz sand for any given porosity. It corresponds to an aggregate of identical and rounded quartz spheres with cubic packing, following the contact-cement model (scheme 1 of Dvorkin and Nur, 1996). The line corresponds to idealized, super-mature, quartz sands with cubic packing and contact cement, and can be considered the upper bound for water-saturated quartz sands. The data, shown as a bi-dimensional histogram, indicates that the green line constitutes a narrower and still reasonable upper bound. This line corresponds to a quartz aggregate of identical spheres with coating cement. The red line, which bounds most of the data, follows the trend of random packs with coating cement. The effect of sorting is

represented by the blue line, with a critical porosity of 0.26, a likely value for clean sands with moderate to poor sorting (Zimmer, 2003).
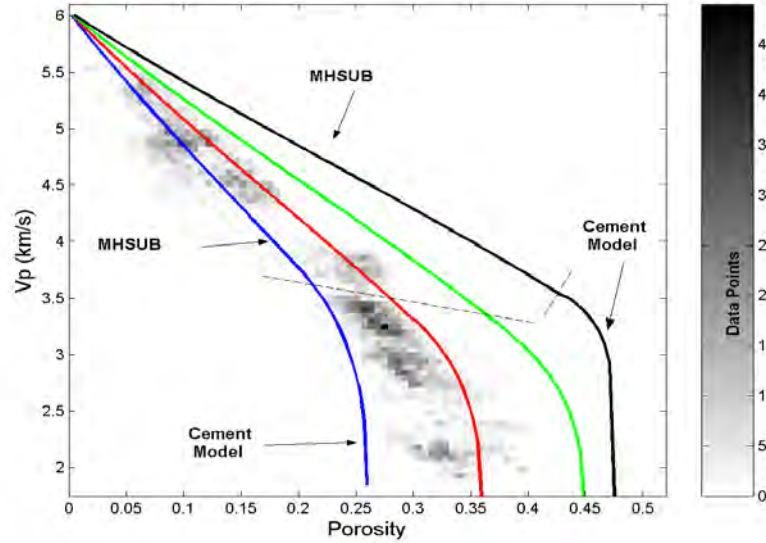
Figure 3.5: Velocity-Porosity bidimensional histogram, obtained from the data shown in Figure 3.1. The trend lines, derived by combining MHSUB and coating-cement models, bound the trend observed in the data.

3.3. Hertz-Mindlin and Cementing Models for Quartzarenites

The Hertz-Mindlin model (Mavko *et al.*, 1998) can also be used to reproduce the steep velocity-porosity gradient observed in the low-velocity range in Figure 3.5. Both the Hertz-Mindlin and the cementing models (Dvorkin and Nur, 1996) use the burial constant *(α=a/R)* to calculate the effective elastic modulus. Stephenson *et al.* (1992) defined the burial constant (*α*) as the ratio of the radius of grain contact *(a)* to the grain-size radius *(R).* In the Hertz-Mindlin model, the effective bulk *(K$_{effHM}$)* and shear modulii *(G$_{effHM}$)* are related to the burial constant by the following expressions:

$$K_{effHM} = \frac{C(1-\phi)G}{3\pi(1-v)}\alpha \,, \tag{3.5}$$

$$G_{effHM} = \frac{C(1-\phi)G}{5\pi}\left[\frac{1}{1-v} + \frac{3}{2-v}\right]\alpha \,, \tag{3.6}$$

where *C* is the coordination number, *G* is the mineral shear modulus, *v* is Poisson's ratio, and *φ* is porosity. Similarly, following Mavko *et al.* (1998), for the case of quartz grains and cement, the expressions for the effective bulk and shear modulus in the cementing model are:

$$K_{effC} = \frac{C(1-\phi_o)G(1-v)}{3(1-2v)}\left[A_n\alpha^2 + B_n\alpha + C_n\right], \tag{3.7}$$

$$A_n = -0.0445; \quad B_n = 0.3039; \quad C_n = 0.0006,$$

$$G_{effC} = \frac{3}{5}K_{effC} + \frac{3}{20}C(1-\phi_o)G\left[A_t\alpha^2 + B_t\alpha + C_t\right], \tag{3.8}$$

$$A_t = -0.116; \quad B_t = 0.5647; \quad C_t = -0.0027,$$

In these equations, ϕ_0 stands for the initial, pre-cementing porosity.

Each model provides a method to calculate the burial constant. In Hertz-Mindlin model, the burial constant depends exclusively on the applied pressure *(P)*, according to this expression:

$$\alpha_{HM} = \left[\frac{3\pi(1-v)}{2C(1-\phi)G}P\right]^{1/3}. \tag{3.9}$$

In the cementing model, the burial constant depends on the cement saturation of the pore space *(S)*, defined as the fraction of the pore space of the uncemented sand (intergranular volume) occupied by cement (Mavko *et al.*, 1998). For the scheme 1, known as the contact-cement model, the burial constant is

$$\alpha_{C1} = 2\left[\frac{S\phi_o}{3C(1-\phi_o)}\right]^{1/4}. \tag{3.10}$$

Similarly, for scheme 2, referred here as the coating-cement model,

$$\alpha_{C2} = \left[\frac{S\phi_o}{3C(1-\phi_o)}\right]^{1/2}. \tag{3.11}$$

For the specific case of water-saturated quartzose sandstones with quartz cement, the Hertz-Mindlin model predicts slightly higher P-wave velocities than the cementing model, as illustrated in Figure 3.6. The ratio Vp_{HM}/Vp_C ranges from 1.05 to 1.1. The difference in shear-wave velocities is larger. The ratio Vs_{HM}/Vs_C varies between 1.2 and 1.15. An important result from this comparison is that, for the same burial constant, the Hertz-Mindlin model consistently predicts either similar or higher velocities than the cementing model.
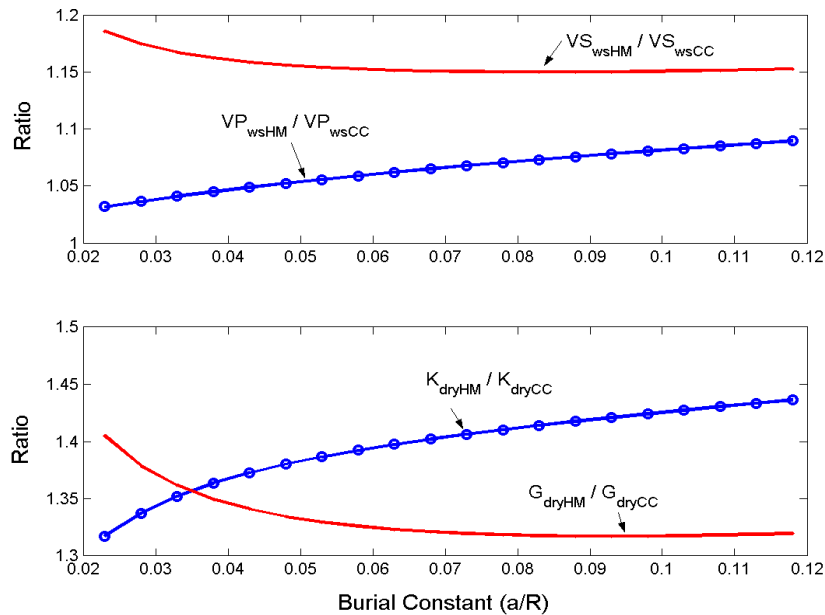
Figure 3.6: Comparison of Hertz-Mindlin (HM) and cementing models (CC), showing the variation of the ratios of the water-saturated velocities (above), and the dry-framework elastic modulus (below), as a function of the burial constant (a/R).

3.4. Pressure-Solution and the Rock-Physics Diagenetic Trend

Pressure-solution models provide methods to link the variations in burial constant to depth, and more specifically to pressure and temperature gradients. Equation 3.9 provides the first estimate, which corresponds to the elastic solution from Hertz-Mindlin theory. Here we discuss two pressure-solution models: the burial-constant model, proposed by Stephenson *et al.* (1992); and a new model named the Digby-Rutter model, a modification of the pressure-solution model established by Rutter (1976).

3.4.1. Stephenson's Burial Constant Model

According to Stephenson *et al.* (1992), for sandstones with specific depositional texture, at compaction equilibrium, the only parameter uniquely defined by its maximum burial depth is the burial constant. This means that we cannot distinguish between cementing and pressure solution as the mechanism incrementing the grain-contact area. For an idealized aggregate of identical spheres with cubic packing, the burial constant (α) is predicted as follows:

$$\alpha = \left[\frac{\sigma_{eff} / \sigma_{qe}}{1 - T / T_A} \right]^{1/2}, \tag{3.12}$$

where T is the current absolute temperature, T_A is the mineral-melting absolute temperature at standard pressure conditions, σ_{eff} is the effective confining stress (overburden), and σ_{qe} is a constant that depends on the mineral properties as follows (Stephenson *et al.*, 1992):

$$\sigma_{qe} = \frac{C(1-\phi_o)A\rho}{4M}, \tag{3.13}$$

where C and ϕ_o are as defined before, ρ is mineral density, A is the mineral activation energy and M is the mineral gram-molecular weight. For the case of high-porosity quartz aggregates ($\phi_o = 0.4$) σ_{qe} is 1883 Pa (Stephenson *et al.*, 1992).

3.4.2. Digby-Rutter Model for Pressure Solution

Rutter (1976) presents a model for pressure solution, where the grain strain rate for a specific depth *(z)* is given by

$$\frac{d\varepsilon}{dt} = \frac{4\chi_q D_b w}{\Gamma T(z) a(t,z)^3 \rho} \sigma_a(t,z), \tag{3.14}$$

where σ_a is the effective normal stress across the grain contacts, χ_q is the concentration of a saturated solution in chemical equilibrium with an unstressed solid, ρ_s is the solid density, a is the radius of grain contact, D_b is the diffusivity of quartz in the water along an intergranular diffusion boundary of thickness w, Γ is the gas constant, and T is the absolute temperature.

An important, and usually neglected, aspect of pressure solution is that as the grain-contact area increases, the effective normal stress across the grain contacts decreases. Hickman and Evans (1995) experimentally demonstrated this effect. To incorporate this concept in Rutter's formulation for pressure solution, we can write Equation 3.14 in terms of the force applied at the grain contact (F) and the radius of grain contact (a):

$$\frac{d\varepsilon}{dt} = \frac{4\chi_q D_b w}{\pi \Gamma T(z) \rho} \frac{F(z)}{a(t,z)^5}. \tag{3.15}$$

According to Digby (1981), F is given by the following expression:

$$F(z) = \frac{4\pi R^2 P(z)}{C(1-\phi)} . \tag{3.16}$$

The initial radius of grain contact (a_0) can be determined from Equation 3.9. Using the expression that relates the normal displacement between two grains (δ) to the radius of grain contact (a) and the grain radius (Mavko *et al.*, 1998, p. 150), the burial constant can be related to the strain rate according to the following expression:

$$\alpha(t,z) \approx \left(\frac{\delta(t,z)}{R(t,z)} \right)^{1/2} = \left(2\varepsilon(t,z) \right)^{1/2} . \tag{3.17}$$

Equations 3.15, 3.16, and 3.17 constitute a new model for pressure-solution, the Digby-Rutter model. Although Equation 3.15 is time dependent, it is important to point out that it implies that for any given depth there is an equilibrium condition for the strain rate. The intergranular force (F) will decrease as a function of the time-dependent increments in coordination number (C), and reduction in porosity (ϕ) and grain radius (R). Similarly, as the deformation goes on, the radius of the grain contact area (a) increases. These combined effects imply that for any given depth there is an equilibrium point beyond which further time-dependent deformation, and therefore further porosity decrease and burial-constant increase, is negligible.

Table 3.1: Values used for the different parameters specified by Rutter's model for pressure solution, and required to run the algorithm based on the proposed Digby-Rutter model. Based on Fowler and Yang (1999).

$\chi_q = V_m\chi_0 M_s$	1.2×10^{-9}	Quartz concentration
V_m	$2 \times 10^{-5} m^3 mol^{-1}$	Molar volume of quartz
χ_0	10^{-4} M	Quartz concentration at equilibrium.
M_s	6×10^{-2} kg mol^{-1}	Quartz molecular weight
$D_b w$	$1 \times 10^{-19} m^3 s^{-1}$	Diffusion coefficient (D_b) and thickness (w) of the thin water film.
Γ	8.3 J mol^{-1}K^{-1}	Gas constant

3.4.3. A New Algorithm for Modeling Pressure Solution

Figure 3.7 illustrates the algorithm for modeling pressure solution, implemented using Equations 3.15, 3.16 and 3.17, and numerical integration. The input data for this algorithm is well-log data. Age determinations for some stratigraphic horizons are necessary in order to build a burial history. Based on this burial history, the algorithm calculates the burial constant $\alpha(t,z)$ for specified time intervals. The depth *(z)* depends on the sedimentation-accumulation rate, and therefore P and T also

change with time. As stated, the algorithm does not account for the effect of uplift and erosion. It estimates the burial constant for quartzose sands at their maximum burial depth, assuming a relatively simple burial history before tectonic deformation.
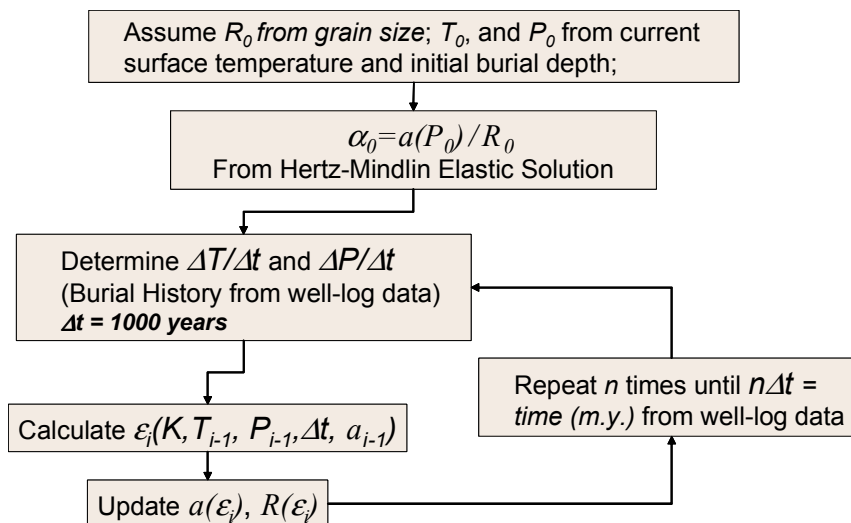
Figure 3.7: Algorithm for modeling pressure solution using the Digby-Rutter model for pressure solution explained above.

3.5. The Diagenetic Trend of High-Porosity Quartzarenites

To evaluate the Digby-Rutter model, and the new algorithm derived from it, I plan to reproduce the velocity-porosity-depth trend observed in high-porosity ($\phi >$ 0.18) quartzarenites. The data correspond to Mesozoic and Cenozoic quartzarenites and quartzose sandstones from the Llanos Basin (Colombia), a Cenozoic foreland basin (Cooper *et al.*, 1995). The velocity and porosity data are illustrated in Figure 3.1. Age determinations are based on published biostratigraphic determinations (Cooper *et al.*, 1995), and correlation of major flooding surfaces across the basin (). The values used for the parameters required to run the algorithm, shown in Table 3.1, are based on Fowler and Yang (1999).

The proposed Digby-Rutter model for pressure solution provides a better fit to the burial-constant trend observed in the data than either the Hertz-Mindlin model or Stephenson's burial-constant model. The velocity data can be used to estimate a burial-constant value for each data point, and determine the burial-constant trend as a function of depth. The results obtained can be compared against the predictions of burial-constant values resulting from the Hertz-Mindlin model, Stephenson's burial-constant model, and the algorithm based on the proposed Digby-Rutter model. This

comparison is shown in Figure 3.9, and clearly illustrates that while the algorithm provides the best fit to the data, Stephenson's model overestimates the burial-constant trend, and below 1000 m, Hertz-Mindlin underestimates the trend.
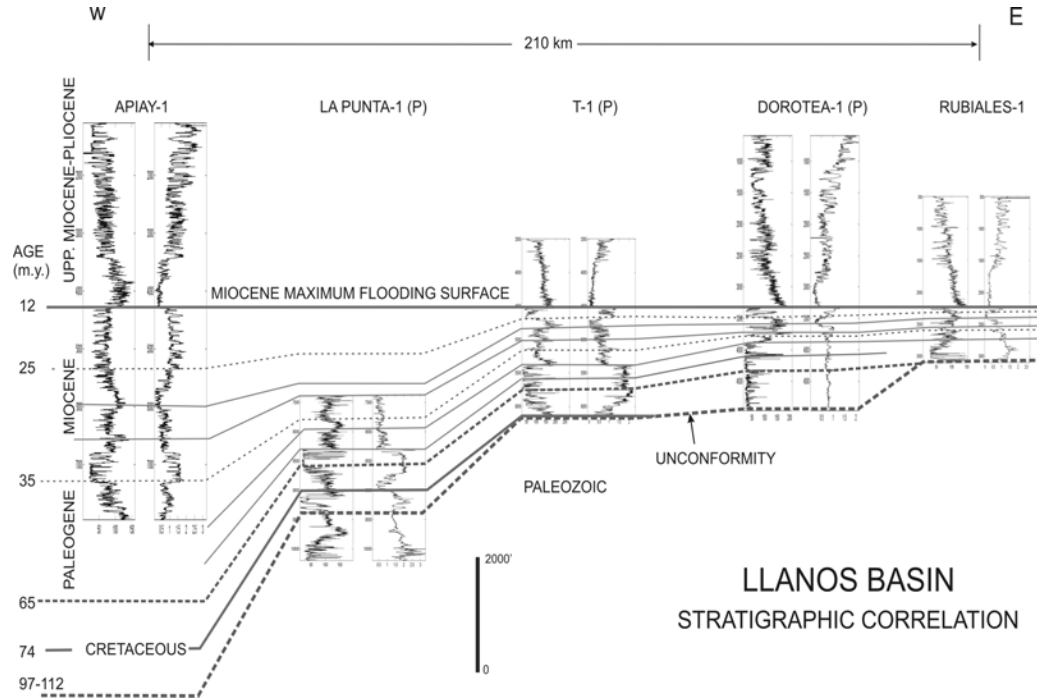
Figure 3.8: Stratigraphic correlation of the five wells used in this study, across the Llanos Basin (Colombia). The age of the key horizons used for correlation are shown on the left.

To calculate P-wave velocities from the burial-constant values obtained from the algorithm we can use the Hertz-Mindlin model. This way, the velocity-depth trend can be reproduced. The coating-cement model, with quartz as the cementing material, could also be used, since the difference between the two models is small (Figure 3.6).

The reproduction of the porosity-depth trend is based on an empirical approach. He *et al.* (2002) derived the following expression for the porosity reduction induced by pressure solution:

$$\phi(z,t) = \frac{\phi_o - \varepsilon(z,t)}{1 - \varepsilon(z,t)}, \qquad (3.18)$$

where the final porosity ϕ depends on the initial porosity ϕ_0 and the grain strain (ε), the later a function of both time (t) and depth (z). The porosity obtained from this, indicated as A in Figure 3.10, overestimates the slope of the porosity-velocity-depth trend, as compared with the data. Given that there is also porosity reduction induced

by mechanical compaction and incremental packing associated with pressure solution, as discussed in the introduction, it is also necessary to consider the porosity reduction by mechanical compaction in rigid grains (Equation 3.1). The assumption of pure mechanical compaction of rigid grains, indicated as B in Figure 3.10, underestimates the slope of the velocity-porosity-depth trend. The final porosity is therefore a combination of both porosity-reduction mechanisms: pressure solution and mechanical compaction. A general expression for this final porosity is

$$\phi(z,t) = \omega_1 \phi_o e^{-0.075z} + \omega_2 \frac{\phi_o - \varepsilon(z,t)}{1 - \varepsilon(z,t)}, \tag{3.19}$$

where ω_1 and ω_2 are the weights for each one of the porosity-reduction mechanisms. The final trend, enhanced as big dots in Figure 3.10, is the arithmetic average of these two mechanisms.
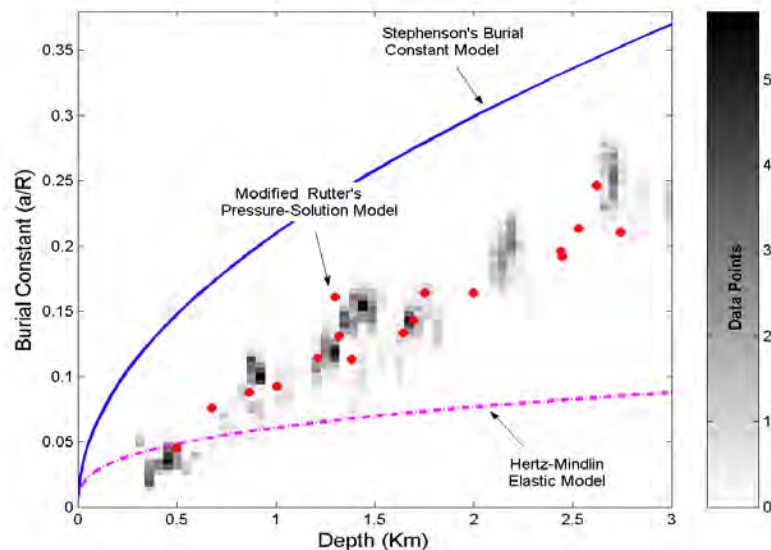
Figure 3.9 : Burial constant as determined from the velocity data shown in Figure 3.1, using Hertz-Mindlin model. The data is compared against three different methods to obtain the burial constant as a function of confining pressure and depth. The digby-Rutter model for pressure solution (red dots) allows a good fit to the data.

The velocity-depth trend obtained from the Digby-Rutter model, combined with the porosity-depth trend resulting from Equation 3.19, generates a velocity-porosity-depth trend that reproduces reasonably well the trend observed in the data. The trend obtained, indicated by colored large dots in Figure 3.10, follows the theoretical path of well-sorted quartzarenites with initial random packing. These would be the anchor points to apply the modified Hashin-Shtrickman lower bound (MLHS) to account for variations associated with sorting or other depositional factors.
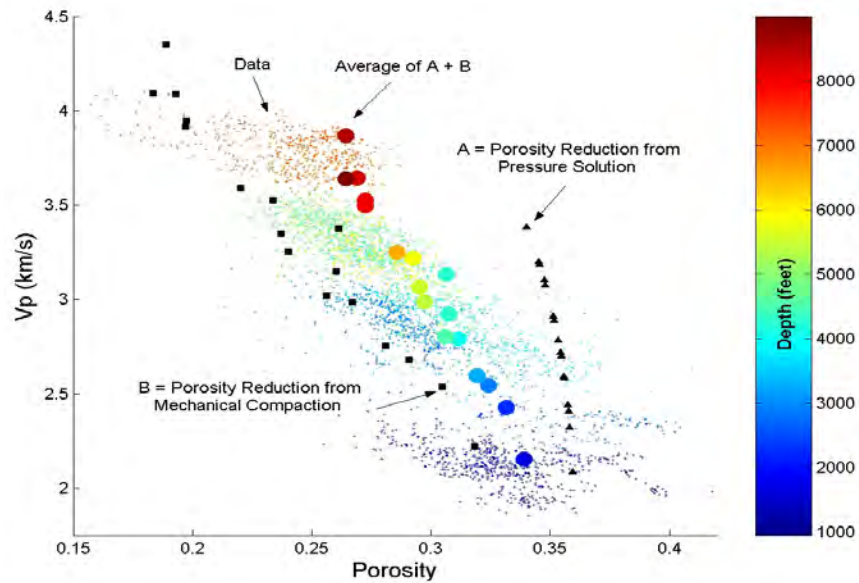
Figure 3.10: Reproduction of the velocity-porosity-depth relationship observed in the data. Velocity calculated using the burial constant derived from the Digby-Rutter pressure-solution model. Porosity reduction estimated as the average of mechanical compaction and pressure solution.

3.6. Discussion

The Digby-Rutter model for pressure solution constitutes a new model that provides the best estimate of the burial constant for a given maximum burial depth. This model results from the combination of Digby's solution for the intergranular pressure (Digby, 1981) and Rutter's model for pressure solution (Rutter, 1976). It explains the deviations from the Hertz-Mindlin model at depths where significant cementation is unlikely. The model also provides a method to estimate the diagenetic trend of high-porosity ($\phi > 0.18$) quartzarenites and quartzose sandstones. In contrast to Rutter's model (Rutter, 1976), the proposed new model implies that for any given depth the deformation will reach an equilibrium point, beyond which further porosity reduction will be negligible. The algorithm implemented takes into account the sediment-accumulation rate as a significant geologic variable that controls the burial-constant values obtained for a given depth.

Combined with cementation models (e.g. Walderhaug, 1994), the model proposed here could be used for forward modeling of seismic and hydraulic properties of quartzose sands in frontier areas. However, this would require a further assessment of uncertainty. Sand aggregates are more complex than the idealized sphere packs used for Digby's derivation of intergranular pressure or the smooth and

flat contact assumed for Rutter's model for pressure solution. The Digby-Rutter model is an approximation to nature's complexity. Digby's derivation of intergranular pressure could also be combined with other pressure solution models. In any case, there are uncertainties associated not only with the assumptions made in the models but also with the values used for the input parameters. Therefore these models should be used with caution.

3.7. Conclusions

The velocity-porosity diagenetic trend of quartzose sandstones shows a steep slope in the low-velocity domain (Vp<~3.5 km/s), which results from significant increments in the burial constant and relatively small changes in porosity. Three processes can explain this trend: elastic deformation, incipient cementation and pressure solution.

The Digby-Rutter pressure-solution model, derived here, provides the best estimates of the burial constant as a function of depth and sedimentation rate. Combining this model with either the Hertz-Mindlin or the coating-cement effective-medium models, and adjusting the porosity to account for the effect of compaction, it has been possible to replicate the velocity-porosity-depth trends observed in the data.

3.8. Acknowledgements

3.9. References

Allen, P. A., and J. R., Allen, 1980, Basin Analysis Principles and Applications, Blackwelll Scientific, London, 451p.

Angevine, C. L., and D. L. Turcotte, 1983, Porosity reduction by pressure solution: a theoretical model for quartz arenites: Geological Society of America Bulleting, **94**, 1129-1134.

Asaro, R. J. and W. A. Tiller, 1972, Interface morphology development during stress corrosion cracking: Part I, via surface diffusion: Met. Trans., **3**, 1789-1796.

Atkins, J. E. and E. F., McBride, 1992, Porosity and packing of Holocene river, dune, and beach sands: American Association of Petroleum Geologists Bulletin, **76**, 339-355.

Avseth, P., J. Dvorkin, G. Mavko, and J. Rykkje, 2000, Rock physics diagnostic of North Sea sands: Link between microstructure and seismic properties. Geophysical Research Letters, **27**, 2671-2764.

Avseth, P., 2000, Combining Rock Physics and Sedimentology for Seismic Reservoir Characterization in North Sea Turbidite Systems, Ph. D. thesis, Stanford University.

Beard, D. C., and P. K. Weyl, 1973, Influence of texture on porosity and permeability of unconsolidated sand. American Association of Petroleum Geologists Bulletin, **15**, 349-369.

Boudreau, B. P., 1997, Diagenetic models and their implementation: modeling transport and reactions in aquatic sediments, Springer Verlag, Berlin, 414 pp.

Carslaw, H. S., and J. C. Jaeger, 1959, Conduction of Heat in Solids, Oxford, Clarendon Press.

Cooper, M A, F. T. Addison, R. Alvarez, M. Coral, R. Graham, A. Hayward, S. Howe, J. Martinez, J. Naar, R. Penas, A. Pulham, and A. Taborda, 1995, Basin development and tectonic history of the Llanos Basin, Eastern Cordillera, and middle Magdalena Valley, Colombia: American Association of Petroleum Geologists Bulletin, **79**, 1421-1443.

Dewers, T., and A. Hajash, 1995, Rate laws for water-assited compaction and stress-induced water-rock interaction in sandstones: Journal of Geophysical Research, **100**, 13,093-13,112.

Digby, P. J., 1981, The effective elastic moduli of porous granular rocks, Journal of Applied Mechanics, **48**, 803-808.

Dvorkin, J., and M. A. Gutierrez, 2001, Textural sorting effect on elastic velocities, part II: elasticity of a bimodal grain mixture, Society of Exploration Geophysicist Annual Meeting, Expanded Abstracts.

Dvorkin, J., and A. Nur, 1996, Elasticity of high-porosity sandstones: Theory for two North Sea datasets, Geophysics, **61**, 1363-1370.

Fowler, A.C. and X. Yang, 1999, Pressure solution and viscous compaction in sedimentary basins, Journal of Geophysical Research, **104**, B6, 12,989-12,997.

Fuchtbauer, H., 1974, Sediments and Sedimentary Rocks 1, in Sedimentary Petrology by W. v. Engelhardt, H. Fuchtbauer and G. Muller, Part II. John Wiley and Sons, New York, 464 pp.

Gal, D., J. Dvorkin, and A. Nur, 1999, A physical model for porosity reduction in sandstones: Geophysics, **63**, 454-459.

Galmudi, D., 1999, Pressure Solution, Porosity Reduction, and Transport in Rocks. Ph. D. dissertation, Stanford University.

Giles, M. R., S. L. Indrelid, and D. M. James, 1998, Compaction-the great unknown in basin modeling, in Basin Modeling: Practice and Progress, B. Duppenbecker, and J. Iliffe (eds.), Geological Society, London, Special Publications, **141**, 15-43.

He, W., A. Hajash and D. Sparks, 2002, A model for porosity evolution during creep compaction of sandstones, Earth and Planetary Science Letters, **197**, 237-244.

Hickman, S., and B. Evans, 1991, Experimental pressure solution in halite: the effect of grain/interphase boundary structure: Journal of the Geological Society of London, **148**, 549-560.

Hickman, S., and B. Evans, 1992, Growth of grain contacts in halite by solution transfer: implications for diagenesis, lithification, and strength recovery: in Fault Mechanics and Transport Properties of Rocks, B. Evans and T. F. Wongs (eds.), Academic Press, 253-280.

Krauskopf, K., and D. Bird, 1995, Introduction to Geochemistry, Third Edition, McGraw-Hill, San Francisco, 657 pp.

Marion, D., A. Nur, H. Yin, and D. Han, 1992, Compressional velocity and porosity in sand-clay mixtures, Geophysics, **57**, 554-563.

Mavko, G., J. Dvorkin, and T. Mukerji, 1998, The Rock Physics Handbook, tools for seismic analysis in porous media, Cambridge University press, New York, pp 329.

Niemeijer, A. R., C. J. Spiers, and B. Bos, 2002, Compaction creep of quartz sand at 400-600°C: experimental evidence for dissolution-controlled pressure solution: Earth and Planetary Science Letters, **195**, 261-275.

Nur, A., Mavko, G., Dvorkin, J., and Gal, D., 1995, Critical porosity: The key to relating physical properties to porosity in rocks, in Proceedings, 65th Annual International Meeting, Soc. Expl. Geophys., 878.

Paxton, S. T., J. O. Szabo, J. M. Ajdukiewicz, and R. E. Klimentidis, 2002, Constructions of an intergranular volume compaction curve for evaluating and prediction compaction and porosity loss in rigid-grain sandstone reservoirs: American Association of Petroleum Geologists Bulletin, **86**, 2047-2067.

Renard, F., A. Park, P. Ortoleva, and J-P. Gratier, 1999, An integrated model for transitional pressure solution in sandstones: Tectonophysics, **312**, 97-115.

Rittenhouse, G., 1971, Pore-space reduction by solution and cementation: American Association of Petroleum Geologists Bulletin, **55**, 80-91.

Rutter, E.H., 1976, The kinetics of rock deformation by pressure solution, Philos. Trans. Royal Soc. London A, **283**, 203-219.

Rutter, E.H., 1983, Pressure solution in nature, theory, and experiment: Journal of the Geological Society of London, **140**, 725-740.

Sorby, H.C., 1863, On the direct correlation of mechanical and chemical forces: Proceedings of the Royal Society of London, **12**, 538-550.

Sprunt, E. S., and Nur, A., 1977, Experimental studies of the effects of stress on solution rate, Journal of Geophysical Research, **82**, 3013-3022.

Stephenson, I. P., W. J. Plumley and V. V. Palciauskas, 1992, A model for sandstone compaction by grain interpenetration, Journal of Sedimentary Petrology, **62**, 11-22.

Stone, N., and R. Siever, 1996; Quantifying compaction, pressure solution and quartz cementation in moderately- and deeply-buried quartzose sandstones from the Greater Green River Basin, Wyoming, in Siliciclastic Diagenesis and Fluid Flow: Concepts and Applications, Crossey, L, *et al.* (eds.): Society of Sedimentary Geology, Special Publications, **55**, 129-150.

Tada, R., and R. Siever, 1986, Experimental knife-edge pressure solution of halite: Geochem. Cosmoche. Acta, **50**, 29-36.

Walderhaug, O., 1994, Temperatures of quartz cementation in Jurassic sandstones from the Norwegian continental shelf –evidence from fluid inclusions: Journal of Sedimentary Research A, **64**, 311-323.

Yang, X. S., 2001, A unified approach to mechanical compaction, pressure solution, mineral reactions and temperature distribution in hydrocarbon basins, Tectonophysics, **330**, 141-151.

Zimmer, M., M. Prasad, and G. Mavko, 2002, Empirical velocity-pressure and porosity-pressure trends in unconsolidated sands, SEG Annual Meeting, Expanded Technical Program Abstracts, **72**, 1866-1869.

Zimmer, M., 2003, Controls on the Seismic Velocities of Unconsolidated Sands: Measurements of Pressure, Porosity and Compaction Effects, Ph. D. dissertation, Stanford University.

Chapter 4

Rock Physics Patterns of Clastic Depositional Sequences

4.1. Abstract

Lithofacies successions from diverse depositional environments show distinctive patterns in various rock-physics planes (Vp-porosity, Vp-density and porosity-Vclay). These patterns are the consequence of textural and compositional variations in the mm- to cm-scale fabric associated with the mechanics of deposition, and coeval post-depositional processes like bioturbation. Four clear examples of decameter-scale lithofacies sequences are documented in this study: (1) fluvial deposits from the Miocene of Colombia show an inverted-V pattern indicative of mm- to cm-scale dispersed fabric in the mixed lithofacies, (2) a fining-upward lithofacies sequence of mud-rich deep water deposits from offshore West Africa shows a linear trend associated with mm- to cm-scale horizontally laminated sand-clay mixtures, (3) sand-rich deep water deposits from offshore Gulf of Mexico present a pattern resulting from the scarcity of mixed lithofacies, and (4) a coarsening-upward lithofacies sequence of shallow marine deposits from Colombia presents evidence of both dispersed and horizontally laminated mixed lithofacies, with predominating dispersed mixtures generated by bioturbation.

The applicability of the patterns observed to predict the seismic properties of larger sequences and away from well control depends on vertical and lateral persistence of the lithofacies assemblage. Syntectonic fluvial deposits from Colombia present good vertical persistence, resulting in remarkable similarity between the rock-physics patterns of decameter-scale and the larger-scale sequences. Shallow marine deposits from the same area constitute a good example of lateral continuity of lithofacies assemblages. In contrast, mud-rich deep water deposits

show a high vertical variability of lithofacies. Three different types of clay-rich lithofacies occur, their vertical distribution apparently controlled by changes in relative sea level.

Extrapolation of the patterns observed to similar depositional settings in other basins depends on the repeatability of the lithofacies assemblage and diagenesis. This study documents the similarity in the rock physics patterns of sand-rich deep water deposits from offshore Gulf of Mexico and the North Sea.

Rock-physics models provide the framework to understand the patterns that clastic lithofacies successions show in the rock-physics planes. The Thomas-Stieber model explains the porosity variation in both dispersed and laminar sand-clay mixtures. The Marion-Yin model demonstrates the concomitant change in elastic rock properties and porosity for dispersed mixtures, which differs from the Backus average applicable to laminar mixtures.

Rock-physics models can also predict the changes that diagenetic processes and confining pressure induce on the velocity-porosity patterns of lithofacies successions. The shape variation with depth of the inverted V, predicted by the Marion-Yin model, coincides with the patterns observed in fluvial deposits at different depths, although rather than confining pressure, the actual mechanism might be either pressure solution or incipient cementation. In addition to this, we document a pattern that agrees with the variation in the inverted-V pattern induced by preferential diagenesis, postulated in the Jizba model.

4.2. Introduction

Besides fluids and pressure, rock texture and lithofacies strongly influence seismic rock properties (e. g. Yin, 1992; Wang, 2001). The lateral variations in elastic properties of an intact, water-saturated, sedimentary rock, under uniform effective pressure and temperature, are determined by the lateral variations in clay content, sorting, packing, mineral composition, or cementation. These textural variations are the result of depositional and diagenetic processes (Figure 4.1). The impact of textural variations in seismic properties constitutes an important source of uncertainty in the prediction of reservoir properties from seismic data. Understanding the relationships between rock texture, fabric, and seismic response can reduce, or at least assess, the uncertainty associated with these predictions.

Lithofacies distribution in sedimentary rocks is not random. Lithofacies, a descriptive term to characterize both texture and fabric of sedimentary rocks

(Teichert, 1958), reflects both the mechanical processes that operated during deposition (e. g. Walker, 1984; Allen, 2001), and the diagenetic processes that affected the rock after burial (e. g. Fuchtbauer, 1974). The terms *depositional* and *diagenetic* lithofacies can be used to distinguish between these processes, although for some parameters, like packing, the distinction between the two is not always evident. The vertical and lateral distribution of depositional lithofacies within a stratigraphic package follows Walter's law of lithofacies superposition (Teichert, 1958). It reflects the variation in the mechanics of deposition and sediment supply as sediments accumulated. The final architectural configuration controls the fluid distribution, the mechanical deformation, and the chemical interactions during diagenesis. The lithofacies distribution reflects, in essence, the depositional and diagenetic history of a sedimentary package.
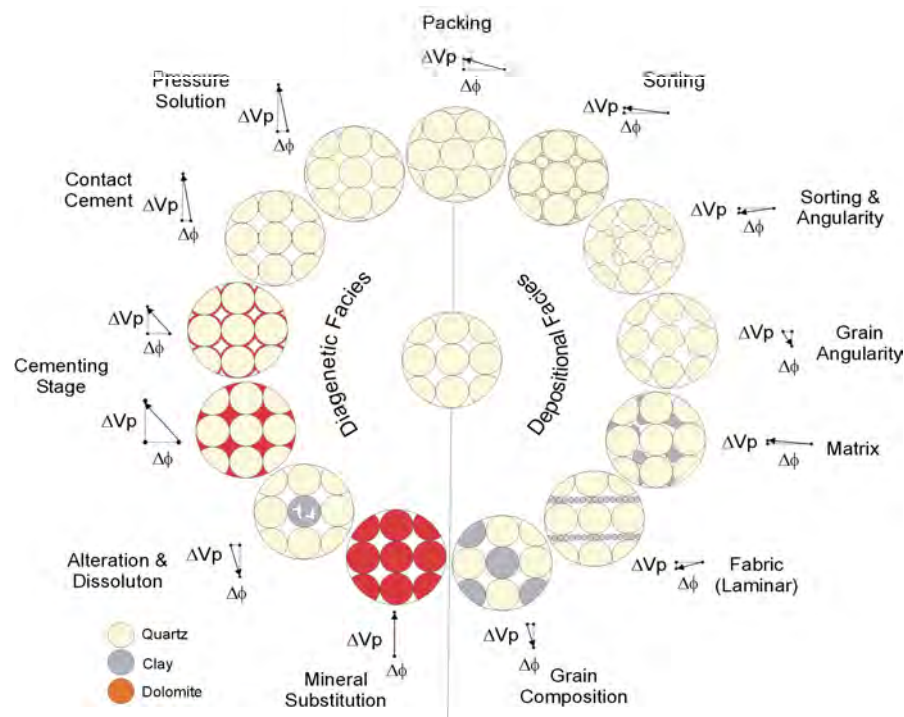
Figure 4.1: Conceptual model illustrating the concomitant changes in porosity and elastic properties of clastic sediments. These textural effects have been documented by previous studies: e.g. Murphy (1982), Han (1986), Marion *et al.* (1992), Dvorkin *et al.* (1994), Dvorkin and Nur (1996), Bachrach *et al.* (1998), Avseth *et al.* (2000), Dvorkin and Gutierrez (2001), and Zimmer (2003).

Rock-physics models, based on theoretical analysis, empirical relationships and laboratory data, provide the basis to understand the variations in seismic properties associated with changes in rock texture and fabric. Mavko *et al.* (1998) document the main effective-medium models for granular materials, based on contact mechanics

(e. g. Mindlin, 1949; Timoshenko and Goodier, 1970) and variational principles (Hashin and Shtrikman, 1963). Tosaya and Nur (1982), and Han (1986) studied the effect of clay, porosity, and confining pressure. Murphy (1982) analyzed the effect of packing and porosity. Yin (1992) analyzed the changes in both petrophysical and elastic properties of dispersed mixtures of sand and clay. Yin's study provided the basis for the Marion-Yin model for sand-clay mixtures (Marion, 1990; Marion *et al.*, 1992). Estes *et al.* (1994), and more recently Avseth *et al.* (2000), Dvorkin and Gutierrez (2001), Gutierrez (2001), and Zimmer (2003) have analyzed the effect of sorting. Dvorkin *et al.* (1994) formulated a mathematical theory to model the effect of cement on granular aggregates. Dvorkin and Nur (1996) presented rocks-physics diagnostics as a technique to determine textural variations from seismic data. The links between rock physics, sedimentology and stratigraphy have been outlined by Avseth (2000), Avseth *et al.* (2000), and Gutierrez *et al.* (2001). The previous chapters of this dissertation add to this knowledge by presenting a comprehensive analysis of the effects of sorting (Chapter 2) and pressure solution (Chapter 3).

This chapter demonstrates that the vertical succession of lithofacies within a specific depositional setting translates into a characteristic pattern in the rock-physics planes. Throughout this thesis I refer to cross plots of velocity-porosity (Vp-ϕ), velocity-density, and porosity-clay fraction (ϕ-Vclay) as rock physics planes. This chapter also illustrates the variations that these characteristic patterns can have as a result of compaction and/or cementation. These results constitute a contribution toward understanding the link between geologic processes and the final seismic properties of sedimentary rocks. This link is the key for seismic forward modeling and for uncertainty assessment of the predictions of reservoir properties from seismic data, away from well control.

4.2.1. Porosity of Sand-Clay Mixtures

Thomas and Stieber (1975) and Marion *et al.* (1992) describe the gradual changes in porosity for dispersed sand-clay mixtures. According to them, the porosity of unconsolidated, clayey sand decreases compared to porosity of clean sands, as clay replaces pore space. The lowest porosity is reached when all the pores in the sand framework are replaced by clay (Figure 4.2). The mixture porosity (ϕ_m) depends on the clean-sand porosity (ϕ_{cs}), the volume fraction of clay (V_{clay}), and the clay porosity (ϕ_{clay}), according to the following expression:

$$\phi_m = \phi_{cs} - V_{clay}(1 - \phi_{clay}).$$ (4.1).

Similarly, compared to pure-clay sediments, the porosity of sandy (or silty) clay decreases as well, as non-porous sand grains replace porous clay. The porosity along this branch is given by

$$\phi_m = V_{clay}\phi_{clay} \tag{4.2}$$

This is equivalent to Equation 4.1, when we make the volume of shale equal to the clean-sand porosity.

In contrast, porosity of laminar mixtures corresponds to the arithmetic average of the clean-sand and pure-clay porosities (Thomas and Stieber, 1975); that is,

$$\phi_m = \phi_{cs}V_{ss} + V_{clay}\phi_{clay} \ . \tag{4.3}$$
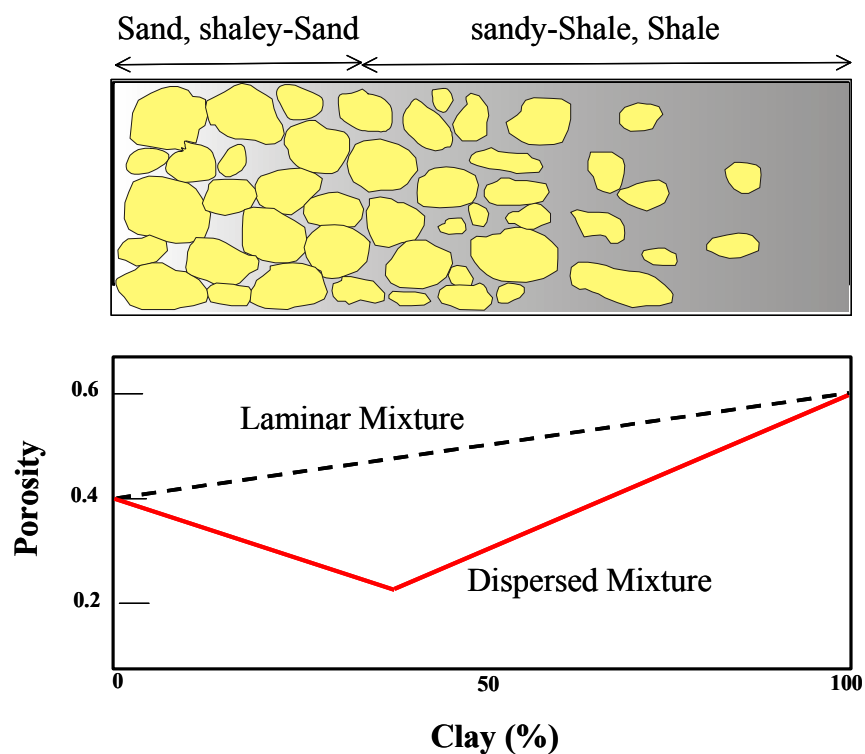
Figure 4.2: Porosity variation for different mixtures of sand and shale, defining different lithofacies. Based on Thomas and Stieber (1975) and Marion *et al.* (1992).

Structural clay refers to clay particles that occur as part of the load-bearing material in sand-supported frameworks (Thomas and Stieber, 1975). Structural clay can occur as intraclasts derived from erosion of adjacent clay layers, or as grain replacement of stiff grains (e.g. kaolinite replacing feldspars). In the case of structural clay, porosity of the mixture is given by

$$\phi_m = \phi_{cs} + V_{clay}\phi_{clay} \ . \tag{4.4}$$

4.2.2. Elasticity of Laminar Mixtures

The effective elastic stiffness of horizontal laminar mixtures for vertically propagating P-waves is given by the harmonic average of the stiffnesses, or Reuss average:

$$M_{eff} = \left(\sum_i f_i M_i^{-1} \right)^{-1}, \quad (4.5)$$

with

$$M_i = K_i + \frac{4}{3} \mu_i, \quad (4.6)$$

where M denotes the compressional (P-wave) modulus, K the bulk modulus, μ the shear modulus, and f_i the volume fraction of the *ith* component. A laminar mixture is a transversely isotropic medium with its elastic stiffness tensor characterized by five independent constants (Mavko *et al.*, 1998). Using abbreviated notation, the stiffness tensor can be written as a 6x6 matrix. This simplifies the notation, even though the matrix is no longer a tensor:

$$C = \begin{bmatrix} c_{11} & c_{12} & c_{13} & 0 & 0 & 0 \\ c_{12} & c_{11} & c_{13} & 0 & 0 & 0 \\ c_{13} & c_{13} & c_{33} & 0 & 0 & 0 \\ 0 & 0 & 0 & c_{44} & 0 & 0 \\ 0 & 0 & 0 & 0 & c_{44} & 0 \\ 0 & 0 & 0 & 0 & 0 & \frac{1}{2}(c_{11} - c_{12}) \end{bmatrix}. \quad (4.7)$$

Backus (1962) derived the expressions for each one of these constants. In terms of the lame constant (λ), shear modulus (μ) and P-wave modulus (M) of the component layers, these constants are as follows:

$$c_{11} = 4 \sum_i f_i (\lambda_i \mu_i + \mu_i^2) M_i^{-1} + \left(\sum_i f_i M_i^{-1} \right)^{-1} \left(\sum_i f_i \lambda_i M_i^{-1} \right)^2, \quad (4.8)$$

$$c_{12} = 2 \sum_i f_i \lambda_i \mu_i M_i^{-1} + \left(\sum_i f_i M_i^{-1} \right)^{-1} \left(\sum_i f_i \lambda_i M_i^{-1} \right)^2, \quad (4.9)$$

$$c_{23} = \left(\sum_i f_i M_i^{-1} \right)^{-1} \left(\sum_i f_i \lambda_i M_i \right), \quad (4.10)$$

$$c_{33} = \left(\sum_i f_i M_i^{-1} \right)^{-1},$$ (4.11)

$$c_{44} = \left(\sum_i f_i \mu_i^{-1} \right)^{-1}.$$ (4.12)

One of the evident differences between laminar and dispersed mixtures is anisotropy. Laminar mixtures are significantly anisotropic, whereas we expect dispersed mixtures to be more isotropic. Although this is one additional aspect that should be considered for seismic modeling, it is not discussed in this study. Throughout this analysis I assume the logs are reading the response to a P-wave propagating along a direction perpendicular to the bedding surfaces. Unless the well is deviated or the layers are significantly tilted, this is a reasonable assumption.

4.2.3. Elasticity of Dispersed Mixtures

Marion *et al.* (1992) analyzed the elasticity of dispersed sand-clay mixtures based on laboratory data. The data show that the point with the lowest porosity in the mixture also corresponds to the point of the highest velocity. The velocities of the end members, clean sand and pure-clay, are the lowest and, at low confining-pressures, about the same (Figure 4.3). As sediments are buried, those with clay as the load-bearing material present a high porosity-reduction gradient, whereas those with sand as the load-bearing material have a lower porosity-reduction gradient. As a result, the pattern depicted by gradual mixtures of sand and clay in the velocity-porosity plane varies from a collapsed-V shape, at low confining pressures, to an inverted-V shape at high confining pressures (Figure 4.4).

Marion *et al.* (1992) applied fluid substitution to calculate the velocities of a dispersed mixture of clay and sand, along the sand load-bearing framework. This method assumes that pore-filling clay acts like a soft mixture of clay and water (like a mush) rather than a solid. The clay stiffens the pore-filling material, without affecting the frame properties of the sand. Following Gassman's equations (Mavko *et al.*, 1998) the elastic properties of the mixture (K_{mix}) depend on the properties of the clay-water mush (K_{mush}), the dry-sand modulus (K_{dry}), the sand-grain mineral modulus (K_{qz}), and the porosity of the clean sand (ϕ_{cs}), as follows:

$$\frac{K_{mix}}{K_{qz} - K_{mix}} = \frac{K_{dry}}{K_{qz} - K_{dry}} + \frac{K_{mush}}{\phi_{cs}(K_{qz} - K_{mush})}$$ (4.13)

$$\mu_{mix} = \mu_{dry}.$$ (4.14)

A consequence of this assumption is that the pore-filling clay would not affect the shear modulus of the rock.

The elastic properties of the clay load-bearing branch are exactly given by the Reuss average (Equation 4.11), since the mixture acts as a suspension of sand particles in clay. The density of the sand-shale mixture where porosity reduces due to pore filling clay can be calculated using the following formula:

$$\rho_{mix} = (1 - \phi_{cs})\rho_{qz} + V_{clay}(1 - \phi_{clay})\rho_{clay} + (\phi_{cs} - V_{clay}(1 - \phi_{clay}))\rho_w, \qquad (4.15)$$

where ρ_{qz}, ρ_{clay}, and ρ_{fl} are the densities of sand grains (quartz), clay mineral and saturating fluid, respectively.
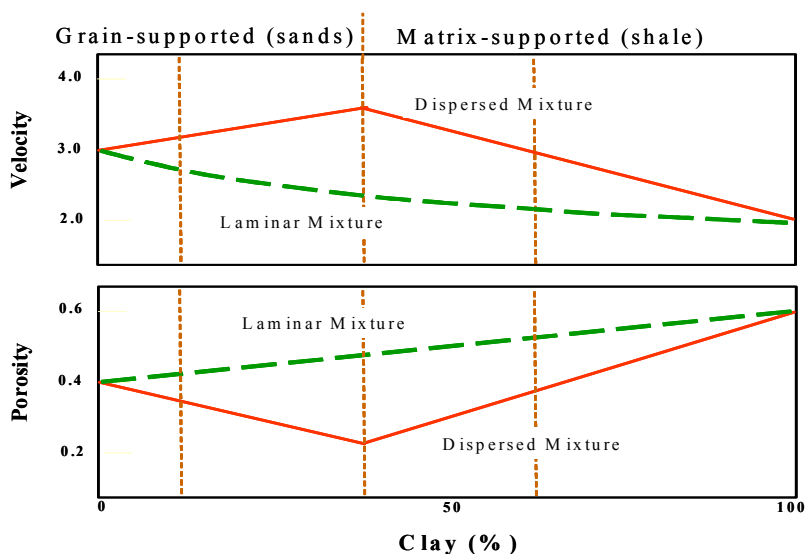
Figure 4.3: Velocity and porosity variation in both laminar and dispersed mixtures of sand and shale, as inferred from the Marion-Yin model.

Instead of using Gassmann theory, we can use the modified lower Hashin-Shtrikman bound to calculate velocity-porosity trends for dispersed mixtures of quartz sand and clay. The method, similar to the one developed by Dvorkin and Gutierrez (2001), uses the unconsolidated sediment model to calculate the elastic properties of the sand and clay end points of the inverted-V, then uses equations 4.1, 4.2, and 4.3 to determine the porosities of the mixtures. Finally, it uses modified Hashin-Shtrikman lower bounds to determine the elastic properties connecting the three end points (clean sand, minimum porosity, and pure clay).

For a mixture of two constituents, the Hashin-Shtrikman bounds (Hashin and Shtrickman, 1963; Mavko *et al.*, 1998) for the effective bulk (K_{eff}) and shear (μ_{eff}) moduli are given by:

$$K_{eff}^{HS} = K_1 + \frac{f_2}{(K_2 - K_1)^{-1} + f_1(K_1 + \frac{4}{3}\mu_1)^{-1}} \qquad (4.16)$$

$$\mu_{eff}^{HS} = \mu_1 + \frac{f_2}{(\mu_2 - \mu_1)^{-1} + \frac{2f_1(K_1 + 2\mu_1)}{5\mu_1(K_1 + 2\mu_1)}}, \qquad (4.17)$$

where K_1, K_2, μ_1, μ_2, f_1, and f_2, are the moduli and the volume fractions of individual phases. The lower bound is computed when the softest material is subscripted 1. The unconsolidated model uses Hertz-Mindlin theory (Chapter 2) and the modified lower Hashin-Shtrikman bound to calculate the elastic properties of sediments with similar composition but different porosity, at specified pressures (Mavko *et al.*, 1998).
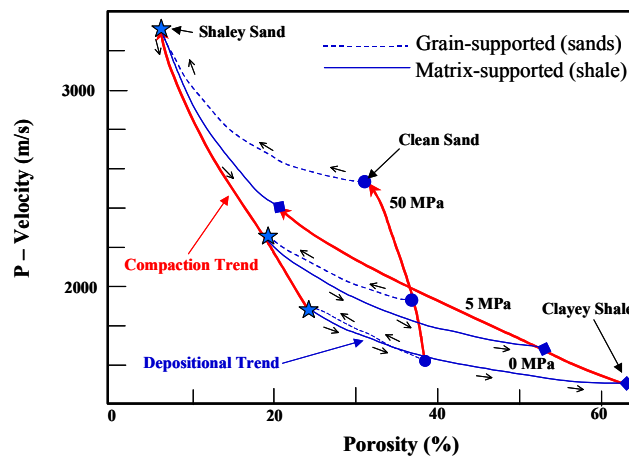
Figure 4.4: Variation of velocity-porosity trends for sand-clay mixtures as a function of confining stress. After Marion (1990).
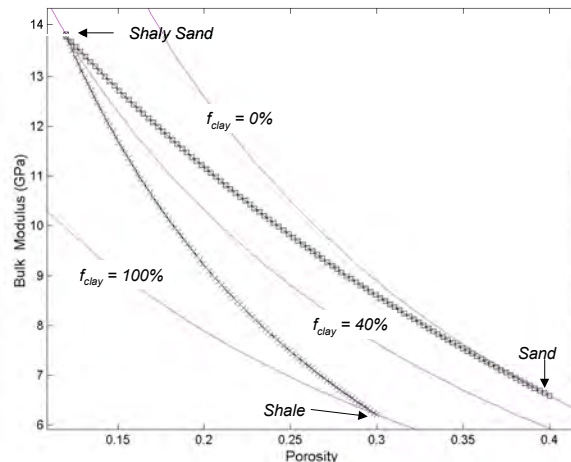
Figure 4.5: Inverted-V pattern calculated from the combination of modified Hashin-Shtrikman lower bounds. The upper branch represents the shaly sands, the lower branch the silty or sandy shale. The three end members are obtained using the unconsolidated sediment model (magenta lines) for specified porosity, composition and pressure.

4.2.4. Rock-Physics Models and Lithofacies Successions

Large stratigraphic sequences are composed of repetitive lithofacies successions derived from either gradual depositional processes or episodic catastrophic events (Ager, 1993). The best example of these repetitive lithofacies successions is the parasequence, a term introduced by Van Wagoner *et al.* (1990) to exclusively refer to the shallow-marine facies successions derived from oscillations in relative sea level, like the deltaic bar shown in Figure 4.6. Another well-known example is the fining-upward lithofacies succession characteristic of meandering fluvial deposits (Walker, 1984; Allen, 2001). The sand-clay mixtures analyzed in the Thomas-Stieber and Marion-Yin models resemble the vertical lithofacies successions observed in parasequences and single depositional events (Figure 4.6).
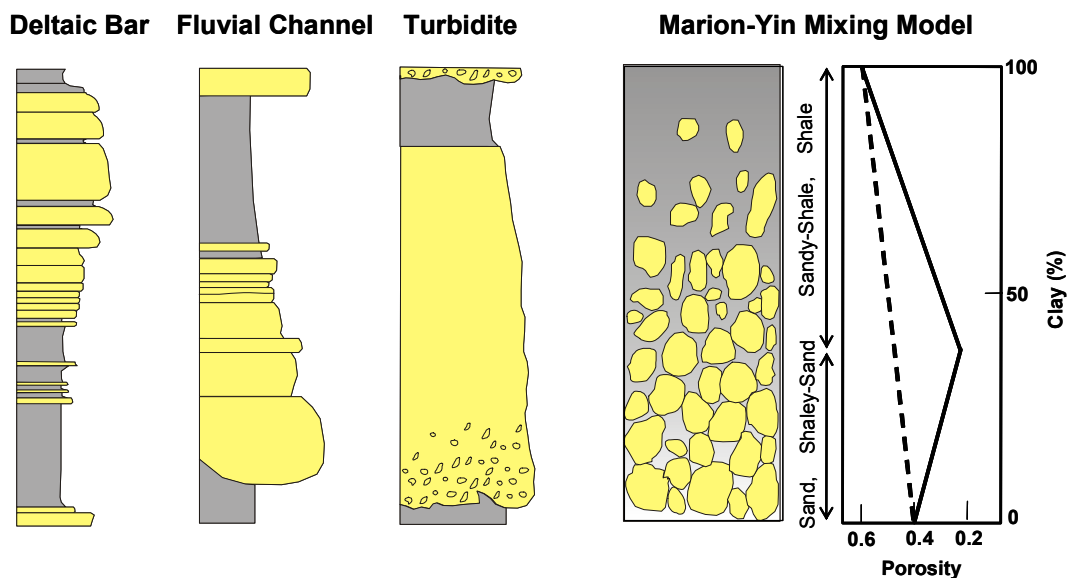
Figure 4.6: Comparison of the Marion-Yin mixing model with the facies succession found in parasequences, and individual depositional cycles and events.

Rock physics models predict the changes in P-wave velocity and porosity of clastic lithofacies successions. These repetitive lithofacies successions are the building blocks of larger stratigraphic sequences. They present relatively simple lithofacies trends: fining upward, coarsening upward, blocky, or serrated. Both fining-upward and coarsening-upward trends show gradual transitions from clay-rich shale to clean-sand lithofacies. Although the textural trends in sedimentary rocks are in general more complex than the lithofacies transitions assumed in the rock-physics models, they capture the essence of these variations: type of mixture, compositional changes associated with clay content, changes in cementation, and changes in

sorting. In principle, we should be able to identify the rock fabric from the velocity-porosity trend observed within a stratigraphic sequence.

In uncemented sands, the differences in the mechanics of deposition should be reflected in the patterns of concomitant velocity and porosity variations of mixed lithofacies. The depositional texture of a sedimentary rock is determined by the mechanics of deposition. The main variables associated with the depositional texture are the load-bearing framework (grains or mud), grain size distribution, grain size, matrix (clay) content, and fabric. Differences in the mechanics of deposition and their transitions might be reflected in the patterns of the simultaneous change in velocity and porosity associated with the textural change. This is the general idea that we will explore throughout this paper.

Rock-physics models can also be used to predict the changes in both elastic and hydraulic properties of sedimentary rocks caused by diagenetic processes. Based on experimental results, Marion (1990) and Yin (1992) postulate that the patterns of sand-clay mixtures will change with confining pressure (Figure 4.4). In general, their model predicts that as confining pressure increases, the pattern will change from a flat collapsed shape to an inverted-V shape. Based on numerical modeling, Jizba (1991) postulated an increase in elastic stiffness of sands compared to the surrounding shale and mixed lithofacies, as cementation takes place. Section 4.5 of this chapter presents clear examples of variations in the Vp-ϕ patterns of depositional sequences that follow the predictions made from these models.

4.2.5. Methodology

This work involved the evaluation of well-log data from different basins and depositional environments. It focuses on the Llanos Basin in Colombia, since after various years of field geology I became familiar with the lithofacies and depositional environments of the different formations in this region. Well logs from other basins and depositional settings were also evaluated and some of them had to be disregarded because of the lack of geologic information or lack of quality control in the data.

I use three main cross plots to perform the analysis and comparison of the variation of elastic and bulk properties (porosity) within clastic depositional sequences: (1) bivariate histograms and color-coded cross plots of P-wave velocity (Vp) and porosity (ϕ); (2) cross plots of porosity as a function of clay fraction

(Vclay); and (3) color-coded cross plots of P-wave velocity and density. In general, I refer to these cross plots as the rock-physics planes.

The rationale behind this approach is the application of rock-physics diagnostics (Dvorkin and Nur, 1996) constrained to stratigraphic sequences (Gutierrez *et al.*, 2001). I analyze the patterns of lithofacies sequences with a clear trend in clay content, inferred from both the gamma ray readings and the difference between neutron (NPHI) and density (PHID) porosities. In the cross plots the porosity corresponds to density porosity (PHID). The analyzed sequences correspond to genetically related lithofacies assemblages that form part of larger stratigraphic sequences.
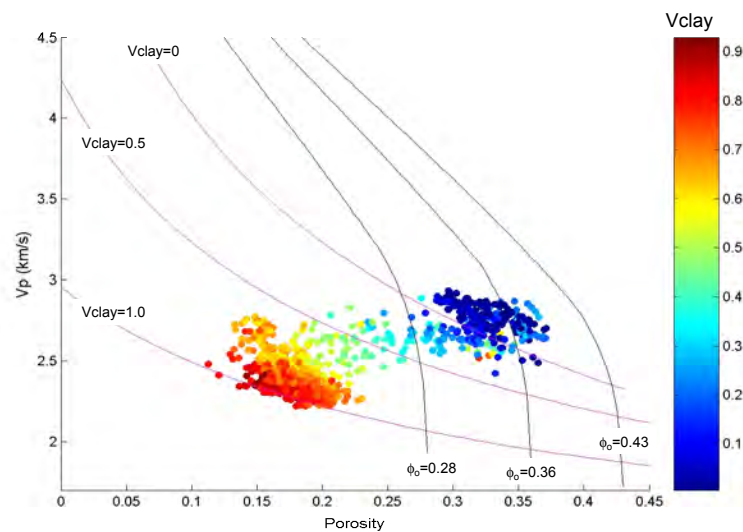
Figure 4.7: Rock-physics template to evaluate the patterns of concomitant variations of porosity and elastic properties within clastic sequences.

Fluid substitution has been applied to velocity and density data in the case of hydrocarbon-bearing sands, in order to remove the fluid effect on the rock's elastic properties. Since the rocks analyzed are at similar pressure and temperature conditions, share a similar burial history, and have similar fluid saturations after fluid substitution, texture and composition are the dominant factors controlling the observed variations in elastic properties and porosity within any analyzed lithofacies sequence.

The rock-physics template shown in Figure 4.7 illustrates one of the frameworks used for rock physics diagnostics. The template was built as follows: the black lines correspond to the diagenetic trend, as explained in Chapter 2. The magenta lines correspond to the unconsolidated sandstone model (Mavko *et al.*, 1998) for different quartz-clay compositions. The anchor point for the unconsolidated model is given by

the Hertz-Mindlin model at 25 MPa, with a correction factor of 0.7 for the shear stiffness. It is important to bear in mind that the purpose of these lines is not to fit the data, although in some cases they do it very well. The lines provide a framework that allows us to identify variations between different data sets, and infer the textural changes that can explain these differences. The inferred textures can be compared with the description of mudlog cuttings, core analysis, or other logging tools.

Rock physics diagnostics encompasses four basic steps: (1) petrophysic analysis and quality control of well-log data, (2) fluid substitution and cross plotting, (3) rock physics analysis, and (4) comparison with cores and other sources of information. The last step is often difficult to perform because cored intervals are not always available and commonly correspond to a limited segment of the sedimentary section.

4.3.   Rock-Physics Patterns of Selected Depositional Sequences

This section presents the patterns observed in four selected lithofacies sequences from different depositional environments, illustrated in Figure 4.8 and Figure 4.9. The first example (Figure 4.8a) corresponds to fluvial deposits of the Miocene Guayabo Formation from the Llanos Basin (Colombia). The following case (Figure 4.8b) corresponds to Miocene, mud-rich, deep-water deposits from offshore West Africa. The third case (Figure 4.9a) shows sand-rich deep-water deposits from offshore Gulf of Mexico. The last case (Figure 4.9b) illustrates a coarsening-upward trend of shallow marine deposits from the Miocene Leon Formation, in the Llanos Basin (Colombia).

The differences between these four lithofacies sequences start to become conspicuous by looking at the cross plot of porosity and clay fraction (Figure 4.10). The fluvial deposits show an approximate V pattern (Figure 4.10a) contrasting with the linear trend observed in the mud-rich deep-water deposits from offshore West Africa (Figure 4.10b). The pattern observed in the fluvial deposits indicates the predominance of mm- to cm-scale dispersed fabric in the mixed lithofacies, whereas the linear trend observed in the deep-water deposits (Figure 4.10b) suggests the predominance of mm- to cm-scale horizontally laminated fabric. These two patterns are also different from the patterns observed in Figure 4.10(c) and Figure 4.10(d). The sand-rich deep water deposits (Figure 4.10c) shows two clouds of data points, corresponding to the sand and shale intervals, without a gradual transition between the two. The coarsening-upward lithofacies sequence (Figure 4.10d) shows another approximate V pattern with higher clay content, and significant scatter for clay

fractions larger than 0.4. In the cases of the fluvial and shallow marine deposits, the lowest porosity occurs at the midpoint between the clean sand and the highest clay content, indicating the presence of dispersed sand-clay mixtures. The mud-rich deep water deposits show a pattern consistent with the predominance of laminar sand-clay mixtures. In contrast, the pattern outlined by the sand-rich deep water deposits suggests the absence of sand-clay mixtures.
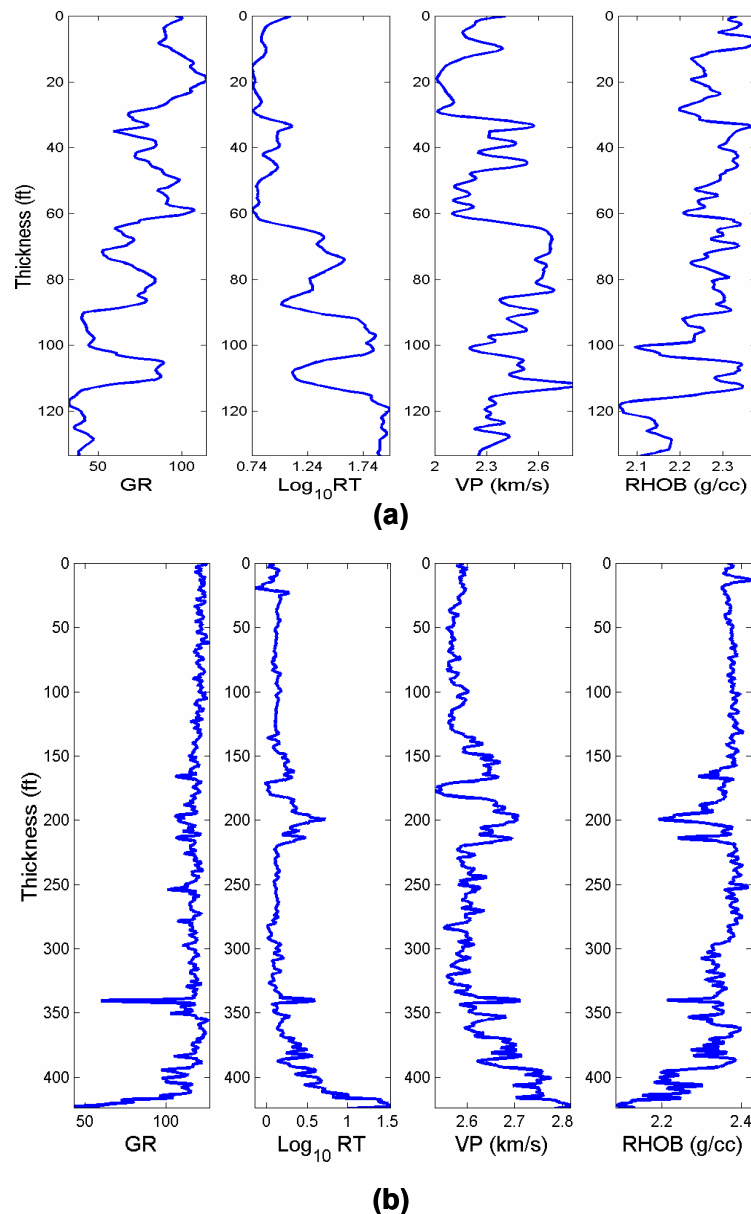
Figure 4.8: Well-log data from two different lithofacies sequences: (a) fining-upward lithofacies sequence from fluvial deposits of the Miocene Guayabo Formation (Llanos Basin Colombia); (b) fining-upward lithofacies sequence from Miocene deep-water deposits offshore West Africa. Fluid substitution has been applied to the velocity and density logs in (b).
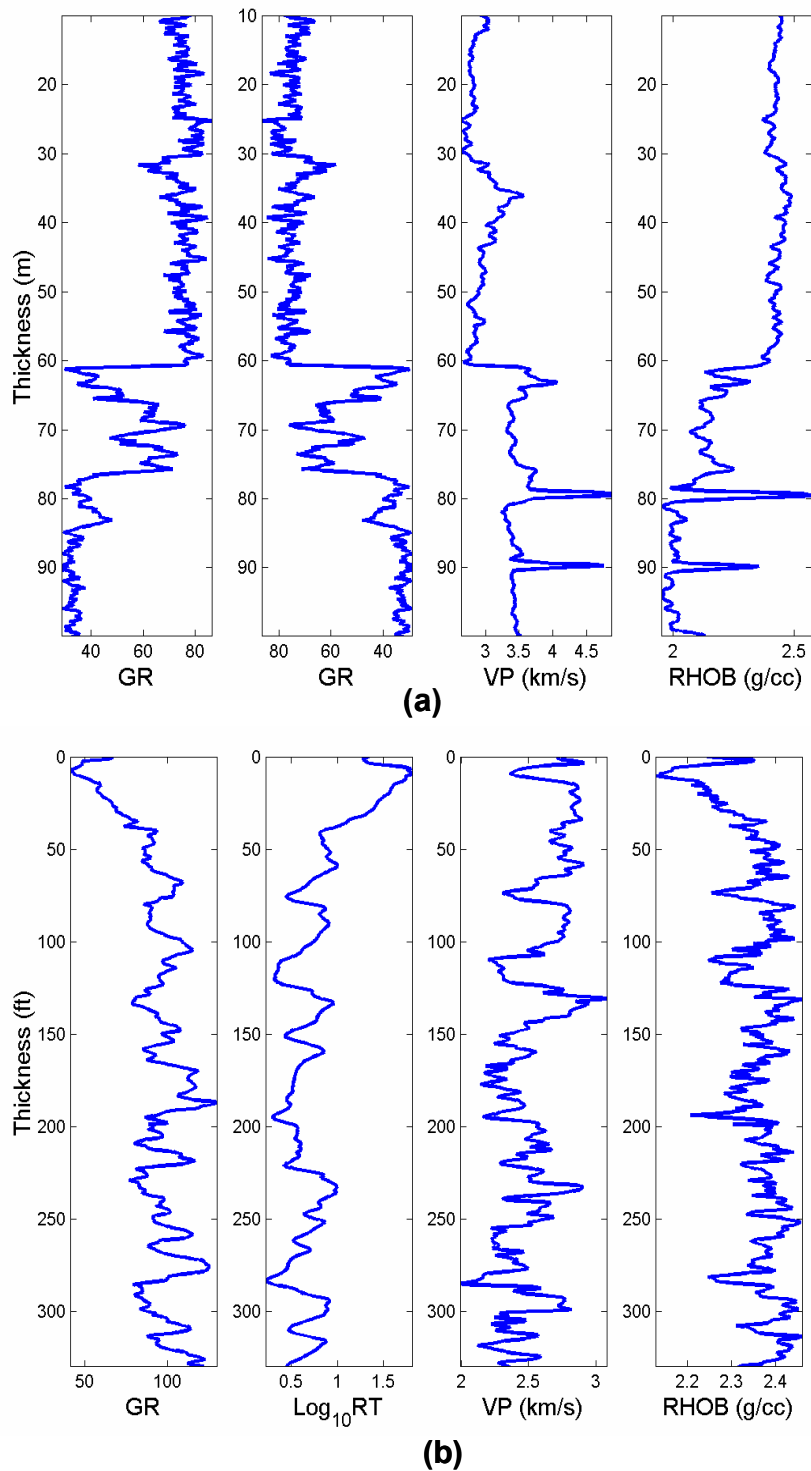
Figure 4.9: Well-log data from two different depositional sequences: (a) deep-water blocky sandstone from offshore Gulf of Mexico; (b) coarsening-upward lithofacies sequence of shallow-marine Miocene deposits from Colombia (Upper Leon, well Apiay-1, Llanos Basin). Fluid substitution has been applied to the velocity and density logs in (a).
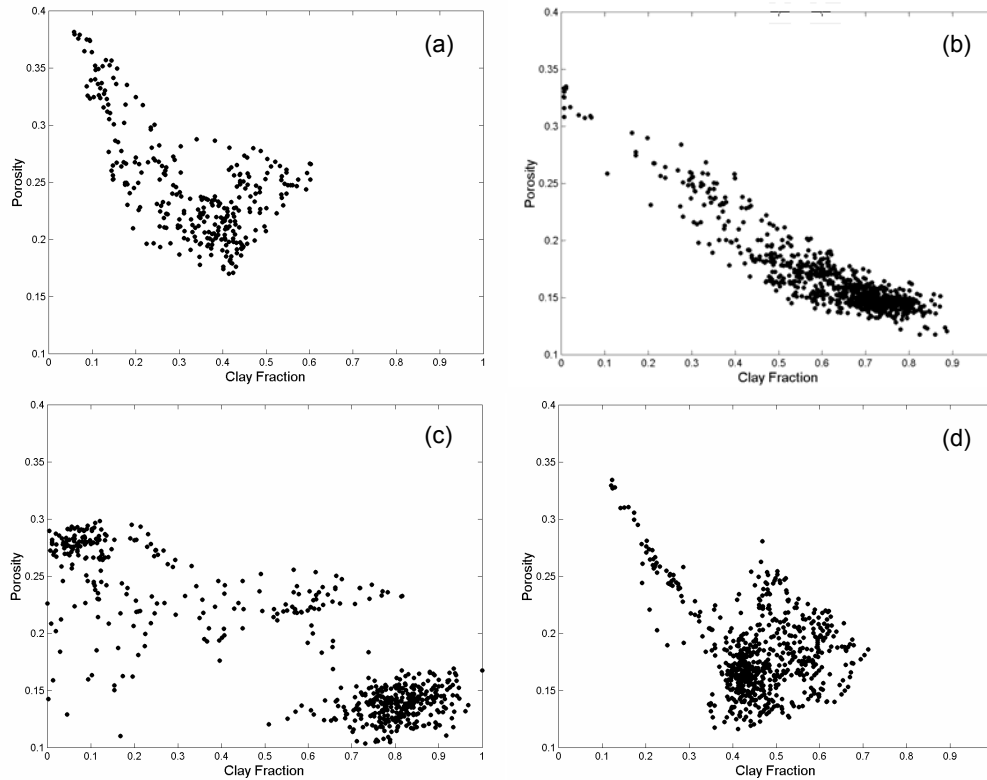
Figure 4.10: Well-log Porosity-Clay Fraction cross plots from the clastic depositional sequences shown in Figure 4.8 (a and b), and Figure 4.9 (c and d). Porosity determined from density and neutron (in sands) logs, clay fraction determined from gamma ray and the difference between neutron and density porosities.

The velocity-density bivariate histograms (Figure 4.11) corroborate the sedimentary fabric inferred from the porosity-Vclay cross plots. In Figure 4.11 the pure end members of the lithofacies sequences are indicated as Q for sand and C for clay-rich shale. As shown in Figure 4.11(a), the fluvial deposits present a clear inverted-V pattern, similar to the one predicted by the Marion-Yin model (Marion *et al.*, 1992). In the case of the mud-rich deep water deposits, Figure 4.11(b) shows a clear linear trend as predicted for horizontally laminated sand-clay mixtures from the Backus average (e.g. Mavko et al, 1998), and the linear variation in porosity as a function of clay content. In contrast, Figure 4.11(c) illustrates the absence of mixed lithofacies in the sand-rich deep water deposits. Finally, Figure 4.11(d) demonstrates the predominance of dispersed sand-clay mixtures in the shallow marine deposits, and suggests the occurrence of some subordinate laminated lithofacies.
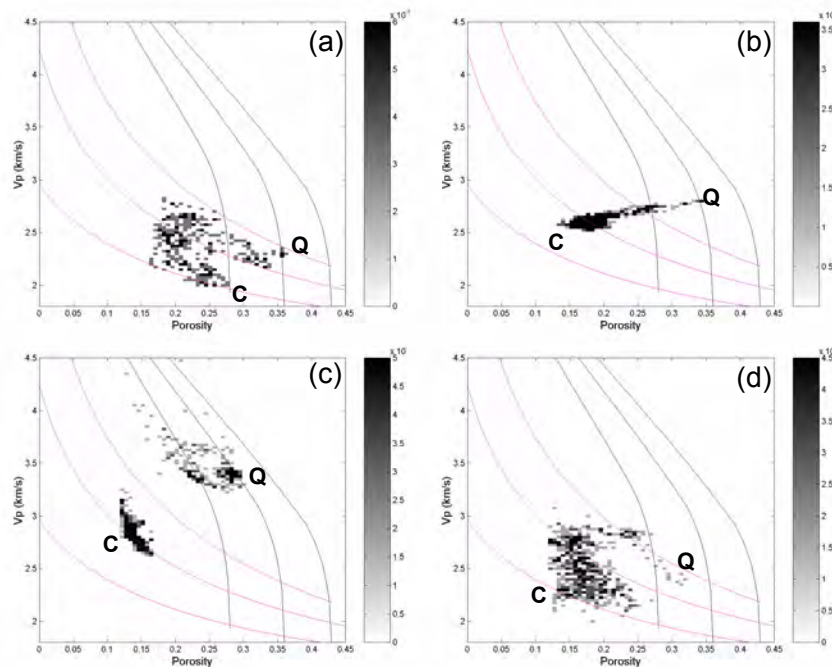
Figure 4.11: Bivariate histograms of well-log P-wave velocity and porosity (PHID) from the four different clastic depositional sequences shown in Figure 4.10. Q indicates the sand points (quartzose sand) and C indicates the clay-rich shale point. Black lines outline the diagenetic trend for quartzose sands; magenta lines outline the depositional trend for sands at 25 MPa, with different proportions of clay (0, 50% and 100%).

The differences between these four lithofacies sequences can be summarized in the velocity-density cross plot color-coded by clay content (Figure 4.12). In this plane, contours of iso-impedance can be superimposed, since acoustic impedance is the product of velocity and density. The cross plots illustrate that the patterns observed are the result of the concomitant variations in density (porosity) and elastic properties (velocity) associated with clay content.

The most striking difference occurs between the pattern outlined by the lithofacies sequence from fluvial deposits, Figure 4.12(a), and the pattern depicted by the lithofacies sequence from mud-rich deep water deposits, shown in Figure 4.12(b). The variations in clay content, density, porosity, and elastic properties observed in the fluvial deposits clearly indicate the predominance of a dispersed fabric in the mixed lithofacies. In contrast, the variations in clay content, density, porosity and elastic properties observed in the mud-rich deep-water deposits clearly indicate the presence of horizontally laminated sand-clay mixtures. Another significant difference is the contrast between the scarcity of mixed sand-clay lithofacies in the sand-rich deep water deposits, Figure 4.12(c), and the abundance of

both dispersed and laminar mixed lithofacies in the shallow marine deposits shown in Figure 4.12(d).
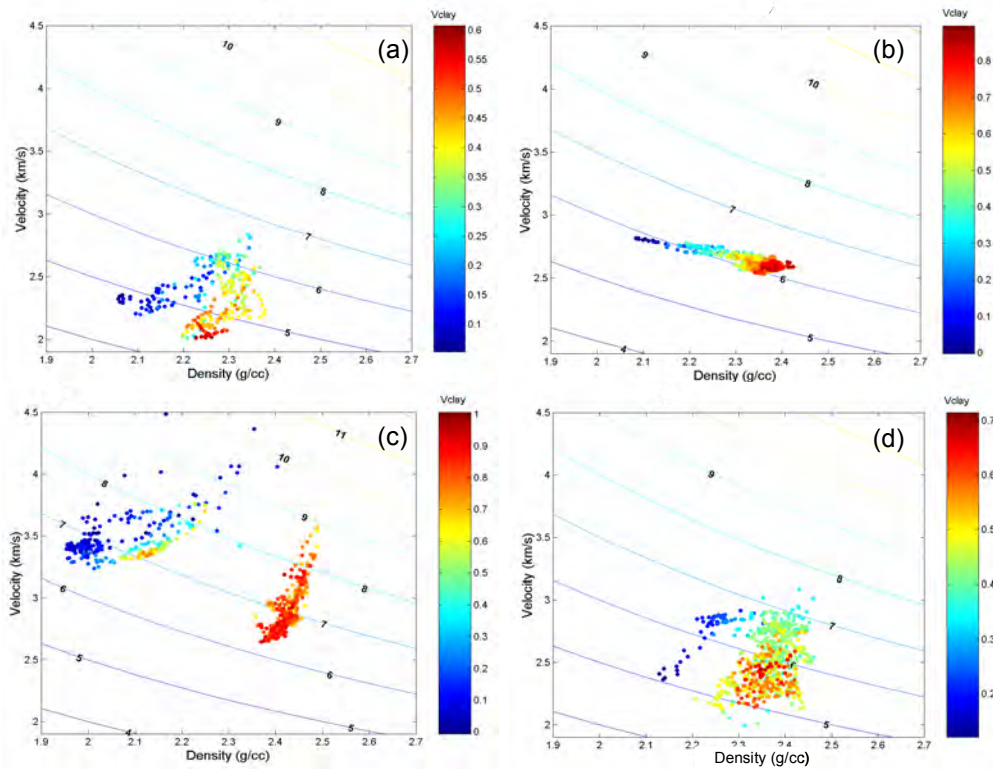
Figure 4.12: Cross plots of well-log P-wave velocity and density color-coded by fraction of clay for the same four different clastic depositional sequences shown in Figure 4.11. The plots also show contours of impedance. Notice that for the cases of (a) and (d) the highest impedances correspond to the mixed lithofacies.

The millimetric and centimetric fabrics of these lithofacies sequences, inferred from the different cross plots, agree with the observed and reported fabrics from outcrops, cores, and image-log analysis. The shallow marine deposits of the Miocene Leon Formation commonly present fine-grained to very-fine grained argillaceous sandstones with horizontal, wavy, and lenticular lamination (Cardona and Gutiérrez, 1995). These rocks also present a massive or dispersed sand-clay fabric associated with intense bioturbation. As shown in Figure 4.13, the mixed lithofacies of the fluvial deposits from the Miocene Guayabo Formation in Colombia are characterized by massive, structureless, variegated, reddish, sandy to silty mudstones and argillaceous fine-grained sandstones (e. g. Aguilera and López, 1994). In contrast, the dominant fabric in the mixed lithofacies from mud-rich deep water deposits is mm- to cm-scale horizontal lamination and interbedding (Figure 4.13). Similar thinly interbedded and laminated sand-clay lithofacies occur in outcrop analogues of mud-rich deep water deposits in Chile (Beaubouef, 2004).
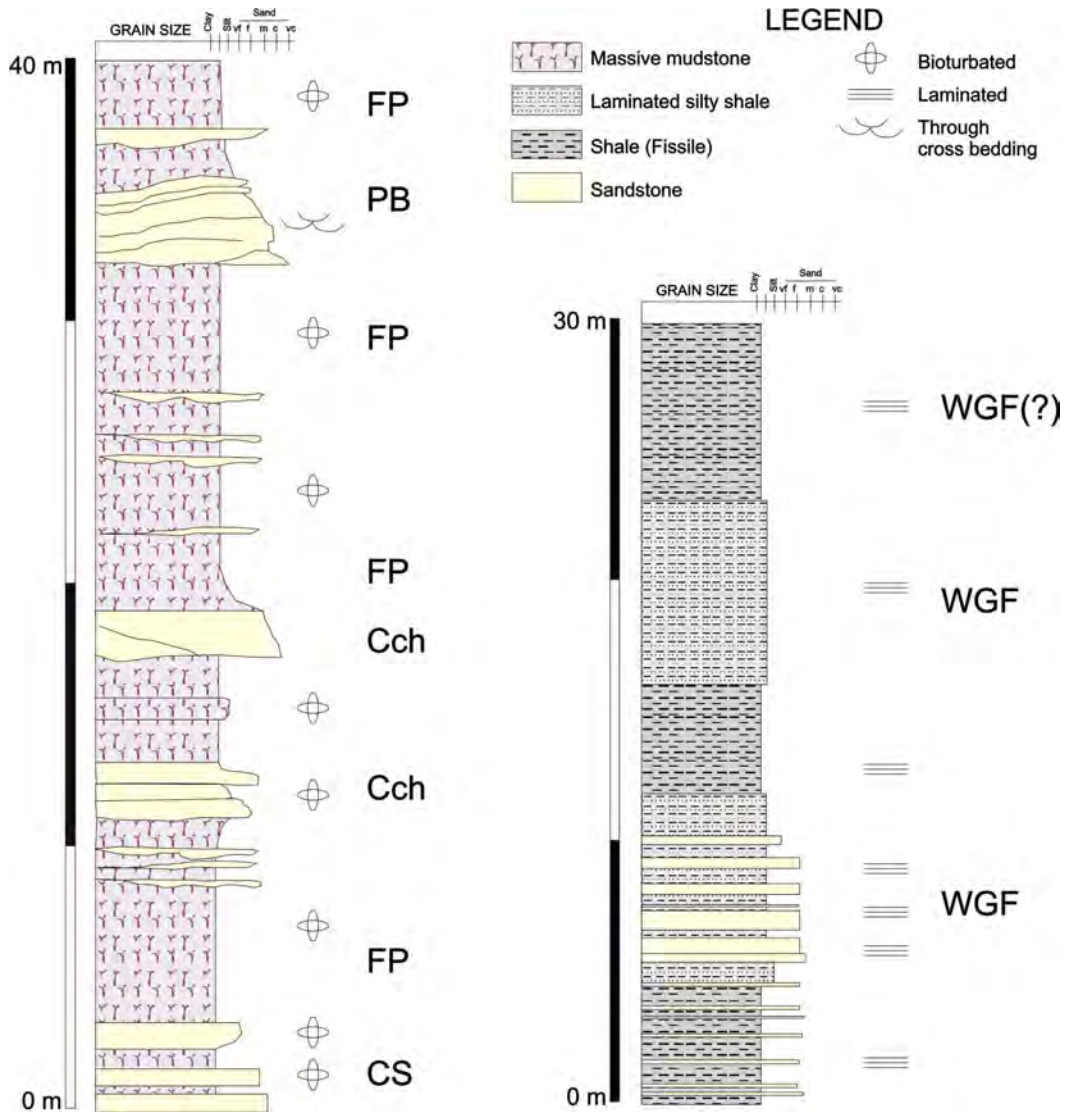
Figure 4.13: On the left, clay-rich lithofacies from fluvial deposits (outcrop description of lower Guayabo Formation), on the right shaly lithofacies from mud-rich deep water deposits (high-resolution, core-calibrated, image-log interpretation, courtesy of ChevronTexaco). The mm- to cm-scale internal fabric is indicated by the symbols: bioturbated or horizontally laminated. The upper case letters refer to the inferred depositional environment or mechanism: floodplain (FP), point bar (PB), crevasse channel (Cch), crevasse splay (CS), and waning gravity flows (WGF).

4.4. Continuity and Repeatability of Rock-Physics Patterns

The similarity or dissimilarity between the rock-physics patterns outlined by decameter-scale lithofacies sequences and those depicted by larger-scale sequences depend on the vertical persistence of lithofacies. This similarity determines the ability to predict, for modeling purposes, the seismic properties of large-scale

sequences from the patterns observed at decameter-scale lithofacies successions. The vertical persistence or variation of lithofacies sequences is the result of the interaction between the rate of space accommodation, of the depositional setting, and the rate of sediment supply (e.g. Emery and Myers, 1996; Miall, 1998). Lithofacies assemblages can be very similar throughout thick stratigraphic intervals, like the case of the lower Guayabo Formation (Figure 4.14); or can have a significant variability, as is the case of mud-rich deep water deposits from offshore West Africa (Figure 4.15).

The applicability of the observed patterns to frontier areas, and regions with scarce well-log data, depends on the repeatability and lateral persistence of lithofacies sequences. Repeatability refers to the similarity between lithofacies sequences accumulated in the same depositional environment at different basins. The lateral persistence relates to the aerial continuity of the lithofacies assemblage within a basin, which again is the result of the interplay between sediment supply and accommodation (Emery and Myers, 1996). As an example of repeatability, I compare the sand-rich deep water deposits from the Gulf of Mexico (Figure 4.9a) with the same type of deposits from the North Sea (Figure 4.16). The Miocene Leon Formation (Figure 4.17), from the Colombian Llanos Basin, is presented as an example of the lateral persistence of lithofacies sequences.

4.4.1. The Patterns of Larger-scale Depositional Sequences

The lower Guayabo Formation presents patterns in the rock-physics planes (porosity-Vclay, velocity-porosity, and velocity-density) very similar to those depicted by the single, dispersed-fabric, fluvial lithofacies sequence analyzed in the section 4.3. The patterns observed in figures 4.10(a), 4.11(a), and 4.12(a) are almost identical to those presented in figures 4.18(a), 4.19(a), and 4.20(a), respectively. The fining-upward cycle analyzed in section 4.3 is part of the lower Guayabo Formation (is located between 100-220 ft in Figure 4.14). The Guayabo Formation is a fluvial syntectonic deposit (Aguilera and López, 1995), accumulated during the uplift of the Eastern Cordillera in Colombia (Cooper et al., 1995). The vertical persistence of this lithofacies assemblage resulted from the dynamic equilibrium between subsidence (accommodation) and sediment supply. This vertical persistence of the lithofacies assemblage produces the resemblance between the single decameter-scale lithofacies sequence and the larger-scale lower-Guayabo Formation.
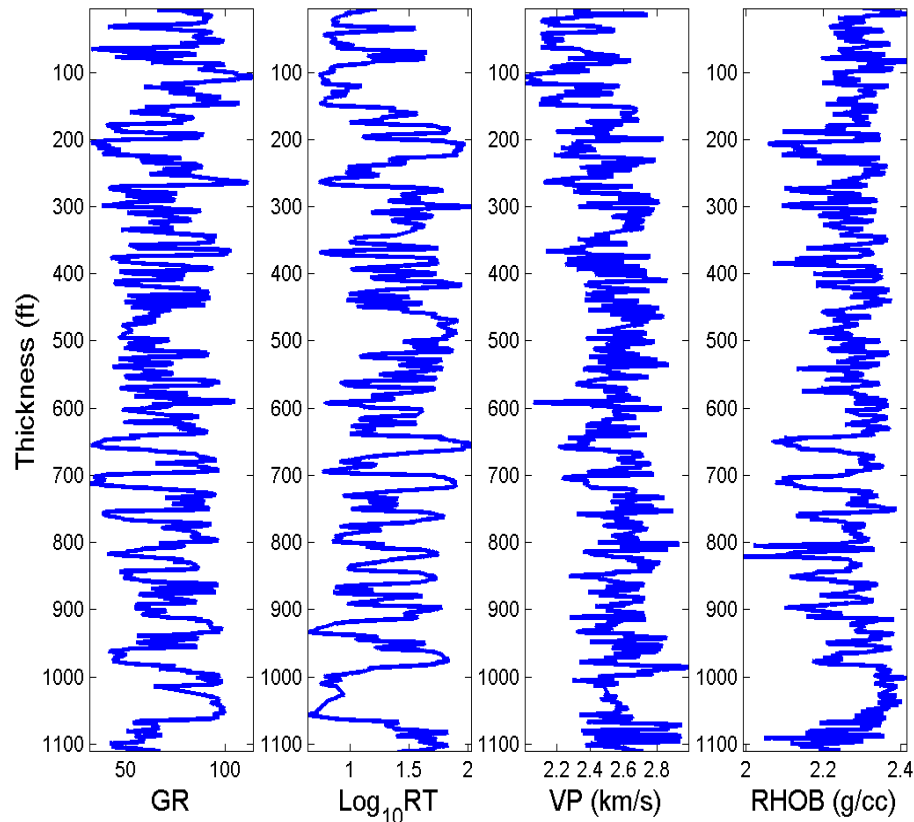
Figure 4.14: Lower-Guayabo Sequence formed by fining upward lithofacies cycles associated with fluvial environments (e. g. Aguilera and López, 1995). Well Apiay-1, Llanos Basin (Colombia).

In contrast, the mud-rich deep water sequence (Figure 4.15), which contains the laminar mixture analyzed in section 4.3, presents patterns significantly different from those associated with a laminar mixture. Exception made of the porosity-Vclay cross plot (Figure 4.18b), the complete sequence shows patterns that resemble those associated with mm- and cm-scale dispersed fabrics (Figure 4.19b, and Figure 4.20b). The main reason for this variation is the presence of shale with different composition and degree of compaction within the same stratigraphic sequence. Notice in Figure 4.18b the high variability in porosity for high clay content. As illustrated in Figure 4.15, the sequence contains at least three types of shale-rich facies. As determined from high-resolution image logs and core descriptions, the shale-rich lithofacies are from base to top: mud flows (MF), overbank deposits (C1), and hemipelagic shale (C2). Mud flow deposits are the stiffest and densest shale-rich deposits. Overbank deposits have an intermediate stiffness and density, whereas hemipelagic shale is the softest and lightest shale-rich lithofacies. Besides, the sands have also slightly different elastic properties, as can be observed in Figure 4.20b.

The sands, however, are mixed only with one type of shale, the overbank deposits, which have an intermediate stiffness.
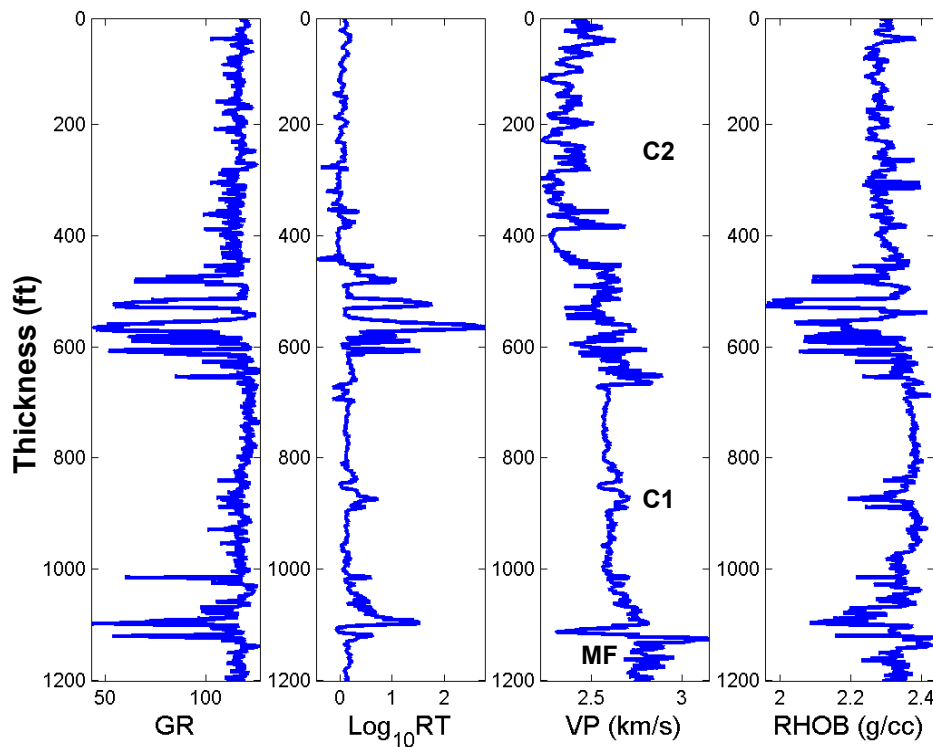
Figure 4.15: Stratigraphic sequence of mud-rich deep water deposits from offshore West Africa. The velocity log identifies three types of clay-rich deposits: hemipelagic shale (C2), overbank shale (C1), and mud flows (MF) at the base. Velocity and density logs after fluid substitution.

The variability of shaly lithofacies within the mud-rich deep water sequence can be explained using sequence stratigraphy. The thicker mud-flow deposits are associated with low relative sea level (low-stand systems tract, LST), and consequently tend to occur towards the base of the stratigraphic sequence. Above them, confined turbidite complex are deposited, which include shale-rich overbank deposits. The thick intervals of hemipelagic shale, in contrast, are associated with periods of relative high sea level (high-stand systems tract, HST).

Both the hemipelagic shale and the mud flows introduce the higher variability in elastic properties in the mud-rich deep water deposits. In addition to a dispersed fabric, mud flows probably have a higher degree of compaction and a higher proportion of silty material than the hemipelagic and overbank shale. Similarly, the overbank shale seems to have a higher proportion of silt and a higher degree of compaction than the hemipelagic shale. The dominant fabric of the mixed lithofacies within the overbank complex is the interposition of mm-scale to cm-scale layers of

relatively clean sand and overbank shale. This fabric can be inferred from the monotonic variation in elastic properties as clay content increases (or decreases) and has been corroborated by core observations and high-resolution image logs (Figure 4.13b).
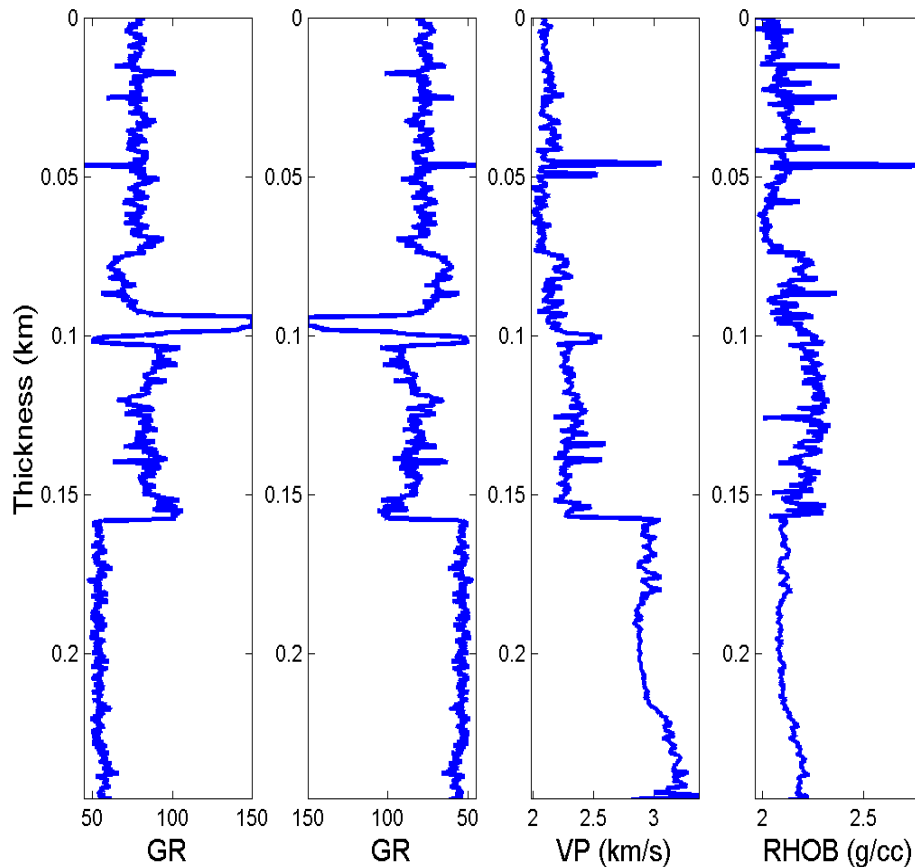
Figure 4.16: Stratigraphic sequence of sand-rich deep water deposits from the North Sea. Velocity and density logs after fluid substitution.

Similar depositional environments generate repetitive lithofacies sequences with comparable elastic properties. The comparison between the rock physics patterns of two sand-rich deep water deposits from different basins, the Gulf of Mexico and the North Sea, provides an excellent example. The patterns of the sand-rich deposit from offshore Gulf of Mexico are illustrated in, Figure 4.10c, Figure 4.11c, and Figure 4.12c. They are very similar to the patterns of the sand-rich deep water deposit from the North Sea, shown in Figure 4.18c, Figure 4.19c, and Figure 4.20c. The absolute velocities are different because of the difference in compaction between these two deposits. The deposit from the Gulf of Mexico is buried about 1 km deeper than the deposit from North Sea. However, the two deposits present a conspicuous contrast in elastic properties between the sandy lithofacies and the shale-rich lithofacies, derived

from the scarcity of mixed lithofacies in this depositional setting. This contrast provides a method to differentiate sand-rich deep water deposits from mud-rich deep water deposits.
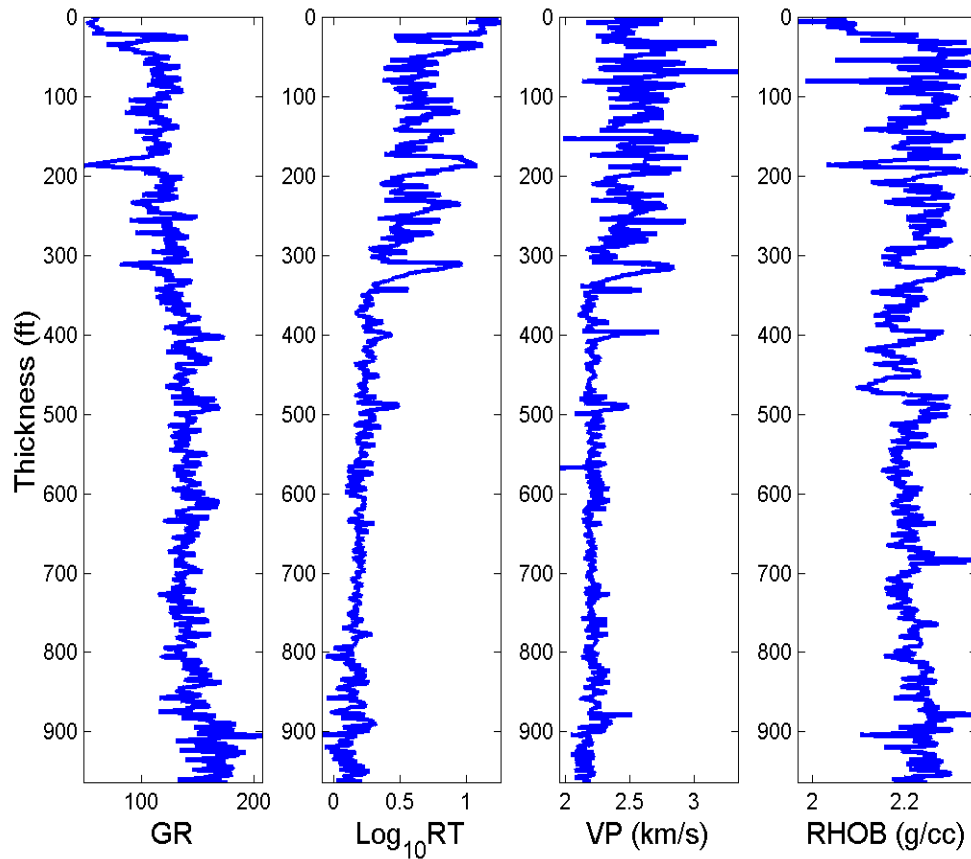
Figure 4.17: Coarsening upward lithofacies sequence from shallow marine deposits, Leon Formation (Miocene), well Tambaquí-1, Llanos Basin (Colombia).

The Miocene Leon Formation (Llanos Basin, Colombia), provides an excellent example of lateral persistence of lithofacies, and therefore elastic properties. This formation consists of a coarsening upward lithofacies sequence (Figure 4.17) accumulated as the result of a tectonically-driven regional flooding event and the posterior basin-filling process. In terms of sequence stratigraphy it can be considered a high-stand systems tract (e.g. Cooper *et al.*, 1995). The rock-physics patterns that this formation presents at the well Tambaquí-1 (Figure 4.18d, Figure 4.19d, and Figure 4.20d), are remarkably similar to the patterns outlined by upper segment of the same formation at the well Apiay-1, about 200 km to the south west, illustrated in Figure 4.10d, Figure 4.11d, and Figure 4.12d.
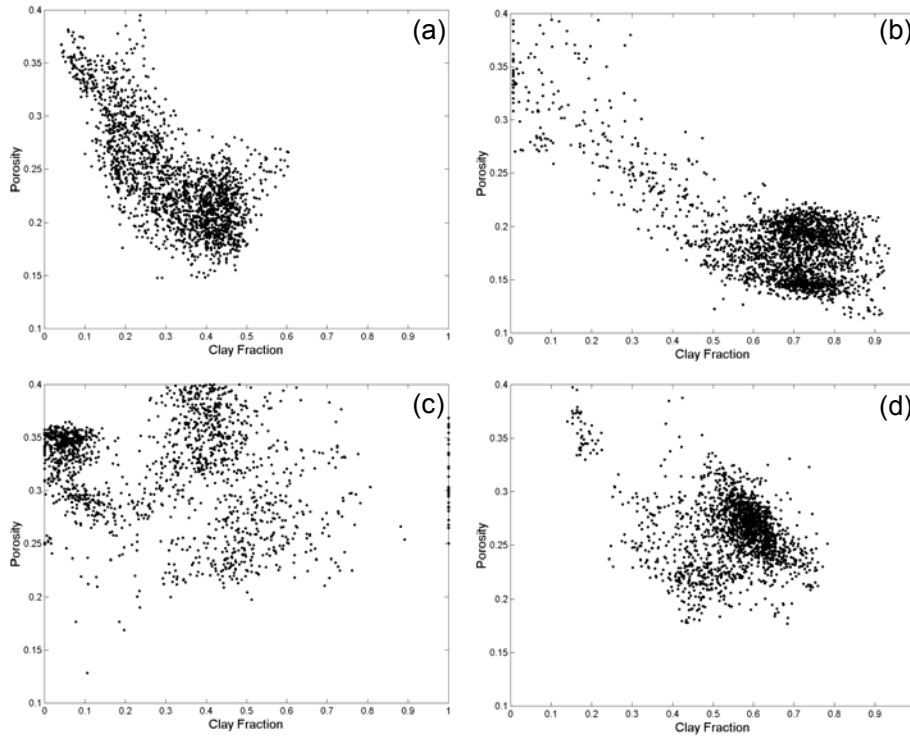
Figure 4.18: Cross plots of Porosity (φ) and clay fraction (Vclay). Figures 4.17 (a), (b), (c) and (d) correspond to the lithofacies sequences presented in Figure 4.14, Figure 4.15, Figure 4.16, and Figure 4.17, respectively.
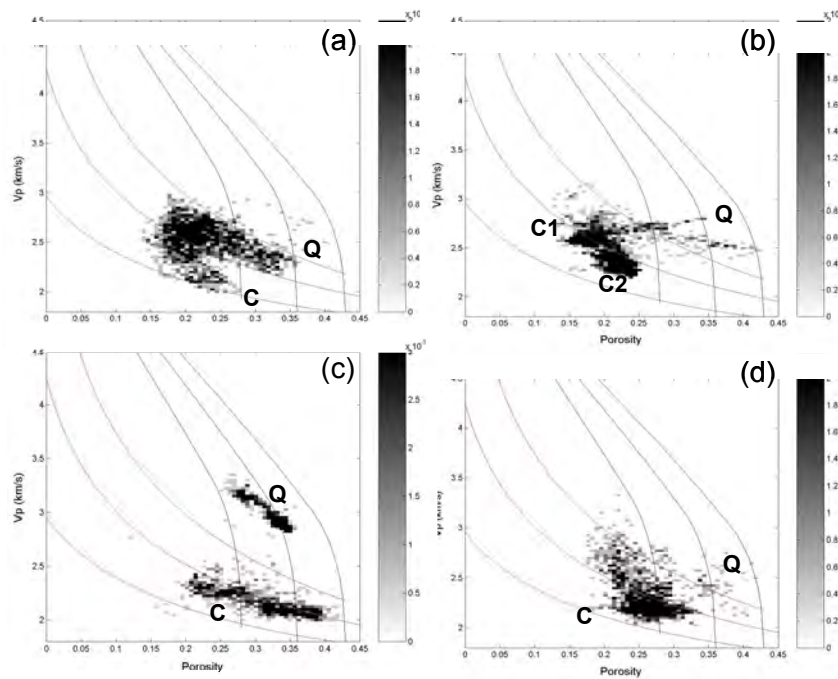
Figure 4.19: Bivariate histograms of P-wave velocity (Vp) and Porosity (φ). Q indicates the sand point, and C indicates the clay-rich points. Figures 4.18 (a), (b), (c), and (d) correspond to the lithofacies sequences shown in Figure 4.14, Figure 4.15, Figure 4.16, and Figure 4.17, respectively.
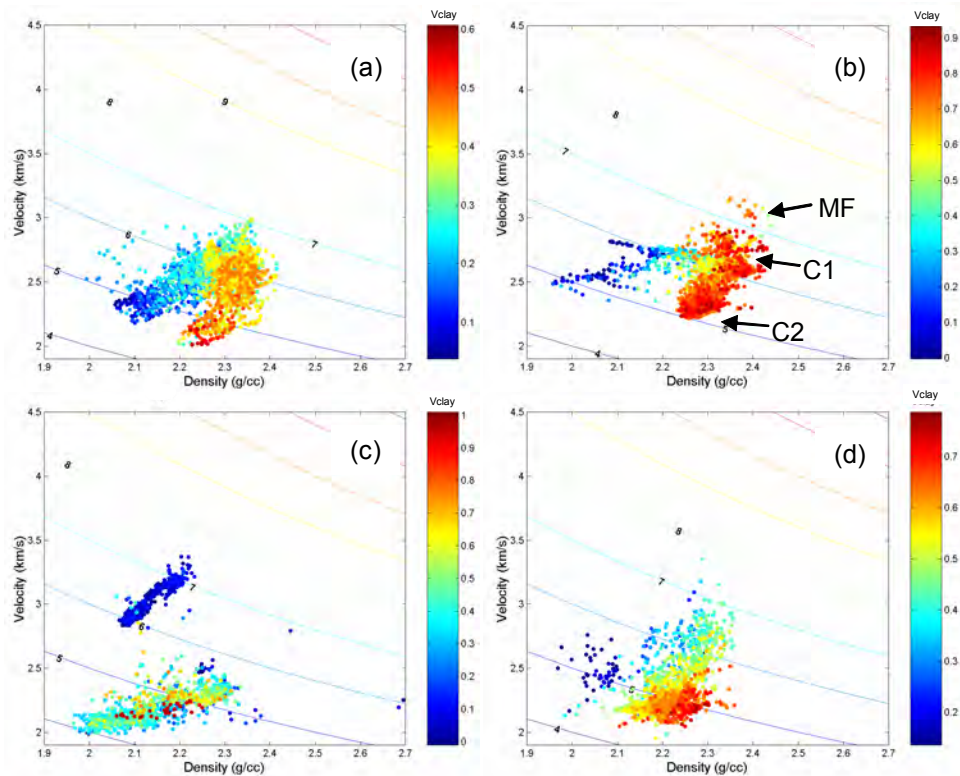
Figure 4.20: P-wave velocity (Vp) and density cross plots, color-coded by clay fraction (Vclay). The data corresponds to different lithofacies sequences: (a) fluvial deposits, (b) mud-rich deep water deposits, (c) sand-rich deep water, and (d) shallow marine to low-energy intertidal deposits. In (c) the arrows indicate the different types of shale.

The rock-physics patterns of large-scale clastic stratigraphic sequences depend on the proportion and type of lithofacies assemblages. Figure 4.18, Figure 4.19, and Figure 4.20 show that these patterns may vary significantly from one depositional setting to another. The most striking difference illustrated in these figures is the contrast between the patterns of sand-rich deep water deposits and those of mud-rich deep water deposits. This contrast is the result of the scarcity of mixed lithofacies in the sand-rich depositional setting. However, as explained in section 4.3, another significant contrast can occur between sequences with predominant mm- to cm-scale dispersed mixed lithofacies and those with mm- to cm-scale horizontally laminated mixed lithofacies.

4.4.2. Depositional Settings and the Fabric of Sand-Clay Mixtures

Although dispersed and horizontally laminated sand-clay mixtures cannot be considered exclusive of a particular depositional setting, their occurrence within a

given environment is associated with specific depositional and post-depositional processes, like bioturbation. In his discussion of the mechanics of deposition of muddy sediments, Allen (2001, p. 142) demonstrates that the net rate of bed deposition (*D*) of muddy deposits is given by

$$D = \rho \chi V_b \left(1 - \frac{\tau}{\tau_{cr}} \right),$$ (4.18)

where ρ is the clay (mud) density, χ is the near-bed fractional volume concentration of clay, V_b corresponds to the terminal fall velocity of the near-bed particles (referenced to the ground), τ is the boundary shear stress due to the fluid motion, and τ_{cr} is the critical stress for mud deposition. Three cases become evident from Equation 4.18, the stage of deposition from a stagnant fluid ($\tau = 0$), the stage of no deposition ($\tau = \tau_{cr}$), and the stage of erosion ($\tau > \tau_{cr}$). For any fluidized flow with clay and sand, fluctuations between these three stages will determine the occurrence and distribution of horizontally laminated sand-clay mixtures.

The ideal conditions for millimetric to centrimetic interposition of clean sand and clay-rich mud occur in flat settings affected by oscillating or seasonal currents. Asymmetrical tides provide an excellent example of these conditions, as discussed by Allen (2001, p. 256). Reineck and Singh (1980) summarize the occurrence of these lithofacies from different depositional settings. They classify these deposits as coarsely interlayered bedding and thinly interlayered bedding (rhytmites), which different authors have found in deposits associated with lakes and transitional environments like tidal flats and estuaries (Reineck and Singh, 1980, p. 123). Howard and Reineck (1972) report the presence of these lithofacies in shallow marine shoreface deposits. Smith (1987) discusses the presence of laminated sand-clay mixtures fluvial deposits, which are commonly associated with areas with high water tables.

Bioturbation (e.g. Reading, 1980, p. 223; Reineck and Singh, p. 387) seems to be the dominant mechanism generating dispersed sand-clay mixtures in water-laid deposits. Fast accumulation rates associated with fluidized flows with high sediment concentration could be an alternative mechanism. Metric to decimetric intervals of silty mudstone and muddy sandstone, associated with fluvial deposits like the Guayabo Formation of Colombia, seem to be the result of burrowing, plant growth, and pedogenetic processes that destroy the primary sedimentary structures (Galloway and Hobday, 1996, p.75).

The final depositional fabric is the result of the predominant depositional mechanism and sediment composition. The examples documented in this chapter show that the proportion of dispersed and laminar mixed lithofacies, and actually the proportion of mixed lithofacies, vary among the different depositional environments. As a general rule, dispersed mixtures result from either bioturbation or the inability of the medium to separate fine and coarse fractions, whereas laminar mixtures indicate cyclic deposition (like tidal deposits and varves) or efficient separation between the traction and suspension fractions. A good example is the differentiation, made by Smith (1987), between fluvial point bars without laminated lithofacies, and fluvio-estuarine point bars with laminated lithofacies. However, the specificities of the mechanics of deposition are normally more complex. For example, in their analysis of textural trends in deep-water turbidite and mass-flow deposits, Sylvester and Lowe (2004) showed that the development of mud-rich sands and slurry beds, with a dispersed mixture of sand and clay, depends on how efficiently the settling sediment traps mud particles. Therefore, at least for the case of turbidite deposits, the difference between the depositional mechanism that generated the laminated turbidites shown in Figure 4.13b, and the mechanism that would have generated a higher proportion of the dispersed-mixture slurry beds might be relatively small.

4.5.   The Diagenetic Effects

The rock physics patterns of clastic depositional sequences can change because of diagenetic effects. Marion (1990) and Yin (1992) analyzed the variations in these patterns associated with confining pressure. Jizba (1991) modeled the effect of differential cementation between clean sands and shaly sands. Dvorkin *et al.* (2002) showed a remarkable continuity in the shale and sand diagenetic trends of deep-water deposits from the Gulf of Mexico and the North Sea. Chapter 3 explains the role that pressure solution can play in the diagenetic trend of quartzose sands. In this section, I present two clear examples of the effect that diagenesis and confining pressure have on the rock physics patterns of clastic sequences.

4.5.1. Confining Pressure, Pressure Solution, and Incipient Cementation

Marion's and Yin's analyses (Marion, 1990; Yin, 1992) postulate that as confining pressure increases, the velocity-porosity pattern of dispersed mixtures of sand and clay change from a flat trend to an inverted-V pattern. Figure 4.21 shows

two fining-upward cycles of fluvial origin. They both come from well Apiay-1, the same well that presented the inverted-V pattern in the whole Pliocene Lower Guayabo stratigraphic sequence. The examples shown below correspond to stratigraphic intervals located above and below the Lower Guayabo. The shallow interval is part of the Upper Guayabo, whereas the deep interval is part of the lower Carbonera, C5 formation. In spite of the similar lithofacies that these intervals show, the rock physics patterns are very different and conform to the predictions of Marion (1990) and Yin (1992). Figure 4.22 shows the velocity-porosity patterns of these two fining-upward sequences. The shallow lithofacies sequence shows a flat pattern, whereas the deep lithofacies sequence presents what is becoming a classical inverted-V pattern.
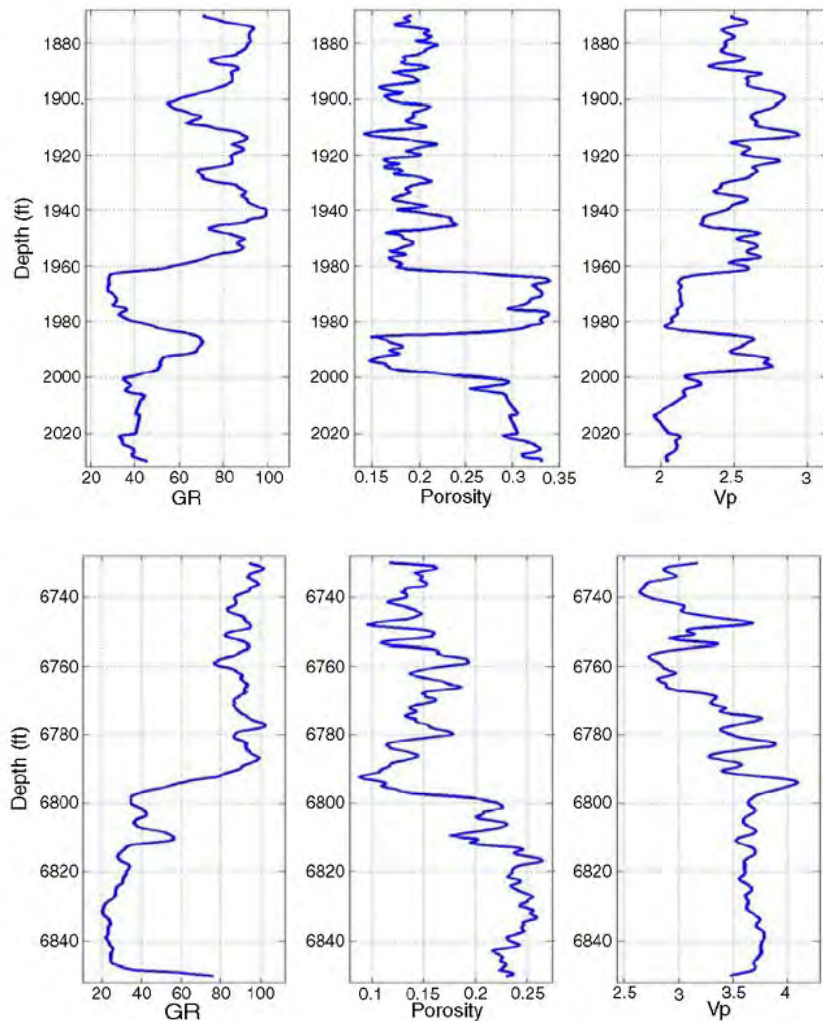
Figure 4.21 Log signature of fining-upward sequences with dispersed sand-clay mixtures, at different burial depths. Well Apiay-1, Llanos Basin (Colombia).

Although the patterns observed follow exactly the predictions from the Marion-Yin model, the actual mechanisms reducing porosity and increasing elastic stiffness may not be the same. Yin's laboratory studies induced an elastic deformation in the samples, and the increase in elastic stiffness was mainly associated with the effect of confining pressure. Although confining pressure definitely plays a role in increasing stiffness, the porosity reduction mechanism operating in nature is not necessarily elastic deformation. Incipient cementation or pressure-solution processes can induce similar changes in porosity and stiffness (see Chapter 3). Following the analysis presented in Chapter 3, the fact that these sandstones are about 2000 ft above the threshold temperature for quartz cementation suggests that pressure solution, an inelastic deformation mechanism, is probably the dominant process in this case.
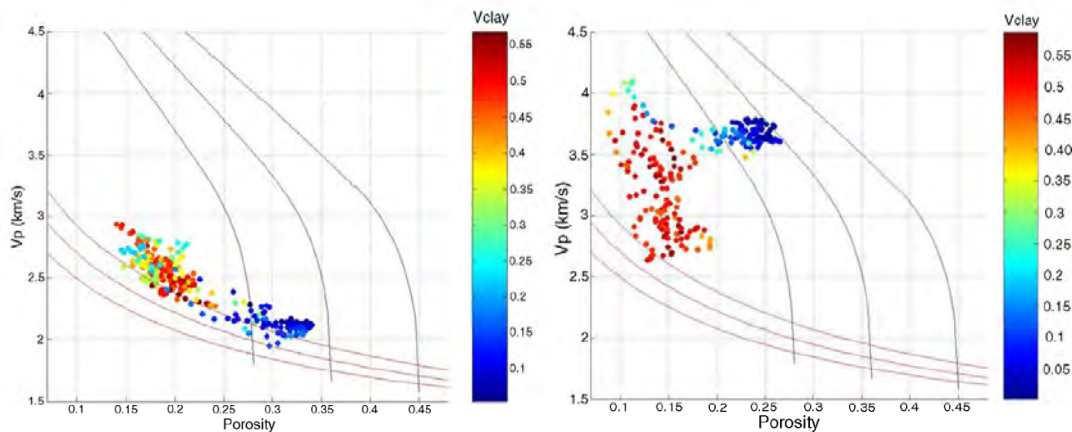
Figure 4.22: Flat (left) and inverted-V (right) patterns of the shallow and deep, respectively, lithofacies sequences shown in Figure 4.21. Well Apiay-1, Llanos Basin, Colombia.

4.5.2. Preferential Diagenesis

It is generally accepted that quartz cementation is the main porosity-reduction mechanism in intermediate to low-porosity quartzose sands (Paxton *et al.*, 2002). The alternative mechanism is compaction enhanced by pressure solution, which although likely, is less common in quartzarenites. Quartz cementation occurs preferentially in clean sands, rather than dirty sands, because clean sands have higher permeability (Jizba, 1991), and have larger surface area for quartz precipitation (e.g. Walderhaug, 1994). Jizba (1991) postulated that the inverted-V pattern of dispersed sand-clay mixtures would be modified by this differential cementation in low-porosity quartzose sands. According to her model, cementation will reduce porosity

and increase stiffness in the clean lithofacies, without altering the properties of the shale and mixed lithofacies (Jizba, 1991).

Figure 4.23 shows the gamma-ray signature and rock-physics patterns of deltaic deposits from the Upper Cretaceous of the Llanos Basin (well La Punta-1). These deltaic deposits contain two types of graded parasequences: 1) deltaic channels, with a fining upward trend similar to that of meandering fluvial channels; and 2) distributary mouth bars (DMB), characterized by a coarsening-upward trend. The depositional sequence shown corresponds to the basal transgressive systems tract that pre-dates the major Turonian-Coniacian transgressions in this basin. From base to top, the depositional sequence consists of: (1) a basal transgressive sandstone (BTS) on top of the Paleozoic, (2) two coarsening-upward parasequences interpreted as prograding distributary mouth bars, (3) two fining-upward trends interpret as deltaic channels, and (4) a marine flooding event on top of the sequence.

The pattern that the complete sequence presents in the velocity-porosity plane is puzzling. Since the sequence is composed of fining-upward and coarsening-upward trends, we should expect an inverted V. However, the pattern looks more like an L, with two types of clean-sandstone end-members. To understand this pattern we have split the sequence into its smaller components, the channel and the DMB parasequences.
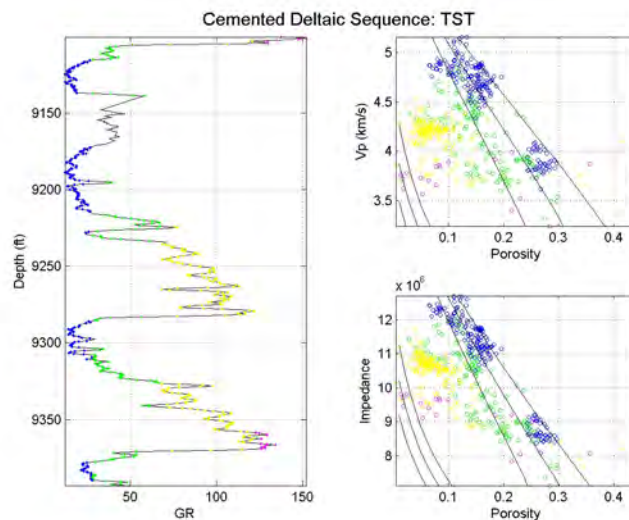
Figure 4.23: A complete prograding deltaic sequence from the Cretaceous of the Llanos Basin. The color code indicates lithofacies: blue is sand, green is shaly sand, yellow corresponds to sandy or silty shale, and magenta to clay-rich shale.

There is a huge contrast in rock properties between the lower and upper sandstones (Figure 4.24). The data from the shaly intervals have been discarded due to wellbore geometry; therefore we are left with the sandstone intervals. The difference in porosity between these two clean sands ranges from 10% to 15%. The fact that, in the Vp-ϕ and Impedance-ϕ planes, the data from the sandstones align along the predicted diagenetic trend for quartzarenites (Hashin-Strickman upper bound) suggests that the cause of this difference in porosity is the amount of cement, and actually that the cement is very likely quartz. An alternative explanation is compaction induced by pressure solution; however this mechanism is not likely to predominate in a low-strain domain like the Llanos basin. Core samples or other detailed data were not available, therefore the presence of calcite cementation cannot be ruled out. However, quartz cementation appears to be the most reasonable explanation for the difference in elastic properties and porosity of these sands.
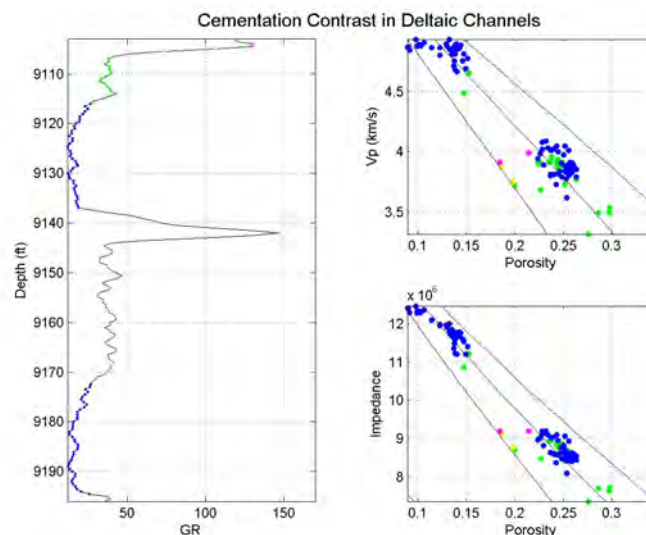
Figure 4.24: Contrast in porosity and velocity between the clean quartzarenites of the deltaic channels. This contrast is considered to be the result of a significant difference in quartz cementation that occurs within less than 100' of burial-depth separation. The sandstones are part of the same stratigraphic sequence.

The pattern of the two DMB parasequences departs from the inverted-V expected for dispersed mixtures, or the linear trend observed in laminar mixtures (Figure 4.25). The observed departure from the inverted-V pattern follows a trend previously modeled by Jizba (1991). Velocities and porosities in the DMB clean sandstones are similar to those of the sandstone in the lower deltaic-channel. On the other hand, although there is scatter in the data, the mixed lithofacies show gradual transitions from either the higher porosity or the lower porosity clean sandstones (Figure 4.23)

to the compacted clay-rich shale (magenta). This indicates that the mechanism driving diagenesis affects the clean sandstones and some of the shaly sandstones, leaving the low-permeability facies intact. Consequently, the pre-existing pattern, which probably was similar to an inverted V, has been modified. The velocity-porosity pattern that these parasequences of DMB deposits show follows exactly the one predicted by Jizba (1991), explained as the result of preferential cementation of the clean sands.
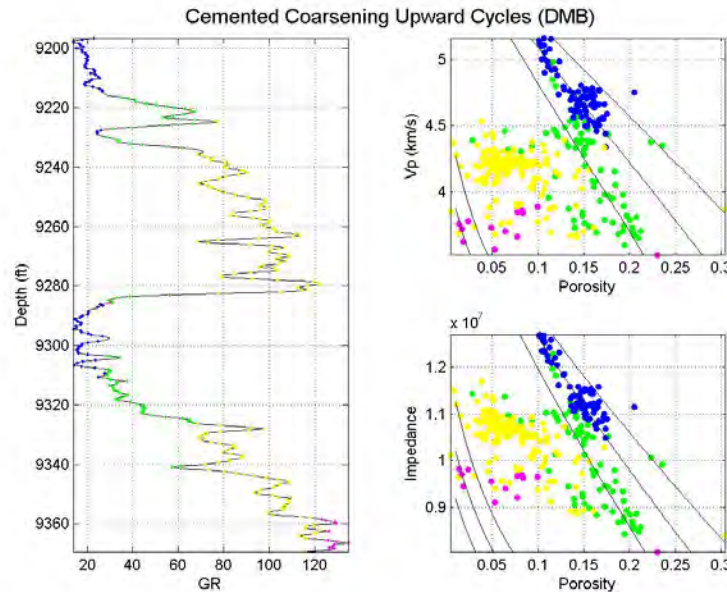
Figure 4.25: Coarsening upward parasequences corresponding to distributary mouth bar deposits (DMB), and their pattern in the velocity-porosity and impedance-porosity plane. The upward shift of the clean sandstone (blue), and some of the shaly sandstones (green) is interpreted to be the result of quartz cementation.

4.6. Discussion

The results presented in this study show that the existing rock-physics models predict the variations in elastic and hydraulic properties associated with the textural trends in clastic depositional sequences. The models, based on laboratory and theoretical analysis, can reproduce the patterns of clastic depositional sequences in the rock-physics planes, based on well-log measurements. Mineral composition, sorting and the type of mixture are the main depositional lithofacies influencing the observed patterns. Cementation, compaction, pressure solution, and confining pressure are the dominant factors influencing the variations associated with diagenesis.

The variations observed among depositional sequences from diverse environments result from the intrinsic relationship that exists between textural trends, or lithofacies successions, and the flow regimes and conditions of sedimentation for each particular setting. These variations are produced by the presence, or absence, of mixed lithofacies and their specific fabrics. Some of the implications of these results are discussed below. In general, ignoring the effect of mixed lithofacies and assuming that seismic reflections come from simple sand and shale interfaces can lead to erroneous interpretations.

4.6.1. The Scales

The dispersed and horizontally-laminated sand-clay mixtures discussed here correspond to mm- to cm-scale fabrics. These are the effective-medium scales for conventional logging tools. The elastic properties of decimeter-scale interbedded deposits depend on the mm- to cm-scale fabric. For example, it is likely to find a sedimentary sequence composed of the interposition of sandy shale and shaly sand, both with an internal dispersed fabric. That sequence might be described as thinly interbedded by a geologist, however the elastic properties would be exactly the Backus average of the two dispersed mixtures (sandy shale and shaly sand) and consequently the interval would look as a dispersed mixture in the rock-physics planes.

Lithofacies proportion and thickness have a determinant impact on the final seismic response of stratigraphic sequences. At the frequencies of conventional seismic surveys, the seismic traces record the effective-medium of meter- to decameter-scale heterogeneities. The final seismic trace results from the convolution of the seismic waves with the sedimentary package. The final seismic response not only depends on the seismic properties of each lithofacies, but also on the geometric arrangement of these lithofacies. Seismic modeling is the best way to evaluate the impact of lithofacies proportion, thickness, and vertical arrangement, on the final seismic response.

4.6.2. Implications for Evaluation of Rock Properties from Well Logs

Thomas and Stieber (1975) developed a method to evaluate net to gross from clay fraction, based on the gamma-ray log. This method can further be improved using the additional information contained in the elastic properties. At least, the calculated fractions of clay and quartz (or other grains) should present a consistent

pattern in both the velocity-porosity and the velocity-density cross plots. Furthermore, the rock-physics planes can be used to evaluate sand-clay mixtures in rocks where the gamma-ray does not work. For example, gamma-ray-derived clay fractions in feldspar-rich sand are inaccurate because feldspars are radioactive. Clay fractions derived from neutron and density logs might be more appropriate in these cases. Since P-wave modulus of quartz and feldspar are similar, the clay fractions determined could be constrained using either the velocity-porosity or the velocity-density cross plot.

4.6.3. Implications for Seismic Interpretation

The significant difference in elastic and petrophysical properties of dispersed and laminar mixtures calls the attention to the need for a better understanding of the seismic response associated with specific facies sequences. Whereas recent techniques for seismic interpretation still use general assumptions about the sand and shale reflectivity (e. g. Brown, 2003) this study demonstrates the need for a more comprehensive approach. The integration of rock physics diagnostics and seismic geomorphology may lead to new breakthroughs in seismic interpretation.
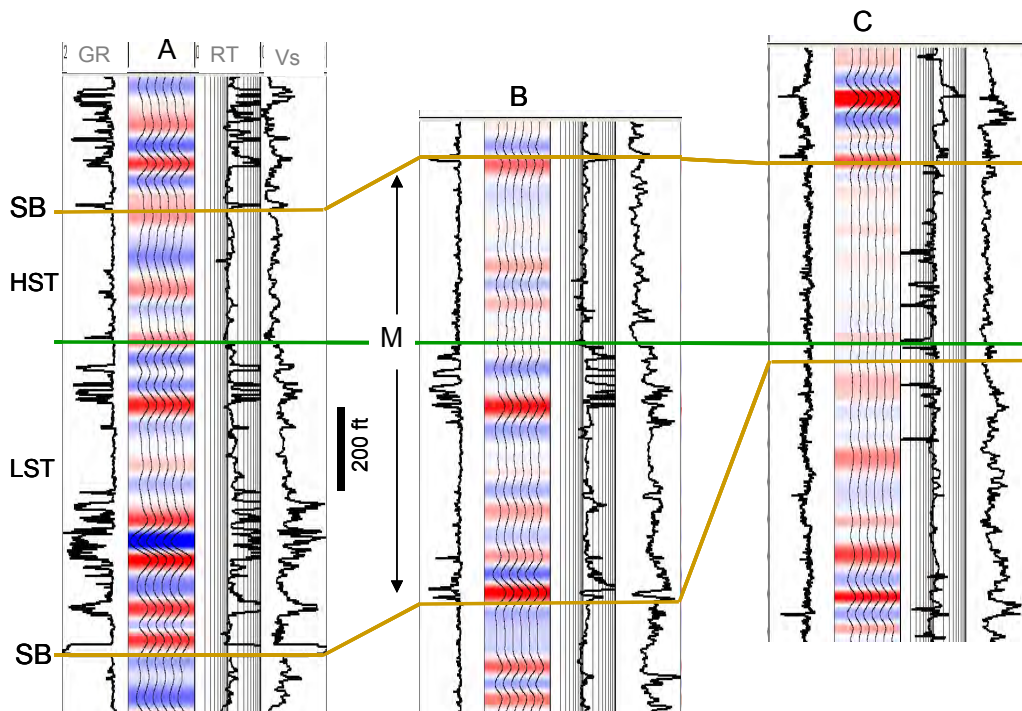
Figure 4.26: Normal-incidence synthetic seismograms and log signatures of a stratigraphic sequence in a mud-rich deep-water depositional environment.

A rock-physics-based interpretation starts by establishing the relationship between the lithofacies succession and its respective seismic response. The lateral variations in seismic lithofacies observed in sequence M of Figure 4.26 helps to illustrate the approach. Sequence M is a deep-water depositional sequence with two main components: the low-stand systems tract (LST) made of the interposition of sands and silty shale (overbank fines) and the high-stand systems tract (HST) composed of the hemipelagic shale. The brown lines in Figure 4.26 are the sequence boundaries. The top of the LST, indicated by the green line, is at the top of the interbedded sandy intervals observed at both wells A and B in Figure 4.26. Four main seismic lithofacies associations can be established in sequence M: (1) thick massive sands, (2) silty shale, (3) interbedded sands, and (4) hemipelagic shale. Well A has both thick massive sands (towards the bottom of the LST) and interbedded sands (towards the top of the LST); well B has interbedded sands at the base and the top of the LST, and a few massive sands that are just a few feet thick; well C has only hemipelagic shale (notice the low Vs and relative scarcity of internal reflections). The thick-massive sands clearly have a characteristic negative high-amplitude signature. If the boundaries of sequence M can be accurately mapped, then intervals with interbedded sands can be seismically distinguishable from the shaly deposits using seismic properties and attributes. However, if the lower boundary cannot be accurately picked, then significant uncertainty is introduced by the fact that the section of shaly deposits (probably mud flows) below sequence M in well C shows a seismic character similar to that associated with interbedded sands.

As is standard nowadays, AVO analysis can be used to differentiate between interbedded sands and the muddy lithofacies at well C. As explained above, the seismic signature of the interbedded sands in wells A and B is somewhat similar to the seismic signature generated by the interposition of soft and stiff shaly lithofacies below sequence M in well C. However, the AVO response of the negative amplitudes is different. As Figure 4.27 and Figure 4.28 illustrate, the negative amplitudes in the muddy intervals show a decreasing reflectivity contrast with offset. On the contrary, most of the hydrocarbon-bearing sands show increasing reflectivity contrast (class III) or a flat trend (class II). However, there are additional complications. The deeper sands in well A show a positive amplitude response, indicative of a change in reflectivity contrast between the sands and the surrounding silty shale. The reflectivity contrast of this sand increases with offset (horizon s12_ss02 in Figure 4.30). Within the same depth interval and the same stratigraphic sequence, a similar lithology shows different seismic behavior. Rock-physics

analysis would help to determine whether this change is due to fluids, local compaction, diagenesis, or dispersed sand-clay mixtures. Then it would be possible to establish whether the change observed should be expected at about the same depth in other localities.
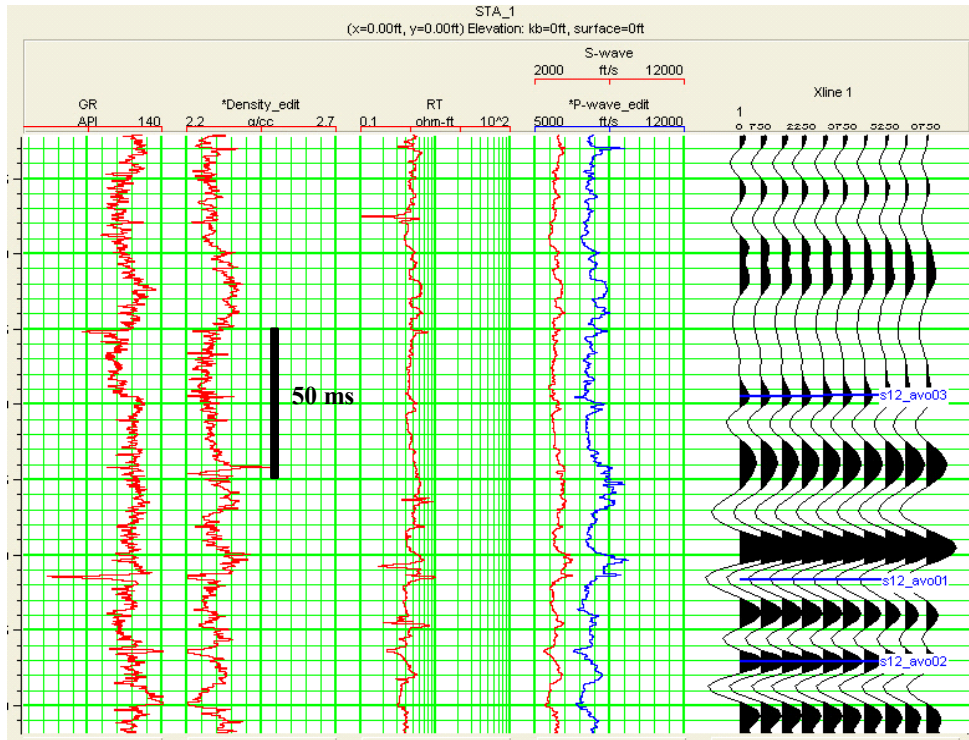
Figure 4.27: Modeling of the seismic response of Well C around Sequence M. The reflections are generated by the impedance contrast between shaly lithofacies (probably mud flows and hemipelagic shale). Although this seismic response resembles the interposition of sand and shale, AVO analysis helps to differentiate between the two cases.
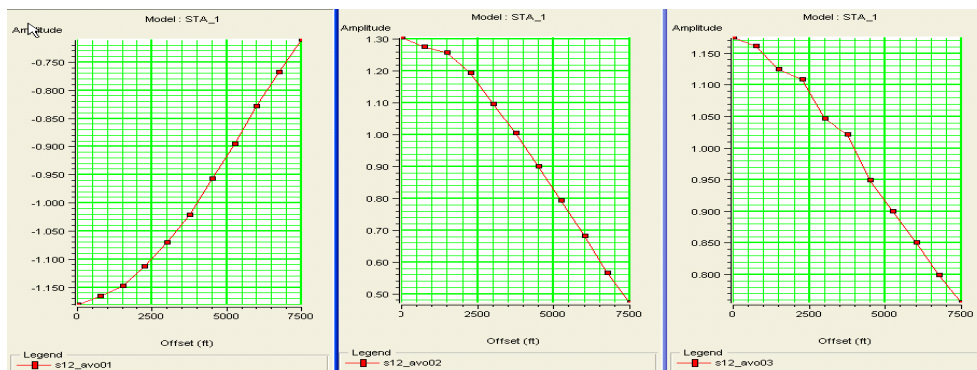
Figure 4.28: AVO response of negative and positive amplitude responses in well C (see Figure 4.27 for reference).
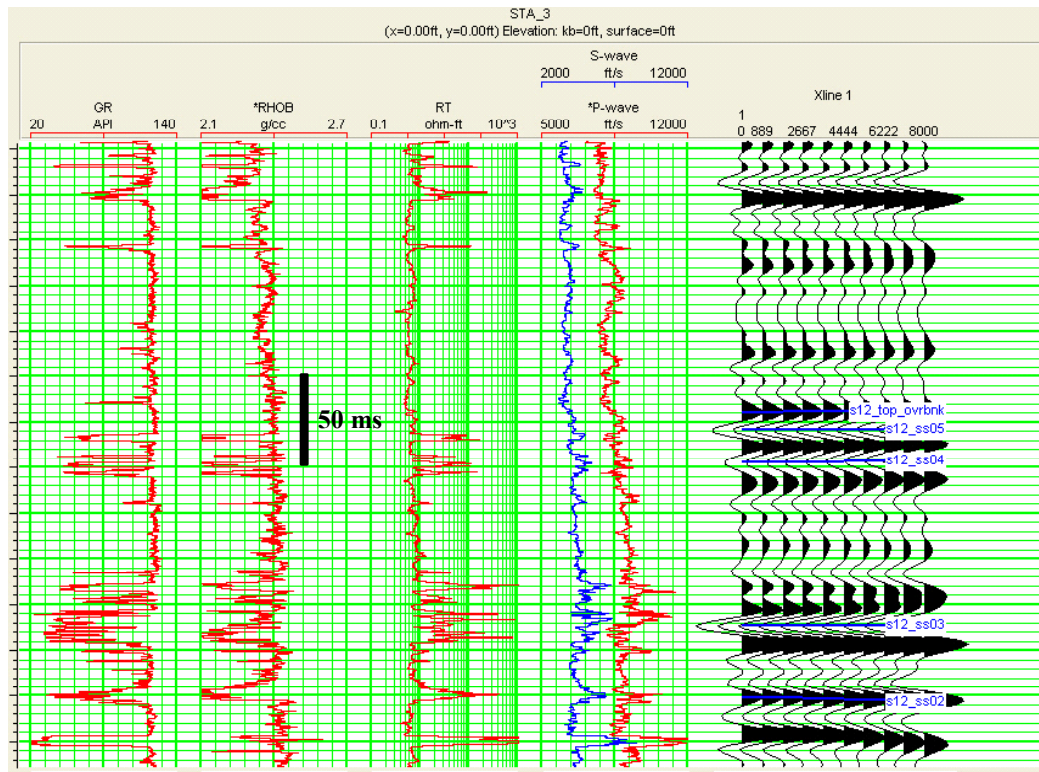
Figure 4.29: Modeling of seismic response of well A around Sequence M. The AVO response allows the identification of most of the intervals with interbedded sands.
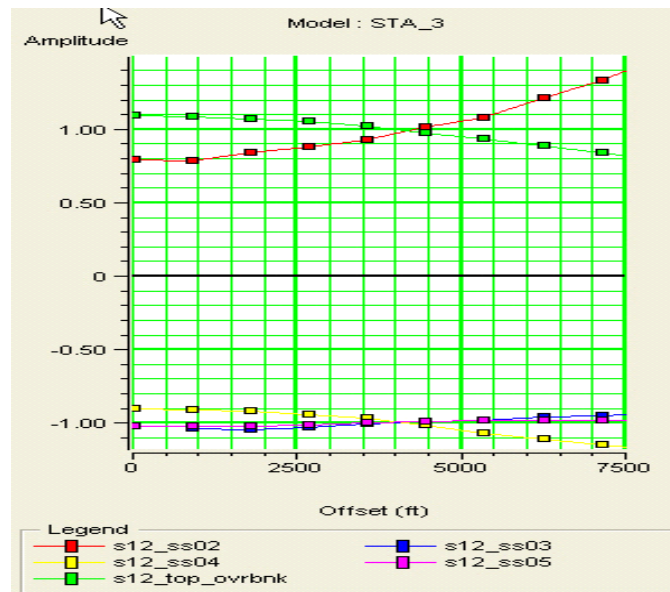
Figure 4.30: AVO response of the top of the overbank deposits and four of the five sand intervals in Well A (see Figure 4.29 for reference).

These observations lead to a broader definition of seismic facies (Mitchum *et al.*, 1977). A seismic lithofacies association can be defined as a rock interval that can be characterized by its lithologic composition, elastic properties (i.e. Avseth, 2000),

shape, and stacking patterns. Each seismic lithofacies association can be associated with a group of seismic characteristics or facies. I identify five fundamental characteristics of a seismic lithofacies association: (1) its seismic trace and the attributes derived from it, (2) its P-wave impedance, (3) its elastic impedance or shear-wave reflectivity, (4) its geomorphic shape, and (5) its stacking pattern. A combination of these characteristics should allow us to map the distribution of the different seismic lithofacies associations that together comprise a depositional system.

4.7.   Conclusions

The patterns of clastic depositional sequences in various rock physics planes (Vp-ϕ, ϕ-Vclay, and Vp-density) follow the trends predicted for dispersed and laminar mixtures of sand and clay. The most important factors controlling these trends are the facies proportion and the type of mixed lithofacies.   Dispersed mixtures of sand and clay constitute the lithofacies with higher velocity, higher impedance, and lower porosity, whereas laminar mixtures present porosities, velocities and impedances that are intermediate between the clay-rich-shale and clean-sand end members.

The patterns of clastic depositional sequences in the rock-physics planes vary depending on the depositional environments, and more specifically on the proportion and type of mixed lithofacies. An example from fluvial deposits shows patterns associated with the predominance of dispersed sand-clay mixtures, whereas mud-rich deep water deposits show linear trends caused by the predominance of mm- to cm-scale laminar mixtures. Sand-rich deep water deposits present scarcity of mixed lithofacies, whereas low-energy shallow marine deposits present abundance of both dispersed and laminar mixed lithofacies.

The vertical and lateral continuity of the rock physics patterns associated with a specific lithofacies sequence depends on the vertical and lateral persistence of the lithofacies. Syntectonic fluvial deposits from Colombia show good vertical continuity, and consequently the rock physics patterns of the large-scale sequence are similar to those of the decameter-scale lithofacies assemblage. In contrast, mud-rich deep water deposits present significant lithofacies within a stratigraphic sequence, not only on the type of lithofacies but also on the degree of compaction of similar lithofacies. Consequently, in spite of the abundance of laminated lithofacies within the sequence, the final patterns differ from those associated with laminar

mixtures. Shallow marine deposits from Colombia show a remarkable lateral continuity, producing similar patterns from wells located about 200 km apart.

The extrapolation of rock physics patterns to stratigraphic sequences from similar depositional settings in different basins depends on the repeatability of the lithofacies assemblage. Sand-rich deep water deposits from the Gulf of Mexico and the North Sea present similar lithofacies assemblages, producing very similar rock physics patterns regardless of the variations associated with compaction. In contrast, mud-rich deep water deposits present very different patterns.

Diagenesis can alter the observed rock physics patterns. However, the diagenetic effects follow trends predicted by rock physics models. This study documents variations in the inverted-V pattern for dispersed mixtures similar to those predicted by the Marion-Yin model (Marion *et al.*, 1992). Although rather than confining pressure, the most likely mechanism is either pressure solution or incipient cementation. The effect of preferential diagenesis on the expected patterns for dispersed mixtures, postulated by Jizba (1991), is also documented in this study.

The rock physics analysis of lithofacies sequences, constrained by stratigraphic sequence boundaries, provides a fundamental understanding of the geologic factors controlling the elastic properties of clastic sedimentary sequences. This analysis, combined with forward seismic modeling, can give an essential understanding of the link between seismic attributes and geologic variables, and therefore can improve the current techniques for seismic modeling and interpretation.

4.8. Acknowledgements

4.9. References

Ager, D., 1993, The Nature of The Stratigraphic Record, third edition, John Wiley & Sons, New York.

Aguilera, R. C. and E. López, 1995, Tectosedimentología de las Formaciones León y Guayabo, Región del Piedemonte Llanero, B. Sc. Thesis, Departamento de Geociencias, Universidad Nacional de Colombia.

Allen, J. R. L., 2001, Principles of Physical Sedimentology, George Allen & Unwin (Publishers), London, 272 p.

Avseth, P., 2000, Combining Rock Physics and Sedimentology for Seismic Reservoir Characterization in North Sea Turbidite Systems, Ph. D. thesis, Stanford University.

Avseth, P., J. Dvorkin, G. Mavko, and J. Rykkje, 2000, Rock physics diagnostic of North Sea sands: Link between microstructure and seismic properties. Geophysical Research Letters, vol. 27, no. 17 p. 2671-2764.

Beaubouef, R. T., 2004, Deep-water leveed-channel complexes of the Cerro Toro Formation, Upper Cretaceous, Chile, American Association of Petroleum Geologists Bulletin, **88**, 1471-1500.

Bachrach, R., 1998, High-resolution Shallow Seismic Subsurface Characterization, Ph. D. thesis, Stanford University.

Backus, G. E., 1962, Long-wave elastic anisotropy produced by horizontal layering, Journal of Geophysical Research, **67**, 4427-4440.

Brown, A., 2003, Interpretation of Three-dimensional Seismic Data, fourth edition, American Association of Petroleum Geologist Memoirs, **42**.

Cardona, P., and G. Gutierrez, 1995, Estratigrafia y Ambientes de Deposito de La Formacion Carbonera al Noroeste de Yopal-Casanare (Colombia), B. Sc. Thesis, Departamento de Geociencias, Universidad Nacional de Colombia.

Cooper, M. A., F. T. Addison, R. Alvarez, M. Coral, R. H. Graham, A. B. Hayward, S. Howe, J. Martinez, J. Naar, R. Peñas, A. J. Pulham, and A. Taborda, 1995, Basin Development and Tectonic History of the Llanos Basin, Eastern Cordillera and Middle Magdalena Valley, Colombia. American Association of Petroleum Geologists Bulletin, v. 79 No. 10, pp 1421-1443.

Dvorkin, J., A. Nur, and H. Yin, 1994, Effective properties of cemented granular materials, Mechanics of Materials, 18, 351-366.

Dvorkin, J., and A. Nur, 1996, Elasticity of high-porosity sandstones: Theory for two North Sea datasets, Geophysics, 61, 1363-1370.

Dvorkin, J., and M. A. Gutierrez, 2001, Textural sorting effect on elastic velocities, part II: elasticity of a bimodal grain mixture, Society of Exploration Geophysicist Annual Meeting, Expanded Abstracts.

Dvorkin, J., M. Gutierrez and A. Nur, 2002, On the universality of diagenetic trends, The Leading Edge, **21**, 40-43.

Emery, D. and K. Myers, 1996, Sequence Stratigraphy, Blackwell Science, Oxford, 279 pp.

Estes, C.A., G. Mavko, H. H. Yin, and T. Cadoret, 1994, Measurements of velocity, porosity and permeability on unconsolidated granular materials Stanford Rock Physics and Borehole Geophysics Project, annual report, 55, p. G1-G9.

Fuchtbauer, H., 1974, Sediments and Sedimentary Rocks 1, in Sedimentary Petrology by W. V. Engelhard, H. Fuchtbauer and G. Muller, Part II. John Wiley and Sons, New York, 464 pp.

Galloway, W. E., 1989, Genetic stratigraphic sequences in basin analysis I: architecture and genesis of flooding-surface bounded depositional units. American Association of Petroleum Geologists Bulletin, **73**, 143-154.

Galloway, W., and D. Hobday, 1996, Terrigenous Clastic Depositional Systems, Springer Verlag, New York, 489 pp.

Gutierrez, M., 2001, Rock Physics and 3D Seismic Characterization of Reservoir Heterogeneities to Improve Recovery Efficiency, Ph. D. thesis, Stanford University.

Gutierrez, M., J. Dvorkin and A. Nur, 2001, Stratigraphy-guided rock-physics reservoir characterization, AAPG Meeting 2001, Expanded Abstracts.

Han, D., 1986, Effects of Porosity and Clay Content on Acoustic Properties of Sandstones and Unconsolidated Sediments, Ph. D. thesis, Stanford University.

Hashin, A., and Shtrikman, S., 1963, A variational approach to the elastic behavior of multiphase materials, Journal of the Mechanics and Physics of Solids, **11**, 127-140.

Howard, J. D., and H. E., Reineck, 1972, Georgia coastal region, Sapelo Island, USA, sedimentology and biology IV, physical and biogenic sedimentary structures of the nearshore shelf, Senckenbergiana Maritime, **4**, 81-123.

Jizba, D., 1991, Mechanical and Acoustical Properties of Sandstones and Shale, Ph. D. Thesis, Stanford University.

Marion, D., 1990, Acoustical, Mechanical and Transport Properties of Sediments and Granular Materials, Ph. D. Thesis, Stanford University.

Marion, D., Nur, A., Yin, H., and Han, D., 1992, Compressional velocity and porosity in sand-clay mixtures, Geophysics, **57**, 554-563.

Mavko, G., T. Mukerji and J. Dvorkin, 1998, The Rock Physics Handbook, Tools for Seismic Analysis in Porous Media, Cambridge University press, New York, 329 pp.

Miall, A. D., 1997, The Geology of Stratigraphic Sequences, Springer Verlag, New York, 433 pp.

Mindlin, R. D., 1949, Compliance of elastic bodies in contact, Journal of Applied Mechanics, **16**, 259-268.

Mitchum R. M. Jr., P. Vail, and J. B. Sangree, 1977, Seismic stratigraphy and global changes of sea level, Part 6: Stratigraphic interpretation of seismic reflection patterns in depositional sequences. In: Payton, C. E., ed., Seismic Stratigraphy –Applications to Exploration, American Association of Petroleum Geologists Memoirs, **26**, 117-133.

Murphy, W. F., III, 1982, Effects of Microstructure and Pore Fluids on the Acoustic Properties of Granular Sedimentary Materials, Ph.D. dissertation, Stanford University.

Paxton, S. T., J. O. Szabo, J. M. Ajdukiewicz, and R. E. Klimentidis, 2002, Construction of an intergranular volume compaction curve for evaluating and prediction compaction and porosity loss in rigid-grain sandstone reservoirs, American Association of Petroleum Geologists Bulletin, **86**, 2047-2067.

Reading, H. G., 1980, Sedimentary Environments and Facies, Elsevier, New York, 557 pp.

Reineck, H. E., and I. B. Singh, 1980, Depositional Sedimentary Environments, 2nd edition, Springer-Verlag, New York, 549 pp.

Smith, D., 1987, Point bar lithofacies models, In: Ethridge, F., R. M. Flores, and M., Harvey: Recent Developments in Fluvial Sedimentology, Society of Economic Paleontologists and Mineralogists, **39**, 83-91.

Sylvester, Z., and D. Lowe, 2004, Textural trends in turbidites and slurry beds from the Oligocene flysch of the East Carpatians, Romania; Sedimentology, **51**, 1-26.

Teichert, C., 1958, Concept of facies, American Association of Petroleum Geologists Bulletin, **42**, 2718-2744.

Thomas, E. C., Stieber, S.J., 1975, The distribution of shale in sandstones and its effect on porosity, Transactions of the SPWLA Annual Logging Symposium, **16**, 1-14.

Timoshenko, S. P., and J. N. Goodier, 1970, Theory of Elasticity, 3rd edition, McGraw-Hill, New York, 567 pp.

Tosaya, C., and A. Nur, 1982, Effects of diagenesis and clays on compressional velocities in rocks, Geophysics Research Letters, v. 9, p. 5-8.

Van Wagoner, J. C., R. M. Mitchum, K. M. Campion and V. D. Rahmanian, 1990, Siliciclastic sequence stratigraphy in well logs, cores and outcrops, American Association of Petroleum Geologists, Methods in Exploration Series 7, 55.

Walderhaug, O., 1994, Temperatures of quartz cementation in Jurassic sandstones from the Norwegian continental shelf –evidence from fluid inclusions: Journal of Sedimentary Research A, **64**, 311-323.

Walker, R. G., 1984, Facies Models, 2nd, ed., Geoscience Canada Reprint Series 1.

Wang, Z., 2001, Fundamentals of seismic rock physics, Geophysics, **66**, 398-412.

Yin, H., 1992, Acoustic Velocity and Attenuation of Rocks: Isotropy, Intrinsic Anisotropy, and Stress-Induced Anisotropy, Ph. D. thesis, Stanford University.

Zimmer, M., 2003, Controls on the Seismic Velocities of Unconsolidated Sands: Measurements of Pressure, Porosity and Compaction Effects, Ph. D. dissertation, Stanford University.

Chapter 5

Fault and Fracture Systems in a Fold-and-Thrust Belt

5.1. Abstract

This chapter presents an outcrop-analogue study of fractures in low-porosity sandstones in the Bolivian Sub-Andean thrust belt. We analyze the evolution of fault and joint systems in these sandstones, quantify their density along the structural trend, and identify the main factors controlling their variability.

We show that faults and joints occur at different scales in a hierarchical fashion, as a consequence of progressive shearing. The first generation is an orthogonal set of joints, one parallel and the other perpendicular to the bedding azimuth. Shearing along these joints transformed them into small faults and created new sets of fractures, oblique to the bedding attitude. Linkage of these small faults facilitated the formation of larger faults with significant strike-slip offset. Shearing along bedding planes created sub-vertical splay joints, which induced the formation of conjugate normal faults. In this thrust belt, subordinate strike-slip and normal faults are concomitant products of compressive deformation.

This study documents a hierarchical correspondence between spacing of structural heterogeneities and stratigraphic architecture. We measured spacings of joints and outcrop-scale faults along the backlimb of the Abra-del-Condor Anticline. We subdivided the structural discontinuities into four main groups: joints, small faults, intermediate faults, and fault zones. Spacing of joints, small faults and intermediate faults has a log-normal distribution, whereas spacing of fault zones shows a normal distribution. The mean of these distributions is about the same as the thickness of the confining stratigraphic intervals. Therefore, spacing and dimensions

of joints and faults have a first-order relationship to the thickness of the confining stratigraphic sequences.

5.2. Introduction

Permeability in low-porosity, cemented sandstones is controlled by fractures. This type of reservoir is common in large gas fields like those existing at Bolivian-Argentinian sub-Andean fold and thrust belts. Prediction of fracture distribution in the subsurface is difficult because of structural complexity and imaging limitations. Outcrop data constitute an important source of information to understand the factors controlling fracture occurrence and localization. This chapter describes a methodology to perform this type of study, and discusses the data, conceptual models, and empirical relationships that can be obtained from outcrops.

5.2.1. The Role of Outcrop Data in Reservoir-Quality Prediction

An accurate prediction of reservoir quality in low-porosity rocks requires a good understanding of the anisotropy and heterogeneity introduced by faults and fractures in the subsurface. In this regard, the critical questions are: how are faults and fractures distributed within folded sedimentary rocks and what are the factors controlling their distribution? The significant answers to these questions continue to represent one of the main tasks in modeling and characterization of fractured reservoirs.

Here we present an outcrop study of the faults and fracture systems within cemented, low-porosity Devonian sandstones, in a fold and thrust belt. These sandstones constitute important gas reservoirs along the Sub-Andean thrust belt around the Tarija Basin, near the Argentinean-Bolivian border (Blangy, 2002). This area has been under an E-W regional compressive tectonic regime for about 60 m.y. (Horton *et al.*, 2001), without apparent significant changes in the orientation and the character of the regional state of stress. These outcrops, located within the transition of the Eastern Cordillera and the Sub-Andean region (Figure 5.1), provide a good opportunity to analyze the evolution of fracture systems in a compressive tectonic setting.

We use a terminology for fractures proposed by Pollard and Aydin (1988) and Aydin (2000). The term *joint* defines a structure with two surfaces that moved predominantly away from each other. A *fault* is a discontinuity in which two sides moved predominantly parallel to the discontinuity. A *fracture* encompasses the

modes of opening and/or shearing. The term usually includes both joints and small faults, and is commonly used when the exact mode cannot be unambiguously determined. A *joint zone* is the localization of two or more joints into a narrow belt. The term *fracture zone* is used to cover zones with mixed-mode discontinuities.

Our usage of the term *damage zone* follows the conceptual model illustrated by Caine *et al.* (1996). According to their model, there are two main architectural elements of a fault: the *fault core*, composed of slip surfaces and comminuted rock material (Kim *et al.*, 2004), which accommodates most of the displacement (Caine *et al.*, 1996); and the *damage zone*, a broader volume of fragmented rock and distributed deformation, which results from the initiation and propagation of slip along faults (Cowie and Scholz, 1992; McGrath and Davidson, 1995). We use *fault zone* to identify zones of deformation that accommodate significant offsets larger than 10 m (32.81 ft), across more than one single fault.

Outcrop studies supply significant qualitative and quantitative information for geologic modeling of fractured reservoirs. From the perspective of reservoir characterization, there are two basic approaches to tackling this problem: stochastic simulation of fracture networks and deterministic modeling based on mechanical principles. For either of these approaches, outcrop descriptions provide constraints to the modeling parameters since 1) they show the spatial variability of fracture density at the reservoir scale, which can be translated to the subsurface modeling using second-order parameters such as the mean, the standard deviation, and the distribution function of fracture populations; 2) they indicate the different mechanisms that generate fractures for specific rock types and deformation styles; and 3) they fill the scale gaps between core, well-log and seismic data.

This paper presents data and concepts that are relevant to folded and fractured reservoirs with similar stratigraphy and deformation style. However, some of the concepts and fracture mechanisms discussed here can be generalized to other reservoirs with similar stratigraphic architecture and different structural style.

5.2.2. Geologic Setting

The study area is located at the southern Bolivian Andes, about 30 km (18.8 miles) east of Tarija, near the boundary between the Sub-Andean Zone and the Eastern Cordillera (Figure 5.1), and is accessible from the Tarija-Villamontes road. We conducted field work at the Abra del Condor and Piedra Larga anticlines, in the hanging wall of the Piedra Larga Thrust, and near the Canaletas Thrust. The Piedra Larga and Canaletas thrusts are respectively marked 1 and 2 in Figure 5.2. The area

of interest is underlain by a major decollement in the Silurian Kirusillas Shale (Psk in Figure 2), but secondary detachment surfaces occur within other shaly units like the Devonian Icla and Los Monos Formations (Labaume *et al.*, 2001). The Eastern Cordillera and the Sub-Andean Zone both form part of a backarc thrust belt. This is an east-verging, Neogene thrust system that involves Paleozoic to Quaternary sedimentary rocks in the Sub-Andean Zone, and incorporates Precambrian basement rocks towards the east, in the Eastern Cordillera. According to Schmitz (1994) and Okaya (1997), the structural shortening observed in the sedimentary cover in the Sub-Andean Zone is linked to the tectonic thickening of the continental crust below the Altiplano and the Eastern Cordillera.

The stratigraphic interval of interest comprises a clastic, shallow marine sequence of Silurian to Devonian age. From base to top, the sequence is composed of the following units: 1) Kirusillas Shale (Psk in Figure 5.2), a thick package of black, fissile and ductile shale; 2) Tarabuco Shale (Pdt), a unit composed of alternating thick packages of medium-gray shale and thin tabular sandstones; 3) Santa Rosa Formation (Pdsr), a cemented quartzose sandstone with a shaly interval in the middle; 4) the Icla Shale (Pdic), a dark gray, fissile and fossiliferous shale, with a meter-thick tabular sandstone towards the middle; 5) the Huamampampa Formation (Pdh), a sandy unit composed of the interposition of sandstones and greenish-gray silty shale; and 6) Los Monos Shale (Pdlm), composed of greenish-gray silty shale with some intercalated sandstones towards the base, and dark-gray fissile shale towards the middle. Measured thicknesses of the Huamampampa and Santa Rosa formations in this locality are 367 m (1294.1 ft) and 297 m (974.4 ft), respectively. Thickness of the Icla Shale is estimated to be 180 m (590.6 ft). Thicknesses of the other units shown in the cross section are estimated from the geologic map and general stratigraphic columns. Figure 5.2(c) shows a composite stratigraphic section of the Huamampampa and Santa Rosa formations measured during this study.

5.2.3. Methodology

This study is based on field mapping of faults and fractures at different scales of observation, with emphasis on the variability of fracture density along the strike azimuth of folded structures. The initial work involved the measurement of stratigraphic sections that allowed an accurate revision of previous geologic maps. The detailed field work involved mapping of faults along the backlimb of the Abra del Condor Anticline (Figure 5.3), and collection of fracture-density data and fracture characteristics along scanlines at the Abra del Condor and Canaletas

outcrops. This detailed work also included the characterization of fractures and their genetic relationships in other localities, especially along the Piedra Larga Anticline. These localities are also indicated in Figure 5.2 and Figure 5.3.
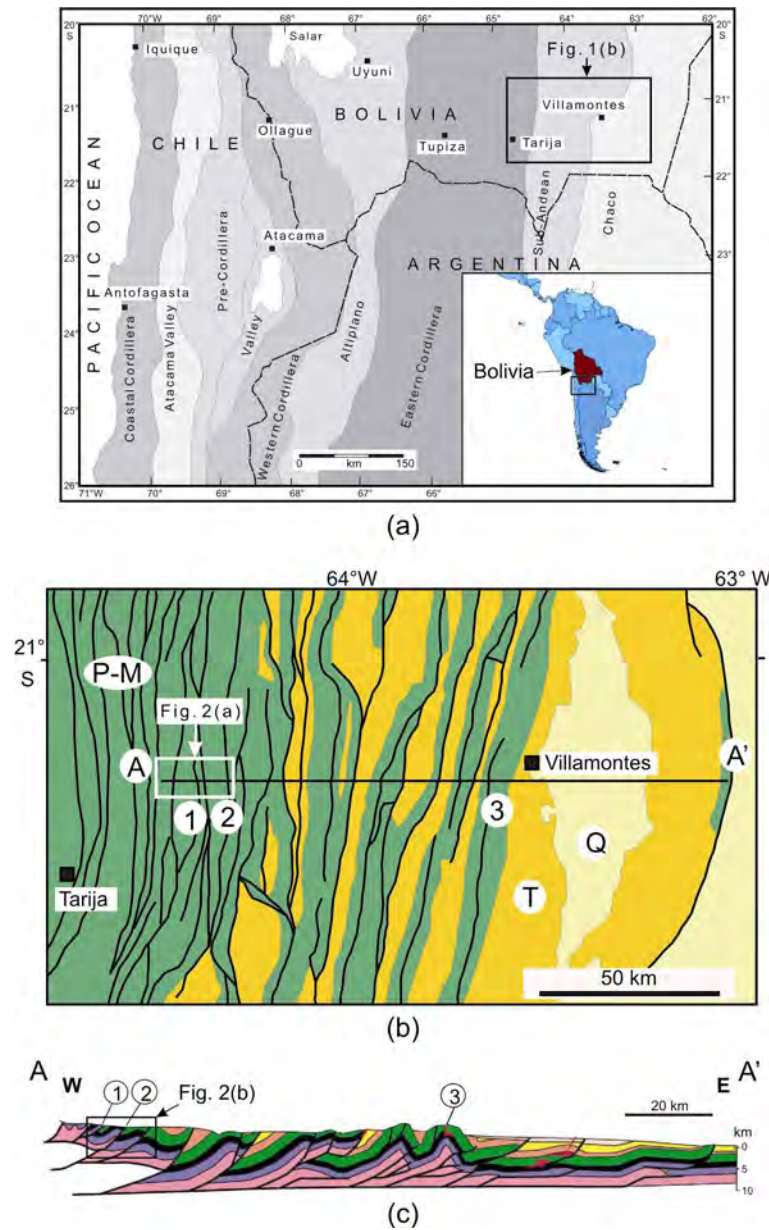
Figure 5.1: Location map and regional geologic setting: (a) major tectonic regions of the Bolivian Andes (Reutter *et al.*, 1988); (b) regional geologic map of the Sub-Andean fold and thrust belt: T stands for Tertiary, Q for Quaternary and P-M for Paleozoic to Mesozoic; (c) regional cross section: (1), (2) and (3) indicate the Piedra-Larga, Canaletas and leading thrusts, respectively. Figures 5.1 (b) and (c) after Labaume *et al.* (2001).
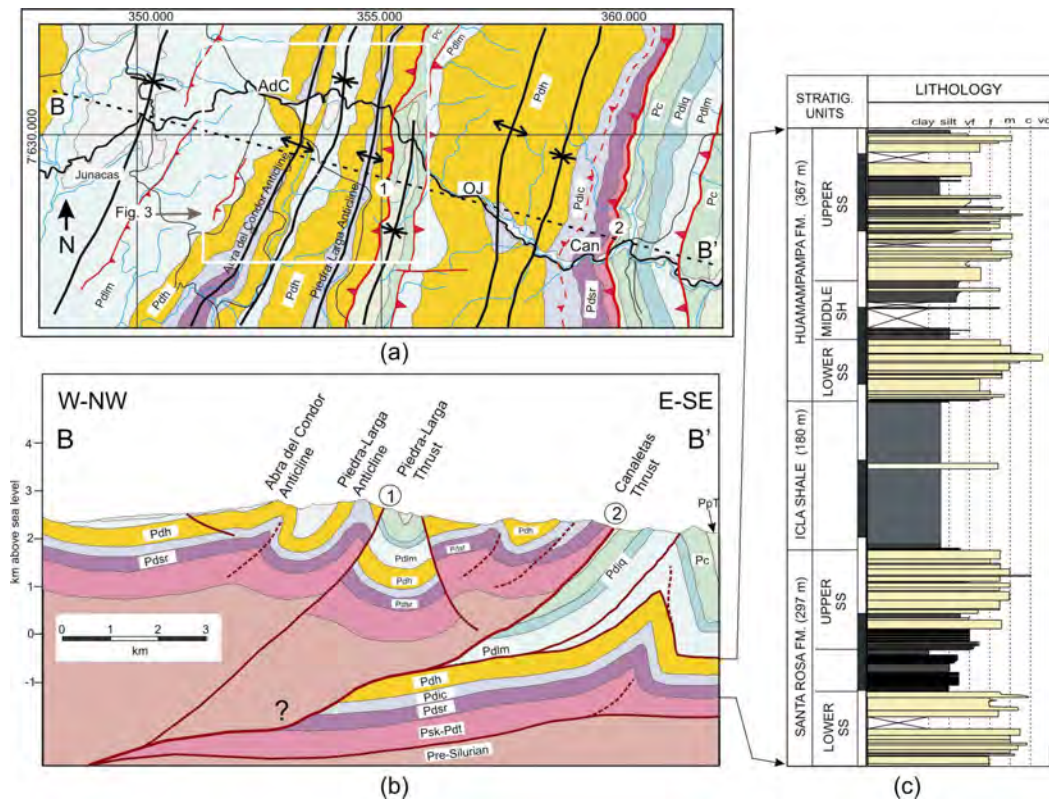
Figure 5.2: Geology of the study area: (a) geologic map of the Abra del Condor-
Canaletas fold and thrust belt, *AdC* indicates the Abra del Condor and *Can*
shows the Canaletas outcrops; (b) cross section, stratigraphy from base to top as
follows: Kirusillas-Tarabuco Shale (Psk-Pdt), Santa Rosa Fm. (Pdsr), Icla Shale
(Pdic), Huamampampa Fm. (Pdh), Los Monos Fm. (Pdlm), Iquire Fm. (Pdiq),
Carboniferous (Pc), and Permo-Triassic (PpT); (c) composite stratigraphic
section from Santa Rosa to Huamampampa formations.

Fracture data were collected along scanlines parallel to the strike azimuth of the
folded structures. A scanline is a traverse with defined orientation, along which data
are systematically documented (Priest and Hudson, 1981; LaPointe and Hudson,
1985). For this study, the data involved fracture type, orientation, offset, position,
filling material, and determination of the genetic relationships between adjacent
fractures. Other characteristics like fracture height and length were locally
documented. The data regarding spacing of joints and small faults come from a
scanline, about 400 m (1,312.33 ft) long, along the backlimb of Abra del Condor
Anticline (SL-1 in Figure 5.3). Data regarding spacing of intermediate faults come
from the same scanline and additional scanlines measured further North (SL-2 in
Figure 5.3). Spacing of fault zones is based on the field-based geologic map
elaborated at scale 1:10,000 (Figure 5.3), which has been complemented with some
photo-interpretation.
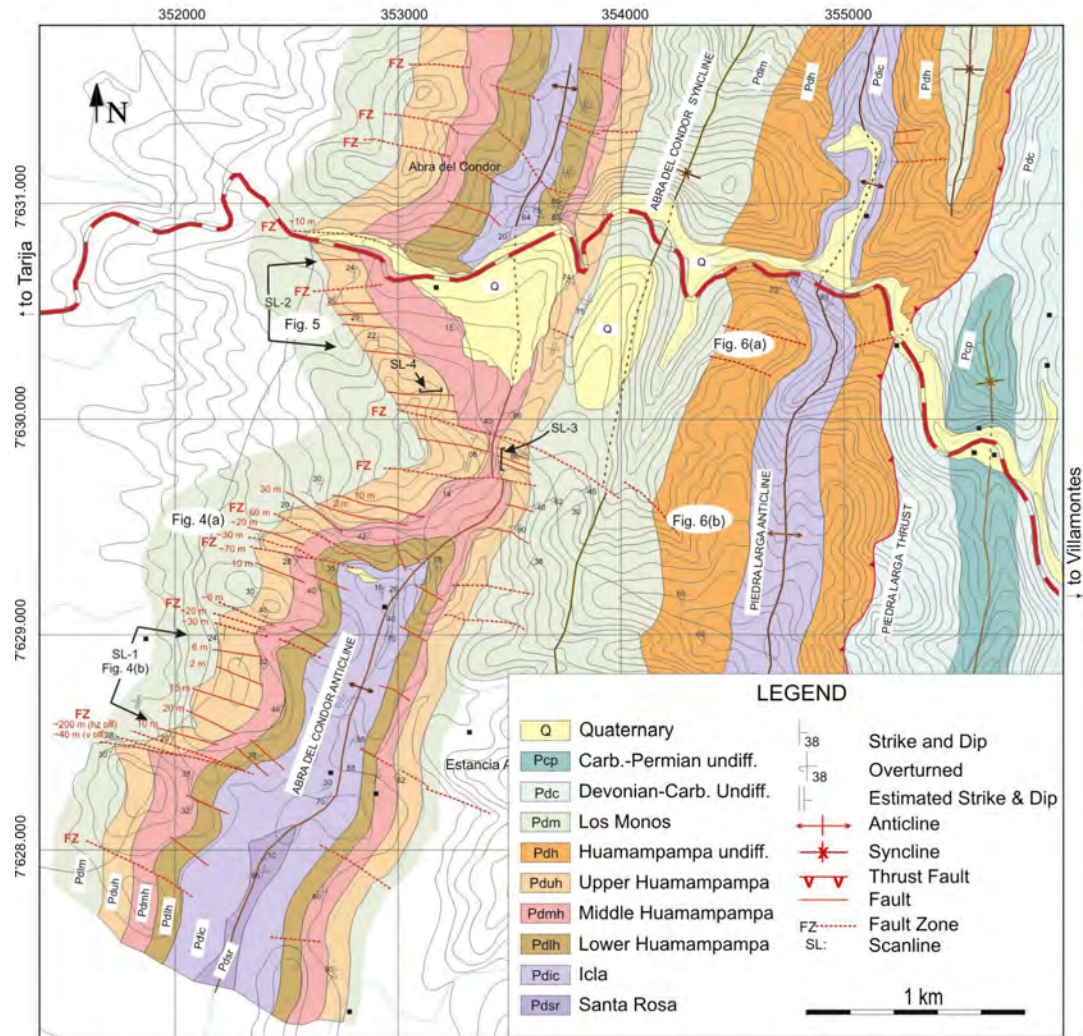
Figure 5.3: Detailed geologic map showing the distribution of fault zones and intermediate faults along the backlimb of Abra del Condor Anticline. The map also shows the locations of strike-parallel scanlines (SL-1 to SL-3), and the structural position of Figures 5.4, 5.5 and 5.6.

5.3. Faults and Fractures

Faults and fractures occur at different scales and hierarchies, with the dominant style depending on the scale of observation and lithology. Figure 5.1(b) is a geologic map at a scale of 1:2,500,000; showing that the dominant tectonic features at this scale are sub-parallel thrust faults trending perpendicular to the regional greatest compressive stress. Thrust faults and the folds associated with them are the dominant features in Figure 5.2(a), a geologic map at a scale of about 1:100,000. Their orientation determines the structural grain. In contrast, in Figure 5.3 the dominant structural discontinuities are fault zones, represented by one or more gross dashed

lines, perpendicular to the structural grain. Figure 5.3 corresponds to a geologic map at an original scale of 1:10,000; and shows the fault zones mapped along the backlimb of the Abra del Condor Anticline. Similar fault zones are also evident in other structures like the Piedra-Larga Anticline. Finally, at outcrop scales (1:1 to 1:1,000), joint patterns and small faults become the outstanding features.

(a)
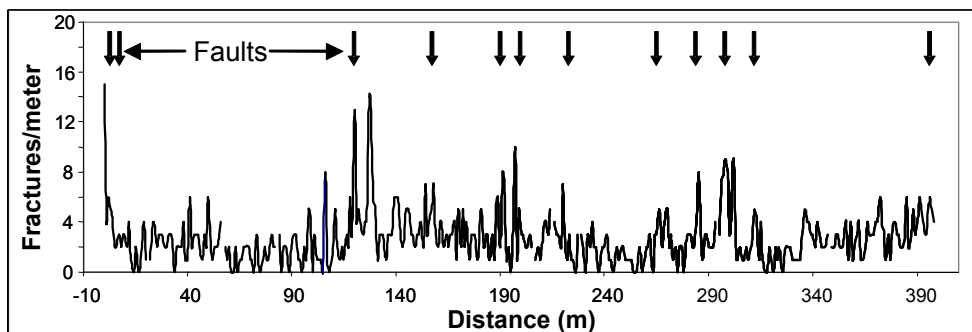
(b)

Figure 5.4: (a) Fault zones at the back limb of the Abra del Condor Anticline. Cumulative lateral offset of the fault zone at the left is about 60 m. This fault zone is composed of at least four major fault segments and many small faults. A narrower fault zone with about 20 m of vertical offset is shown towards the right. (b) Strike-parallel variability of fracture frequency (density) away from large fault zones (scanline 1 in Figure 5.3); picks correspond to areas near small and intermediate faults.

5.3.1. Fracture Types and Patterns

The predominant fracture types found in the study area are joints and sheared-joint-based faults. We have subdivided the faults into three main categories: 1) fault zones, 2) intermediate faults, and 3) small faults and/or sheared-joints. First we discuss the fault zones, and then we describe the patterns and characteristics of the other two fault categories in the "outcrop-scale faults" section. Finally, in the last section we describe the joints.

5.3.1.1 Fault Zones

Fault zones are characterized by a wide damage zone and offset of stratigraphic markers along two or more coalescing faults. As Figures 5.3 and 5.4(a) illustrate, these fault zones appear as low-relief zones along otherwise outstanding layers of competent sandstones. Each fault zone is composed of several interconnected faults with varying offset, forming a wide zone of heavily fractured rock, or a damage zone. These low-relief damage zones separate wider regions or blocks with relatively intact rock. The width of the damage zone associated with these fault zones increases with cumulative offset, which in general ranges from 10 m (32.8 ft) to about 200 m (656.2 ft). We mapped some of these fault zones along the backlimb of the Abra del Condor Anticline, where most of them are at a high angle to the anticline axis (Figure 5.3). Unfortunately, even though axial fault zones may also occur, erosion of the anticline crest and outcrop limitations prevent their study.

5.3.1.2 Outcrop-scale Faults (Intermediate to Small Faults)

Fracture spacing, and therefore fracture density, varies significantly along bedding strike azimuth within the blocks located between the fault zones. We carried out two scanline surveys, SL-1 and SL-2 in Figure 5.3, to document the variability of fracture density and the presence of small faults within these relatively intact regions. Figure 5.4(b) shows the fracture density measured along one of these scanlines. Along these blocks, the zones with higher fracture density, therefore lower fracture spacing, are associated with faults with offsets ranging from about 10 m (32.8 ft) to a few centimeters.

Shearing along pre-existing or earlier joints is one of the most common mechanisms for fault initiation and development in these low-porosity sandstones. At its initial stage, shearing can only be inferred from the presence of splay and tail joints around the sheared fracture, or from the presence of asymmetric, en-echelon, opening-mode fractures. Some of these sheared joints have slickenlines on the

fracture surfaces. An advanced state of shear can be determined directly from the offset of stratigraphic markers.
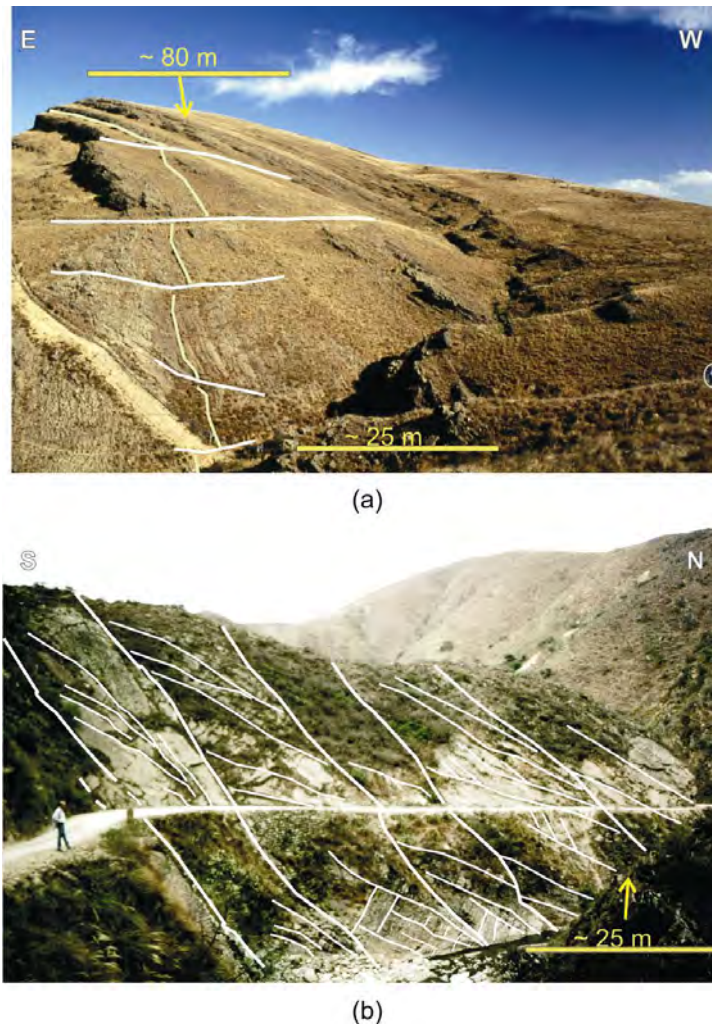
Figure 5.5: Comparison of patterns of intermediate and small faults between the Abra del Condor and Canaletas outcrops: (a) Widely-spaced, dip-parallel, intermediate faults along the backlimb of Abra del Condor Anticline. (b) Fault and fracture pattern at Canaletas outcrop showing closely spaced dip-parallel intermediate faults (larger faults), with well-developed sets of oblique small faults abutting against the larger faults. The small faults have their own set of splay joints abutting against them.

As the degree of deformation increases, the patterns of intermediate and small faults vary from orthogonal cross and axial sets, derived from the pre-existing orthogonal joint sets, to oblique asymmetric features. Orthogonal sets of sheared joints and small faults are prevalent at relatively low strain areas, like the backlimb of Abra del Condor (Figure 5.5 a), whereas oblique sets become dominant at areas with a higher degree of deformation, like the Santa Rosa outcrop near Canaletas (Figure 5.5b). This difference in fault patterns has also been observed along a single

structure. For example, along the backlimb of the Piedra-Larga Anticline, the oblique pattern is dominant near the Tarija-Villamontes road (Figure 5.6a), whereas the orthogonal pattern prevails further south (Figure 5.6b). Where the oblique patterns occur, faults with larger offset are dip-parallel (cross faults), while oblique fractures are either joints or smaller faults that abut against the larger ones, indicating a genetic relationship between the two sets.

Normal-fault shear along sub-vertical joints is another mechanism for fault development and growth. These small normal faults abut against bedding surfaces. As shown in Figure 5.7, they occur in conjugate sets without any cross-cutting relationship. Commonly, at the intersection of these conjugate sets, the smaller faults abut against the larger ones. In some cases, the larger fault is composed of connecting fault segments, and the conjugate fault starts from the tip of one of these segments. The fracture density within the area enclosed by two conjugate normal faults is commonly larger than the fracture density in the adjacent rock mass.

5.3.1.3 Joint patterns

The dominant joint patterns are either orthogonal (Figure 5.8a) or oblique joint sets (Figure 5.8). Orthogonal joint sets are normal to the bedding surfaces (Figure 5.8c), as are the oblique joints associated with strike-slip shearing. In contrast, oblique joint sets associated with conjugate normal faults, and faults with an oblique sense of shearing, are inclined with respect to the bedding surfaces (Figure 5.8d).

In low-strain domains, where the characteristics of the earliest-formed systems are preserved, the dominant fractures are two orthogonal sets, one parallel and the other perpendicular to the fold axis. Joints parallel to the strike of beds or the axes of anticlines make up the strike set, whereas joints orthogonal to this set conform to the dip-parallel set, known as the cross set in geological literature (e.g. Rawnsley *et al.*, 1992; Rives *et al.*, 1992; Bai *et al.*, 2002). Figure 5.8(a) is a map showing both strike and cross-joints in the Huamampampa sandstone at Abra del Condor. A similar orthogonal set is observed at an outcrop near the crest of the broad anticline between the Piedra-Larga and Canaletas thrusts (Figure 5.9). In Figure 5.8(a) the strike set is dominant, whereas the cross set prevails in Figure 5.9. The abutting relationships between the two sets are reciprocal, suggesting that these two joint sets are contemporaneous. Moreover, the cross-cutting relationship with splay fractures associated with faults, as shown in Figure 5.9, suggests that these orthogonal joints are the oldest fractures.
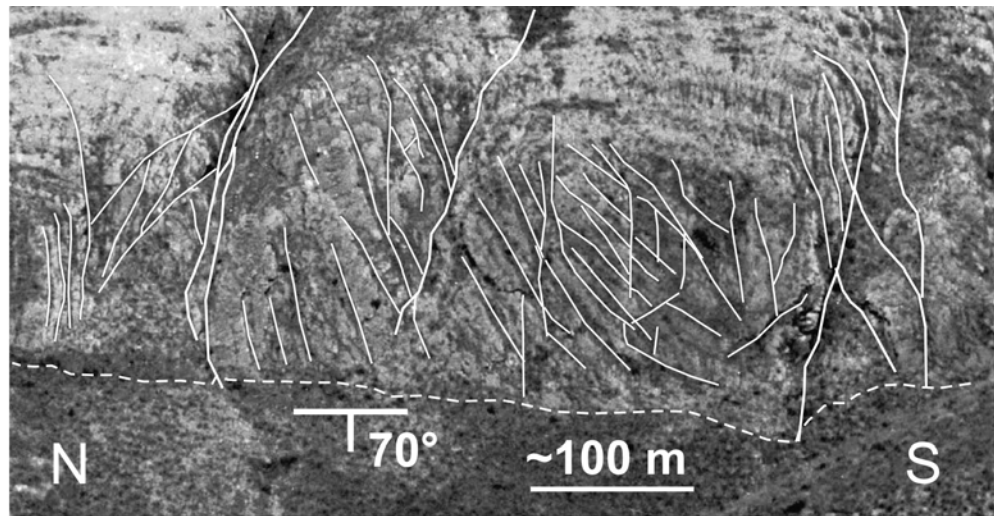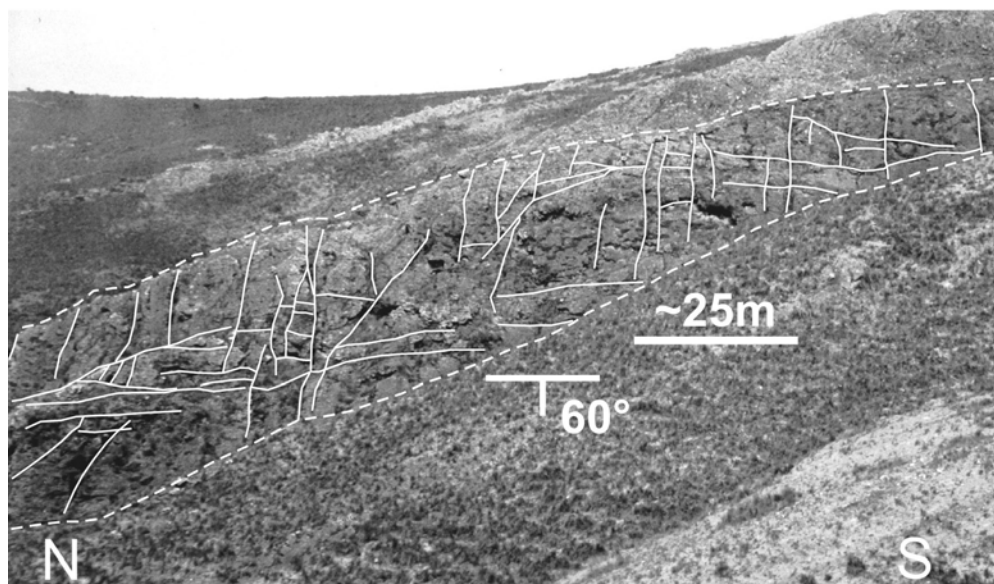
Figure 5.6: Variability of patterns of small-faults and sheared joints along the backlimb of the Piedra-Larga Anticline (see Figure 5.3 for location). (a) Oblique pattern of small faults observed near the intersection of the anticline with the Tarija-Villamontes road. (b) Orthogonal pattern of sheared joints and small faults, perpendicular and parallel to bedding azimuth, observed about 1 km south of outcrop shown in (a).

Younger generations of joints share the characteristic of being oblique to either the bedding attitude (Figure 5.8b) or the normal of the bedding surface (Figure 5.8d), or both. These oblique joint sets abut against larger fractures parallel to the pre-existing orthogonal sets with evidence of shear, such as slickenlines and offset. As explained in the previous section, these fractures are sheared joints and small faults

derived from shearing of the pre-existing orthogonal joints. The oblique fractures associated with them are splay or tail joints and fractures. The sets associated with incipient strike-slip faults are normal to the bedding surfaces, whereas splay joints associated with normal faults present an oblique angle with respect to the normal of the bedding surface (40° to 20°). Splay joints, related to faults with an oblique sense of shearing, show oblique angles to both bedding attitude and the normal of the bedding surface. All these sets can occur within the same stratigraphic interval and contain different generations of splay joints and fractures, creating a dense network of fractures with a complex pattern (Figure 5.10).
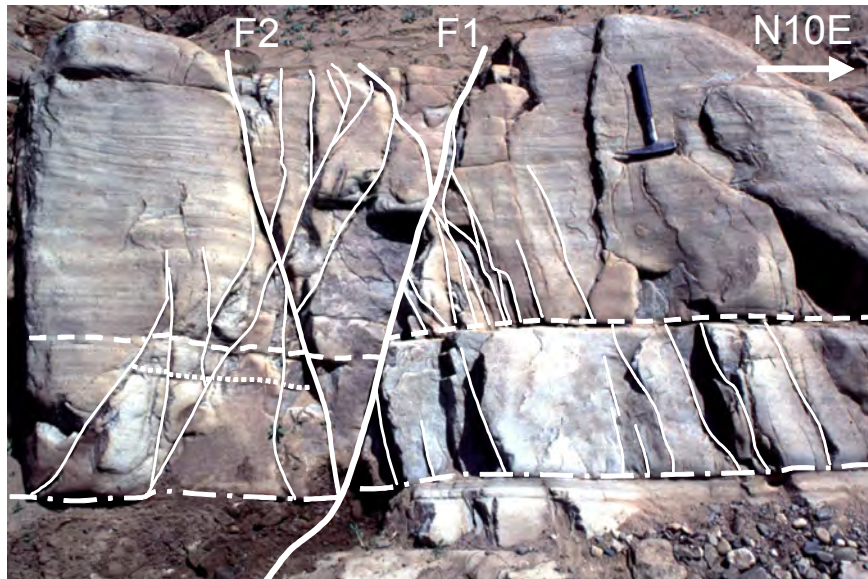
Figure 5.7: Set of small-scale conjugate normal faults observed at the Canaletas outcrop (notice the hammer for scale). The bed-confined oblique joints are considered to be splay joints derived from interlayer slip. Notice, in the center, the hierarchical relationship between small faults and their splays: oblique joints abut against the smaller fault (F2), which abuts against the longer fault (F1). This hierarchical relationship indicates the evolution of conjugate-fault patterns from hierarchical shearing and progressive deformation.
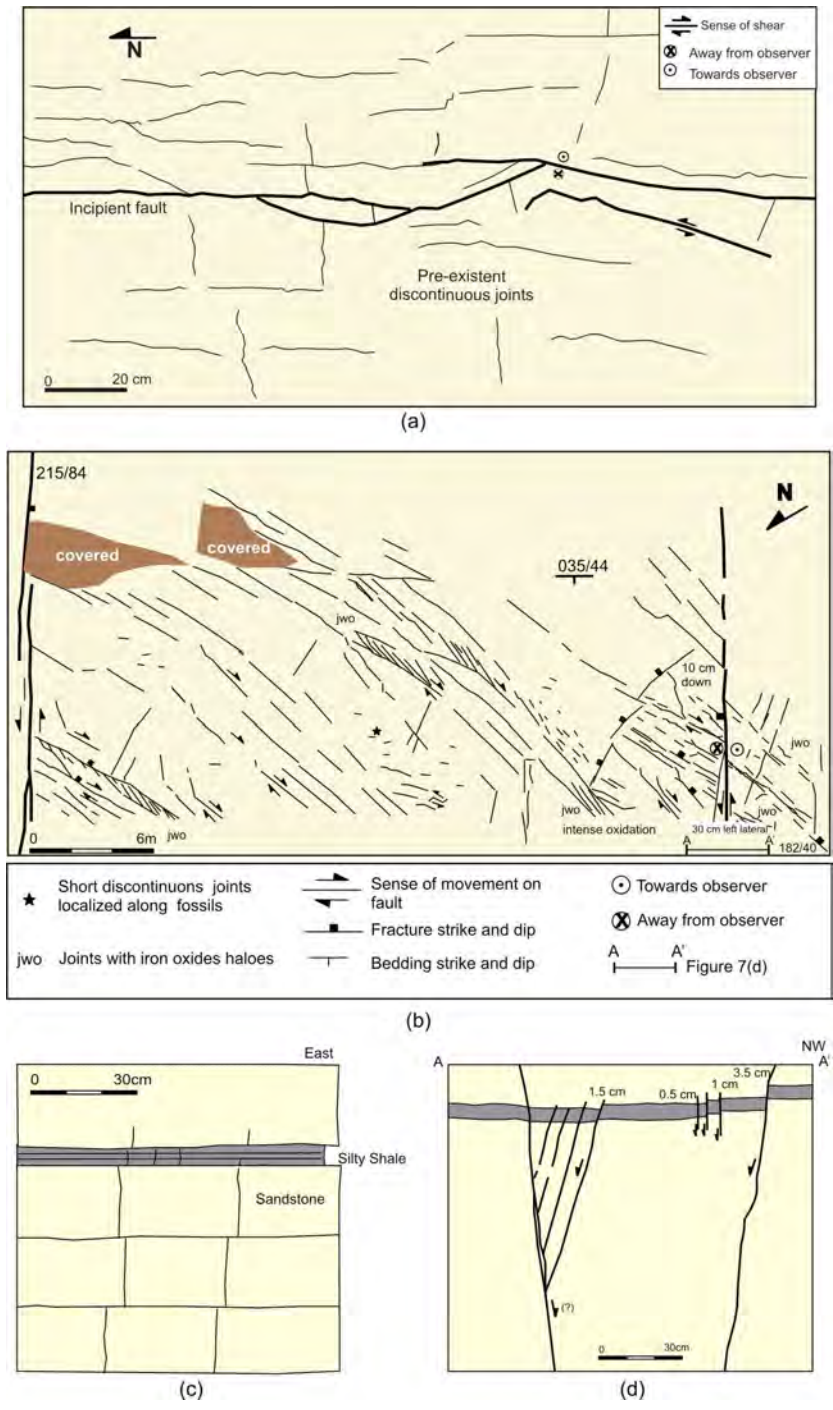
Figure 5.8: Variability of joint patterns: (a) pavement map showing the orthogonal set of joints within Huamampampa Formation at Abra del Condor; (b) pavement map from Canaletas outcrop showing oblique splay joints and fractures caused by shearing along pre-existing dip-parallel fractures; (c) cliff view of the orthogonal joint set, showing that joints abut against thin shale layers; and (d) cliff view across one of the sheared fractures (small fault) shown in (b), illustrating the development of oblique splay joints and small normal faults. Sketch by Marco Antonellini.
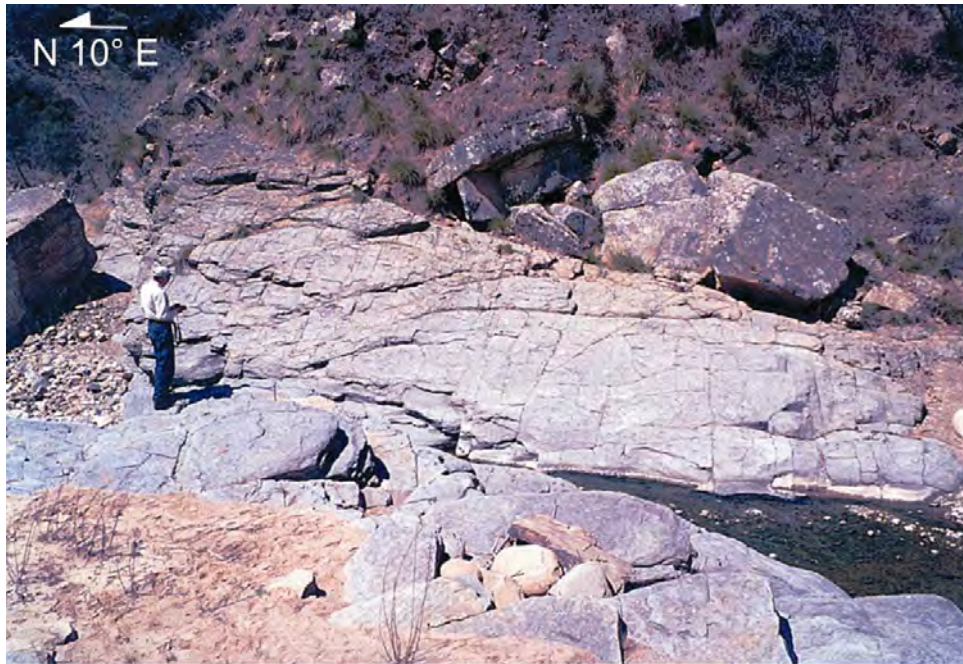
(a)
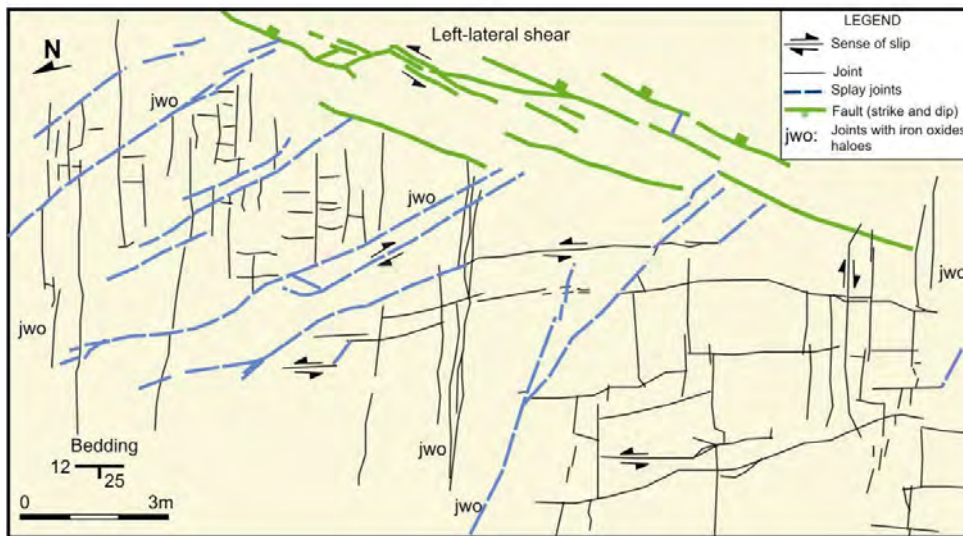
(b)

Figure 5.9: Pavement map corresponding to the outcrop located near the core of the anticline at the footwall of the Piedra-Larga thrust (OJ in Figure 5.2a). Notice the dominant set of joints perpendicular to the strike azimuth, the subordinate joint-set orthogonal to it, and the younger set of splay fractures derived from the normal fault. Sketch by Marco Antonellini.
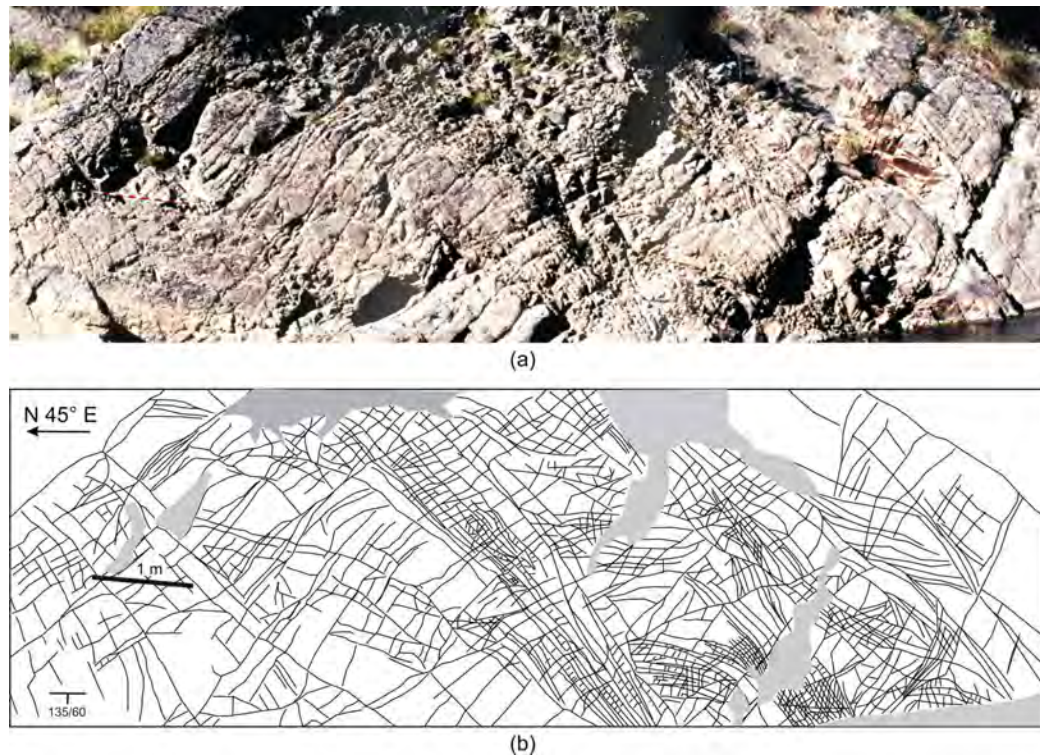
Figure 5.10: Complex fracture pattern observed on a bedding surface of Santa Rosa sandstones, at the Canaletas outcrop. Fracture density varies from a few fractures per meter to more than 50 fractures per meter. In the areas with higher fracture density, the rock is basically breccia. This outcrop is located towards the bottom of the outcrop shown in Figure 5.5(b).

5.3.2. Fracture Statistics

We performed a quantitative characterization of the variability of fracture intensity along the backlimb of the Abra del Condor Anticline. Data for joints and small faults are based on the scanline presented in Figure 5.4. Data for intermediate faults come from two strike-parallel scanlines, marked in Figure 5.3. Mapping and spacing data of fault zones are based on field observations and photo-interpretation. To quantify areas with high fracture frequency, we also performed an 80-m-long scanline along the forelimb of the Abra del Condor Anticline, near one of the cross strike-slip faults (SL-3 in Figure 5.3).

The fracture-spacing data, shown in Figure 5.11(a, b, c, and d), indicates the predominance of log-normal distribution functions for the different fracture types, and the first-order dependence between fracture spacing and stratigraphy. We found that in this area the spacings of cross-joints, small faults and intermediate faults have log-normal distribution functions, as deduced from quantile-quantile plots (e.g. Fillben, 2004) like those shown in figures 5.11(e) and 5.11(f). The distribution

function of fault-zone spacing is closer to a normal distribution. Mean spacing of these distributions has a first-order relationship with the thickness of the stratigraphic intervals that comprise them, as shown in Table 5.1.

Table 5.1: Mean spacing (S) of fracture hierarchies, compared to the thickness (T) of the confining stratigraphic intervals; the ratio T/S for intermediate and small faults increases significantly at the Canaletas outcrop, with respect to those observed at the backlimb of the Abra del Condor Anticline.

Outcrop	Fracture Hierarchy	Mean Spacing (S)	Confining Stratigraphic Interval	Measured or Estimated (~) Thickness (T)	Ratio T/S
Backlimb of Abra del Condor Anticline; Huamampampa Formation	Fault Zone	361 m 1184.4 ft	Sequence (Fm.)	367 m 1204.1 ft	1.0
	Intermediate Fault	59 m 193.6 ft	Parasequence Set	64.5 m 212.6 ft	1.1
	Small Fault	4.2 m 13.78 ft	Bedset	10 m 32.81 ft	2.4
	Joint	0.49 m 1.61 ft	Bed	~ 0.5 m ~ 1.64 ft	1.0
Canaletas; Santa Rosa Fm.	Intermediate Fault	19.3 m 63.32 ft	Parasequence Set	82.5 m 270.7 ft	4.3
	Small Fault	0.76 m 2.49 ft	Bedset	~ 9 m ~ 29.5 ft	11.8

The significant variation of fracture density within the Abra del Condor Anticline is illustrated by the fracture frequency distributions measured in two areas with different structural positions, shown in figures 5.11(g) and 5.11(h). The low-density area corresponds to a block located between two fault zones (SL-1 in Figure 5.3). The high-fracture-density zone is located near two faults, at the forelimb, near the crest of the anticline (SL-3 in Figure 5.3). The data from the low-fracture-density area shows a log-normal distribution with a mean of 3 fractures per meter, and a standard deviation of 2. The data from the high-fracture-density area has a more symmetric distribution, closer to a slightly skewed normal distribution, with mean of 29 fractures per meter, and a standard deviation of 11. As Figure 5.11(i) illustrates, the combination of the two data sets has an exponential distribution.

Mean spacing of joints and outcrop-scale faults varies significantly between outcrops at different structural positions. The statistics discussed above correspond to data from the backlimb of the Abra del Condor Anticline, located 3 km (1.89 miles) to the west of the Piedra-Larga thrust, a fault with about 1 km (0.63 miles) offset (Figure 5.2). A higher fault density is found at the Canaletas outcrop, located 1 km (0.63 miles) to the west of the Canaletas thrust, a fault with more than 10 km (6.3 miles) offset. At the Canaletas outcrop, mean spacings of small and intermediate faults are 0.76 m (2.49 ft) and 19.3 m (63.32 ft), respectively. At Abra del Condor,

mean spacings of small faults and intermediate faults are 4.2 m (13.78 ft) and 59 m (193.6 ft), respectively, three to four times larger.
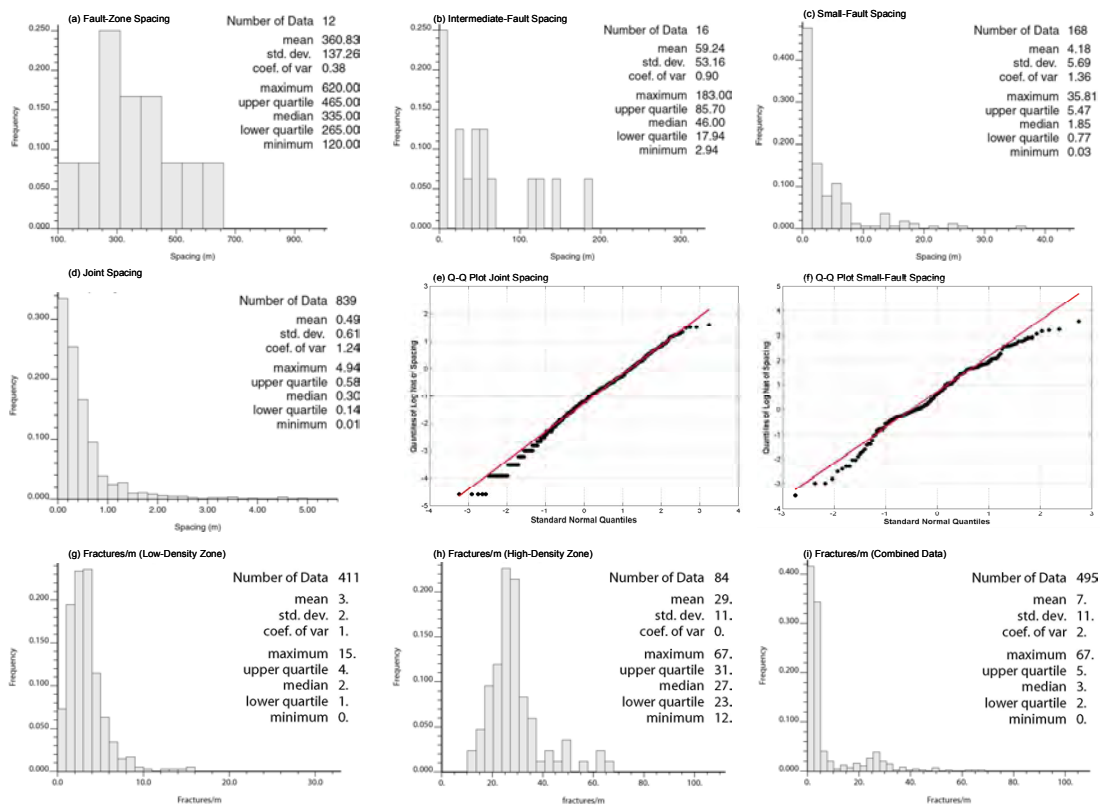
Figure 5.11: Fracture statistics. Histograms of fracture spacing corresponding to: (a) fault zones, (b) intermediate faults, (c) small faults, and (d) joints. Figures 5.11 (e) and (f) show the quantile-quantile (Q-Q) plots for spacing of joints and small faults. These plots demonstrate that joint spacing and small-fault spacing have log-normal distribution functions. Figures 5.11 (g), (h), and (i) show, respectively, the histograms of fracture density from a low-fracture-density zone (SL-1 in Figure 5.3), a high-fracture-density zone (SL-3 in Figure 5.3), and the combination of the two.

5.4. Discussion

Rigorous and accurate geologic modeling and characterization of fractured reservoirs requires field observations and statistical data to constrain the spatial heterogeneity of the model, the inferred deformation mechanisms operating at the subsurface, and key relationships between stratigraphy and fracture hierarchies that can be extrapolated to the subsurface. Essential to this is the understanding of both the evolution of fracture types and patterns, and their spatial heterogeneity. Here we compare subsurface fracture data with our surface observations, and develop a conceptual model for fracture distribution in anticlines of the Bolivian Sub-Andean

fold-and-thrust belt. In the model, we emphasize that stratigraphic architecture and shear strain have an important impact on the spacing and localization of faults and fractures.

5.4.1.   Evolution of Fracture Patterns

Our observations suggest a model of progressive deformation and fracture development due to hierarchical shearing. The first generation of fractures corresponds to the orthogonal set of axial and cross joints, symmetric to the fold axis and the regional direction of tectonic transport. Contemporaneous sets of axial and cross joints can result from local stress transitions due to joint saturation (Bai *et al.*, 2002). These joints may have formed at an early stage of folding. Local rotation of the stress field induced shear failure along some of these pre-existing joints, generating new sets of oblique splay joints and fractures. Interaction of these faults allowed them to grow, following a process similar to that described by Segall and Pollard (1983) and Martel (1990), in granitic rocks of the Sierra Nevada, USA. See also Flodin and Aydin (2004) for a development of fault patterns in sandstones at the Basin and Range province of the USA. A similar evolution mechanism has been described in limestone in the Albanian Fold and Thrust belt (B. Graham, 2004, personal communication).

As a consequence of this progressive deformation, joint and fault patterns evolve from orthogonal sets, where splay fractures are poorly developed, to oblique sets determined by the presence of well-developed splay fractures that propagate from one cross fault to the adjacent one. The progressive deformation induced by shear strain is reflected in the spatial variation of joint and small-fault patterns. Low-strain areas preserve the orthogonal set of older joints. As strain increases, the oblique-joint pattern characteristic of splay joints increases and become dominant. A similar variation is observed in small faults. In areas with moderate shear strain, most of the small faults are derived from shearing along the orthogonal joints, and consequently preserve the orthogonal orientation (b). In areas where a higher degree of shear strain is evident, shearing of oblique joints increases, and oblique small faults become one of the dominant sets (Figures 5.5b and 5.6a). Therefore, changes in joint and small-fault patterns can be used as indicators of the degree of shear strain.
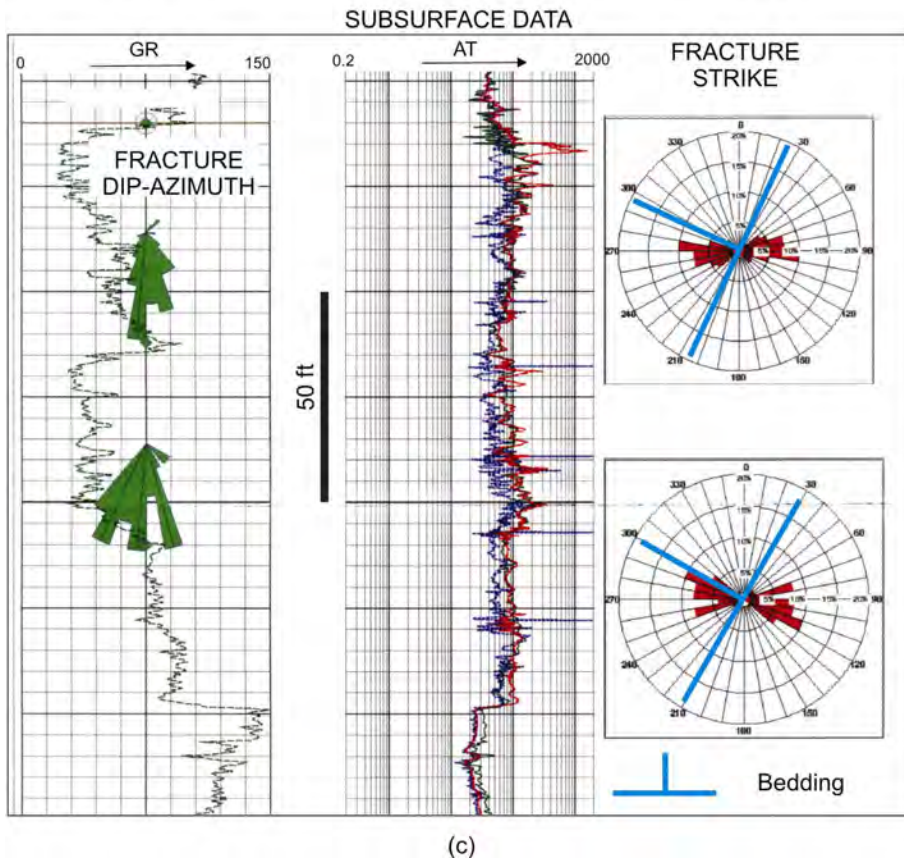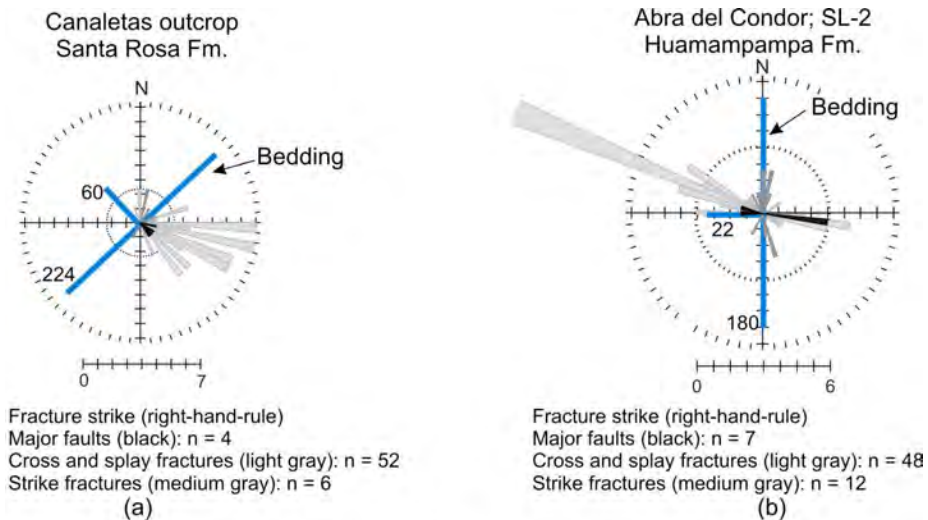
Figure 5.12: Fracture orientation at the Canaletas (a) and the Abra del Condor (b) outcrops, compared to that observed in the subsurface (c). In both Canaletas and Abra del Condor there are abundant oblique splay joints and fractures oriented at less than 45° with respect to the dip-azimuth. These oblique fractures are the result of shearing along pre-existing dip-parallel fracture sets. Left-lateral shearing is dominant in Canaletas whereas right-lateral shearing is dominant at Abra del Condor. In the subsurface, the fracture orientation with respect to bedding resembles that observed at outcrops. Consequently, for the subsurface data we infer left-lateral shearing along the dip-parallel fractures, similar to the case observed at Canaletas.

Splay joints abutting against bedding surfaces

Splay-confining bedding surfaces

(a)

Cross joints as preferential fluid pathways

(b)
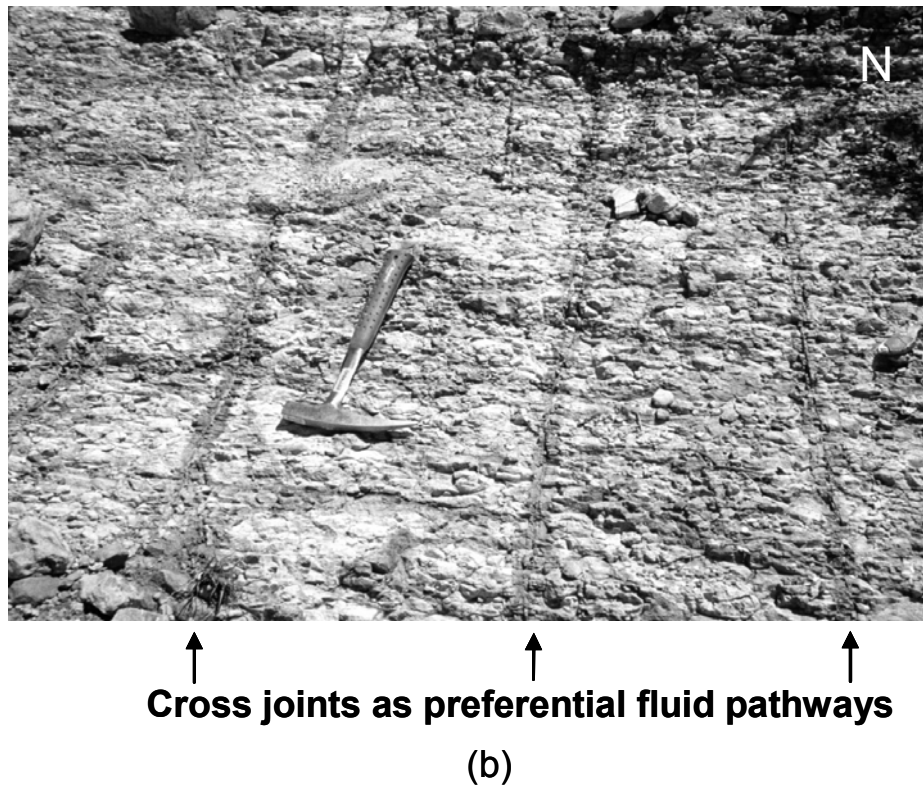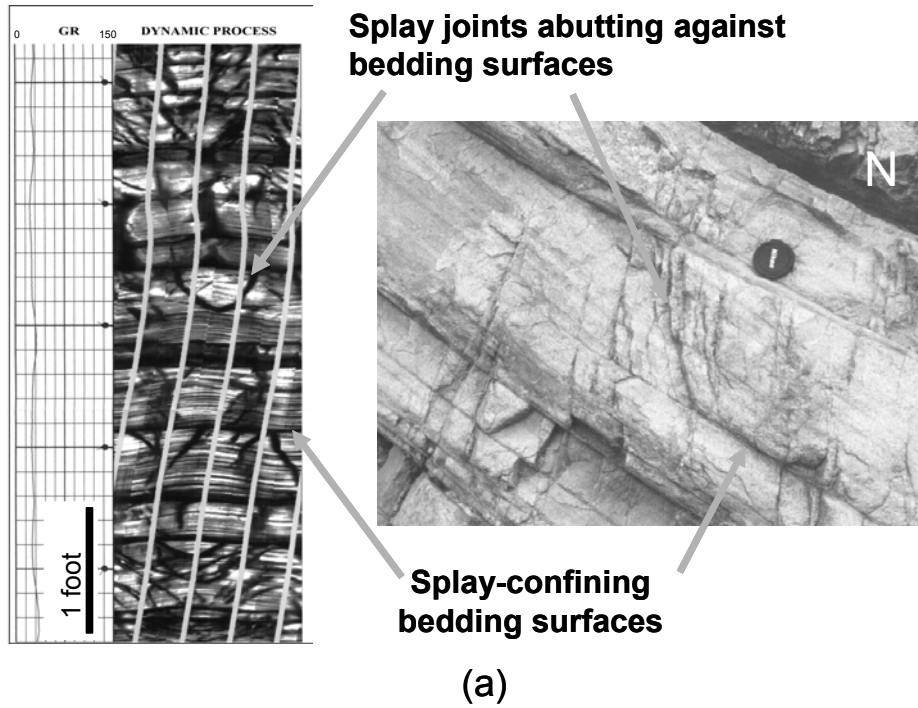
Figure 5.13: (a) Comparison of subsurface image and outcrops, both showing abutting relationships between joints and bedding surfaces, indicating that they correspond to splay joints associated with interlayer slip. (b) Oxidation halos along cross joints within low-permeability siltstones of Huamampampa Formation, illustrating how joints and fractures act as fluid pathways.

5.4.2.   Comparison to Subsurface

There are many similarities between the fracture systems observed at outcrops and those found in the subsurface. We used resistivity wellbore-image logs to compare our outcrop data with subsurface information. Fracture orientations found in the subsurface resemble those observed at outcrops (Figure 5.12). We interpret the abundance of oblique fractures, with respect to either dip-azimuth or strike-azimuth, as the result of the development of splay fractures from cross and axial faults. The dominant orientation depends on the sense of shear. For example, in this case the subsurface data show fracture orientations consistent with left-lateral shear along cross faults. On the other hand, there is evidence that fracture types and mechanisms are also similar. The wellbore images show open fractures initiating at bedding surfaces, similar to the splay joints found at outcrops (Figure 5.13a). The outcrop observations also indicate the presence of iron oxides along splay joints and cross joints that served as conduits for paleo-fluid flow (Figure 5.13b).

5.4.3.   Conceptual Model

Figure 5.14 (a) presents a conceptual model of faults and fractures in an anticline, as part of a fold-and-thrust belt, which summarizes the observations made along the Abra del Condor-Canaletas thrust belt. The model shows the hierarchical relationships that exist between fault zones, intermediate faults, and smaller features (sheared joints, joints and splay joints). The conceptual model also illustrates the relationship between the scale of stratigraphic intervals and structural discontinuities, illustrated more explicitly in Figure 5.14(b). Fault zones extend across the whole Huamampampa Formation, whereas intermediate faults stop at the thick, middle Huamampampa shale. Similarly, sheared joints can extend throughout some bedding surfaces but may stop at meter-thick shale layers. Finally, joints are confined within single mechanical layers, and splay joints related to flexural slip always abut against the sheared bedding planes.

These conceptual models show that the predominant faults and fractures are either parallel or normal to the structural grain, with respect to fold axes. In the case under study, this symmetry between fracture orientation and fold geometry reflects a uniform and stable regional state of stress, probably related to the continuous E-W compression operating since Late Cretaceous (Horton, 2001). Such a symmetric relationship is not always the case (i.e. Nelson *et al.*, 2000). In fact, as progressive deformation and rotation caused by shear strain evolves, splay fractures may extend

and form oblique patterns like those observed near the Tarija-Villamontes road at the Piedra-Larga Anticline (Figure 5.6a), or at the Santa Rosa outcrop near Canaletas (Figure 5.5b). In any case, oblique patterns with respect to the fold axis are the result of local or regional rotations of either the stress field or the deforming rocks (e.g. Fischer and Wilkerson, 2000).

Two different mechanisms can explain the variation in the sense of shear along cross faults shown in Figure 5.14(a). The first mechanism is the generation and subsequent shearing of splay fractures at angles smaller than 40° with respect to the parent fault. This mechanism implies a rotation of the cross joints with respect to the local or remote stress field (or a rotation of the stress field). Shearing along the cross joints generates a cross fault with oblique splays. If the direction of the local maximum compressive stress bisects the angle between the parent cross fault and the splays, then the sheared splays will have sense of shear opposite that of the parent fault, as illustrated in the left side of Figure 5.14(a). According to Davatzes and Aydin (2003), the angle between the parent fault and the splay fracture depends on both the loading mode and the mechanical properties at the fault tip. This mechanism has been also documented by Flodin and Aydin (2004).

The second mechanism relates the sense of shear to the relative displacement between adjacent blocks. Significant variations in the displacement direction of adjacent blocks might be introduced by abrupt changes in the displacement gradient in underlying faults, or may originate from local bedding-parallel slip patches created within underlying ductile lithologies, like the one suggested by the *P* in Figure 14 (a). This is in essence similar to the inchworm motion process postulated by Couples *et al.* (1998). Joint localization associated with interlayer slip has been previously documented and modeled by Cooke and Pollard (1997), Dholakia *et al.* (1998), and Cooke *et al.* (2000). Similar processes have been also analyzed by Shamir and Eyal (1995), Tindall and Davis (1999), and Roznovsky and Aydin (2001). The configuration resulting from this mechanism is outlined on the right side of Figure 5.14(a). Our observations suggest that both mechanisms operate in the Abra del Condor area.
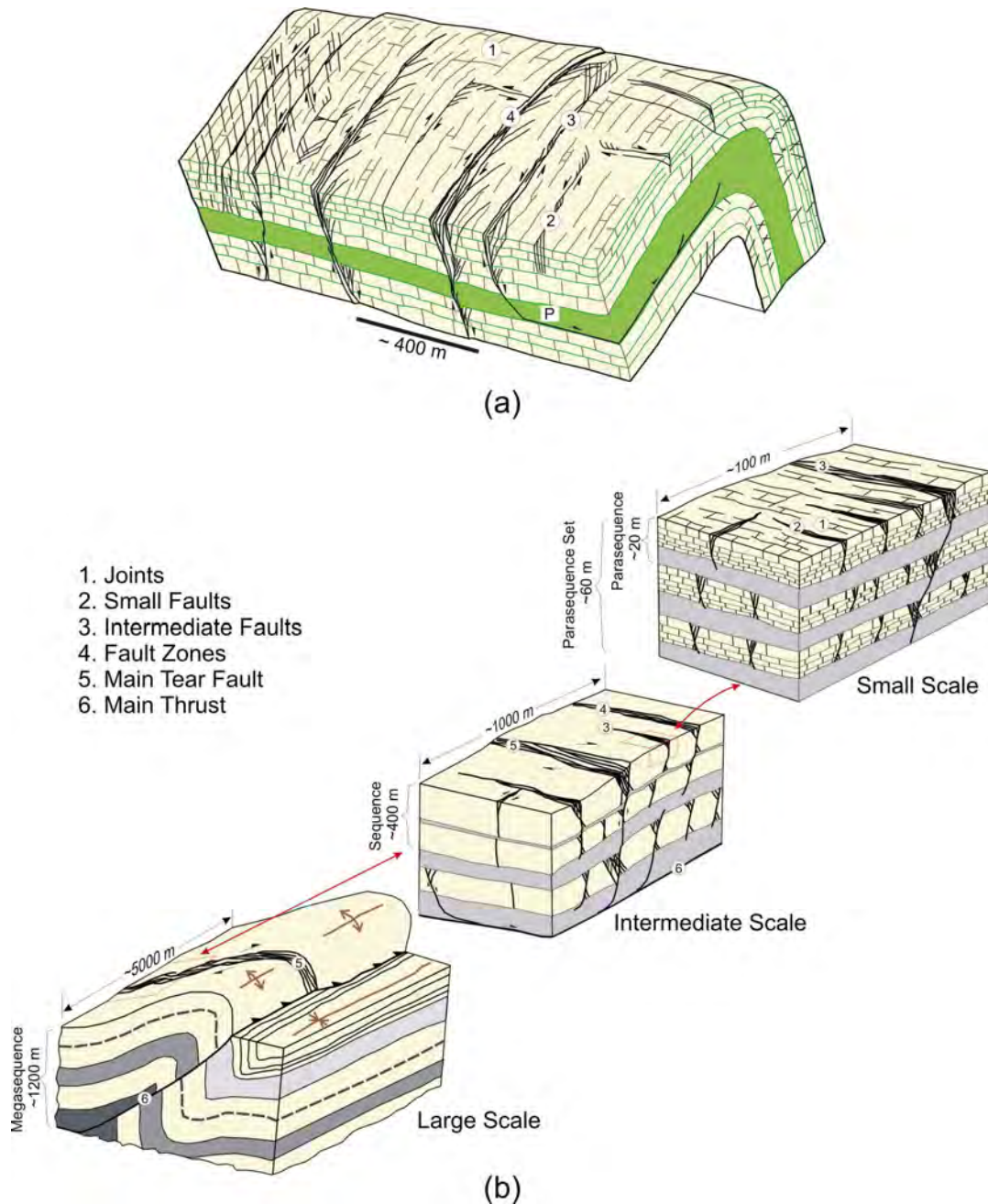
Figure 5.14: (a) Conceptual model of fracture distribution along one Anticline, showing the different fractures hierarchies: (1) joints, (2) small faults, (3) intermediate faults, and (4) fault zones; and the two different mechanisms for variation in the sense of shear of sub-parallel cross faults. (b) Relationship between stratigraphic architecture and fracture hierarchies: the dimensions and spatial frequency of each fracture hierarchy are controlled by the thickness of the respectively confining stratigraphic hierarchy (megasequence, sequence, parasequence set, parasequence, bedset, and bed); whereas joints (1) and small faults (2) are confined to beds and bedsets, the main thrust (6) and main tear faults (5) involve larger stratigraphic intervals.

5.4.4.   Fracture Hierarchies and Sequence Stratigraphy

There is a correspondence between the mean spacing of the different fracture hierarchies (from joints to fault zones) and the stratigraphic unit that contains them: Mean joint spacing maintains a first order relationship with respect to bed thickness, while mean spacing of small faults is of the same order of magnitude as the thickness of sandstone bedsets. Similar relationships exist between intermediate faults and parasequences (*sensu* Van Wagoner *et al.*, 1990), and fault zones and sequences (Figure 5.14b). Since there are other factors, such as the magnitude of the normal strain (Wu and Pollard, 1995; Gross and Engelder, 1999; Bai and Pollard, 2000) or the shear strain, that also influence fault and joint spacing, this correspondence should be expressed as follows:

$$S = \alpha T ,$$ (Eq. 5.1)

where α is a factor related to extensional or shear strain, T is the thickness of the relevant stratigraphic package and S is the mean spacing of either the joints or the confined faults. For the case of joints, a linear relationship between spacing and thickness is well known in the geologic literature (Lachenbruch, 1961; Hobbs, 1967; Narr, 1990; Narr and Suppe, 1991; Gross *et al.*, 1995; Bai and Pollard, 2000).

The thickness of shale units seems to play an important role in the hierarchical correspondences between fracture hierarchies and stratigraphic sequences. For faults with a specific range of maximum offset, the confining stratigraphic interval is bounded by the shale layers that those faults cannot break. The thicker the shale, the larger the fault offset necessary to connect faults across the shale interval. In addition to this, if a relationship exists between fault height and fault length, then the thickness of the confining stratigraphic interval also constrains the length of the confined faults.

Log-normal distributions of joint spacing, similar to those documented in this study, have been previously documented by Narr and Suppe (1991) and Rives *et al.* (1992). Narr and Suppe (1991) also found a relationship between the median of joint spacing and the thickness of mechanical layers. Rives *et al.* (1992) showed that the distribution function of joint spacing may evolve from exponential to log-normal and normal, as extensional strain increases and the joint system is well-developed. A similar transition from log-normal to normal distribution functions can be inferred from the comparison between the histograms of fracture frequency from a low-density area (Figure 5.11g), and from a high-density area (Figure 5.11h). Using the quantile-quantile plot method, we found that the former has a clear logn-ormal

distribution function, whereas the latyer is more symmetric, closer to a normal distribution function.

5.4.5.   Factors Controlling Fracture Density

Shear strain and stratigraphic architecture are among the most important factors controlling the distribution of fracture density in our study area. Other well-known factors are rock properties, stretch and loading mode (e.g. Huang and Angelier, 1989; Narr and Suppe, 1991; Gross *et al.*, 1995; Wu and Pollard, 1995; Gross and Engelder, 1999; Bai and Pollard, 2000). To illustrate the influence of shear strain on fracture density, we took the fracture frequency shown in Figure 5.4(b), and calculated the average fracture frequency for intervals of 50 m (164 ft). Shear strain was obtained by adding the offset of all the faults within each interval and dividing by 50. To avoid the effect of the adjacent fault zones, we excluded the initial and final 50-m intervals. The results show the increment of fracture frequency as shear strain increases (Figure 5.15). Moreover, the role of shear strain becomes evident from the comparison of fault and fracture density between the Abra del Condor and Canaletas outcrops. Mean spacing of small and intermediate faults is three times smaller in the high-strain area (the Canaletas outcrop) than in the low-strain zone (the backlimb of the Abra del Condor Anticline).
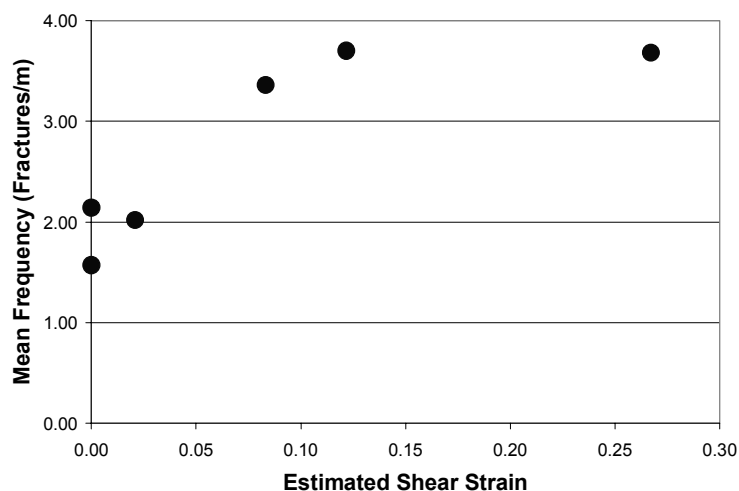
Figure 5.15: Relationship between mean fracture frequency (fractures/m) and shear strain, as calculated for intervals of 50 m along the scanline shown in Figure 5.4(b). The extremes of the scanline are not taken into account because of the influence of the adjacent fault zones.

The effect of stratigraphic architecture on fracture density is likely to be similar to that of bed thickness on joint spacing, explained by Wu and Pollard (1995), and Bai and Pollard (2000). The importance of stratigraphy has previously been discussed by other authors (e.g. Lorenz *et al.*, 1997; Fischer and Jackson, 1999). Narr (1990) defined the fracture spacing index *(I)* as the ratio of layer thickness *(T)* to average fracture spacing *(S)*. Bai and Pollard (2000) proposed that there is a threshold value of the fracture index *(I≤1)*, above which the stress field between the joints becomes compressive, inhibiting additional joint infilling. They called this stage fracture saturation. Our results suggest a similar relationship between each fracture hierarchy and its confining stratigraphic interval. However, a better understanding of this relationship requires additional experimental and theoretical studies.

For the specific case of joint density, we propose a method to upscale the fracture spacing index *(I)* to account for the hierarchical character of sedimentary sequences. Simple geometric analysis shows that, although the thickness of individual beds control the spacing of joints within each bed, the density of joints in bedsets and parasequences depends on the thickness ratio *(R)* between these stratigraphic intervals and the individual beds that compose them. For bedsets with similar thickness, joint density will increase proportionally to the thickness ratio *(R)*. Another important factor to take into account is the proportion of brittle to ductile lithologies within the stratigraphic package. In fractured reservoirs, this ratio is commonly proportional to the net-to-gross ratio *(N)*. Therefore, it follows that the joint density of bedsets and parasequences *(I_b)* can be obtained from the expression

$$I_b = RN\frac{T}{S}.$$ (Eq. 5.2).

This equation means that for bedsets with similar thickness and lithology, but different thickness of individual layers, joint density will be higher in the bedset with thinner layers. It also indicates that the joint density of stratigraphic packages decreases linearly with the proportion of shale intervals.

The purpose of Equation 5.2 is to upscale the fracture index *(I)* defined by Narr (1990), and should be used with caution. In this expression we assume that the rocks have been fractured under similar strain conditions. It is important to point out that decreasing the thickness of the brittle layers may decrease the extensional strain under similar geologic conditions. For example, for the case of bending an unfractured layer of thickness *(T)*, the maximum tensional stress *(σ)* within the

bending layer depends on the radius of curvature *(ρ)* and the Young's modulus *(E)*. Following Fung (1994), we can express the greatest tensional stress associated with bending as follows:

$$\sigma = E\frac{T}{2\rho} \,.$$

(Eq. 5.3).

From this equation we can see that the maximum tensional stress within the bending layer decreases linearly with the layer thickness. It may decrease to a point below the threshold for fracturing, which in practical terms means that the rock mass would have a ductile behavior. Therefore, Equation 5.2 cannot be generalized for any bed thickness. It should be used only to upscale the fracture spacing index of joints within individual layers, to larger rock volumes involving thicker stratigraphic intervals.

5.5. Conclusions

In summary, this study shows that faults and fractures occur at different scales and hierarchies, the dominant fault and fracture style depending on the scale of observation and lithology. In the case of the Sub-Andean fold-and-thrust belt in Bolivia, we have shown that fault zones and small faults perpendicular to the structural grain are among the features most relevant to fluid and gas flow at the reservoir scale.

The orientation and patterns of fractures observed in the subsurface are similar to those found at outcrops. Our comparison of subsurface and outcrop data shows the relevance of outcrop studies for geologic modeling and characterization of fractured reservoirs.

The deformation mechanism within the sandstone units is that of hierarchical shearing of joints, generation and growth of splay joints, and shearing of the splay joints. This process repeats itself several times, giving rise to multiple generations of joints and sheared joints. As the process evolves, the patterns of joints change from symmetric to asymmetric, or oblique. The symmetric pattern presents two orthogonal sets of systematic joints; one set parallel (N-S) and the other normal (E-W) to the strike of bedding. The asymmetric pattern is distinguished by joints that are oblique in respect to bedding attitude. Outcrop-scale faults present a similar variation in patterns, as the effect of progressive deformation associated with shear strain increases.

Our results document a significant variability of fracture density along the azimuth of folded structures. This variability is interpreted to be caused by the variation in shear strain accommodated by fault zones, intermediate faults, and small faults. Fault-zone spacing has a distribution function close to normal, with the mean comparable to the thickness of the stratigraphic sequence that contains them. The spacings of intermediate faults, small faults and joints have log-normal distribution functions. The mean of these distributions have a first-order relationship with the thickness of the confining stratigraphic sequences.

We conclude that stratigraphic architecture, hence sequence stratigraphy, and shear strain are two of the most important factors controlling the density and localization of faults and fractures within a fold and thrust belt, especially along the strike azimuth of folded structures.

5.6.   Acknowledgements

5.7.   References

Aydin, A., 2000, Fractures, faults, and hydrocarbon entrapment, migration and flow: Marine Petroleum Geology, **17**, 797-814.

Bai, T. and D. Pollard, 2000, Fracture spacing in layered rocks; a new explanation based on the stress transition: Journal of Structural Geology, **22**, 43-57.

Bai, T., L. Maerten, M. Gross, A. Aydin, 2002, Orthogonal cross joints: do they imply a regional stress rotation: Journal of Structural Geology, **24**, 77-88.

Blangy, J. P., 2002, Target-oriented, wide-patch, 3-D seismic yields trap definition and exploration success in the sub-Andean thrust belt Devonian gas play, Tarija Basin, Argentina: The Leading Edge, **21**, 142-151.

Caine, J. S., J. P. Evans, and C. B., Foster, 1996, Fault zone architecture and permeability structure: Geology, **24**, 1125-1128.

Cooke, M. L., and D. D. Pollard, 1997, Bedding-plane slip in initial stages of fault-related folding, in Anastasio, D., E. A. Erslev, D. Fisher, M Donald, and J. P. Evans, fault-related folding: Journal of Structural Geology, special issue, **19**, 567-581.

Cooke, M. L., P. N. Mollema, D. D. Pollard, and A. Aydin, 2000, Interlayer slip and joint localization in the East Kaibab Monocline, Utah; field evidence and results from numerical modeling, in Cosgrove, John W, and M. S. Ameen, eds., Forced folds and fractures: Geological Society Special Publications, **169**, 23-49.

Couples, G. D., H. Lewis, and P. W. G. Tanner, 1998, Strain partitioning during flexural-slip folding, *in* Coward, M. P., T. S. Daltaban, and H. Johnson, eds., Structural Geology in Reservoir Characterization: Geological Society Special Publication, **127**, 149-165.

Cowie, P. A., and C. H. Scholz, 1992, Physical explanation for the displacement-length relationships of faults, using a post-yield fracture mechanics model: Journal of Structural Geology, **14**, 1133-1148.

Davatzes, N. and A. Aydin, 2003, The formation of conjugate normal fault systems in folded sandstone by sequential jointing and shearing, Waterpocket monocline, Utah: Journal of Geophysical Research, B10, **108**, 2478, doi: 10.1029/2002JB002289.

Dholakia, S. K., A. Aydin, D. D. Pollard, and M. D. Zoback, 1998, Fault-controlled hydrocarbon pathways in the Monterey Formation, California: American Association of Petroleum Geologists Bulletin, **82**, 1551-1574.

Fillben, J. 2004, Exploratory Data Analysis, in: Croarkin, C. and P. Tobias, eds., *NIST/SEMATECH e-Handbook of Statistical Methods*, Chapter 1, electronic publication accessible at http://www.itl.nist.gov/div898/handbook/eda/section3/qqplot.htm.

Fischer, M. P., and S. Wilkerson, 2000, Predicting the orientation of joints from fold shape; results of pseudo-three-dimensional modeling and curvature analysis: Geology, **28**, 15-18.

Fischer, M. P., and P. Jackson, 1999, Stratigraphic controls on deformation patterns in fault-related folds: a detachment fold example from the Sierra Madre Oriental, northeast Mexico: Journal of Structural Geology, **21**, 613-633.

Flodin, E., and A. Aydin, 2004, Evolution of a strike-slip fault network, Valley of Fire, southern Nevada: Geological Association of America Bulletin, January/February, **116**, 42-59.

Fung, Y. C., 1994, A First Course in Continuum Mechanics, New Jersey: Prentice Hall, Englewood Cliffs, USA, 311 pp.

Gross, M. R., M. P. Fischer, T. Engelder, and R. J. Green field, 1995, Factors controlling joint spacing in interbedded sedimentary rocks: interpreting numerical models with field observations from the Monterrey Formation, USA, *in* M. S. Ameen, ed., Fractography: Fracture Topography as a Tool in Fracture Mechanics and Stress Analysis: Geological Society Special Publication, **92**, 215-233.

Gross, M. R., and T. Engelder, 1999, Strain accommodated by brittle failure in adjacent units of the Monterrey Formation, USA: scale effects and evidence for uniform displacement boundary conditions: Journal of Structural Geology, **17**, 1303-1318.

Hobbs, D. W., 1967, The formation of tension joints in sedimentary rocks, and explanation: Geological Magazine, **104**, 550-556.

Horton, B. K., B. A., Hampton and G. L. Waanders, 2001, Paleogene synorogenic sedimentation in the Altiplano plate and implications for initial mountain building in the central Andes: Geological Society of America Bulletin, **113**, 1387-1400.

Huang, Q. and J. Angelier, 1989, Fracture spacing and its relation to bed thickness, Geological Magazine, **126**, 355-362.

Kim, Y. S., D. C. P. Peacock, and D. J. Sanderson, 2004, Fault damage zones: Journal of Structural Geology, **26**, 503-517.

Lachenbruch, A. H., 1961, Depth and spacing of tension cracks: Journal of Geophysical Research, **66**, 4273-4292.

Labaume, P., S. Sheppard, and I. Moretti, 2001, Fluid flow in cataclastic thrust fault zones in sandstones, Sub-Andean Zone, southern Bolivia: Tectonophysics, **340**, 141-172.

LaPointe, P. R., and J. A. Hudson, 1985, Characterization and interpretation of rock mass joint patterns: Geological Society of America Special Paper, **199**, 37 p.

Lorenz, J. C., H. Farrel, C. Hanks, W. Rizer, and M. D. Sonnenfeld, 1997, Characteristics of natural fractures in carbonate strata, in Palaz, I., and Marfurt, K. J., eds., Carbonate Seismology, Geophysical Development Series, **6**, 179-201.

McGrath, A. G., and I. Davidson, 1995, Damage zone geometry around fault tips, Journal of Structural Geology, **17**, 1011-1024.

Martel, S. J., 1990, Formation of compound strike-slip fault zones, Mount Abbot quadrangle, California: Journal of Structural Geology, **12**, 869-882.

Narr, W., 1990, Fracture density in the deep subsurface; techniques with application to Point Arguello oil field: American Association of Petroleum Geologists Bulletin, **75**, 1300-1323.

Narr, W. and J. Suppe, 1991, Joint spacing in sedimentary rocks: Journal of Structural Geology, **13**, 1037-1048.

Nelson, R. A., E. P. Moldovanyi, C. C. Matcek, I. Azpiritxaga and E. Bueno, 2000, Production characteristics of the fractured reservoirs of the La Paz field, Maracaibo basin, Venezuela: American Association of Petroleum Geologists, **84**, 1791-1809.

Okaya, N., S. Tawackoli and P. Glese, 1997, Area-balanced model of the late Cenozoic tectonic evolution of the central Andean arc and back arc (lat 20°-22°S): Geology, **25**, 367-370.

Pollard, D., and A. Aydin, 1988, Progress in understanding jointing over the past century: Geological Society of America Bulletin, **100**, 1181-1204.

Priest, S. D., and J. A. Hudson, 1981, Estimation of discontinuity spacing and trace length using scan line surveys: International Journal of Rock Mechanics and Mining Sciences and Geomechanics Abstracts, **18**, 183-197.

Rawnsley, K. D., T. Rives, J.-P. Petit, S. R. Hencher, A. C. Lumsden, 1992, Joint development in perturbed stress field near fault: Journal of Structural Geology, **14**, 939-951.

Reutter, K. J., P. Giese, H. J. Gotze, E. Scheuber, K. Schwab, G. Schwarz and P. Wigger, 1988, Structures and crustal development of the Central Andes between 21° and 25° S, in: Bahlburg, H., Ch. Breitkreuz, and P. Giese,. eds., The Southern Central Andes-Lecture Notes in Earth Sciences, New York, Springer Verlag, **17**, 231-261.

Rives, T., M., Razak, J-P. Petit, and K. T. Rawnsley, 1992, Joint spacing; analogue and numerical simulations, in: Burg, J-P., D. Mainprice, and J-P Petit, eds., Mechanical instabilities in rocks and tectonics; a selection of papers: Journal of Structural Geology, **14**, 925-937.

Roznovsky, R., and A. Aydin, 2001, Concentration of shearing deformation related to changes in strike of monoclinal fold axes; the Waterpocket Monocline, Utah: Journal of Structural Geology, **23**, 1567-1579.

Schmitz, M., 1994, A balanced model of the southern Central Andes: Tectonics, **13**, 484-492.

Segall, P., and D. Pollard, 1983, Nucleation and growth of strike slip faults in granite: Journal of Geophysical Research, B-1, **88**, 555-568.

Shamir, G., and Y. Eyal, 1995, Elastic modeling of fault-driven monoclinal fold patterns: Tectonophysics, **245**, 13-24.

Tindall, S. E., and H. Davis, 1999, Monocline development by oblique-slip fault-propagation folding: the East Kaibab monocline, Colorado Plateau, Utah: Journal of Sructural Geology, **21**, 1303-1320.

Van Wagoner, J. C., R. M. Mitchum, K. M. Campion, and V. D. Rahmanian, 1990, Siliciclastic Sequence Stratigraphy in Well Logs, Cores, and Outcrops: Concepts for High-Resolution Correlation of Time and Facies: American Association of Petroleum Geologists Methods in Exploration Series, **7**, Tulsa, Oklahoma, USA, 55 pp.

Wu, H., and D. Pollard, 1995, An experimental study of the relationship between joint spacing and layer thickness: Journal of Structural Geology, **17**, 887-905.

Chapter 6

Probabilistic Modeling of Fracture Density Using Outcrop Data

6.1.   Abstract

This chapter presents a methodology for building static geologic models of fractured reservoirs using outcrop data, stochastic simulation and geomechanics. First, a comparison of outcrop and subsurface data shows the relevance of outcrop information for characterizing deformation mechanisms and spatial heterogeneity in the subsurface. Then, the descriptive statistics of fault and fracture systems collected at an outcrop are used to create geostatistical models of fracture-density distribution, which replicate the spatial heterogeneity observed at the outcrop.

The probability density function characterizing the fracture density in a given area may vary between exponential, log-normal or normal, depending on the degree of fracture localization.   The mean of these distributions depends not only on the strain, but also on the stratigraphic architecture. In general, low-fracture-density zones are the rock volumes with relatively low shear-strain, bounded by localized fracture swarms associated with faults. Mean fracture density within the faults' damage zones can be up to one order of magnitude higher than the background fracture density.

We test the applicability of sequential Gaussian simulation (SGS), and sequential indicator simulation (SIS) to generate models of joint frequency. SGS can reproduce the statistics of the outcrop data, even though it cannot replicate the architecture. Variogram-based SIS can generate large and continuous high-fracture-density zones, which resemble the fracture corridors associated with small faults; however it cannot successfully handle diverse orientations for the background, low-fracture-density zones.

To generate models with different orientations for large faults, small faults and joints, an object-based indicator approach is used. In this approach, maps of the spatial distribution of faults and damage zones are first generated using the statistics of outcrop data, stochastic techniques, and some geomechanical principles. The maps are filled with SGS realizations for high- and low-fracture-density zones, using the cookie-cutter technique. This method assures the lateral continuity of high-density fracture corridors associated with faults, regardless of the orientation of the low-density fracture background.

6.2.   Introduction

Seismic methods for fracture detection provide direct information about the geometry and the elastic properties of the reservoir; however an accurate interpretation of seismic data requires inputs from other sources of information, like outcrop analogues. The limited resolution, the inherent uncertainties, and the non-uniqueness of the solutions to the inversion of seismic properties require the use of additional information about the subsurface fracture system, such as analog outcrop data (Teng, 1998). In her dissertation, Teng (1998) showed that seismic analysis can help to constrain predictions of the spatial distribution of fracture densities, which have a very important impact on fluid flow responses. However, the inference of fracture densities from shear-wave-splitting analysis can be unreliable because of uncertainties about some key parameters, including fracture specific stiffness, fracture orientation, and background lithology. Teng (1998) explained that the length, connectivity and orientation distribution of the fractures are crucial features of the fracture systems and have an important impact on fluid recovery.

Outcrop studies supply significant qualitative and quantitative information for geologic modeling of fractured reservoirs. The effective use of this information remains problematic. From the perspective of reservoir characterization, there are two basic approaches to the use of outcrop data, stochastic simulation of fracture networks and deterministic modeling based on mechanical principles. For any of these approaches, outcrop descriptions provide constraints to the modeling parameters since: 1) they show the spatial variability of fracture density at the reservoir scale, which can be translated to subsurface modeling using statistical parameters such as the mean, the standard deviation, and the distribution function of fracture populations; 2) they indicate the different mechanisms that generate

fractures for specific rock types and deformation styles; and 3) they fill the scale gap between core, well-log and seismic data (Figure 6.1).

Contrary to the case of stratigraphic heterogeneities, where detailed outcrop studies and geostatistical modeling are widely used for reservoir modeling, there are no standard techniques to incorporate outcrop studies or geostatistical methods into the modeling of fractured reservoirs. In the case of stratigraphic heterogeneities, conceptual stratigraphic models, combined with relevant statistical data, are commonly used as constraints or conditioning data for SGS or SIS. However, the direct use of outcrop data for geologic modeling of fractured reservoirs is commonly limited to the comparison of fracture orientation at outcrops and in the subsurface.

The problem we intend to solve in this paper is how to translate the descriptions and data obtained at outcrops into relevant information for seismic modeling and engineering characterization of fractured reservoirs. Throughout this chapter, we use the results obtained from an outcrop-analogue study in Bolivia, and explore different geostatistical techniques to create a static numerical model that can reproduce the spatial heterogeneity observed at the outcrops. The following section reviews the data and main conclusions derived from an outcrop study of faults and fractures in a fold and thrust belt (Florez *et al.*, 2003). After that section, we discuss the statistical parameters required to generate geostatistical models. Then, the results from SGS and SIS are presented. That section also shows an alternative technique for modeling fracture density; in this method an indicator map of tectonic-facies (or damage-zone indicator) is modeled, and then filled with realizations from SGS using different fracture densities. Finally, I discuss the results in terms of their applicability to seismic and reservoir modeling, and present the conclusions.
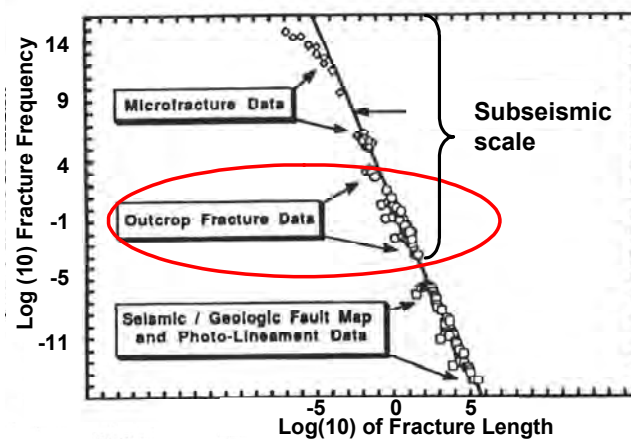
Figure 6.1: Log-log plot of fracture-length frequencies, normalized for area and class intervals (after Heffer and Bevan, 1990). The figure shows how outcrop data fills the gap between core or well-log data, and seismic data.

6.3. Results from an Outcrop-Analogue Study

The previous chapter shows that faults and joints occur at different scales in a hierarchical fashion, as a consequence of progressive shearing. The first generation of fractures is an orthogonal set of joints, one parallel and the other perpendicular to the bedding azimuth. Shearing along these joints transforms them into small faults and creates new sets of fractures, oblique to the bedding attitude. Linkage of these small faults facilitates the formation of larger faults with significant strike-slip offset. Shear along bedding planes creates sub-vertical splay joints that induced the formation of conjugate normal faults. Subordinate strike-slip and normal faults are concomitant products of compressive deformation. These ideas are summarized in the conceptual model shown in Figure 6.2.

The previous chapter also documents a hierarchical correspondence between spacing of structural heterogeneities and stratigraphic architecture. There are four main groups of structural discontinuities at the Abra del Condor (AdC) Anticline: joints, small faults, intermediate faults, and fault zones. Along-strike spacing of joints, small faults and intermediate faults have log-normal distribution functions, whereas spacing of fault zones shows a more symmetric, normal distribution function. The mean of these distributions is about the same as the thickness of the confining stratigraphic intervals. Therefore, spacing and dimensions of joints and faults have a first-order relationship to the thickness of the confining stratigraphic sequences.

6.3.1. Conceptual Model

A conceptual model is the first result that can be derived from an outcrop study. For example, Figure 6.2 presents a conceptual model of fault and fracture systems at the AdC Anticline. The model, explained in detail in Chapter 5, shows the hierarchical relationships that exist between fault zones, intermediate faults, and smaller features (sheared joints, joints and splay joints). This conceptual model also illustrates the relationship between the scale of stratigraphic intervals and structural discontinuities. A model like this provides a useful visualization of the concepts developed by the geologist after an outcrop study. However it does not provide quantitative information about the subsurface. Actually, it does not provide data at all. Nevertheless it is a first step toward understanding the reservoir in the subsurface.

For the case of the AdC-Canaletas fold-and-thrust belt, the dominant faults and fractures are either parallel or normal to the structural grain (determined by the fold axis), however in areas with relatively higher deformation, the splay fractures extend and form a secondary oblique pattern. This variation in fracture pattern is schematically illustrated in Figure 6.2, and is interpreted to be associated with an increase in shear strain. Therefore, as a general rule we can establish that areas with parallel faults and joints are characteristic of low shear-strain domains, whereas areas with abundant oblique splay fractures are characteristic of intermediate shear-strain domains. The high-shear strain domains are the wide damage zones associated with fault zones.
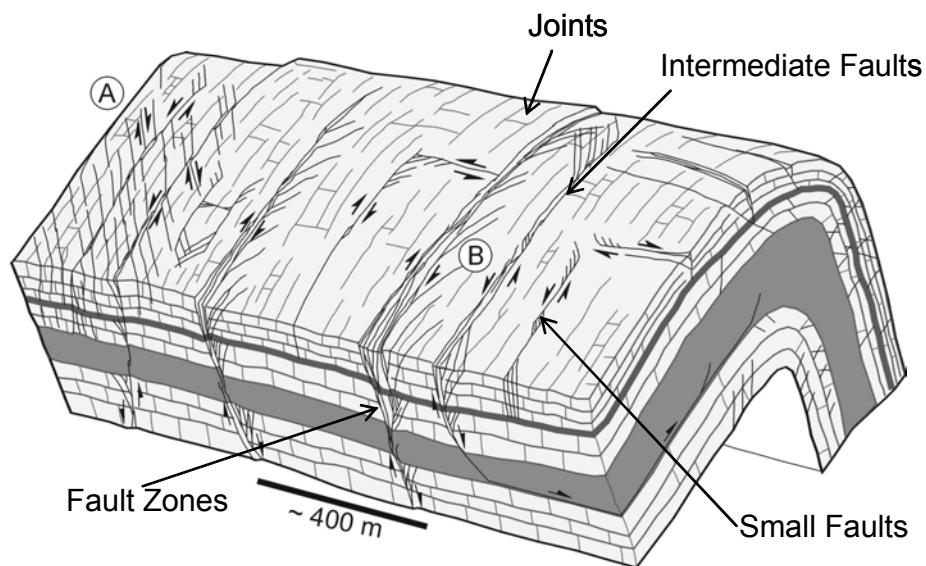
Figure 6.2: Conceptual model of distribution of faults and fractures in a fault-cored Anticline. A indicates and area with higher shear strain than B.

6.3.2. Shear Strain and Fracture Density

Outcrop studies help to identify the main factors controlling the localization – lack thereof– of fracture density. In the case of the AdC-Canaletas fold-and-thrust belt, shear strain and stratigraphic architecture are among the most important factors controlling the distribution of fracture density. Figure 6.3 illustrates the effect of shear strain; as it increases, the average fracture density measured at 50-meter intervals increases. The variation in fracture density is caused by small faults along a strike-parallel scanline measured at the backlimb of the AdC Anticline (Figure 6.4). The details are explained in Chapter 5.

From outcrop data, a clear correspondence between shear strain and fracture density can be established. This relationship is supported by both the data shown in Figure 6.3 and the histograms presented in Figure 6.5. The log-normal distribution observed in the low-shear-strain area has a mean of 3 fractures/m, whereas the normal distribution characteristic of the high-shear-strain area has a mean of 29 fractures/m, that is one order of magnitude higher. The combination of the two data sets results in an exponential distribution with a mean of 7 fractures/m. The exponential distribution indicates significant heterogeneity, since major differences in fracture density occur, whereas the normal distribution evidences more homogeneity.
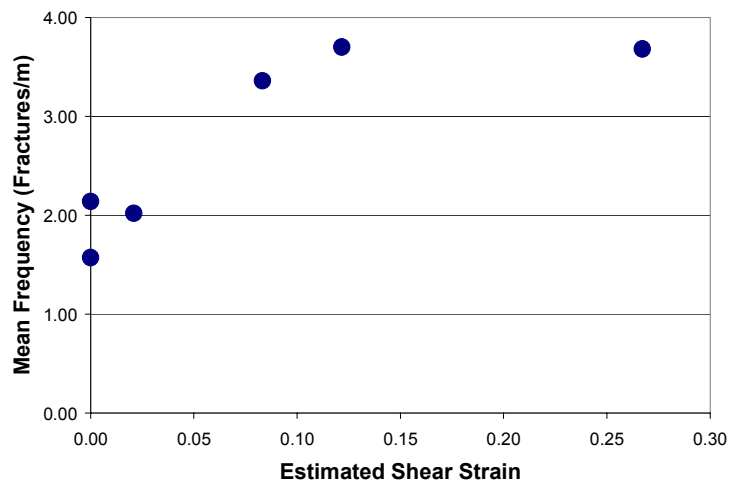
Figure 6.3: Relationship between mean fracture frequency and shear strain, as calculated for intervals of 50 m along the scanline shown in Figure 6.4. The extremes of the scanline are not taken into account because of the influence of the adjacent fault zones.
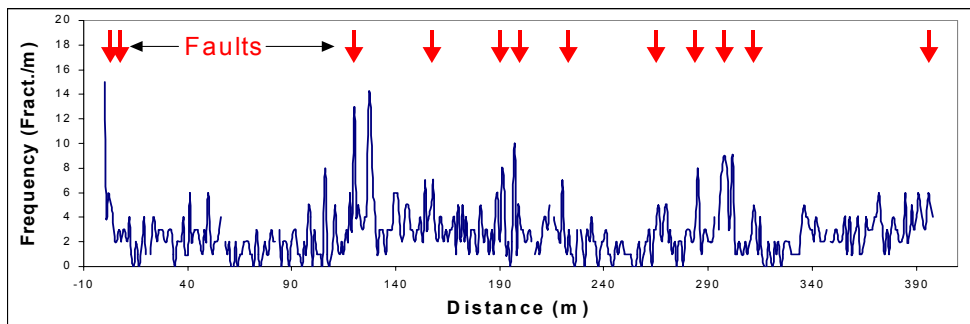
Figure 6.4: Scanline along the azimuth of a low shear-strain block, within the backlimb of the Abra del Condor Anticline.

In the AdC-Canaletas fold-and-thrust belt, fracture-density distributions vary between exponential, log-normal and normal (Figure 6.5). These variations depend on shear strain and the scale of observation, since the former depends on the latter. Fracture spacing and fracture density have the properties of Jeffrey's parameters (e.g. Tarantola, 2004): positive numbers where one is the inverse of the other. Jeffrey's parameters tend to have exponential and log-normal distribution functions.
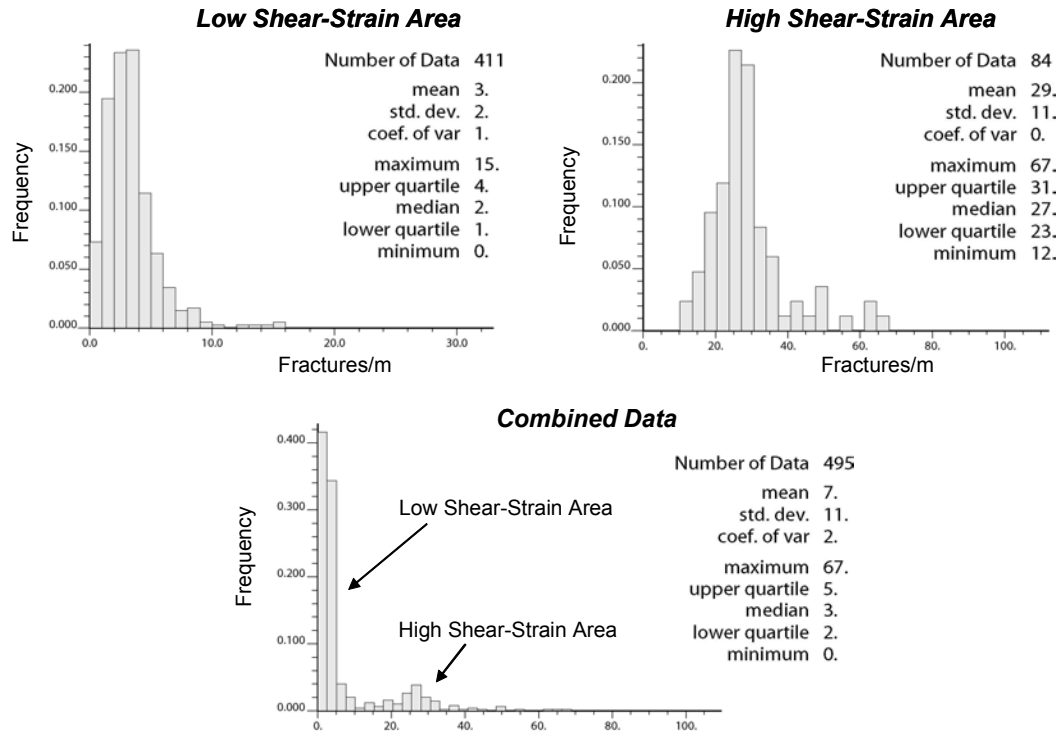
Figure 6.5: Histograms of fracture densities from areas with different degrees of shear strain.

6.3.3. Fracture Hierarchies and Sequence Stratigraphy

The outcrop study at the AdC-Canaletas fold-and-thrust belt documents a correspondence between the mean spacing of fracture hierarchies and the confining stratigraphic interval. For example, mean joint spacing keeps a first-order relationship with respect to bed thickness, while mean spacing of small faults is of the same order of magnitude as the thickness of the sandstone bedsets (see Chapter 5). Similar relationships exist between intermediate faults and parasequences and fault zones and sequences. Since other factors, like extensional (e.g. Wu and Pollard, 1995; Bai and Pollard, 2000) and shear strain, also influence fault and joint spacing, this correspondence should be expressed as follows:

$$M = \alpha T , \tag{Eq. 6.1}$$

where α is a factor related to shear or extensional strain, T is the thickness of the relevant stratigraphic package and M is the mean spacing of the joints or confined faults.

The hierarchical character of sedimentary sequences requires a method to upscale the fracture spacing from one low-order hierarchy to the higher-order hierarchies. For the specific case of joint density, a simple geometric analysis shows that even though the thickness of individual beds controls the spacing of joints within each bed, the density of joints in bedsets and parasequences depends on the thickness ratio *(R)* between these stratigraphic intervals and the individual beds that compose them. For bedsets with similar thickness, joint density will increase proportionally to the thickness ratio *(R)*. Another important factor to take into account is the proportion of brittle to ductile lithologies within the stratigraphic package. In fractured reservoirs, this ratio is commonly proportional to the net-to-gross ratio *(N)*. Therefore, it follows that the joint density of bedsets *(I_b)* can be obtained from bed thickness *(T)* and joint spacing *(S)* from the following expression:

$$I_b = RN\frac{T}{S} . \tag{Eq. 6.2}$$

The ratio *T/S* was defined as the fracture-spacing index *(I)* by Narr (1990); however for the case of joints it should be specified as the joint-spacing index.

6.3.4. Outcrop and Subsurface Fractures

There are many similarities between the fracture systems observed at outcrops and those found in the subsurface, as can be deduced from the comparison between wellbore images from the subsurface and the outcrop data. Fracture orientations found in the subsurface resemble those observed at outcrops. As explained in the previous chapter, outcrop observations can be used to interpret the origin and hierarchical relationships between fracture as in the subsurface.

The comparison between subsurface and outcrop observations indicates that fracture mechanisms and types are also similar. Figure 6.6 shows a high-fracture density zone overlying a low-fracture-density interval. A similar contrast in fracture density has been observed at outcrops, and corresponds to the damage zone associated with small normal faults, like the one shown at the bottom of Figure 6.6.

Similarly, splay fractures abutting against bedding surfaces are observed both in the subsurface and at outcrops.
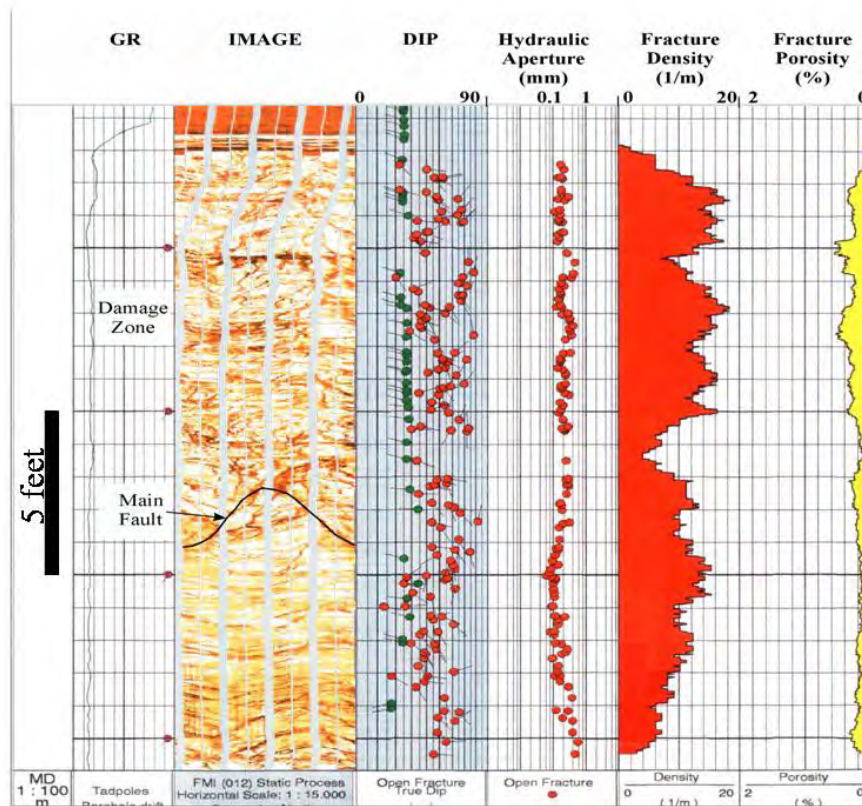
Figure 6.6: Comparison between subsurface and outcrop observations. The contrast in fracture density observed in the subsurface can be interpreted as a damage zone associated with a small fault, like the one shown below.

In spite of the striking similarities found, the extrapolation of outcrop data to the subsurface must be cautiously done. Many fractures may have formed during the uplifting of rocks to the surface. In addition to this, the confining stresses in the subsurface will tend to close many of the fractures observed at outcrops. This implies the need to apply a correction factor, to convert fracture densities measured at outcrops to the expected fracture densities in the subsurface.

6.4. Statistical Parameters for Sequential Simulation

The use of outcrop analogues, or any analogue, is a decision of stationarity (see Deutsch and Journel, 1998, p. 12), on which the analogue information is chosen as relevant and representative of what should be expected in the reservoir. The purpose of geostatistical simulation is to reproduce the spatial heterogeneity and the statistics of the constraining information, which in this case is the analogue data. The parameter to be modeled is fracture density, defined as fractures per meter. The constraining information is the histogram of fracture density as measured along the scanline shown in Figure 6.4, and the variograms obtained from this scanline.

6.4.1. Histograms: Equally Probable Fracture-Density Distributions
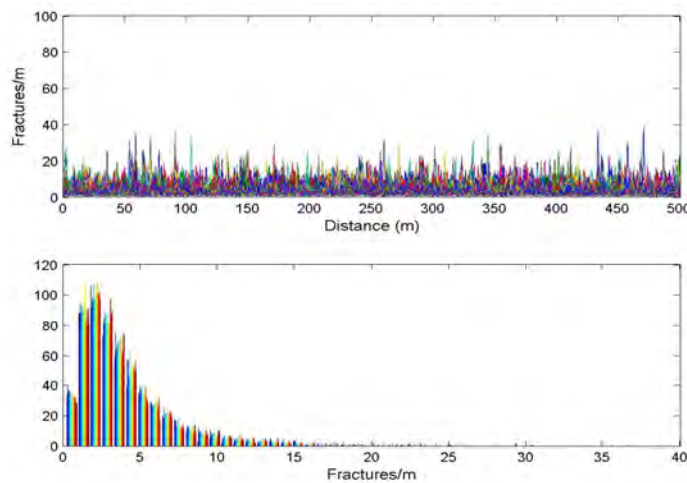
Figure 6.7: Many fracture-density distributions obtained from Montecarlo simulation using a log-normal distribution of fracture density. All these equally-probable fracture-density distributions honor the histogram of fracture density obtained from the scanline shown in **Figure 6.4**.

The first source of uncertainty comes from the fact that there are many fracture-density distributions that can generate the same histogram. The histogram we want to reproduce is that of the low-shear-strain area, shown in Figure 6.5. This histogram

can be approximated by a log-normal distribution with mean and variance obtained from the data. We can generate many statistical replicates of the scanline shown in Figure 6.4, by randomly drawing from this distribution a large number of samples (Figure 6.7). However, the spatial order of the fracture-density values will be different for each case. One of these realizations is shown in Figure 6.8. In practical terms this means that although is possible to predict the presence of fracture swarms associated with faults within a given rock volume, it is not possible to predict the exact location of these fracture swarms. For simulation purposes, the empirical cumulative distribution function (CDF) derived from the original data has been used (Figure 6.9).
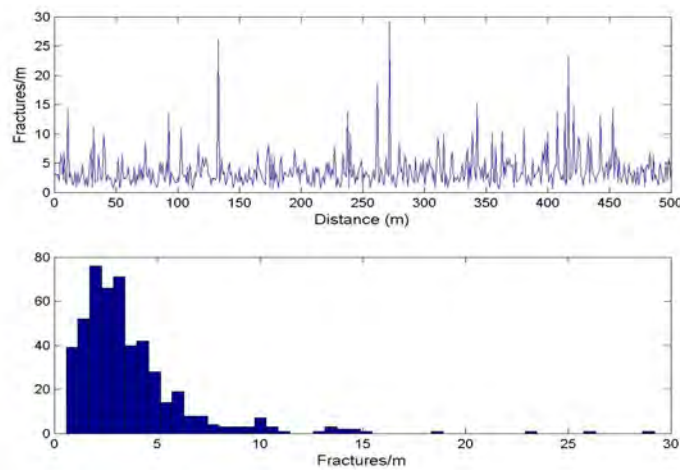
Figure 6.8: Randomly selected fracture-density distribution. This virtual scanline is statistically equivalent to the scanline measured along the low-shear-strain zone, shown in Figure 6.4.
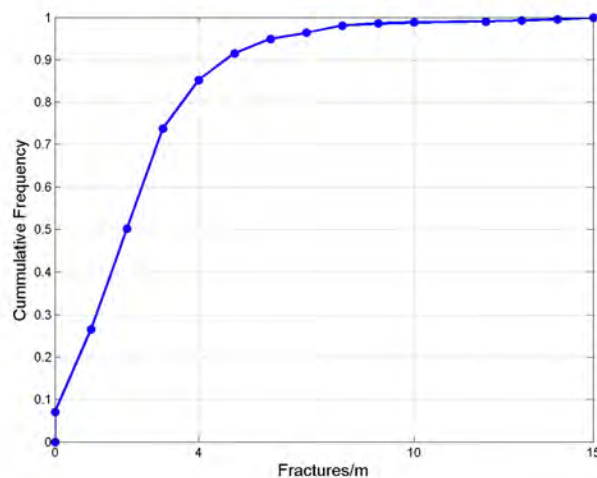
Figure 6.9: Empirical Cumulative Distribution Function (CDF) obtained from the original scanline shown in Figure 6.4.

6.4.2. Variogram Models

In sequential Gaussian simulation (SGS), the spatial heterogeneity of the reservoir model is constrained by the variogram model. Since for the particular case of Abra del Condor outcrops, the dominant fractures are either parallel or normal to the dip direction, the variogram is defined following these two orientations. The data from the scanline (Figure 6.4) indicates that an exponential variogram is a good approximation (Figure 6.10). The correlation length, or range, for the azimuth direction can also be obtained from the scanline data. The focus of this simulation is on dip-parallel fractures, therefore we apply a large correlation length in this direction.
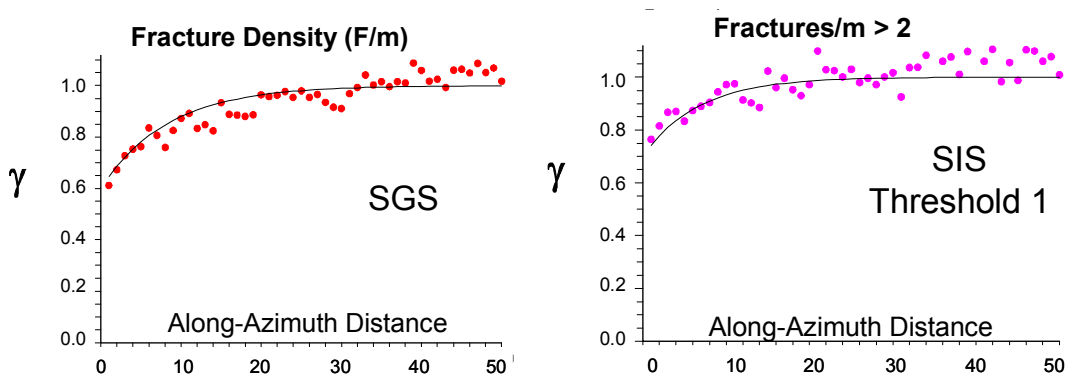
Figure 6.10: Along-Azimuth Variogram models from the scanline shown in Figure 6.4. Left: variogram model for the whole data set. Right: variogram model for fracture densities larger than 2 fractures per m.
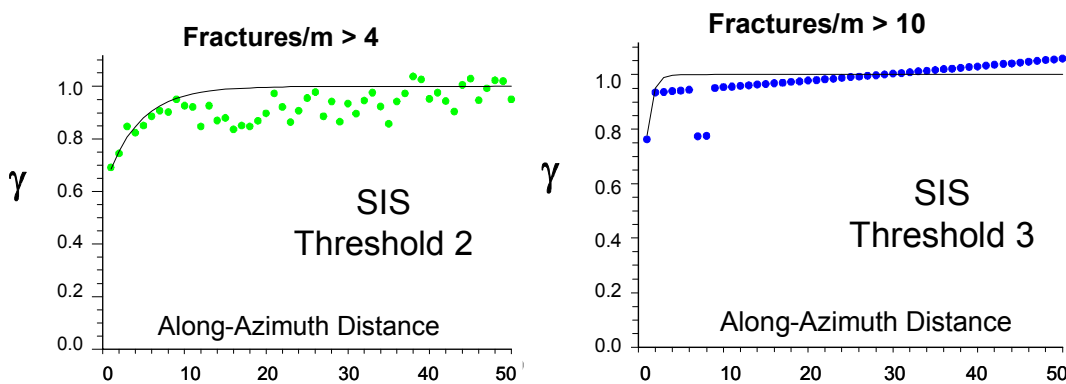
Figure 6.11: Variogram models for sequential indicator simulation, for thresholds 2 (left) and 3 (right). Fracture density of 10 fractures per meter is used as an indicator of small or intermediate faults.

In variogram-based sequential Indicator simulation (SIS), we can use threshold values of fracture-density and apply different variogram models for each threshold. The threshold values can be related to fracture hierarchies in terms of the fracture

density. For example, the presence of 10 fractures per meter can be used as an indicator of small or intermediate faults. In principle, this technique should allow us to assign different correlation lengths and anisotropies for each fracture-density class. The variogram models used for each threshold value are illustrated in Figure 6.11.

```
┌──────────────┐   ┌──────────────┐   ┌──────────────┐       ┌──────────┐   ┌──────────────┐
│ Determine    │   │ Perform      │   │ Check        │  Yes  │ Run      │   │ Backtransform│
│ Univariate   │→  │ Normal Scores│→  │ Bivariate    │──────→│ sgsim    │→  │ Simulated    │
│ CDF for the  │   │ Ttransformation│  │ Normality    │       │          │   │ Normal Scores│
│ Entire Data  │   │              │   │              │       └──────────┘   │              │
│ set          │   │              │   │              │                      │              │
└──────────────┘   └──────────────┘   └──────────────┘                      └──────────────┘
                                              │ No
                                              ↓
                                    ┌──────────────────┐
                                    │ Consider         │
                                    │ Alternative      │
                                    │ Models: Split    │
                                    │ the data set     │
                                    └──────────────────┘
```

(a)

SGSIM

```
┌──────────────┐
│ Define Random│
│ Path         │
└──────────────┘
       │
       ↓
┌──────────────┐
│ Proceed to   │                      At each node (u)
│ the first    │
│ node (u)     │
└──────────────┘
       │
       ↓
┌──────────────┐   ┌──────────────┐   ┌──────────────┐   ┌──────────────┐
│ Retain       │   │ Determine μ  │   │ Draw a       │   │ Add the      │
│ specified    │   │ and σ of the │   │ simulated    │   │ simulated    │
│ # of         │→  │ ccdf of the  │→  │ value y^l(u) │→  │ value y^l(u) │
│ conditioning │   │ RF Y(u) at u │   │ from the ccdf│   │ to the data  │
│ data; both   │   │              │   │              │   │ set          │
│ original (y) │   │              │   │              │   │              │
│ and          │   │              │   │              │   │              │
│ previously   │   │              │   │              │   │              │
│ simulated(y^l)│  │              │   │              │   │              │
└──────────────┘   └──────────────┘   └──────────────┘   └──────────────┘
       ↑                                                          │
       │                                                          ↓
       │                                                 ┌──────────────┐
       │                                                 │ Proceed to   │
       │                                                 │ the next     │
       │                                                 │ node (u)     │
       │                                                 └──────────────┘
       └─── Loop until all nodes (u) are simulated ──────────────┘
```

(b)

Figure 6.12: Diagrams showing the steps required to perform sequential Gaussian simulation: (a) check for bivariate normality after normal score transformation; (b) algorithm for sgsim, (Deutsch and Journel, 1998).

6.5.   Stochastic Modeling of Fracture Density

This section explores different geostatistical methods to generate numerical models that reproduce the spatial variability of fracture density observed at outcrops. First we use variogram-based sequential simulation techniques –SGS (Figure 6.12) and SIS (Goovaerts, 1997; Deutsch and Journel, 1998)– to try to reproduce this variability and spatial continuity. After that we use a more deterministic approach

that resembles the object-based indicator-simulation method (Deutsch and Journel, 1998). In this approach, the spatial distribution of faults and fault zones is modeled first, generating an indicator map of the damage zones and faults. This volume can be considered a tectonic-facies indicator map. Afterwards, this indicator map is populated with realizations obtained from SGS. The damage zones and faults are populated with results from SGS realizations for high fracture densities and their respective variograms, whereas the background areas are filled with results from SGS realizations for low fracture densities and their respective variograms. This combination of stochastic fault modeling and SGS allows us to reproduce the spatial heterogeneity observed at outcrops.

6.5.1. Sequential Gaussian Simulation (SGS)

SGS performs stochastic sequential simulation under the assumption of a multi-Gaussian random-function model (Goovaerts, 1997). Figure 6.12 presents a sketch diagram of the steps to perform SGS, and the algorithm sgsim implemented in GSLib (Deutsch and Journel, 1998).
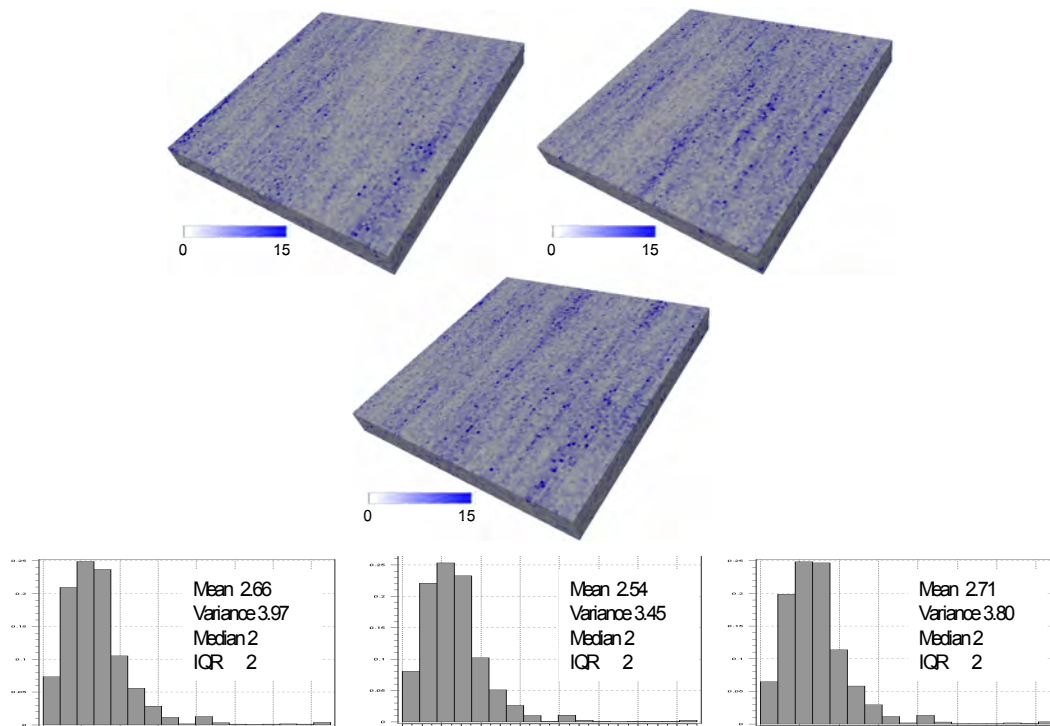

Figure 6.13: Equally probable realizations for fracture density (fractures per meter) obtained from Sequential Gaussian Simulation (SGS), and their respective histograms.

As can be observed in Figure 6.13, SGS generates statistical replicas of the outcrop data, however it can not reproduce the geometric or architectural distribution of fracture densities. In this technique we are using the global variogram for fracture density, shown in the left side of Figure 6.10. However, the large azimuth-parallel range observed in this variogram, about 25 m, corresponds more to the correlation length of low-fracture-density areas. Along the azimuth, the high-fracture-density areas have an almost pure nugget effect, as shown in the right side of Figure 6.11. The ability of SGS to reproduce the architecture of a fractured reservoir may improve if we have more data. However, from these results we conclude that SGS is not the most appropriate technique to model fractured reservoirs.

6.5.2. Variogram-Based Sequential Indicator Simulation

SIS is a non-Gaussian simulation technique, which allows one to account for class-specific patterns of spatial continuity through different variogram models (Goovaerts, 1997, p.395). Figure 6.14 schematically illustrates the algorithm for SIS. The variograms for the different threshold values are shown in Figure 6.10 (right side) and Figure 6.11.
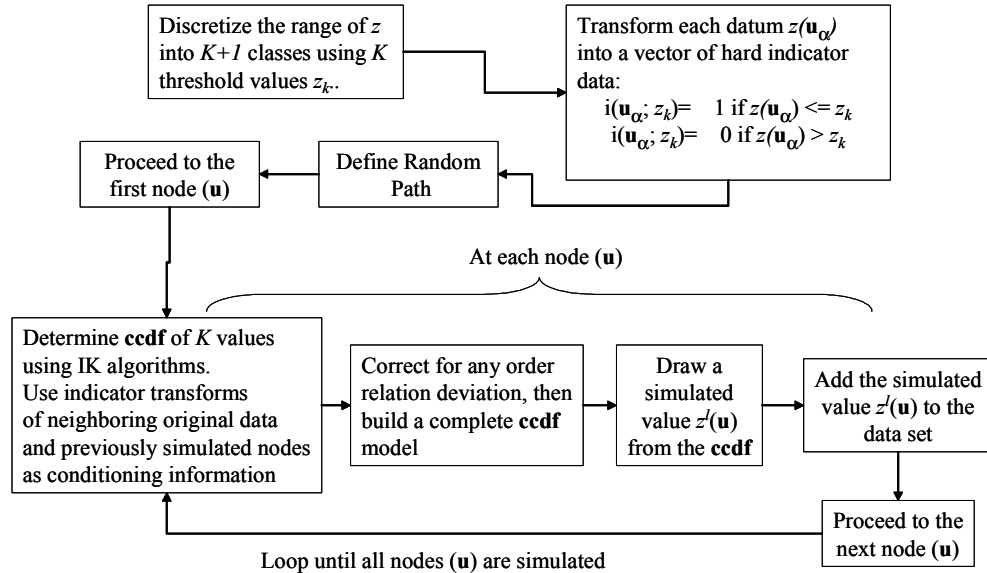

Figure 6.14: Diagram illustrating the sequential indicator simulation algorithm (Goovaerts, 1997; Deutsch and Journel, 1998).

In the case of parallel high- and low-fracture-density zones, corresponding to faults and joints respectively, SIS generates fracture-density models that replicate the architecture observed at outcrops. As shown in Figure 6.15, SIS generates high-

fracture-density corridors similar to those associated with small faults at outcrops. The fracture-density models in Figure 6.15 are more appropriate for fractured reservoirs than those presented in Figure 6.13.

However, for the case of diverse orientations for high- and low-fracture-density zones, SIS cannot generate the laterally continuous high-fracture-density corridors. In other words, the anisotropy of the low-fracture-density class, which is the most likely and dominant class in the empirical CDF (Figure 6.9), overrides the anisotropy of the high-fracture-density corridors (Figure 6.16).
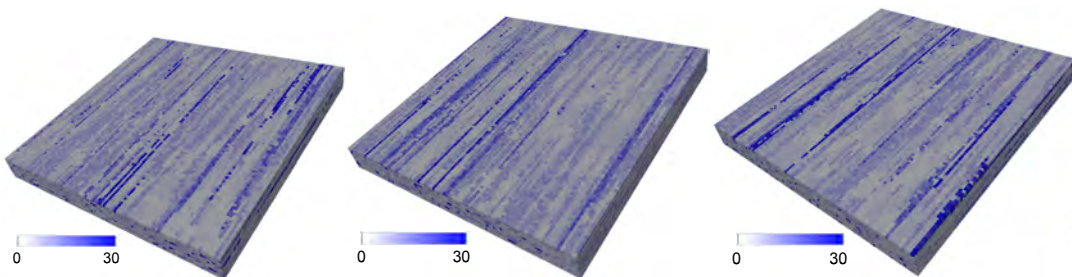
Figure 6.15: Results from sequential indicator simulation algorithm (sisim), for the case of parallel variograms for both high and low fracture densities.
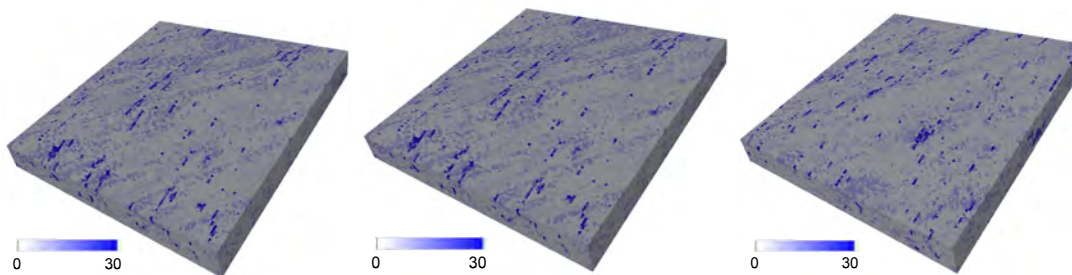
Figure 6.16: Results from the variogram-based sequential indicator simulation algorithm (sisim), for the case of diverse orientations of high-fracture-density zones and low fracture-density background.

6.5.3. Stochastic Fault Modeling and Sequential Simulation

To overcome the limitations of SGS and SIS for modeling of fractured reservoirs, we propose to use an object-based indicator approach: first simulating the distribution of faults and damage zones (i. e. a tectonic-facies indicator map), then populating this indicator map with realizations from SGS.

Stochastic fault modeling is proposed as a method to generate maps of tectonic-facies indicators. Starting from one of the equally probable scanlines illustrated in Figure 6.7, this method uses Montecarlo simulation to model fault locations, fault dimensions, and the width of the fault-damage zone, as outlined in Figure 6.17. The tectonic-facies architecture is modeled in 2D, for undeformed grids (stratigraphic

framework). Further improvements of this method will require the implementation of three-dimensional models and the interpolation to a deformed, structural grid.

Generate Scanline from given PDF of Fracture Density	→	Locate Faults along the Azimuth: If FD >10= Fault	→	Draw values for: Dip-coordinate, Fault length, and damage-zone width	→	Map Faults, their damage zones, and the indicator

Figure 6.17: Flow diagram for stochastic fault modeling. Currently the method is implemented for two-dimensional configurations of relatively simple faults, in undeformed grids.
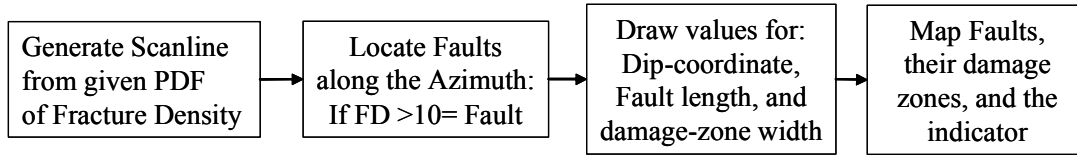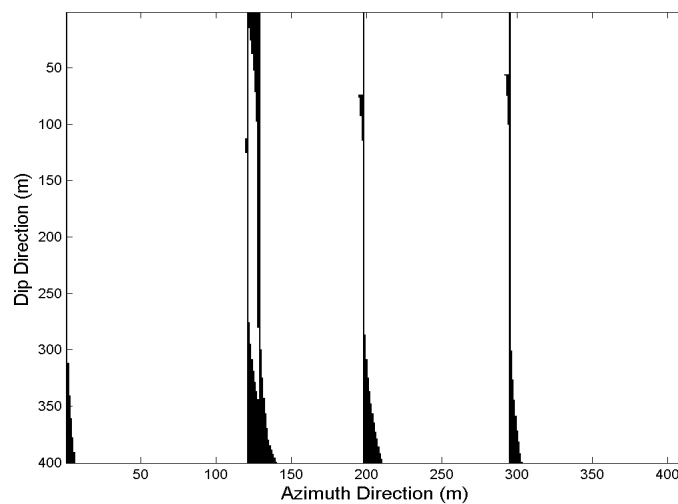

Figure 6.18: Stochastic fault model for an area with low shear-strain. The architecture corresponds to small strike-slip faults with left-lateral shear.

The asymmetric distribution of damage zones follows the asymmetric distribution of tensional and compressional stresses expected from fault-induced stress perturbations. It is well known that shear along faults produces an asymmetric distribution of the stress field. Outcrop observations document asymmetric distributions of fracture density associated with the localization of the tensional quadrants (e. g. Figure 6.6). The shape of the fault can be obtained from a symmetric power function that uses the center of the fault as origin.

The indicator maps obtained from stochastic fault modeling (SFM) are shown in Figure 6.18 and Figure 6.19. In the first case (Figure 6.18), the indicator map reproduces the fault architecture expected for an area with low shear strain, with large spacing between faults and narrow damage zones. In the second case (Figure 6.19), the indicator map replicates the most likely fault architecture for an area with moderate shear strain, where the spacing between faults decreases, and the width of

damage zones increases. In both cases, the architecture corresponds to that generated by left-lateral strike-slip faults, with wider damage zones asymmetrically localized towards the tips of the faults.

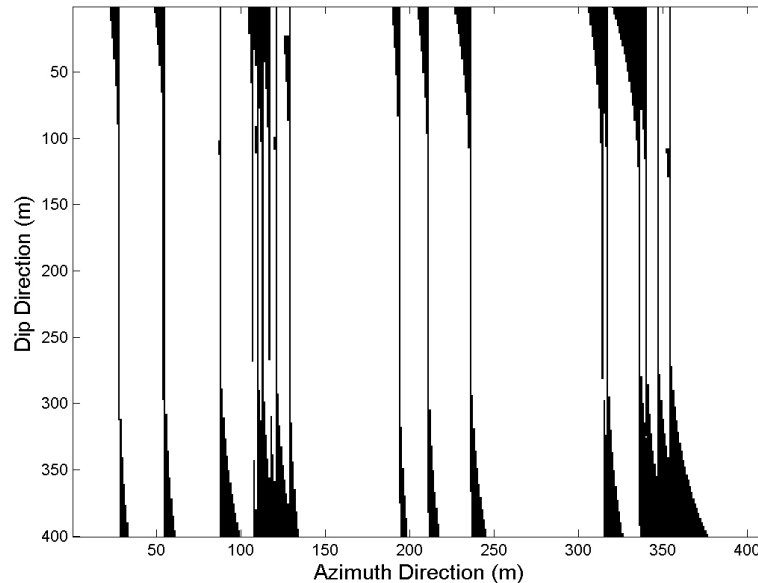Figure 6.19: Tectonic-facies indicator map obtained from stochastic fault modeling. The model resembles the architecture expected for small faults with left-lateral shear, in a region with moderate shear-strain. Fault spacings are smaller and damage-zone widths are larger than those simulated for a low shear-strain area (Figure 6.18).

The tectonic-facies indicator maps are populated with fracture-density values obtained from SGS realizations. The low-fracture-density areas, background areas in the indicator maps, are populated with realizations for low fracture densities. Similarly, the high-fracture-density zones, or damage zones, are filled with realizations from SGS with higher fracture densities. The final result is the combination of the two populations. This technique is an object-based indicator simulation method, extensively discussed by Wang (1998), and outlined by Deutsch and Journel (1998). The final fracture-density maps are illustrated in Figure 6.20, for the low-shear-strain area, and in Figure 6.21 for the high-shear-strain area. Figure 6.22 presents a comparison between the two models, representing areas with different degrees of shear strain.

It is important to emphasize that a reservoir model should, at least, reproduce the mean and variance of the analogue. In many cases the outcrop data is reduced to use the mean spacing for specific areas, without regarding the variance. For example, a comparison of the histograms of the two reservoir models shown in Figure 6.23 demonstrates that the mean of these histograms is relatively close, about 3; however

the variance is significantly different. The higher variance in the histogram corresponding to the moderate-shear-strain area reflects the presence of more high-fracture-density corridors in this area. The overall higher fracture density of the moderate-shear-strain area is clearly illustrated by the quantile-quantile plot (Figure 6.24).
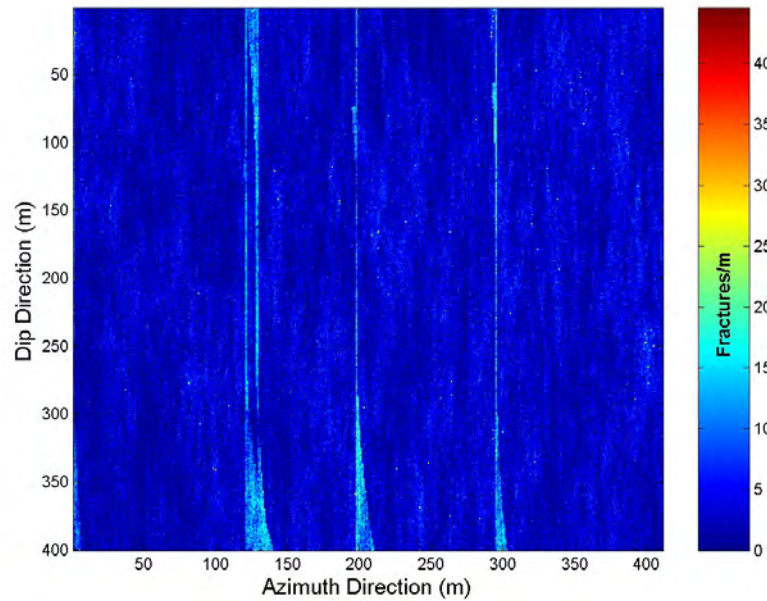
Figure 6.20: Fracture-density map obtained from the combination of SFM and SGS. Low-shear-strain area.
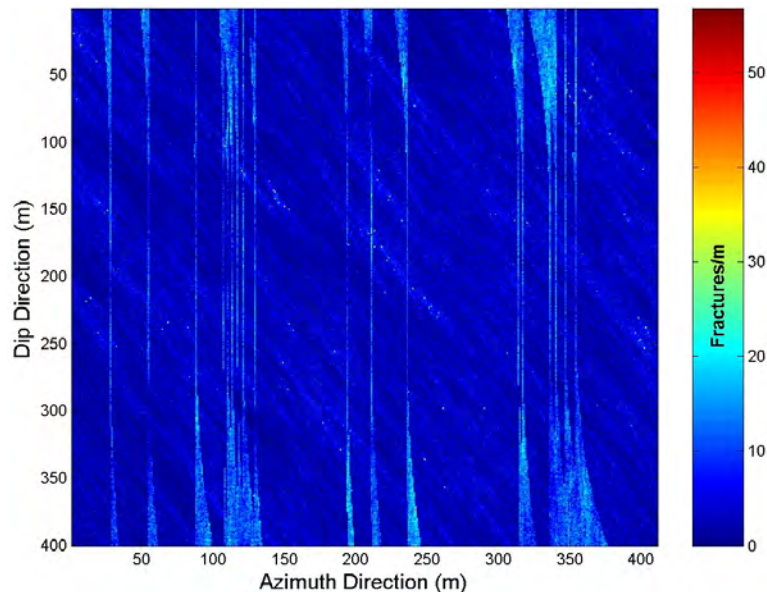
Figure 6.21: Fracture density model obtained from the combination of SFM and SGS. The model reproduces the spatial heterogeneity of FD observed at areas with moderate shear strain.
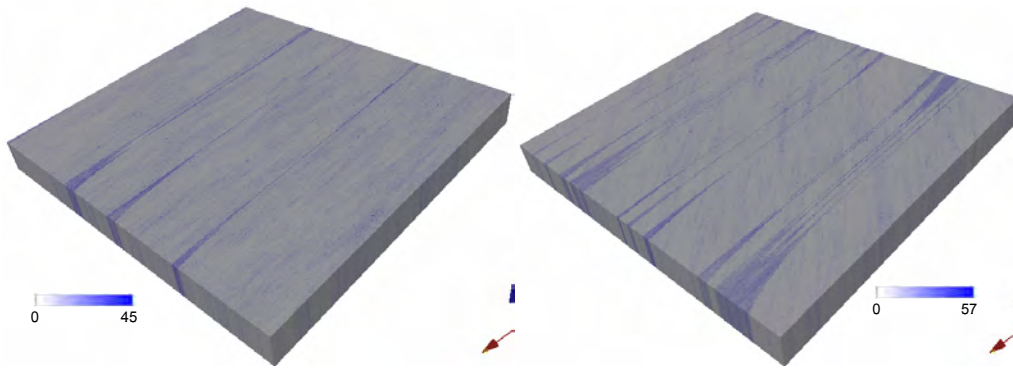
Figure 6.22: Comparison of the models obtained from combining SFM and SGS. The model to the left represents a low shear-strain area, where faults and fractures are parallel. The model to the right represents a moderate shear-strain area, where faults are parallel and secondary fractures are oblique, replicating the geometry of splay fractures derived from shear along the faults.
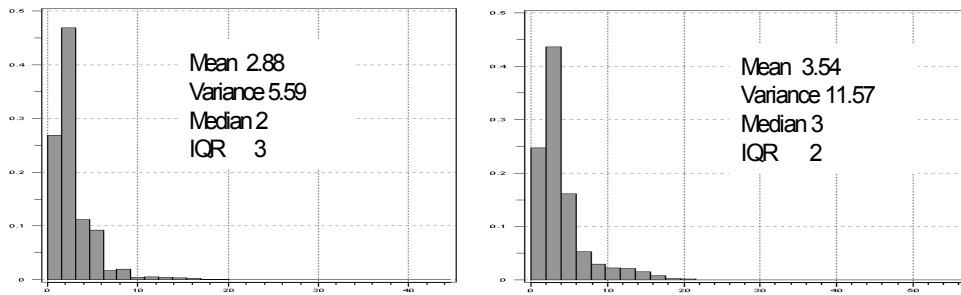
Figure 6.23: Left: histogram for the low shear-strain area. Right: histogram for the moderate shear-strain area. Notice that the mean of these two histograms is about the same, however the variance is significantly different. The higher variance in the model of the moderate shear-strain area reflects the overall higher fracture density in this model.
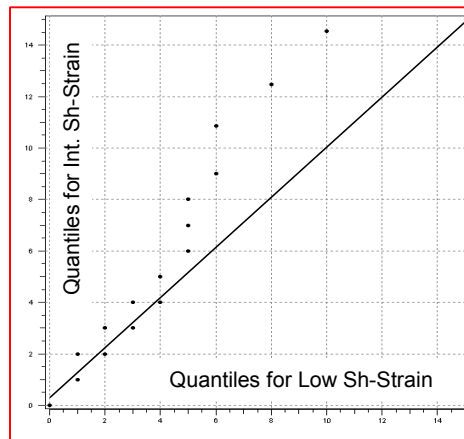
Figure 6.24: Quantile-Quantile plot comparing the fracture density populations of the two models. These plot shows that the fracture density in the model of the moderate (intermediate) shear-strain area is higher than the fracture density in the model of the low shear-strain area.

The combination of SFM and SGS generates statistical replicas of the outcrop data, which reproduce the spatial heterogeneity observed at outcrops. Figure 6.25 presents a comparison between the generated models and the outcrop architecture. This method is an object-based indicator technique. The indicator maps are generated using stochastic methods to select the values for parameters that describe the fault architecture. The maps obtained reproduce the lateral continuity of narrow fault zones, which could not be reproduced using pixel-based simulation techniques like SIS.
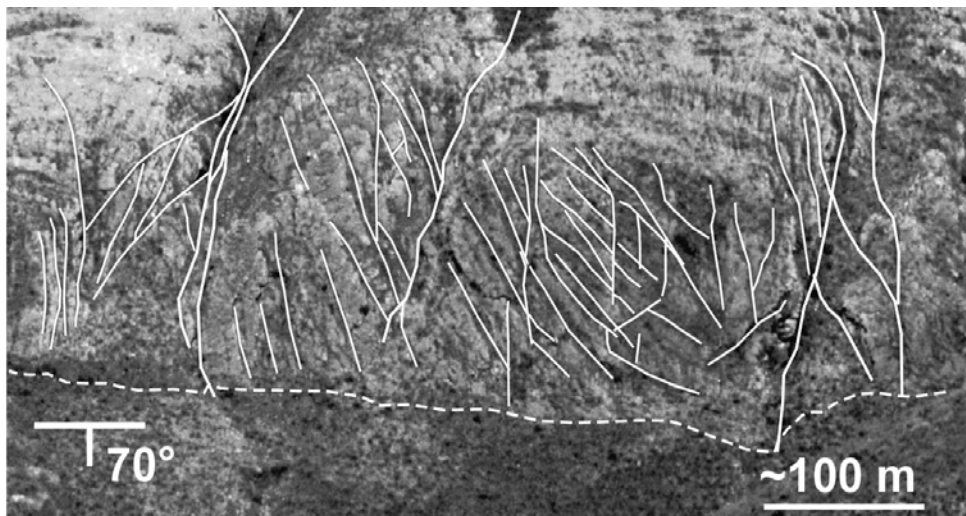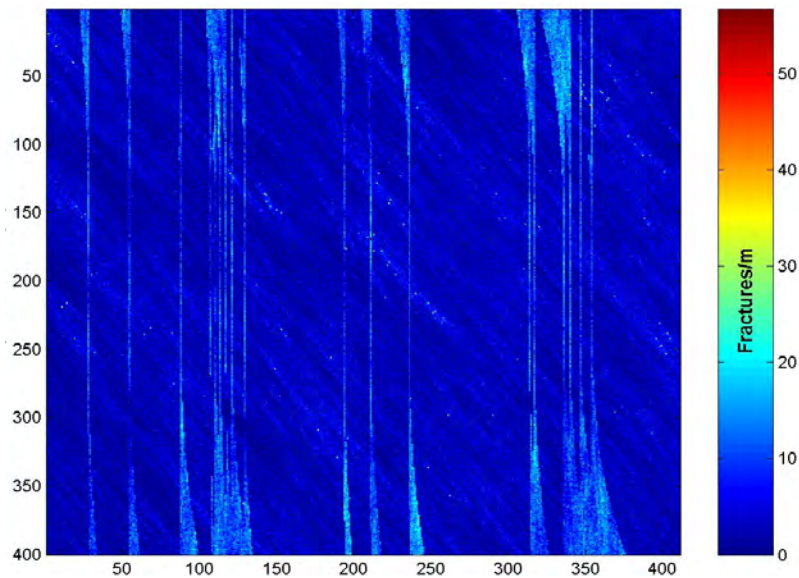
Figure 6.25: Comparison of the spatial heterogeneity simulated from the SFM-SGS technique, and the fracture distribution observed at outcrops.

6.6. Discussion

The combination of SFM and SGS allowed us to reproduce the spatial heterogeneity of fracture density observed at outcrops; however the method requires further improvements. The technique, which is an object-based indicator method, is an alternative method for modeling fractured reservoirs. The fact that fracture density is the modeled variable might facilitate the implementation of methods for seismic modeling that use crack density as the main parameter; e.g. Hudson's model (Mavko *et al.*, 1998). However, there are still many issues to be resolved before this technique can be applied to real cases: How can we go from fracture density to crack density? How do you incorporate the fracture orientation at meter (pixel) scale? How do we upscale these models? How do we incorporate the effect of confining stress on these fracture-density values? We briefly discuss these questions in the following paragraphs.

6.6.1 Fracture Density, Crack Density and the Effect of Confining Stress

The transformation from fracture density to crack density strongly depends on the applied stress field and the rugosity of the fracture surfaces. To better understand this, it is convenient to think of each fracture as a set of aligned cracks. The closure of each crack will depend on the applied normal stress and the aspect ratio of the crack. As a rule of thumb, the crack-closing stress is numerically proportional to $\alpha_0 E_0$, where α_0 is the initial aspect ratio of the crack and E_0 is the Young's modulus of the intact material (Mavko *et al.*, 1998). The rugosity of the fracture surfaces, or mismatch, controls the original aspect ratios. The final closure of a fracture depends on the initial aspect ratios of the aligned cracks along the fracture. This concept is similar to the concepts of crack-induced stress anisotropy and the crack-induced velocity dependence on pressure (Nur and Simmons, 1969), applied at a larger scale.

For a specific stress field, the relationship between fracture density and crack density can be approximated as linear. In general, for a set of fractures larger than the volume under study, the relationship between the number of fractures per volume *(N)* and the volumetric crack density *(ε)* can be expressed as follows:

$$\varepsilon \approx K(\sigma)\frac{N}{8}, \tag{4}$$

where $K(\sigma)$ is a scaling factor that largely depends on the applied stress field. In fact, K depends not only on the magnitude of the normal stress applied to the fracture, but

also on the shear stress. That is the essence of the role of active faults on fractured reservoirs documented by Barton *et al.* (1995) and Wiprut and Zoback (2000). Other factors, like diagenesis and cementation, may affect the final number of open cracks and their proportional ratio to the number of fractures. In short, the total number of fractures within a reservoir may remain the same; nevertheless the number of open cracks is sensitive to the applied stress field. As a first approximation to extrapolate from outcrops to the subsurface, we can assume that the crack density decreases non-linearly with confining stress (depth), and is linearly proportional to the fracture density.

6.6.2   Fracture Orientation at Meter Scale and Upscaling

Incorporating the meter-scale fracture orientation and upscaling are two intimately related issues. The fracture density models generated so far implicitly assume a random or isotropic fracture orientation, which also implies that these fracture-density values can be treated as scalars for upscaling purposes. A more rigorous approach requires the incorporation of fracture orientation. To take into account the orientation of fractures at meter (or pixel) scales, the upscaling procedure becomes more complicated. In that case, it is necessary to define a tensor for the property to be upscaled. For example, to upscale the elastic properties, we need to establish a stiffness tensor based on the crack-density values, and apply the Backus average (e.g. Mavko *et al.*, 1998) to these stiffness tensors. A somewhat similar procedure would be required for permeability. In addition to this, the average fracture or crack densities of different fracture sets have to be computed first, and then added together. Although this upscaling scheme would not take into account the effect of crack interaction, it seems to be the viable approach. Upscaling is a complex issue that requires a more extensive and detailed analysis, and it must take into account the anisotropy induced by fracture orientation.

6.7.   Conclusions

Rigorous outcrop-analogue studies provide information relevant to understanding the spatial heterogeneity and deformation mechanisms of fractured reservoirs in the subsurface. We have shown examples of striking similarities between the image-log data from a reservoir in the subsurface and its outcrop analogue.

Sequential Gaussian simulation (SGS) can reproduce the statistics of the outcrop analogues, but cannot replicate the architecture. The different, equally probable realizations obtained from SGS do not generate the laterally continuous, high-fracture-density corridors associated with faults.

Variogram-based sequential indicator simulation (SIS) can replicate both the statistics and the architecture of parallel fracture sets of different hierarchies, faults and background joints; however it cannot successfully handle fracture hierarchies with different orientations.

The combination of stochastic fault modeling (SFM) and SGS allows us to reproduce the spatial heterogeneity of fracture density observed at outcrops. This approach is an object-based indicator approach, in which the SFM method maps the distribution of damage zones associated with faults, generating a tectonic-facies-indicator map. Afterwards, the indicator map is populated with realizations of different fracture densities, generated with SGS.

The technique illustrated in this paper provides an alternative method for modeling fractured reservoirs; however there are still important issues to be solved. The most important issues are the reduction of crack density as a function of the applied stress field, and upscaling of elastic and hydraulic properties.

6.8. Acknowledgements

6.9. References

Bai, T. and D. Pollard, 2000, Fracture spacing in layered rocks; a new explanation based on the stress transition, Journal of Structural Geology, **22**, 43-57.

Barton, C.A., Zoback, M.D., and Moos, D., 1995, Fluid flow along potentially active faults in crystalline rock: Geology, **23**, 683-686.

Deutsch, C., and A. Journel, 1998, GSLIB Geostatistical Software Library and User's Guide, second edition, Oxford University Press, New York. pp. 369.

Flórez, J-M., A. Aydin, G. Mavko, M. Antonellini and A. Ayaviri, 2003, Faults and fractures systems in a fold and thrust-belt: an example from Bolivia, Proceedings of the Stanford Rock Physics and Borehole Project Workshop.

Goovaerts, P., 1997, Geostatistics for Natural Resources Evaluation, Oxford University Press, New York, pp. 483.

Heffner, K. J., and T. G. Bevan, 1990, Scaling relationships in natural fractures, data, theory and applications. SPE 20981. Proceedings of Europec 90, The Hague, Netherlands.

Mavko, G., T. Mukerji, and J. Dvorkin, 1998, The Rock Physics Handbook, Tools for Seismic Analysis in Porous Media, Cambridge University Press, 329 pp.

Narr, W., 1990, Fracture density in the deep subsurface; techniques with application to Point Arguello oil field, American Association of Petroleum Geologists Bulletin, **75**, 1300-1323.

Nur, A., and G. Simons, 1969, Stress-induced velocity anisotropy in rocks: An experimental study, Journal of Geophysical Research, **74**, 66-67.

Tarantola, A., 2004, Inverse Problem Theory for Model Parameter Estimation, SIAM, 290 pp.

Teng, L., 1998, Seismic and Rock Physics Characterization of Fractured Reservoirs, Ph. D. dissertation, Stanford University.

Wang L., 1998, Modeling Complex Reservoir Lithofacies, Ph D dissertation, Stanford University.

Wiprut, D., and Zoback, M.D., 2000, Fault reactivation and fluid flow along a previously dormant normal fault in the northern North Sea: Geology, **28**, 595-598.

Wu, H., and D. Pollard, 1995, An experimental study of the relationship between joint spacing and layer thickness, Journal of Structural Geology, **17**, 887-905.

Chapter 7

Geomechanic and Seismic Modeling of Fracture Swarms

7.1. Abstract

Fracture localization around fault zones has an important impact on both seismic and hydraulic properties of fractured reservoirs. Understanding the mechanics of fracture localization and its associated seismic signature provides insight into the seismic interpretation of these reservoirs. This chapter integrates three studies that are closely related to this problem: (1) outcrop-based geomechanical analysis that explains fracture localization as the result of the generation of conjugate faults; (2) synthetic one-dimensional seismic modeling that uses outcrop information to outline the expected seismic signature of these fracture swarms; and (3) a case study that compares the geologic and seismic interpretation of fracture-swarms associated with small faults. This combined study illustrates the application of concepts derived from outcrop observations and mechanical models to the interpretation of seismic data.

Outcrop observations and geomechanical numerical modeling of conjugate faults show that there are two key factors influencing the fault-associated localization of fracture swarms in brittle rocks: (1) the development of conjugate fault systems from splay and tail joints due to shearing of pre-existing discontinuities like joints or thin shale layers; and (2) the orientation of the remote maximum compressive stress with respect to the newly formed faults and the pre-existing sheared discontinuities. The ideal condition for fracture localization occurs when the remote maximum compressive stress bisects the angle formed by the former sheared surface and the latter conjugate fault.

Modeling of the seismic signature of fracture swarms associated with small faults shows that amplitude dimming and flexure can be used as fault indicators. An

outcrop-based fracture density scanline is translated into a scanline of proportional crack density, using a relationship between fracture intensity and Hudson's crack-density parameter (ε), and a method to evaluate the effect of stress on crack density. Amplitude anomalies caused by highly fractured intervals prevail as fault indicators, while flexure can only reveal faults with offsets larger than one-sixteenth of the wavelength.

The comparison of the geologic analysis of logging while drilling (LWD) logs and the seismic interpretation of a walk-away VSP provides the opportunity to test these concepts. Amplitude anomalies and subtle offset of seismic horizons coincide with the fracture swarms and small faults inferred from the LWD logs. Although a limitation of this technique is its inability to uniquely determine fracture orientation, LWD logs and VSP surveys can be used to identify fracture swarms were image-logs are not available.

7.2. Introduction

Fracture swarms associated with subseismic faults are important conduits for fluid flow. They occur as the result of fracture localization, and commonly are associated with subseismic faults (e.g. see Chapter 5). The importance of subseismic faults for fluid flow has been realized and analyzed by numerous previous studies (e.g. Maerten *et al.*, 2000), although in most of the cases they are considered fluid barriers rather than flow conduits. The now familiar drilling of horizontal wells in fractured reservoirs has demonstrated the existence of localized fracture swarms that cannot easily be imaged by conventional seismic surveys.

Conjugate normal faults have been observed in a variety of natural settings and at various scales, from outcrops (i.e. Aydin, 1973; Horsfield, 1980; Antonellini and Cruikshank, 1992; Watterson *et a.l*, 1998; Young, 2000) to 2D and 3D seismic data (Nicol *et al.*, 1994; Gutierrez and Nur, 2001). They have been found in a variety of tectonic settings: at the crest of salt anticlines (Nilsen *et al.*, 1995), in salt withdrawal basins, in the hanging walls of listric normal faults (Dula, 1991), and associated with wrenching (Gutierrez and Nur, 2001). They have been also generated in sandbox and clay models (McClay, 1995; Withjack *et al.*, 1995). They are particularly conspicuous in the northern Gulf of Mexico basin (Diegel *et al.*, 1995; Peel *et al.*, 1995).

Conjugate normal faults can play a significant role in accumulation of hydrocarbons and reservoir compartmentalization (Jev *et al.*, 1993; Morley *et al.*,

1990; Gutierrez and Nur, 2001). According to Ferril *et al.* (2000), conjugate faults may be an important factor in the development of permeability anisotropy in reservoirs. Understanding the potential effects of normal faults on reservoir permeability provides a key to understanding the development of migration pathways and traps, reservoir compartments and baffles, and reservoir permeability anisotropy. From the rock-physics point of view, understanding the architecture of subseismic faults provides a way to interpret and model their impact on elastic properties and, therefore, on seismic impedance and anisotropy.

Recent studies explain conjugate faults in terms of hierarchical shearing and progressive deformation (Florez and Mavko, 2002; Davatzes *et al.*, 2003; Flodin and Aydin, 2004). Previous models used rock-mechanics laboratory experiments as analogues, and explained conjugate faults in terms of the shear fractures formed under triaxial compression (e.g. Anderson, 1942). Studies of rock failure under compression have demonstrated that progressive shearing and crack interaction explains the development of these so-called shear fractures in the laboratory. The shear fractures are the final product of an intrinsically more complicated process. In spite of these advances, the relationship between the development of conjugate faults and the generation of fracture swarms has not been analyzed in depth.
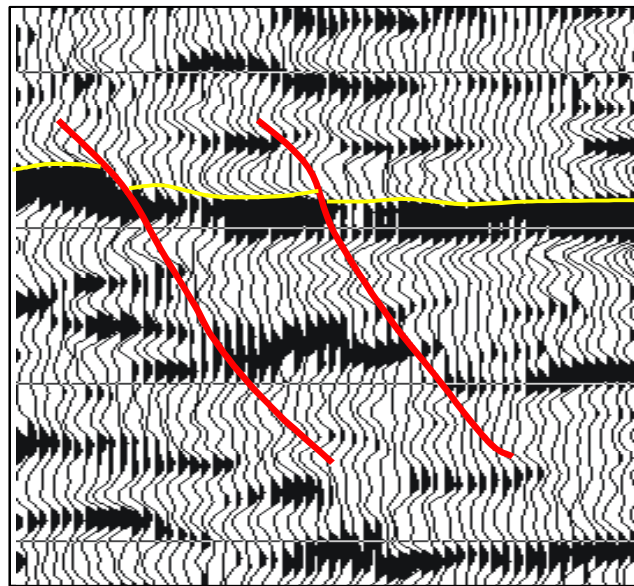

Figure 7.1: Asymmetric dimming effect (yellow horizon) associated with small
normal faults. Albian James Limestone at Texas.

The dimming or loss of reflectivity along high-impedance reflectors, commonly observed associated with faults, also requires further analysis. Although it seems intuitively reasonable to expect lower impedances at the damage zones around faults,

so far there is no clear mechanical explanation about how these fracture swarms are formed and why they create these dimming-amplitude anomalies. The fact that not all the faults show a dimming effect, and that the dimming effect in some cases is asymmetric with respect to the faults (Figure 7.1), shows the need for a more comprehensive explanation.

This study demonstrates that antithetic conjugate faults create fracture swarms that significantly reduce elastic impedance, causing the amplitude dimming. The analysis is based on outcrop observations and geomechanical modeling performed using Poly3D (Thomas, 1993). Outcrop fracture-spacing data are also used to model the expected seismic response of fracture swarms associated with small faults. The final section of this chapter shows a case study where a walk-away VSP is interpreted based on the application of the concepts learned from geomechanics and seismic modeling.

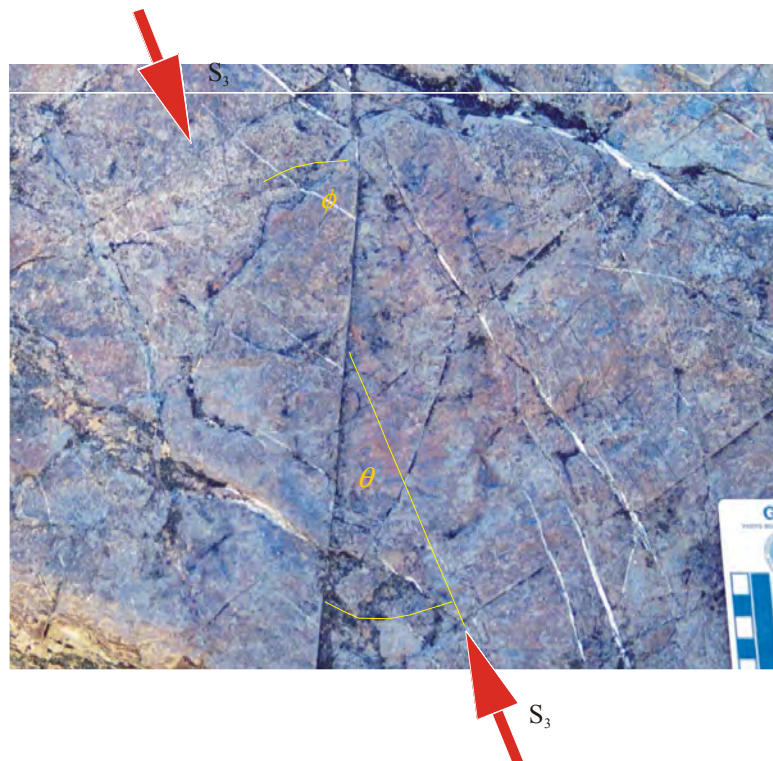## 7.3.   Geomechanics of Conjugate Faults and Fracture Localization

Figure 7.2: Field example of quartz-filled splay joints caused by shearing along a pre-existing fracture. The development of fracture swarms depends on the angle between the parent fracture and the splay (ϕ), and the angle between the remote stress S_3 and the parent fracture θ.

Conjugate faults in brittle rocks can develop as the result of hierarchical shearing of pre-existing and coeval discontinuities associated with progressive deformation (Davatzes *et al.*, 2003; Flodin *et al.*, 2004). Synthetic conjugate faults have the same sense of shearing, whereas antithetic conjugate faults have opposite sense of shearing. Depending on their orientation with respect to the remote stress field (Figure 7.2), splay joints generated at the tensional quadrants of sheared pre-existing discontinuities can suffer synthetic shearing, antithetic shearing, or no shearing at all (Table 7.1). The ideal condition for fracture localization occurs when the remote stress field bisects the splay fracture and the parent fracture. This is the condition for antithetic shearing of the splay fracture. In this case the highest tensional stress, or least compressive stress, concentrates within the region bounded by the antithetic conjugate faults.

7.3.1. Evolution of Conjugate Faults
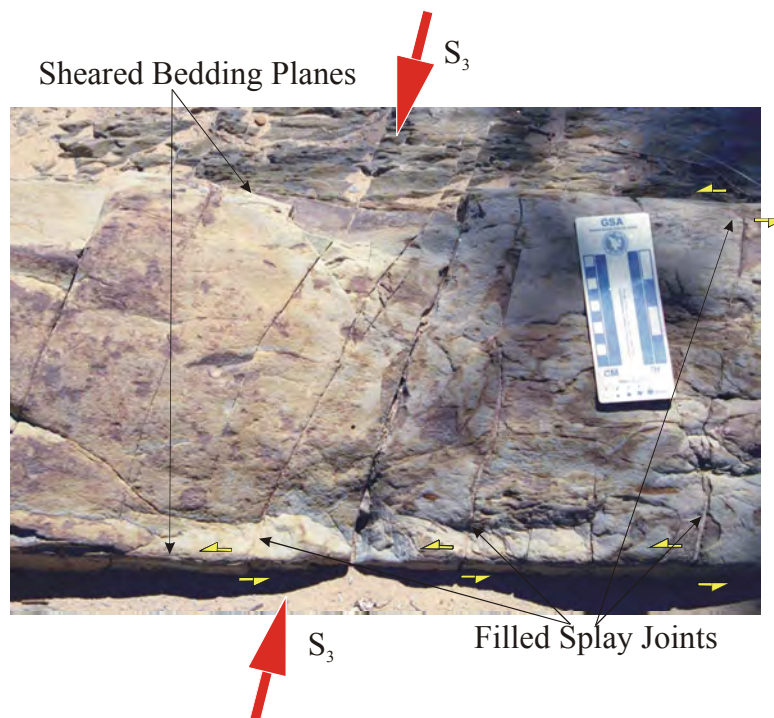
Figure 7.3: Example of splay joints resulting from shearing along bedding planes.

Conjugate faults result from the generation of splay fractures associated with shearing. Davatzes andn Aydin (2003) and Chapter 5 show good examples of this process. The stress perturbation around a sheared fracture is asymmetric around the feature, creating quadrants of tension and compression (i.e. Segall and Pollard, 1983). New opening-mode fractures can form when the tensional stress overcomes

the rock strength. These joints are known as splay or tail joints and their orientation is oblique with respect to the parent sheared fracture. Although in the subsurface the magnitude of the stress perturbation is small compared to the mean compressive stress, the existence of veins corresponding to filled splay joints indicate that tension does occur and facilitates the formation of new fractures, oblique to the pre-existing sheared discontinuities. Figure 7.2 and Figure 7.3 document clear examples of these quartz-filled splay joints.

Figure 7.4. Subvertical splay joints, formed due to slip along bedding planes, constitute new weak planes along which shear failure may occur. Slip along these splay joints (arrows indicating shear) generates a new stress perturbation that creates new splay joints. If the failure is dip-slip, as this case, these new splay joints will have the same azimuth as the previous ones but opposite dip direction.

The different stages of fracture development and progressive fracturing can be summarized in the following steps: (1) slip along pre-existing discontinuities; (2)

generation of splay joints within the adjacent brittle layers due to the stress field created by slip along the discontinuity; (3) synthetic or antithetic shearing along the new subvertical splay joints, depending on the orientation of the remote stress field (see Table 7.1), (4) formation of a second generation of splay joints, as shown in Figure 7.4 and Figure 7.5; and (5) linking and interaction of meter-scale faults to create larger faults and conjugate fault systems. The dominant mechanism in this process is hierarchical shearing of pre-existing discontinuities. The process may continue as progressive deformation goes on.
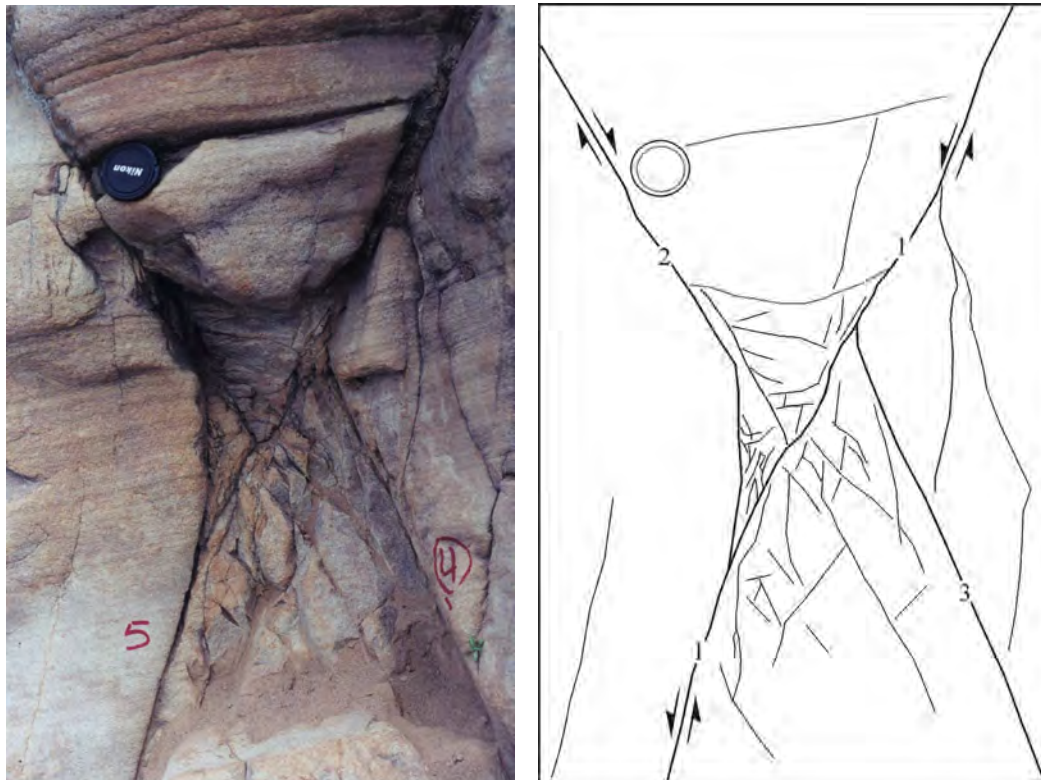
Figure 7.5. Picture and sketch showing a detailed view of the intersection of a set of conjugate faults. The parent fault is marked 1 in the sketch and 5 in the photograph. The secondary faults are marked 2 and 3 in the sketch, and one of them is marked 4 in the photograph. Notice the contrasting rock fragmentation inside and outside the region bounded by the faults, especially in the lower half. Also notice that the secondary faults bend and abut against the parent fault.

7.3.2. Geomechanic Model for Fracture Localization

Antithetic conjugate faults create the ideal condition for fracture localization and generation of fracture swarms (Figure 7.6). The stress perturbation around active conjugate faults depends on the orientation of the remote stress field and the newly formed splay with respect to the original discontinuity or parent fault (Florez and

Mavko, 2002). Figure 7.2 shows the geometric configuration, where ϕ is the angle between the splay and the sheared fracture, and θ is the angle between the remote stress field (inferred from the distribution of closed and open fractures) and the sheared fracture. A summary of the results obtained from geomechanic modeling by Florez and Mavko (2002) is presented in Table 7.1. These results show that fracture localization occurs when the angle between the remote stress field and the parent fault is smaller than the angle between the splay fault and the parent fault. This is the condition for generation of antithetic conjugate faults, since the sense of shear along the newly formed splay is opposite to the sense of shearing in the parent fault.
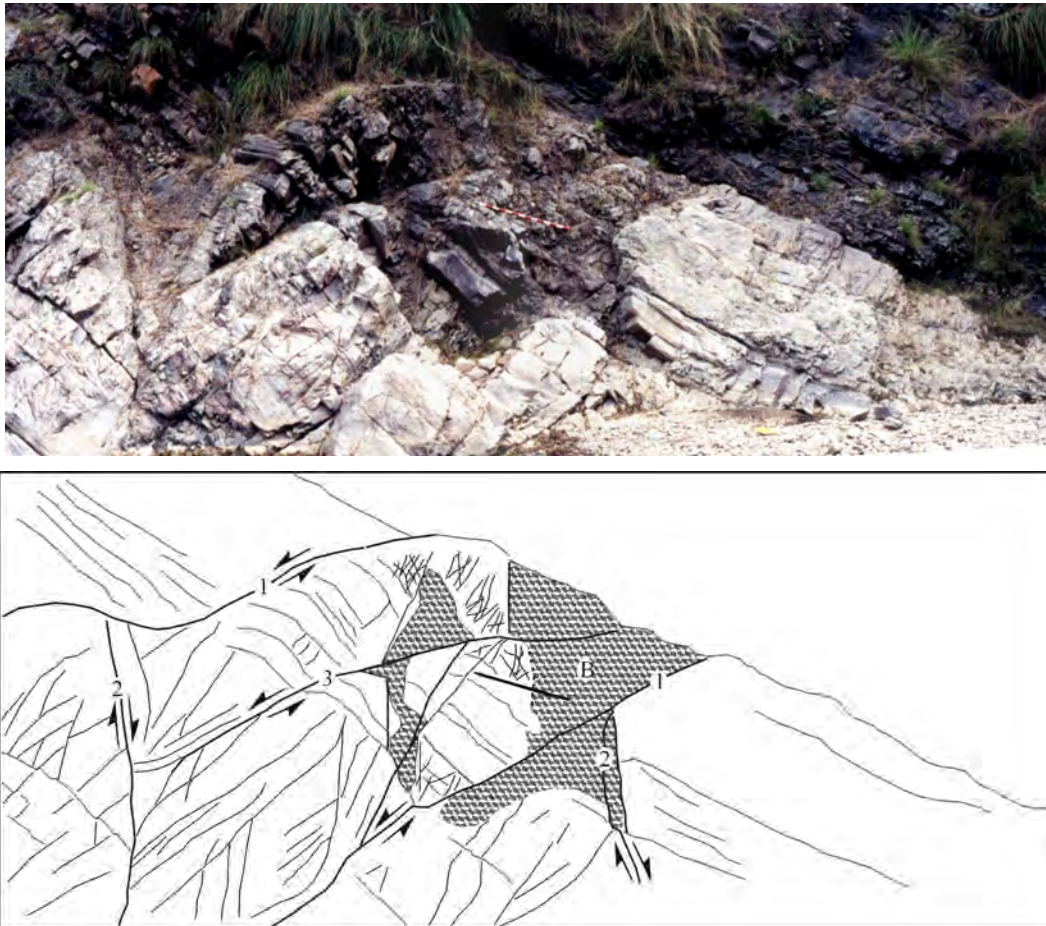
Figure 7.6: Tilted conjugate normal faults at 10-m scale. The number on each fault indicates the age relationship and the hierarchy: (1) parent faults created by link and interaction of splay fractures: (2) main conjugate or antithetic set formed from splays created by slip along 1: (3) secondary synthetic set formed from splays created by slip along 2. The stick scale is 1.5 m long. B= Breccia zones

In active antithetic conjugate faults, fracturing tends to be concentrated in the area bounded by the larger conjugate faults. As illustrated in the geomechanical model shown in Figure 7.7, the highest tensional stress or least compressive stress

occurs in the region bounded by the antithetic conjugate faults. If the conditions are appropriate for fracturing (high pore pressure or isolated inclusions in brittle rocks), this bounded region is where fractures will occur first. Field observations, like the one shown in Figure 7.6, demonstrate that this is actually the region where fracturing concentrates, creating abrupt lateral variations in fracture density along the same bed.
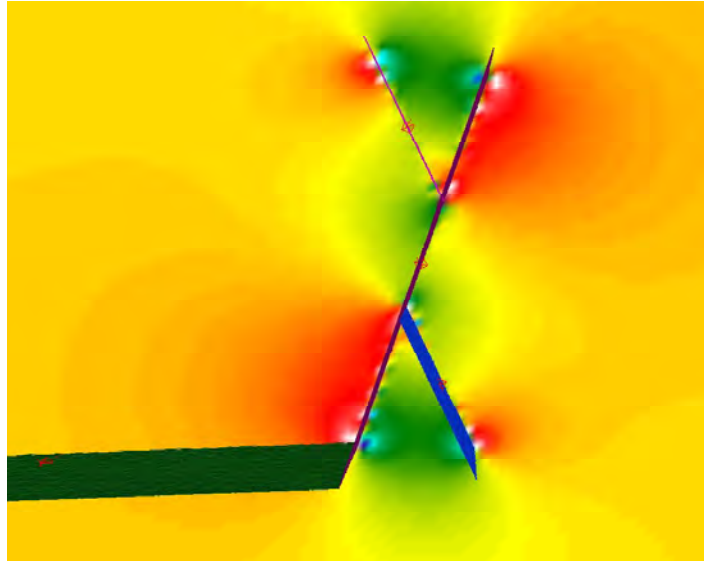

Figure 7.7: Geomechanic model of the stress distribution resulting from normal faulting along opposite-dipping subvertical discontinuities. Red color shows areas of highest compression (lowest tension), and blue and green colors show areas of highest tension (least compression).

Table 7.1: Summary of results from a geomechanical model of the stress distribution and splay-jointing resulting from shearing along conjugate faults (Florez and Mavko, 2002). Figure 7.2 shows the geometric configuration.

S_3 (θ) and splay (ϕ) orientation	Splay Development	Shearing	Fracture Distribution
$\theta > \phi$	Outside region between conjugate faults.	Synthetic (same sense)	Widespread fracturing
$\theta = \phi$	No new splays formed.	Not shearing	Splay growth
$\theta < \phi$	Inside region between conjugate faults.	Antithetic (opposite sense)	Fracture localization

7.4. Outcrop-based Seismic Modeling of Small Faults

I use an outcrop-based conceptual-model of along-azimuth fracture-density variation to model the seismic signature of small faults. The conceptual model of

fracture-density distribution is based on the fracture density-scanlines described in Chapter 5, and specifically corresponds to the fracture density that one may find when crossing fault zones like those documented in Figure 5.4. This fracture density scanlines can be translated into relative values of crack density. The final results show that flexure can depict faults with offsets larger than l/16 of the wavelength. Faults with smaller offsets can generate amplitude anomalies if they have an associated fracture swarm.

7.4.1. From Fault Spacing to Crack Density

Fracture density can be translated into crack-density values, assuming all the fractures have similar wall roughness. A subsurface can be idealized as two rough surfaces in contact, creating an aligned set of small cracks. These small cracks can be represented as penny-shaped cracks with different aspect ratios and approximate radius c_i. The free surface area (A_{cr}) at the fracture walls can be expressed as follows:

$$A_{cr} = \pi \sum_{i=1}^{k} n_i c_i^2 ,$$ (7.1)

where n_i is the number of cracks with approximate radius c_i. This free surface area can also be represented by a single large crack of equivalent radius c_e given by the following expression:

$$A_{cr} = \pi c_e^2 .$$ (7.2)

In a layer of thickness T, as shown in Figure 7.8, Hudson's crack-density parameter ε is by definition (Hudson, 1981; Mavko *et al.*, 1998):

$$\varepsilon = \frac{N c_e^3}{LWT} = \frac{c_e^3}{SLT} ,$$ (7.3)

where N is the number of fractures within a width interval W, and the spacing S is the ratio W/N. Taking a length interval equal to T ($L = T$), and considering that c_e can always be expressed as a fraction of $T/2$, the crack-density parameter can be expressed in terms of the fracture index (Narr, 1990):

$$\varepsilon = \frac{\beta^3 T^3}{8SLT} = \frac{\beta^3 T}{8S} = \frac{\beta^3 I}{8} ,$$ (7.4)

where β represents the ratio between c_e and $T/2$, which ranges between 0 and 1. Narr (1990) defined the fracture index (I) as the ratio of bed thickness to fracture spacing (T/S). Bai and Pollard (2000) defined the fracture saturation as the stage where the

fracture index reaches a value of 1. At saturation stage the crack-density parameter is about $0.125\beta^3$.
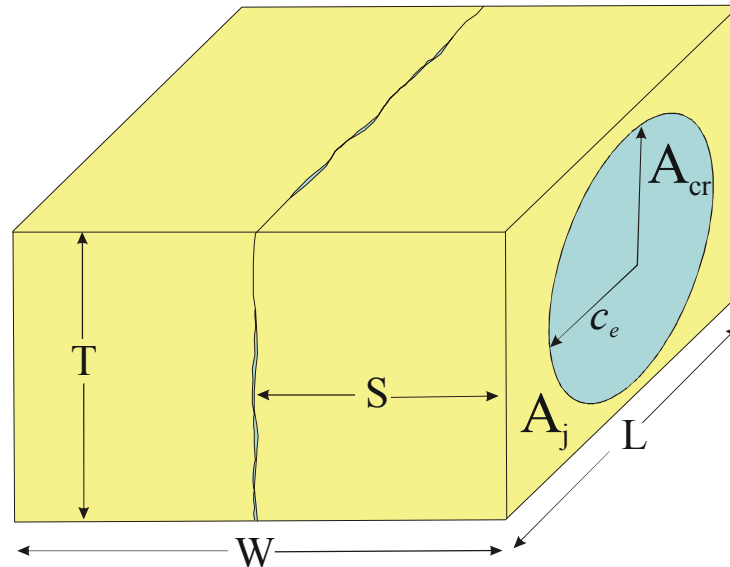

Figure 7.8: Diagram to illustrate the relationship between fracture spacing (S) and Hudson's crack-density parameter. See text for explanation.

A critical crack density can be defined as the point where the rock completely loses its strength and behaves as a suspension. Two conditions are required to reach this stage: (1) fractures are continuous across the rock volume under consideration; (2) most of the areas of both fracture surfaces are not in contact. The first condition is approximately reached at the fracture saturation stage (*I=1*). The second condition is reached when β is about 1. Under these assumptions, a reasonable value for the critical crack-density parameter is 0.125.

7.4.2. The Effect of Confining Stress

Fracture closure caused by confining stress considerably decreases the crack density estimated from fracture-spacing data. Joint and fracture closure under confining stress has been the subject of considerable research in engineering for decades (i.e. Bandis *et al.*, 1983). Ideally, a fracture with very smooth surfaces will be closed at very low confining stresses. In reality, roughness of fracture surfaces impedes fracture closure, and the stress required to close the fracture increases as the contact surface area of the fracture walls increases.
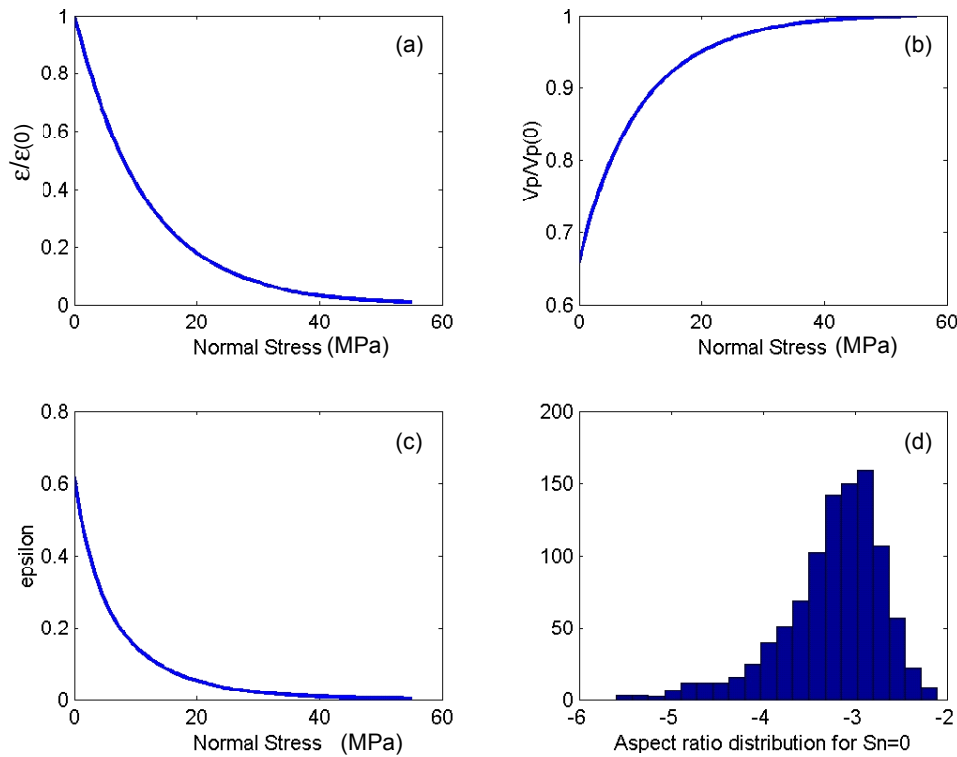
Figure 7.9: Summary of the method to approximate the effect of confining stress on crack density. Figures (a), (b), and (c) show normalized results as a function of the applied normal stress: (a) crack density parameter ε; (b) P-wave velocity; (d) epsilon anisotropy parameter. Figure (d) shows the assumed initial crack density population and the respective aspect ratios.

This process can be approximately modeled assuming that a single fracture is composed of a population of small cracks with different aspect ratios. Mavko *et al.* (1998) summarize the solutions for the confining stress required to close two-dimensional cracks. Although the aspect ratio of any crack decreases as confining stress increases, crack closure depends on the initial aspect ratio (the aspect ratio at zero confining stress). Following Mavko *et al.* (1998), in the case of lenticular cracks with smoothly tapered tips, the closure aspect ratio (α_{closed}) for any given confining stress can be obtained from the following expression:

$$\alpha_{closed} = \frac{4(1-\nu^2)}{3E} S_n . \qquad (7.5)$$

In this expression, ν and E correspond to the Poisson's ratio and the Young's modulus of the solid material, respectively, and S_n is the normal confining stress. The population of open cracks gradually reduces as the confining stress increases, and more fractures with larger initial aspect ratios are closed. This method allows us to

model the effect of confining stress on crack density, as illustrated in Figure 7.9. A scanline with variations in fracture spacing similar to those presented in Figure 5.4 can be reduced to a crack density scanline using Equation 7.4 (assuming β=1) and the method to incorporate the effect of confining stress described above. The blue line in Figure 7.10 shows the results obtained for a hypothetical scanline crossing two fault zones. Normalization to a maximum crack density of 0.1 was also applied, since this is the maximum value allowed by the classical Hudson's model (i.e. Mavko *et al.*, 1998). The red line in Figure 7.10 illustrates the final result.
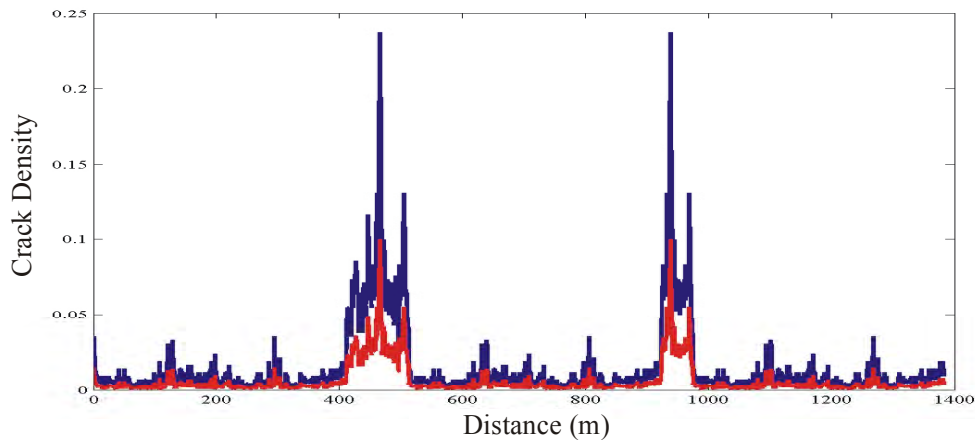

Figure 7.10: Scanline of crack density obtained from fracture spacing data. This hypothetical scanline shows the expected crack density distribution associated with two fault zones located at 400 m and 900 m. The red line is normalized to the maximum crack density allowed by the Hudson's model.

7.4.3. Synthetic Seismograms

The crack density scanline depicted by the red line in Figure 7.10 can be transformed into velocity and impedance using Hudson's model for cracked media (Mavko *et al.*, 1998, p. 133), and the expression for the quasi-longitudinal wave in a transversely isotropic media (Mavko *et al.*, 1998, p. 22). This obviously assumes that there are not lateral variations in elastic properties or density of the unfractured material. The final results are illustrated in Figure 7.11. As expected, the effect on velocity increases with the angle of incidence. This effect cannot be captured by one-dimensional (normal incidence) synthetic seismograms.
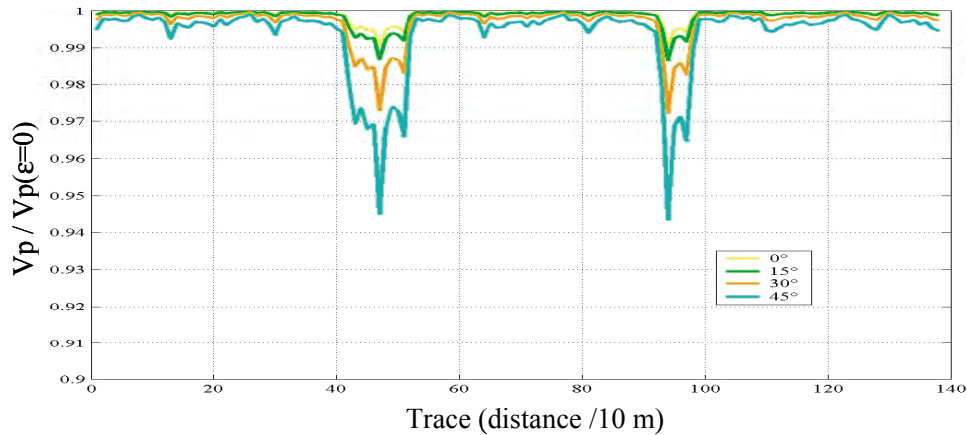
Figure 7.11: Modeled lateral velocity variations caused by subvertical fault zones along otherwise homogeneous material. The effect increases with the angle of incidence.

The synthetic seismograms, based on the modeled lateral variations in elastic properties caused by small faults and their associated fracture swarms, illustrate the expected seismic response of these small faults. The model consists of a half space with positive contrast in reflectivity. The contrast in reflectivity varies laterally due to the effect of high fracture-density zones or fracture swarms. Seismic wavelets of 50 and 25 hertz are used, and an average velocity of 4000 m/s, resulting in wavelengths of 80 and 160 m, respectively. Faults with offsets of 10 and 5 m are modeled. The results show that offsets of about $\lambda/8$ and up to $\lambda/16$ can be resolved by small variations in flexure (see Figure 7.12). Faults with offsets below $\lambda/16$ cannot be identified from the seismic section (Figure 7.13), but the associated fracture swarms generate an amplitude anomaly (Figure 7.14) that might be identified with analysis of seismic attributes.
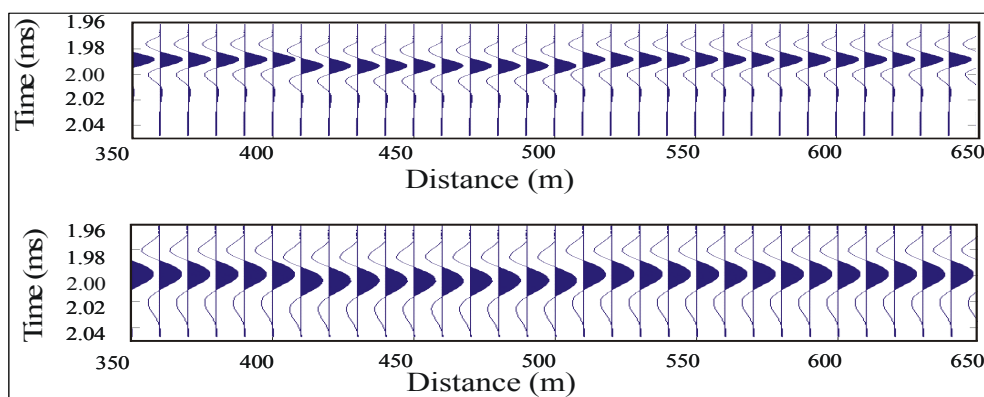

Figure 7.12: Synthetic seismograms for a small fault with 10 m of vertical offset, for high (50) and low (25) frequencies. The offset is still observable at high frequencies but disappears when the wavelength increases. Offset to wavelength ratios are 1/8 (above) and 1/16 (below).
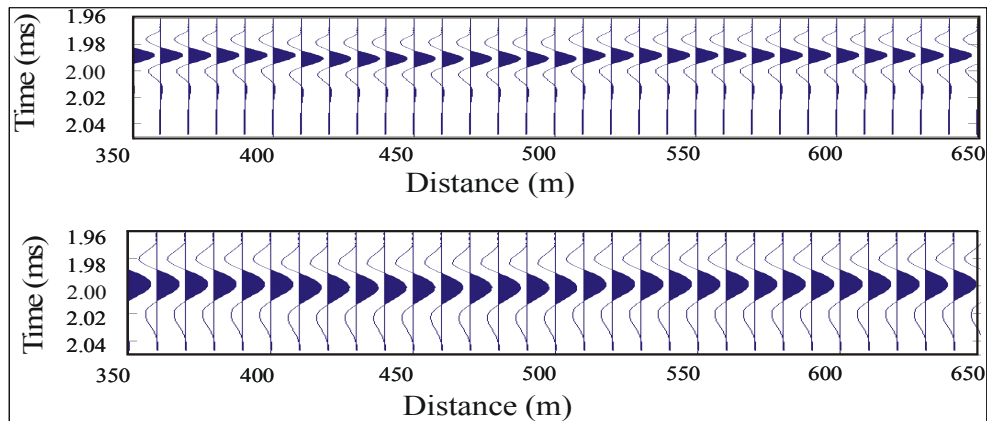
Figure 7.13: Synthetic seismograms for a small fault with 5 m of vertical offset. The offset is not longer discernible from the seismic section. Offset to wavelength ratios are 1/16 (above) and 1/32 (below).
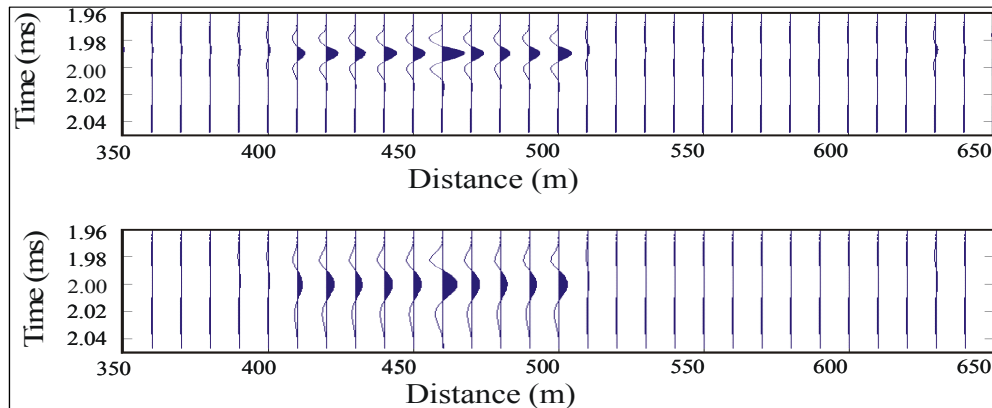
Figure 7.14: Amplitude variation in the seismic response for the case of a small fault with 5 m of vertical offset. Although the offset is not discernible from the seismic section, the amplitude anomaly shows the fracture swarm. This effect increases when incorporating lateral offsets.

7.5. Interpretation of a Walk-away VSP

This section presents the interpretation of a walk-away VSP based on the combination of information obtained from logging-while-drilling (LWD) tools and the concepts discussed in the previous sections. The data come from the well Hendersson-1, Neuville Field, east Texas. The reservoir rocks are Aptian to Albian limestones known as the James Limestone (Figure 7.15). Outcrop exposures at Yates Field (Figure 7.16 and Figure 7.17) can be used as an analogue for the fault and fracture systems of the James Limestone at Neuville Field.

Figure 7.15: Geologic model of James Lime along the Hendersson-1 path, based on LWD gamma ray (Courtesy of Marathon).

The seismic interpretation of the VSP is based on the analysis of seismic attributes and the match to geologic markers resul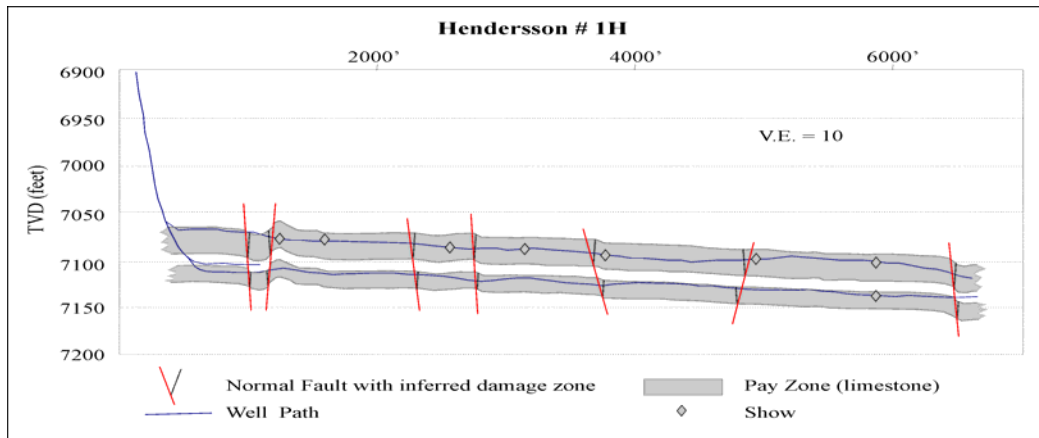ting from the time-to-depth conversion. The time-to-depth conversion, is based on check-shot data (Figure 7.18). Different attributes have been calculated to help in the seismic interpretation of the VSP: amplitude, instantaneous phase, instantaneous frequency, frequency centroid, pseudo-impedance, the instantaneous amplitude (envelope), and the true amplitude. A significant lateral variation in amplitude occurs along the horizon of interest, and is interpreted to be the effect of the change in the angle of incidence (AVA effect). Instantaneous phase and true amplitude were the most useful attributes to identify small faults in the seismic data.

7.5.1. Outcrop Analogue

The Cretaceous exposures just north of the Yates field (Midland, Texas) can be used as an analogue for the James Limestone at Neuville Field (Texas). Regularly spaced normal faults (Figure 7.16), with relatively small and laterally variable offsets (Figure 7.17), dominate the structural style at this locality. Very localized fracture swarms are associated with these small faults. The structural grain at Yates is WNW, but may differ at Neuville Field. Although a detailed description of these faults was not performed, these general observations provide a conceptual framework for the James Limestone at Neuville Field.
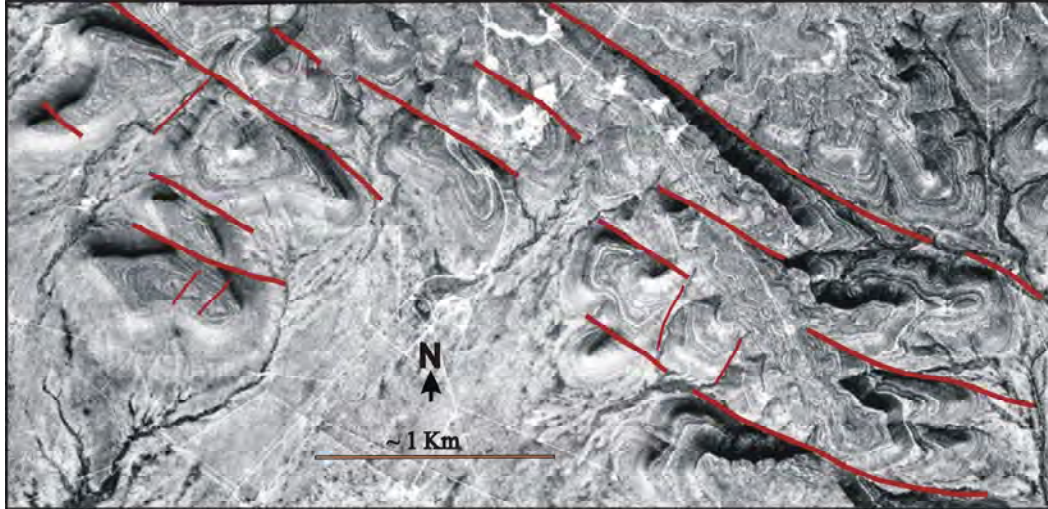
Figure 7.16: Radar image showing the dominant structural style north of Yates Field, Texas. The red lines correspond to normal faults.

Figure 7.17: Cliff exposure corresponding to the small normal fault located at the extreme west of Figure 7.16. The abundance of vegetation along the fault trace follows a higher fracture density near the fault, in the hanging wall.

7.5.2. Seismic Attributes

The check-shot (Figure 7.18) allows an accurate location of top James Lime on the VSP seismic section (Figure 7.19). Top James Lime is located at 1.295 milliseconds (TWT). The interval velocity at this depth is 7000 ft/s, and since the James Lime at this locality is only about 70 ft thick (Figure 7.15), this limestone unit corresponds to only 20 to 30 milliseconds in the TWT seismic section. The location of top James Lime in the VSP seismic section indicates a change in polarity. A positive reflectivity contrast should be expected between the James Lime and the Bexar shale above it. The VSP section shows a negative reflectivity contrast.

The instantaneous amplitude and instantaneous phase are the two attributes that provide a better image of the reservoir structure and the lateral variations in reflectivity. The seismic attributes calculated are those related to the amplitude, frequency or phase of the recorded signal, including the pseudo-impedance (Table 7.2). The amplitude envelope, or reflection strength, measures the total energy of the

seismic wave and can be obtained from the analytical signal of the trace. The instantaneous phase is the natural logarithm of this transform, and the instantaneous frequency is the derivative of the instantaneous phase. Table 7.2 presents a summary of the seismic attributes calculated and the main transforms required to calculate them.
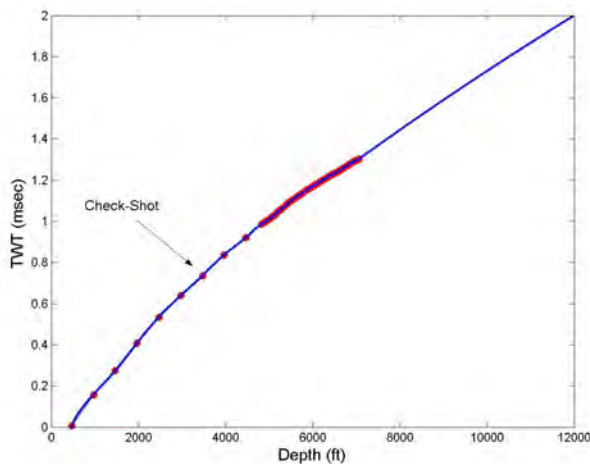

Figure 7.18: Time-to-depth table based on check-shot data.

The attributes related to the amplitude are the amplitude itself (Figure 7.20), the pseudo-impedance (Figure 7.21), the instantaneous amplitude (Figure 7.22), and the true amplitude (Figure 7.23). In essence, the amplitude-based attributes are equivalent, and all of them carry the same information; however the true amplitude (Figure 7.23) provides an image of the reservoir with better resolution of the subtle amplitude anomalies along the reflector that approximately corresponds to the James Limestone.

The VSP shows evidence of AVA (Amplitude Variation with Angle) effects superimposed on the amplitude anomalies. A good example of these AVA effects occurs at the James Lime interval itself, and is particularly evident in the true amplitude section (Figure 7.23). Notice that between 7050 ft and 7100 ft, there is a constant gradient of amplitude reduction along the well trajectory. The angle of incidence varies between 20° to 30° from the near to the far offset along the well path.

The frequency-based attributes, instantaneous frequency (Figure 7.24) and frequency centroid (Figure 7.25), do not show significant attenuation effects. The instantaneous frequency helps to outline the lateral continuity of the reflections (Figure 7.24). The frequency centroid (Figure 7.25) shows that the dominant frequencies in the VSP seismic section range from 40 to 70 Hertz.

The instantaneous phase (Figure 7.26) provides the best image to analyze the lateral continuity of the reservoir. Since it is calculated by taking the natural logarithm of the instantaneous amplitude, it enhances both the pick, the troughs and the inflection points of the wavelet, providing an image with better continuity and resolution. This image, however, does not preserve any information about the seismic properties of the horizons.
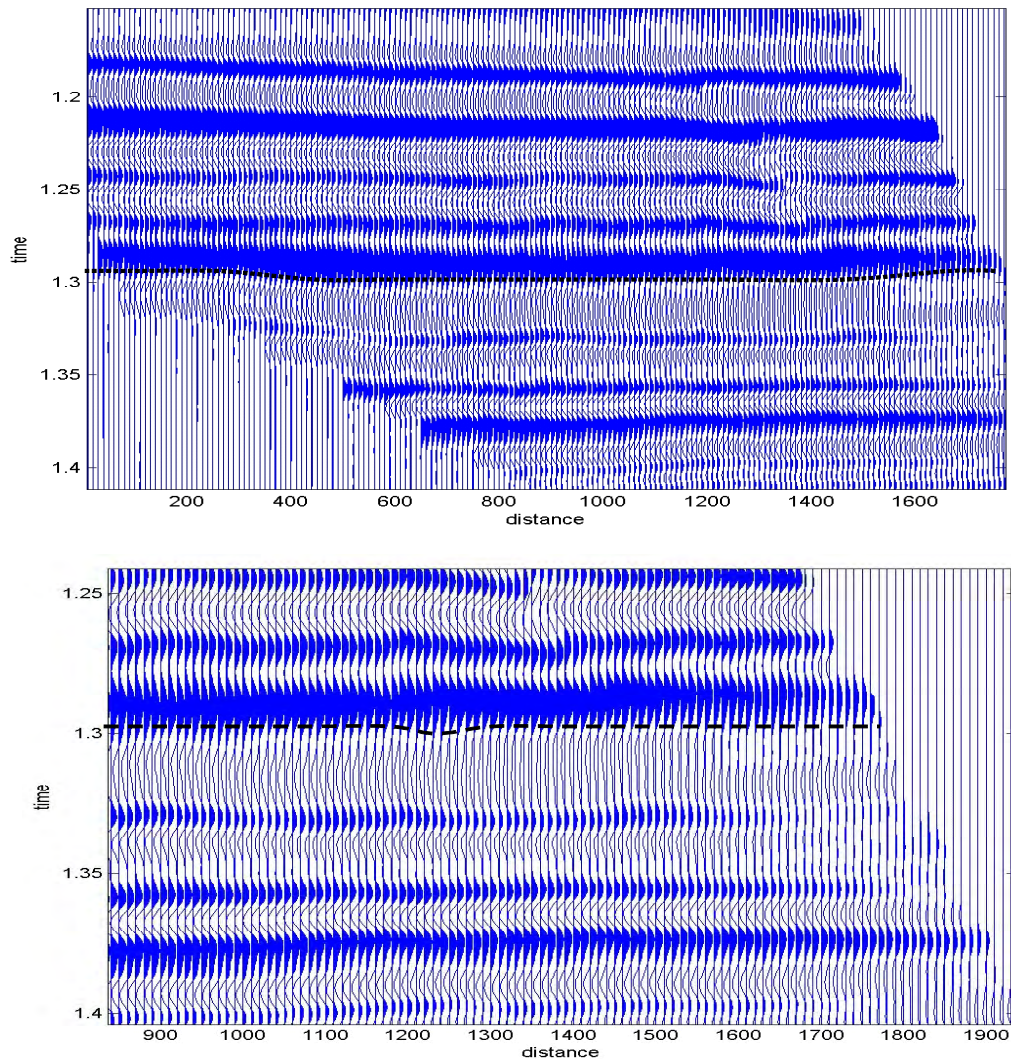

Figure 7.19: Seismic sections from the 5700-offset VSP, showing the location of top James Lime.

Table 7.2: Attributes of the seismic trace and the transforms used to calculate them
(Bracewell, 1965; Sheriff and Geldart, 1995; Mavko *et al.*, 1998).

Attribute or transform	Expression	Comments
Amplitude	$A = f(t) = S(t)e^{\varphi}$	Trace
Fourier transform	$F(v) = \int_{-\infty}^{\infty} f(t)e^{-i2\pi vt} dt$	v: frequency.
Hilbert transform	$F_{Hi} = F_e(v) + i\left(-\dfrac{1}{\pi v}\right) * F_e(v)$	F_e: Fourier transform of the even part of $f(t)$.
Analytical signal	$S(t) = f(t) - iF_{Hi}(t)$	
Instantaneous envelope	$E(t) = \left(f^2(t) + F_{Hi}^2(t)\right)^{1/2}$	Instantaneous amplitude
True amplitude	$A_{\varphi=0}(t) = F(0,t) = \int_0^t f(t)dt$	
Instantaneous phase	$A = \varphi(t) = \text{Im}[\ln(S(t))]$	
Instantaneous frequency	$\omega(t) = \dfrac{d\varphi(t)}{dt}$	
Pseudo-impedance	$Z(t) = Z_0 e^{k\int_0^t f(t)dt}$	Z_0 and k integration constants
Frequency centroid	$C(t) = \dfrac{F'(0,t)}{i2\pi F(0,t)}$	

Figure 7.20: VSP seismic section showing the variation of amplitude (seismic trace) along the path of Hendersson-1. The asterisks (*) indicate the location of faults according to the interpretation of the LWD gamma ray.
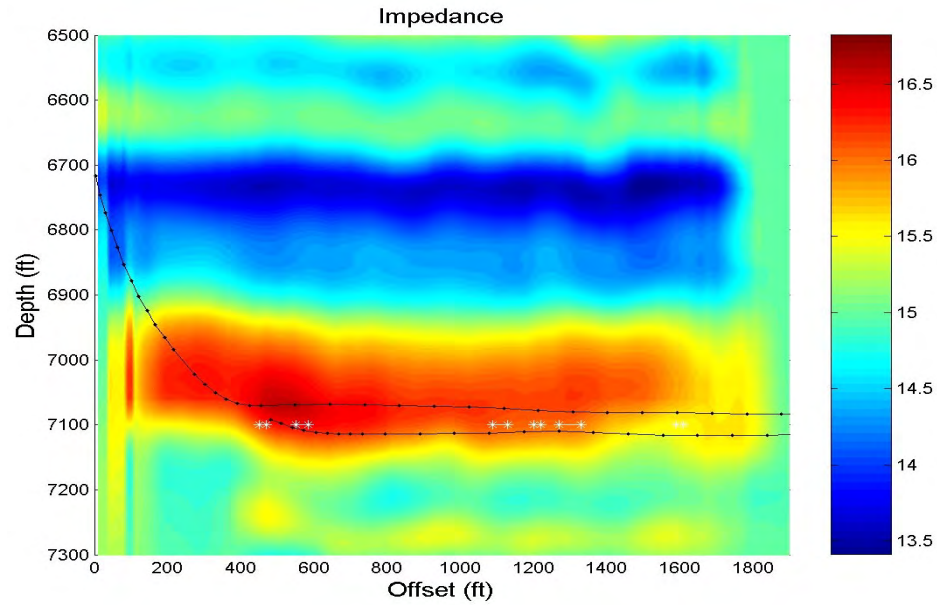
Figure 7.21: VSP seismic section showing the variation of pseudo-impedance along the path of Hendersson-1. The asterisks (*) indicate the location of faults according to the interpretation of the LWD gamma ray.
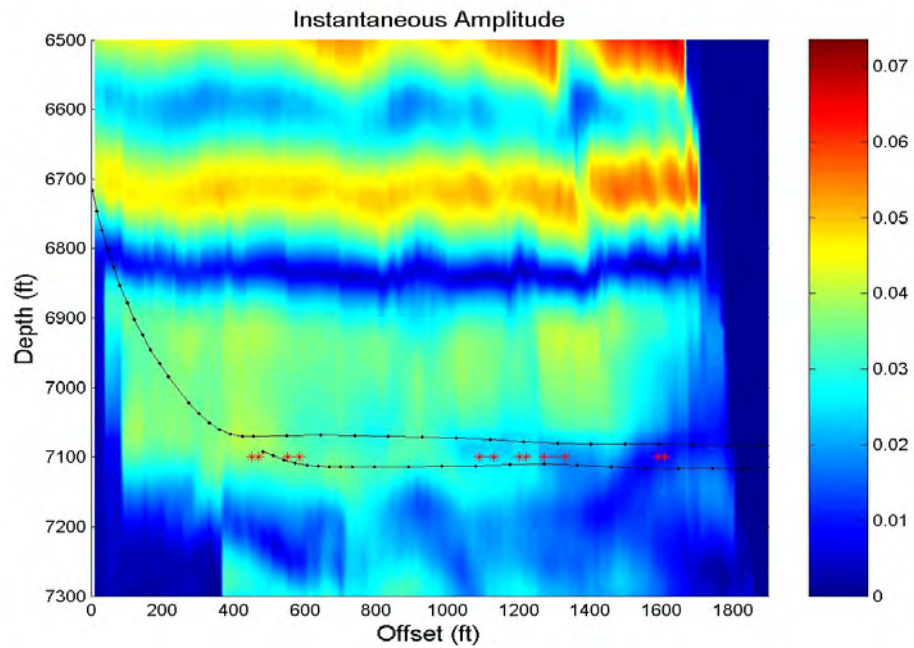
Figure 7.22: VSP seismic section showing the variation of instantaneous amplitude (envelope) along the path of Hendersson-1. The asterisks (*) indicate the location of faults according to the interpretation of the LWD gamma ray.
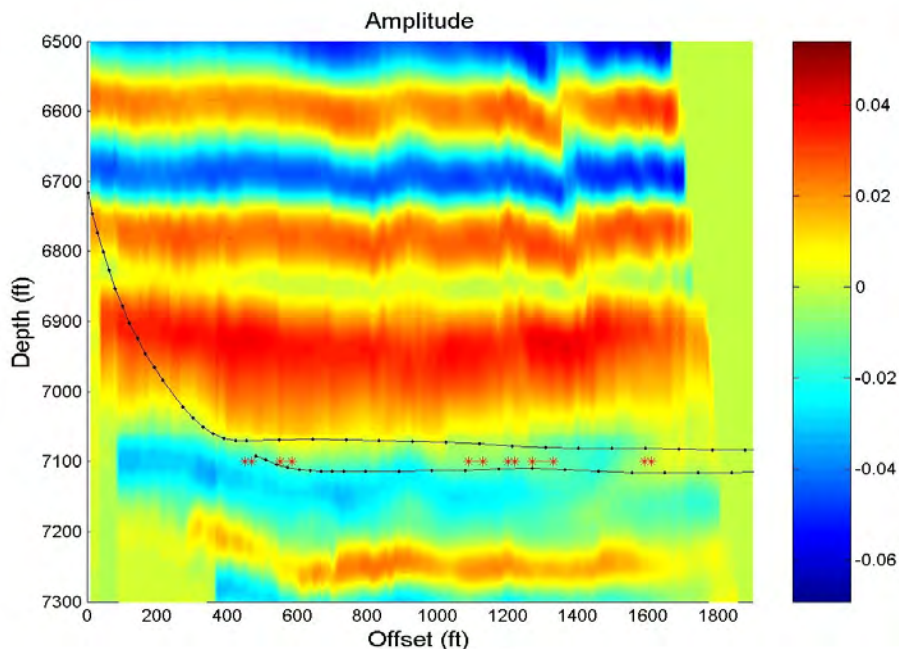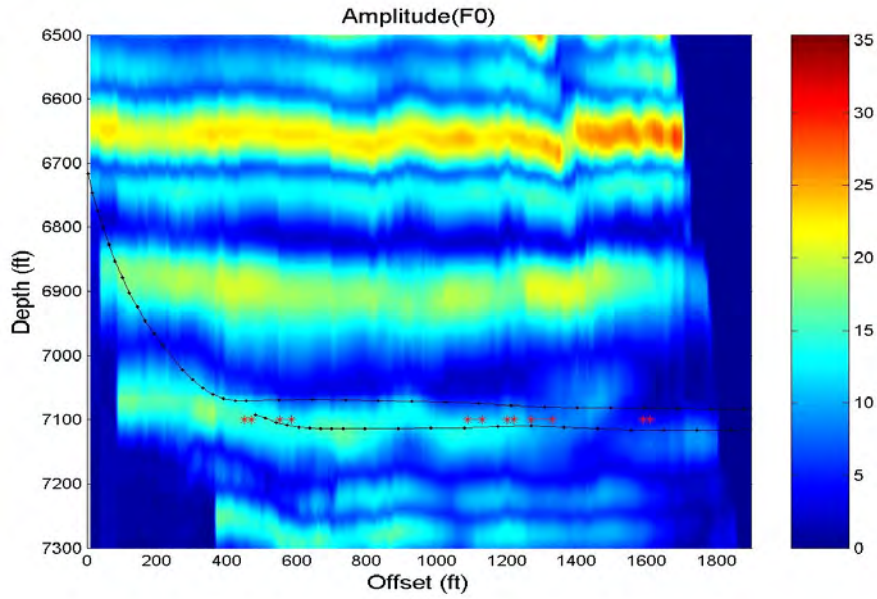
Figure 7.23: VSP seismic section showing the variation of true amplitude along the path of Hendersson-1. The asterisks (*) indicate the location of faults according to the interpretation of the LWD gamma ray.
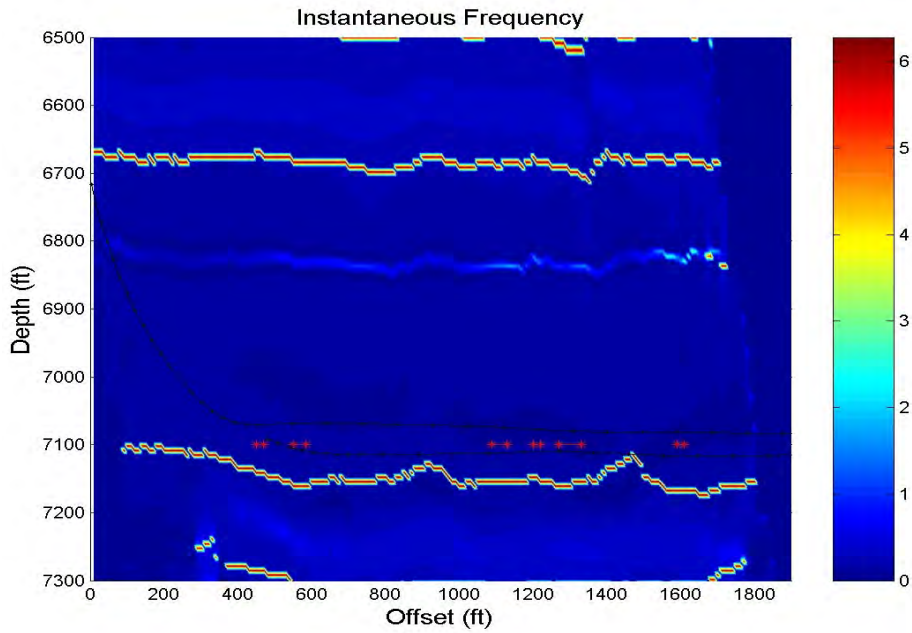
Figure 7.24: VSP seismic section showing the variation of instantaneous frequency along the path of Hendersson-1. The asterisks (*) indicate the location of faults according to the interpretation of the LWD gamma ray.

Figure 7.25: VSP seismic section showing the variation frequency centroid along the path of Hendersson-1. The asterisks (*) indicate the location of faults according to the interpretation of the LWD gamma ray.

Figure 7.26: VSP seismic section showing the variation of instantaneous phase along the path of Hendersson-1. The asterisks (*) indicate the location of faults according to the interpretation of the LWD gamma ray.

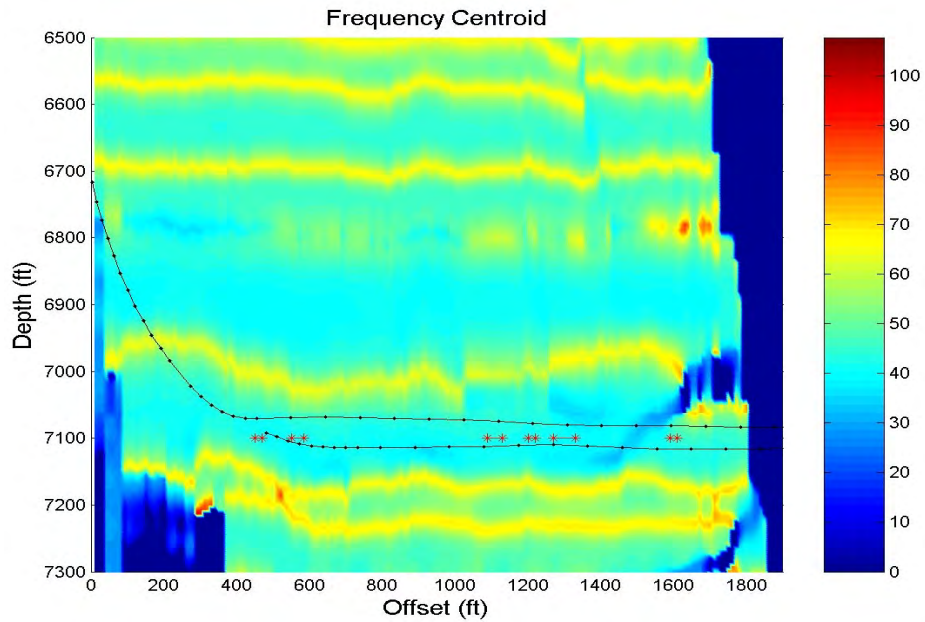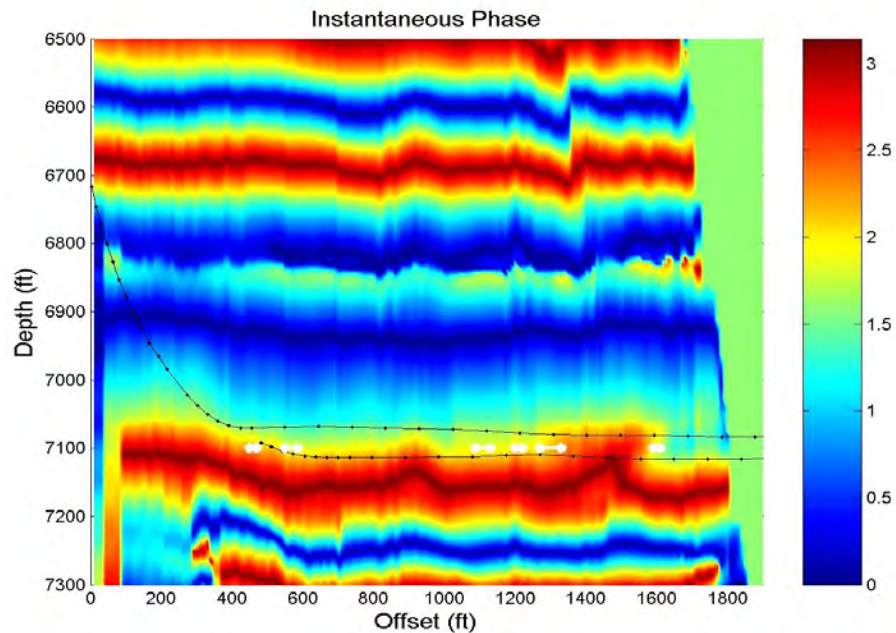### 7.5.3. VSP interpretation and Comparison with Lateral Boreholes

The combination of the VSP seismic sections and the geologic interpretation of the LWD gamma ray allow us to locate small faults along the path of Hendersson-1. The gamma ray LWD log and other information collected during the drilling of Hendersson-1, such as drilling rate (DR) and calcite (CALC) content in the mudlog, were used to generate a preliminary interpretation of small faults along the well path (Figure 7.27 and Figure 7.28). The final interpretation was superimposed on the VSP sections, as discussed above. The coincidence of offsets or amplitude anomalies with the interpreted fault locations provide an additional evidence of the presence of faults and probable fracture swarms at these locations; the final interpretation is shown in Figure 7.28 and Figure 7.29.

The horizontal boreholes at Hennndersson-1 demonstrate the presence of fracture swarms and small faults within the James Limestone. Although most of these faults cannot be imaged with conventional seismic techniques, the walk-away VSP can be used to identify them. According to Marathon's interpretation, there are at least six normal faults along the horizontal sections of Hendersson-1. We reviewed Marathon's interpretation, especially along the section between 0 to 2000' offset, which is the interval relevant for the comparison with the VSP data.
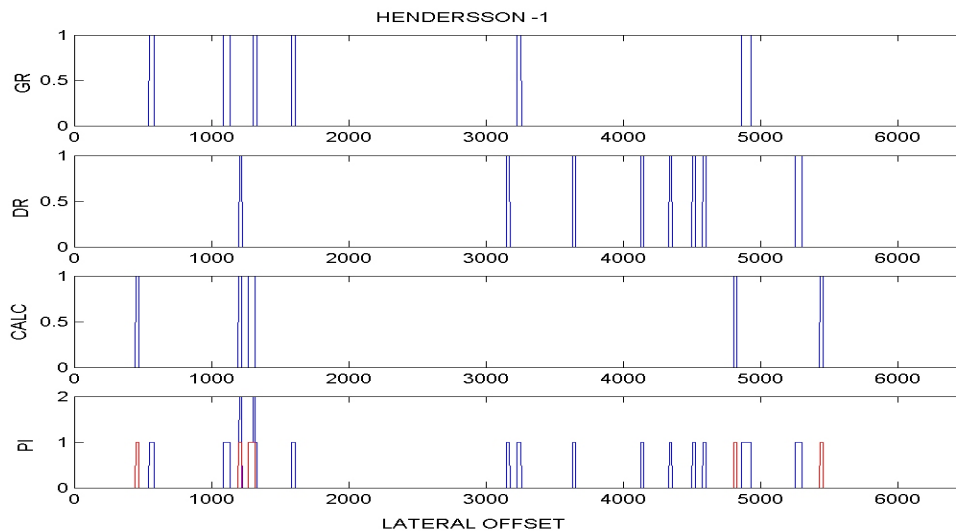
Figure 7.27: Location of probable faults along the upper lateral wellbore of Hendersson-1. PI stands for Probability Indicator and corresponds to the number of fault-indicators (GR, DR or CALC) overlapping over a given location, within a window of 20 feet. Calcite (CALC, and red in the lower graph) overlaps in one case with the drilling rate (DR) and in another case with the gamma ray (GR). The indicator anomalies corresponding to these two locations are considered to have a higher probability of being faults.

To evaluate the uncertainty related to the different faults interpreted along the lateral wellbores of Hendersson-1, we apply a systematic analysis to the main parameters that may indicate faults along the wellbore: (1) gamma ray log, (2) drilling rate, and (3) the presence of calcite. In this analysis, I add both the indicator absolute value and the derivative, and apply a threshold, leaving only those points that correspond not only to high values, but also to high or abrupt changes. Afterwards, I give a value of one for each fault location derived from each parameter, and sum all them together using a match window of 20 feet. As a result, if two indicators overlap they sum together; then the higher the value obtained for each position, the higher the probability that a fault is located at that lateral offset (Figure 7.27).

In addition, we compare the fault locations along both the upper and lower lateral wellbores. A window of 50 feet was used to compare the fault locations. As explained above, when the fault locations are within the window, the indicators are summed, resulting in a higher probability indicator for a fault at that particular offset. The results are shown in Figure 7.28. Taking only the zones where fault indicators occur in the two wellbores would miss some of the faults, since only four faults would remain. This comparison would omit, for example, the fault at 1600 ft of lateral offset, considered to be the fault with the largest offset in Marathon's interpretation (Figure 7.15).
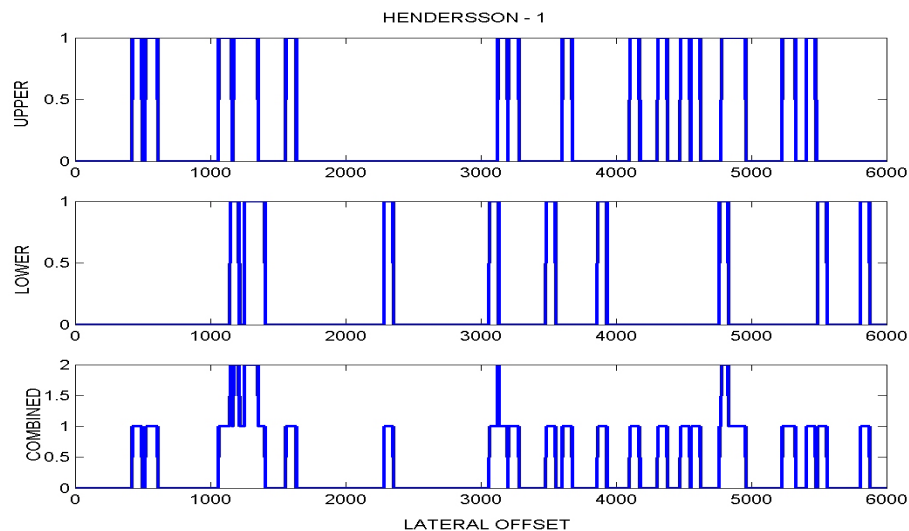

Figure 7.28: Location of probable faults along the upper lateral and lower wellbores of Hendersson-1, and comparison between the two (combined). The location of faults along each lateral is given by any of the indicators shown in Figure 7.27 (GR, DR or CALC). The comparison uses an overlapping window of 50 feet.
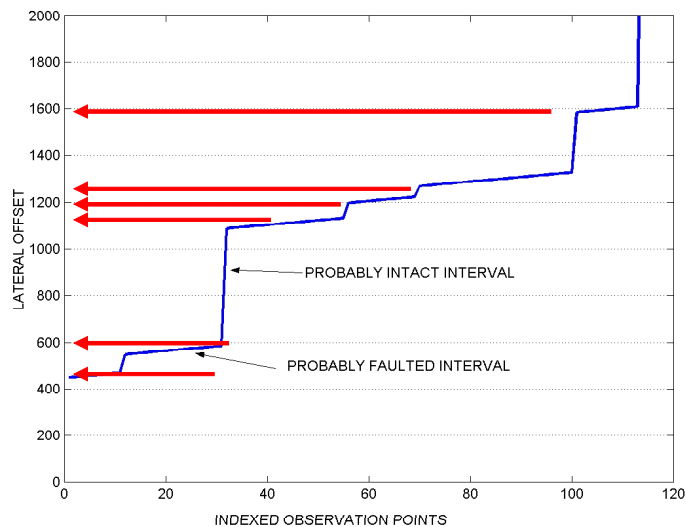
Figure 7.29 Visualization of the distribution of probable fault zones along the lateral section of Henderson-1, from 0' to 2000' offset. The subhorizontal line segments correspond to probably faulted intervals, whereas the subvertical segments correspond to probably non-faulted or intact intervals. This graph is based on the results of the combination of fault indicators (GR, DR and CALC) on both the upper and the lower lateral.

The final interpretation of faults along the horizontal boreholes is the result of a different method of comparison. This method also uses an overlapping window of 50 feet, but instead of assigning a fault where fault indicators occur in both wellbores, we add 1 to a counter (plotted as indexed observation points in Figure 7.29) if the probability indicators are positive in the overlapping window. The change in the slope of the graph shown in Figure 7.29 becomes the fault indicator. Six breaks in the slope are identified along the segment between 0 and 2000' of lateral offset, and seem to correspond to four faults located at about 450', 600', 1200' and 1600' of lateral offset. The location of faults obtained from this analysis constitutes the most likely scenario, which can be compared to the distribution of amplitude anomalies along the 152°-azimuth VSP.

The comparison of the VSP data and the geologic interpretation shows that amplitude anomalies and vertical offsets observed in the VSP section coincide with fault locations. The true-amplitude section provides the image with better resolution (Figure 7.30). In spite of the presence of AVA effects, the largest faults predicted from the gamma ray log coincide with significant amplitude anomalies along the James horizon in Figure 7.30. Similarly, the instantaneous phase images (Figure 7.31) clearly outline the offset of seismic horizons, which coincide with the interpreted faults and the amplitude anomalies. These three independent lines of evidence provide enough support to the final seismic interpretation of the VSP data,

shown in Figure 7.30 and Figure 7.31. Four faults have been finally interpreted, with offsets between 40 ft and less than 10 ft, all of them associated with amplitude anomalies caused by fracture swarms, and three of them associated with clear evidence from the LWD gamma ray and the mudlog.
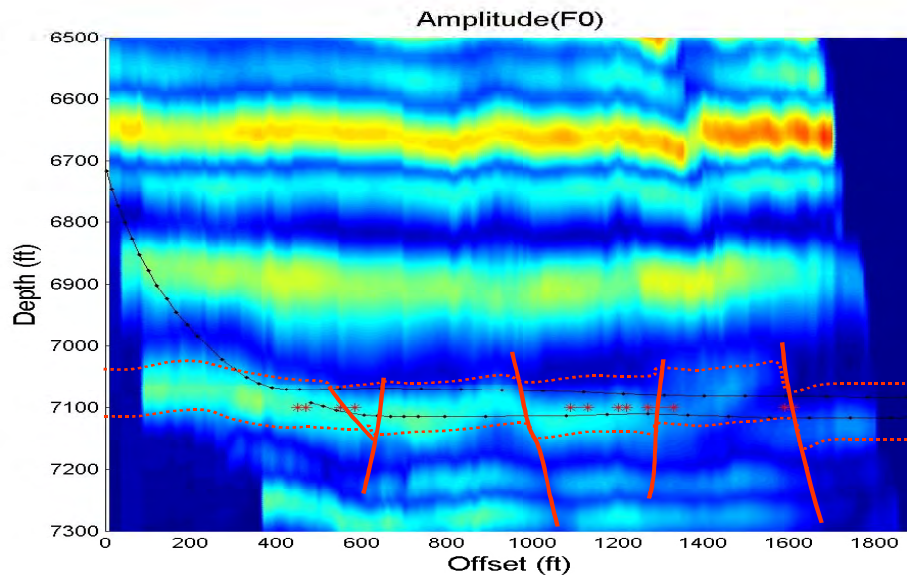
Figure 7.30: Interpretation of the VSP seismic section based on amplitude anomalies and the LWD gamma ray. The well path is shown in black and the asterisks (*) indicate the location of faults according to the interpretation of the LWD gamma ray.
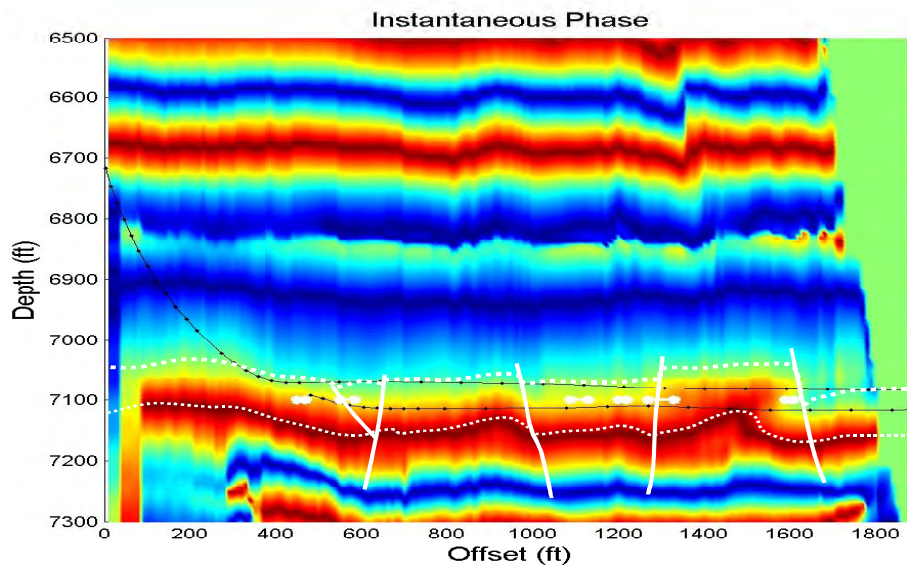

Figure 7.31: Interpretation of the VSP seismic section based on vertical offset of some reflectors and the LWD gamma ray. The well path is shown in black and the asterisks (*) indicate the location of faults according to the interpretation of the gamma ray.

7.6. Discussion

This study demonstrates the intrinsic relationship between antithetic conjugate faults and fracture swarms. The model of generation of conjugate faults as the result of hierarchical shearing and progressive deformation has been proposed by previous authors (Davatzes and Aydin, 2003), and follows the concepts initially established by Segall and Pollard (1983). In addition to introducing more evidence in support of this concept, this study explains the mechanics of fault-induced fracture localization, and establishes the conditions where it should be expected. Fracture localization can also occur associated with other processes, specially bending. However, the dominant mechanism of bending-induced fracturing in the subsurface might be normal faulting, since all-around tension over large regions is unlikely to occur in the subsurface.

The method employed to transform fracture spacing data into crack-density data uses assumptions and approximations that preclude its use in a more quantitative way. However, local calibration with other sources of information, like production data or well-log images, might allow a quantitative analysis. The method illustrates the relationship between fracture spacing at outcrops, confining stress, and crack density in the subsurface. It shows the value of outcrop data, and also their limitations.

Crack-density values obtained from fracture spacing, assuming $\beta=1$, overestimate the actual crack density in the subsurface. The critical crack density under the assumption of fracture saturation is 0.125, a value close the upper limit of 0.1 for the classical Hudson's model for cracked media. Rocks with crack densities above the critical crack density might elastically behave as suspensions, since they would have lost their elastic strength. If this is correct, the normalization to a maximum crack density of 0.1, applied to use Hudson's model, might be a more realistic representation of crack density distribution in the subsurface.

The combined interpretation of the walk-away VSP and LWD gamma-ray logs constrains the geologic model of the Hendersson-1 well at Neuville Field, Texas. Although overall the offsets and amplitude anomalies found in the seismic data agree with the location of fault zones interpreted from the log data, there are some discrepancies. Not all the amplitude anomalies correspond to fault zones, nor do all the fault zones show amplitude anomalies. Calcite-filled fractures might explain some of these discrepancies. A comparison to image-logs, rather than LWD gamma ray, would have been preferable. However, in the absence of image logs, the

combination of LWD gamma ray and resistivity logs with VSP surveys constitute an alternative for the identification of small faults and fracture swarms.

7.7.   Conclusions

Antithetic conjugate faults in brittle rocks constitute the ideal conditions for the development of fault-associated fracture swarms. Conjugate faults develop as the result of hierarchical shearing and progressive deformation. Antithetic conjugate faults develop when the remote maximum compressive stress field bisects the parent and splay faults. In this situation, the highest tension, or least compression, concentrates within the region bound by the faults.

Outcrop-based fracture-spacing data can be translated into subsurface crack-density data assuming that parallel fracture sets have similar surface roughness. This assumption is also necessary to incorporate the effect of confining stress. Although the assumptions made preclude a more rigorous quantitative analysis, the method can be used to model the seismic response of fracture swarms and small faults.

The concept of critical crack density is introduced to analyze the elastic behavior of fractured rocks. Above the critical crack density, the rock loses its elastic strength and behaves as a suspension. Under the assumption of fracture saturation, the critical crack density is about 0.125. This value is close to upper limit of 0.1 for Hudson's model for cracked media.

Seismic modeling indicates that flexure and amplitude anomalies can be used as indicators of small faults. Flexure can help to image faults with offsets of about 1/16 of the wavelength. Amplitude anomalies occur when the fault has a wide-enough fracture swarm (or damage zone) associated with it.

True amplitude and instantaneous phase provide the best images of subseismic faults from VSP data at Hendersson-1, Neuville Field. The seismic interpretation has been compared with a geologic interpretation of LWD gamma ray and mudlog data. Three out of the four faults observed in the seismic are also evidenced in the LWD log data. In the absence of image logs, the combination of VSP seismic and LWD logs constitute an alternative for identifying small faults.

7.8.   Acknowledgements

7.9.   References

Anderson, E. M., 1942, Dynamics of Faulting and Dyke Formation, Oliver and Boyd, Edinburgh and London, 191 pp.

Antonellini and Cruikshank, 1992, Geometry of Faults and Joints in Entrada Sandstone, Arches National Park, Utah: Stanford Rock Fracture Project Field Guide.

Aydin, A., 1973, Field Study and Theoretical Analysis of Some Small Faults in Montana, Wyoming, and Utah. M. Sc. Thesis: Stanford University.

Bai, T. and D. Pollard, 2000, Fracture spacing in layered rocks; a new explanation based on the stress transition, Journal of Structural Geology, **22**, 43-57.

Bandis, S. C., A. Lumsden, and N. Barton, 1983, Fundamentals of rock joint deformation, International Journal of Rock Mechanics and Mining Sciences & Geomechanics Abstracts, **20**, 249-26

Bracewell, R., 1965, The Fourier Transform and its Applications, McGraw-Hill Book Co., New York, 381 pp.

Davatzes, N. and A. Aydin, 2003, The formation of conjugate normal fault systems in folded sandstone by sequential jointing and shearing, Waterpocket monocline, Utah, Journal of Geophysical Research, B10, **108**, 2478, doi: 10.1029/2002JB002289.

Diegel, F.A., J.F. Karlo, D.C. Schuster, R.C. Shoup, and P.R. Tauvers, 1995, Cenozoic structural evolution and tectono-stratigraphic framework of the northern Gulf coast continental margin, in M. P. A. Jackson, D.G. Roberts, and S. Snelson, eds, Salt tectonics: a global perspective: AAPG Memoirs, **65**, 109-151.

Dula, W. F., Jr., 1991, Geometric models of listric normal faults and rollover folds, AAPG Bulletin, **75**, 1609-1625.

Ferril, D., A. Morris, J. Stamatakos and D. Sims, 2000: Crossing conjugate normal faults, AAPG Bulletin, **84**, 1543-1559.

Flodin, E., and A. Aydin, 2004, Evolution of a strike-slip fault network, Valley of Fire, southern Nevada, Geological Association of America Bulletin, **116**, 42-59.

Florez, J. M., and G. Mavko, 2002, Conjugate faults and fracture localization in brittle rocks. Eos Trans. AGU, **83**(47), Fall Meet. Suppl., Abstract T21B-1085.

Jev, B.I., C. Kaars-Sijpesteijn, M. Peters, N. Watts and T. Wilkie, 1993, Akaso Field, Nigeria, use of integrated 3-D seismic, fault slicing, clay smearing, and RFT pressure data on fault trapping and dynamic leakage: AAPG Bulletin, **77**, 1389-1404.

Gutierrez, M. and A. Nur, 2001, 3-D seismic interpretation of tectonic wrenching and faulting in La Cira-Infantas, The Leading Edge, **20**, 752-760.

Horsfield, 1980, Contemporaneous movement along crossing conjugate normal faults: Journal of Structural Geology, **2**, 305-310.

Hudson, J. A., 1981, Wave speeds and attenuation of elastic waves in material containing cracks. Geophysic. Journal Royal Astronom. Soc., **64**, 133-150.

Maerten, L., Pollard, D. D., Karpuz, R., 2000, How to constrain 3-D fault continuity and linkage using reflection seismic data: a geomechanical approach: American Association of Petroleum Geologist, **84**, 1311-1324.

Mavko, G., T. Mukerji, and J. Dvorkin, 1998: The Rock Physics Handbook, Tools for Seismic Analysis in Porous Media, Cambridge University Press, 329 pp.

McClay, K. R., 1995: 2D and 3D analogue modeling of extensional fault structures: templates for seismic interpretation: Petroleum Geoscience, **1**, 163-178.

Morley, C.K., R. Nelson, R. Patton and S. Munn, 1990, Transfer zones in the East African Rift system and their relevance to hydrocarbon exploration in rifts: AAPG Bulletin, **74**, 1234-1253.

Narr, W., 1990, Fracture density in the deep subsurface; techniques with application to Point Arguello oil field, American Association of Petroleum Geologists Bulletin, **75**, 1300-1323.

Nicol, A., J. Watterson, J. J. Walsh and C. Childs, 1994, The shapes, major axis orientations and displacement patterns of fault surfaces, Journal of Structural Geology, **5**, 483-495.

Nilsen, K. T., B. C. Venderville, J. T. Johansen, 1995, Influence of regional tectonics on halokinesis in the Nordkapp Basin, Barents Sea, in M. P. A. Jackson, D. G. Roberts, and S. Snelson, eds., Salt tectonics: a Global Perspective, AAPG Memoirs, **65**, 413-436.

Peel, F.J., C.J. Travis, and J.R. Hossack, 1995, Genetic structural provinces and salt tectonics of the Cenozoic offshore U.S. Gulf of Mexico: a preliminary analysis, in M. P. A. Jackson, D.G. Roberts, and S. Snelson, eds., Salt Tectonics: a Global Perspective, AAPG Memoirs, **65**, 153-175.

Sheriff, R., and L. P. Geldart, 1995, Exploration Seismology, 2nd edition, Cambridge University Press, 520 pp.

Segall, P., and D. Pollard, 1983, Nucleation and growth of strike slip faults in granite, Journal of Geophysical Research, **88**, 555-568.

Thomas, A., 1993, Poly3D: A Three-Dimensional Polygonal Element, Displacement Discontinuity Boundary Element Computer Program with Applications to Fractures, Faults and Cavities in The Earth's Crust, M. Sc. Thesis, Stanford University, 221 pp.

Watterson J., A. Nicol, J. J. Walsh and D. Meier, 1998, Strains at the intersections of synchronous conjugate normal faults: Journal of Structural Geology, **17**, 847-862.

Withjack, M.O., Q. Islam, and P. La Pointe, 1995, Normal faults and their hanging-wall deformation, an experimental study, AAPG Bulletin, **79**, 1-18.

Young, S., 2000, Conjugate normal faults in layered sedimentary rocks, Stanford Rock Fracture Project, Vol. 11, A-1.

Chapter 8

Conclusions

The purpose of this work has been the development of methods and concepts that integrate geology, rock physics and seismology for predicting reservoir quality with seismic data. This research has analyzed two separate aspects of this problem. The first chapters explore and exploit the concept of facies, since it is the fundamental link between sedimentology and rock physics. Chapters 2 and 3 review the concepts of depositional and diagenetic rock-physics trends and improve the current understanding of effective-medium models for sedimentary rocks, showing the distinction between sorting and packing effects in both elastic stiffness and porosity, and the role of pressure solution in the rock-physics diagenetic trend. Chapter 4 explores the patterns of various sedimentary sequences in different rock-physics planes, and shows how these patterns agree with predictions from models derived from theoretical and experimental studies. The last chapters analyze the case of fractured reservoirs. This part of the research focuses on the use of outcrop information and seismic data to predict fracture distribution in the subsurface. Based on outcrop descriptions, Chapter 5 shows a fundamental link between fracture hierarchies and sequence stratigraphy. Fracture distribution and dimensions are constrained by stratigraphy. It also documents clear examples of hierarchical shearing and progressive deformation, a new concept in geomechanics that explains the evolution of faults and fracture systems. Chapter 6 presents a method to create digital static models of fractured reservoirs that constitutes an alternative to the current techniques. Chapter 7 demonstrates a truly integrated approach, starting from the fundamental geomechanical understanding of fracture localization, analyzing the expected seismic response using rock-physics concepts, and finally applying these concepts to the interpretation of seismic attributes.

8.1. Rock-Physics Models for Granular Materials

Depositional lithofacies and, consequently, sequence stratigraphy play a definite role in the elastic and hydraulic properties of sedimentary rocks. This is particularly true in the case of uncemented, high-porosity sandstones, since sorting, clay-content and packing control the textural effect on both elastic and hydraulic properties, as demonstrated by several previous studies. This study shows that in the case of clean sandstones, the modified Hashin-Shtrickman lower bound can be used to distinguish between the effects of sorting and packing on the velocity-porosity plane.

Diagenetic lithofacies take a dominant role in controlling the elastic and hydraulic properties of clastic sedimentary rocks with depth. Although less critical, the influence of depositional lithofacies and sequence stratigraphy still remains, since they control the diagenetic processes. The effect of cementation has been extensively explained in previous studies. This work analyzes the effect of pressure solution, showing that it can produce an effect similar to the effect of incipient cementation. For the data set analyzed, pressure solution provides a more consistent model to explain the sudden increase in elastic stiffness at depths above the threshold temperature for quartz cementation. Although in principle it is difficult to distinguish between the effects of pressure solution and incipient cementation in the velocity-porosity plane, in the case of pressure solution the slope of the diagenetic trend may vary depending on the proportion of associated mechanical compaction.

The Digby-Rutter pressure solution model, derived in Chapter 3, constitutes the best estimate of the burial constant for high-porosity quartzarenites, given a burial history. The burial constant, the ratio between grain-contact area and grain radius, is the physical variable uniquely determined by the maximum burial depth. Three mechanisms can increase the grain-contact area: cementation, pressure-solution, and elastic deformation. Hertz-Mindlin elastic solution can be used to estimate the burial constant at shallow depths, although for low confining pressures Hertz-Mindlin overestimates the elastic stiffness mainly because of grain rotation and sliding. The depth interval where Hertz-Mindlin predictions match the actual data can be considered the interval where the aggregate has reached grain stabilization and pressure solution is not significant. In the data set analyzed this depth interval starts at about 500 m and ends at about 1000 m of maximum burial depth. Deeper intervals depart from Hertz-Mindlin predictions of burial constant and elastic stiffness, showing higher values than those predicted. In the data set analyzed, this departure occurs at depths well above the threshold temperature for quartz cementation. The

Digby-Rutter model demonstrates that this increment in the grain-contact area can be explained as the result of pressure solution.

8.2.   Rock-Physics Patterns of Clastic Depositional Sequences

The existing rock-physics models can be used to predict the patterns of clastic depositional sequences in the different rock-physics planes (velocity-density, velocity-porosity). The match between the predictions and the observed patterns goes beyond the well-known patterns predicted by the Marion-Yin model. In high-porosity uncemented sands, the most important factors controlling these trends are the proportion and type of mixed lithofacies. Dispersed mixtures of sand, silt and clay constitute the lithofacies with the highest impedance and the lowest porosity; whereas laminar mixtures present porosities and impedances that are intermediate between the clay-rich-shale and clean-sand end members.

The rock physics planes help to differentiate the mm- to cm- scale fabric of lithofacies using well log data. Patterns of sand-clay mixtures with mm- to cm-scale dispersed fabrics distinctively differ from those of mm- to cm-scale laminated fabrics. Four examples of decameter-scale lithofacies sequences have been documented, shown the differences between fluvial deposits, mud-rich deep water deposits, sand-rich deep water deposits, and low-energy shallow marine deposits.

The applicability of the observed patterns to predict the seismic properties of larger-scale sequences, or laterally away from well control, depends on the vertical and lateral persistence of the lithofacies assemblage. Similarly, the extrapolation of this patterns to similar depositional environments in other basins depends on the repeatability of these lithofacies assemblage and the diagenetic effects.

The variations in the rock physics patterns of clastic depositional sequences caused by diagenesis also follow the predictions from existing rock-physics models. As predicted by the Marion-Yin model, the inverted-V pattern for dispersed mixtures changes with depth; however, rather than confining pressure, the most likely mechanism is either pressure solution or incipient cementation. Preferential diagenesis in clean sandstones creates a pattern similar to the one predicted by the Jizba model.

8.3.   Characterization and Static Modeling of Fractured Reservoirs

The characterization of fractured reservoirs in the subsurface requires a fundamental understanding of the processes and properties controlling fracture distribution. Chapter 5 presents an outcrop study that analyzes the distribution of faults and fracture systems in a fold-and-thrust belt. The study demonstrates an important relationship between fracture hierarchies and stratigraphic hierarchies. Joints are confined by single beds, small faults by groups of beds (bedsets or parasequences), intermediate faults by sets of parasequences, and larger faults and fault zones by sequences. Spacing and dimensions of these different fracture hierarchies are controlled by both the thickness of the confining stratigraphic interval and the degree of shear strain. The evolution of fracture and fault systems is explained as the result of shearing of pre-existing features, development of splay fractures, and linking and growth of faults zones and splays. Overall, this process can be described as hierarchical shearing and progressive deformation.

A geostatistical method is proposed to generate static geologic models of fractured reservoirs. The technique constitutes an alternative to the discrete fracture networks currently used for this purpose. First, the fault architecture is modeled using stochastic simulation. Then, the fault zones are filled with different realizations of high-fracture-density, and the background is filled with low-fracture-density realizations. Both high-fracture-density and low-fracture-density realizations are generated using sequential Gaussian simulation. Outcrop descriptions provide the statistical parameters for both the stochastic fault modeling and the sequential Gaussian simulations. The technique, in essence an object-based indicator-simulation method, allows the reproduction of the fracture distribution observed at outcrops.

Antithetic conjugate faults in brittle rocks constitute the ideal conditions for the development of fault-associated fracture swarms, which produce dimming-amplitude anomalies in the seismic data. Outcrop-based geomechanical analysis documents fracture swarms associated with antithetic conjugate faults, and demonstrates that the concentration of the highest tensional, or least compressive, stress occurs when the remote stress field bisects the parent and splay conjugate faults. Seismic modeling shows that flexure and amplitude anomalies can be used as indicators of small faults in seismic data. These concepts have been successfully tested in the interpretation of VSP data at well Hendersson-1 (Neuville Field, east Texas). True amplitude and instantaneous phase provided the best image of sub-seismic faults from the VSP data. A comparison between the VSP interpretation and the geologic interpretation of

faults, based on LWD gamma ray and mudlog data, shows that three out of four seismically imaged faults where also interpreted in the LWD log. In the absence of image logs in horizontal wellbores, the combination of VSP seismic and LWD logs constitute and alternative to identify small faults.